Università degli Studi di Ferrara

DOTTORATO DI RICERCA IN
FISICA

CICLO XXVII

COORDINATORE Prof. Guidi Vincenzo

A multiwavelength view of the transient sky: gamma-ray bursts and other fast transients from optical to gamma-rays

Settore Scientifico Disciplinare FIS/05

Dottorando
Dichiara Simone

Relatore
Dott. Guidorzi Cristiano

Correlatore
Dott. Lorenzo Amati

Anni 2012/2014

Abstract

In this thesis I tackled several issues connected with the modern time domain astronomy focusing on the study of fast transient events, especially gamma–ray bursts (GRBs), which are the most energetic transient phenomena on stellar scale observed in the Universe.

Specifically, I studied the temporal variability of GRBs by means of Fourier analysis. To do this I adopted two different approaches: studying the average properties of all the GRB power density spectra (PDS) and then analysing each individual PDS.

I carried out the average PDS analysis on a sample of bright GRBs detected by the *BeppoSAX* Gamma–Ray Burst Monitor and the *Fermi* Gamma–ray Burst Monitor. The *BeppoSAX*/GRBM data, in the energy range 40–700 keV and with 7.8 and 0.5 ms time resolutions, allowed me to explore the average PDS at a unprecedented high frequencies (up to 1 kHz). It revealed a break around 1–2 Hz, previously found in *CGRO*/BATSE data. This break provide an important hint on the physical mechanism involved. It can be linked to several possible interpretations (intrinsic variability of the central engine, Lorenz factors distribution, wind thickness, etc.) The *Fermi*/GBM data, in the energy band 8–1000 keV, allowed me to explore the average PDS within a unprecedented broad energy range. My results confirm the energy dependence of the PDS slope extending it over a broader energy range, according to which harder photons have shallower PDS slope. Their physical implications are still not clear and will hopefully be matter of future study in the literature.

In the second approach I focused on the study of the individual PDS of different samples of long GRB. The PDS are modelled with a power–law or a bent power–law depending on the results of a specific Bayesian analysis based on a Markov Chain Monte Carlo algorithm. The PDS slope is found to correlate with both the peak energy $E_{\rm p}$ of the νF_ν spectrum and marginally the high–energy power–law index $\beta_{\rm B}$ estimated with a Band function. I also found that GRBs with a short dominant time–scale (τ, the typical duration of the pulses in the light curve) and long overall event duration ($T_{5\sigma}$)

are either very rare or do not exist at all, and according to the most popular models, in particular the so–called "internal shocks", there is no reason why this should be the case.

The same approach was adopted to search for periodic and quasi–periodic signal in the prompt emission of a sample of 44 bright short GRBs detected with *Fermi*/GBM, *Swift*/BAT, and *CGRO*/BATSE. The study of short GRB PDS had never been done before. The aim was to look for the observational signature of quasi–periodic jet precession which is expected from black hole–neutron star mergers, but not from double neutron star systems. Thus, this kind of search holds the key to identify the progenitor systems of short GRBs and represents the only direct way to constrain the variety of the progenitors, waiting for the gravitational wave detections. I tailored my search to the expected signal by properly stretching the light curves by an increasing factor with time. I calibrated the technique on synthetic curves first and then I applied it on the observed ones. I found no evidence of periodic or quasi–periodic signals in our GRBs sample. In particular, for the 7 unambiguously short GRBs with best S/N, I obtained significant upper limits for the amplitudes of the possible oscillations. This result suggests that BH–NS systems do not dominate the population of short GRB progenitors as described by the kinematic model of Stone et al. (2013).

Concerning the optical fast transients analysis, I explored the potential of a relatively new technique called "Singular Spectrum Analysis", which so far has found very few applications in high–energy astrophysics in spite of its versatility and potential. I used the two–dimensional extension of this technique to decompose the images collected by the RINGO3 optical polarimeter mounted at the focus of 2–m robotic Liverpool Telescope. In this way I can easily identify various noise components (statistical and systematic) and suppress the distortion elements. As a result, I noticed a slightly enhanced S/N ratio. The gain in terms of S/N (moving from the "raw" to the "processed" images) increased with longer exposure times.

Furthermore, a GRB optical followup activity was performed using the Las Cumbres Observatory Global Telescope Network (LCOGT). I developed dedicated software to carry out a rapid re–pointing and an effective photometric analysis of GRB optical counterparts. My work also contributed to improve the system efficiency through of a close interaction with the LCOGT team in its prime helping to calibrate the new instrumentation and testing of the network as a whole.

Finally I searched and compiled a catalogue of all the solar X–ray flares detected by *BeppoSAX*/GRBM. Using a properly accustomed detection algorithm I passed through-

out the satellite lifetime looking for possible transient events which mostly resembled solar X–ray flares. I reported information about position, duration and spectral hardness for each event spotting the cases for which a common *CGRO*/BATSE or Geostationary Operational Environmental Satellite (GOES) detection was recognised.

Summing up, I carried out multi–wavelength analysis, explored and applied several advanced timing analysis, statistical techniques and their applications to optical imaging to astrophysical transients with particular emphasis on GRBs, combining it with code development which is being used in real–time followup activity and prompt optical data analysis in the context of time domain astronomy.

Contents

Abstract ii

List of Figures vii

List of Tables xiii

Introduction 1

1 Average PDS of GRBs 7
- 1.1 Introduction . . . 7
- 1.2 Data analysis . . . 9
  - 1.2.1 *Fermi*/GBM data selection . . . 9
  - 1.2.2 *BeppoSAX*/GRBM data selection . . . 11
  - 1.2.3 PDS calculation . . . 12
  - 1.2.4 PDS fitting . . . 13
- 1.3 Results . . . 14
  - 1.3.1 Average PDS at different energy bands . . . 14
  - 1.3.2 FRED sub-sample . . . 16
  - 1.3.3 Average PDS up to high frequency . . . 17
- 1.4 Discussion . . . 20
- 1.5 Conclusions . . . 23

2 Clues on the GRBs prompt emission from PDS 33
- 2.1 Introduction . . . 33
- 2.2 Data analysis . . . 35
  - 2.2.1 Data selection . . . 35
  - 2.2.2 PDS modelling . . . 37
- 2.3 Results . . . 39
  - 2.3.1 White noise level . . . 43
  - 2.3.2 Dominant timescale vs. duration . . . 45
  - 2.3.3 Dominant timescale vs. Energy . . . 47
  - 2.3.4 PDS and peak energy $E_{\rm p}$ . . . 47
  - 2.3.5 GRBs with redshift . . . 50
  - 2.3.6 PDS and energy spectrum slope . . . 50
- 2.4 Conclusions . . . 53
- 2.5 AppendixA . . . 54
  - 2.5.1 PDS modelling: details . . . 54

3 A search for pulsations in SGRBs **86**
3.1 Introduction . . . 86
3.2 Theoretical Model . . . 87
3.3 Data selection . . . 90
3.3.1 Sample selection . . . 90
3.3.2 Short vs. intermediate GRBs . . . 91
3.4 Data analysis procedure . . . 92
3.5 Results . . . 96
3.6 Discussion and Conclusions . . . 102
3.7 AppendixB . . . 109
3.7.1 Calibration of the stretched PDS search . . . 109

4 2D–SSA and its applications **112**
4.1 Introduction . . . 112
4.2 Ringo3 . . . 113
4.3 Metod 2D-SSA . . . 114
4.4 Noise suppression procedure . . . 119
4.5 Results from the RINGO3 frames analysis . . . 121
4.5.1 Source extractor analysis . . . 122
4.6 Conclusions . . . 127
4.7 AppendixC . . . 130
4.7.1 R procedure - Removal by subtraction . . . 130
4.7.2 R procedure - Removal by division . . . 132

5 Optical followup **135**
5.1 Introduction . . . 135
5.2 Las Cumbres Observatory Global Telescope Network . . . 136
5.3 Software development . . . 137
5.4 GRBs Followup activity . . . 140
5.4.1 GRB 141121 Optical rebrightening . . . 142
5.5 Interactive Debugging and Response times . . . 144
5.5.1 2D-SSA on LCO frames . . . 147
5.6 Conclusions . . . 147

6 Solar X–Ray Flare Catalogue **149**
6.1 Introduction . . . 149
6.2 Detection Algorithm . . . 150
6.3 Solar Flare Sample . . . 155
6.3.1 May 04, 1998 – A spurious event . . . 156
6.4 Conclusions . . . 159

Conclusions **169**

Bibliography **173**

Acknowledgement **181**

List of Figures

0.1 The basic features of the fireball shock model are illustrated in this figure 3

0.2 This figure was taken from Beloborodov et al. (2000). It shows four different GRB light curves (background subtracted) alongside the related individual PDS. 5

1.1 Different time scales in terms of arrival times of photons A, B, C and D. From Piran (1999). 9

1.2 T_{90} distributions of a sample of 786 GRBs detected by *Fermi*/GBM in the 8–1000 keV energy band and of the subsample of 205 long GRBs selected for the analysis of the present work. 126 GRBs have $T_{90} < 3$ s, corresponding to $\sim 16\%$ of the whole sample. 10

1.3 Top (bottom) data show the average PDS for a sample of 205 (96) *Fermi*/GBM GRBs in the 8–1000 keV energy range with 64–ms (0.5–ms) time resolution. Solid lines show the best–fitting model obtained on the 64–ms data set, which shows a low frequency break at 5.5×10^{-2} Hz. The same model renormalised to the 0.5–ms data set, which was shifted for the sake of clarity. The bottom data set clearly exhibits a further break at high frequencies ($f \geq 1$ Hz). 14

1.4 Different slopes observed in the average PDS extracted on the three main energy ranges using a time resolution of 64 ms. Upside–down triangles, circles, and triangles show the 8–40, 40–200, and 200–1000 keV energy bands, respectively. The spectrum becomes shallower moving from low to high energies. 15

1.5 Average PDS of *Fermi* sample in the 15–150 keV energy range (circles) compared with the *Swift*/BAT result (squares) provided by G12. Both are calculated from 64–ms binned light curves. The two independent measures are compatible. The dashed line shows the best fit model for Fermi data. 16

1.6 The 10 FRED used in our PDS analysis. Each curve has a 64–ms bin time and is expressed in units of counts s^{-1} as a function of time. . . . 17

1.7 The average PDS of the FRED sample (detected with GBM) is shallower than the average PDS of the full *Fermi* sample. The energy band is 8–1000 keV for both sets with 64 ms time resolution. 18

1.8 The top, mid, and bottom average PDS refer to the *BeppoSAX* 0.5–ms, 7.8–ms resolution samples and to the *Fermi* subsample with S/N$\geq$ 60, respectively, for the 40–700 keV band. The break around 1–2 Hz is present in each set. The common best–fitting model is also shown, for both the *BeppoSAX* and *Fermi* data sets. The corresponding model parameters were bound to be equal for all the data sets, except for the normalisation terms. Upper limits are given at 2σ confidence. Data were shifted vertically for the sake of clarity. 19

1.9 The average PDS obtained from *BeppoSAX* samples without the white noise subtraction. The break at 1–2 Hz is still evident thanks to the signal being more than one order of magnitude higher than the white noise level. This rules out any bias due to possibly wrong white noise subtraction. 20

1.10 The power–law index of the average PDS in the frequency range $10^{-2} < f/\mathrm{Hz} < 1$ obtained from different data sets as a function of energy. Dashed line ($\alpha_2 \propto E^{-0.09}$) illustrates the α_2 dependence on energy as estimated from Fermi data. 22

2.1 Examples of individual PDS. Dashed lines show the corresponding best–fitting model. Blue and cyan dotted lines show the 2σ and 3σ threshold for possible periodic pulsations. *Top*: the PDS of GRB 101126A can be fitted with a simple PL model and background. *Bottom*:fitting the PDS of GRB 130504C significantly improves with a BPL model. 38

2.2 *Top panel*: sketch of a BPL PDS (thick solid line) as the result of the superposition of PDS of different pulses (thin dashed lines). The overall variance is dominated by pulses with similar timescales (thick dashed lines), whose frequency break there corresponds to the dominant time. The white noise level is also shown (dotted line). *Bottom panel*: the PL PDS is the result of the superposition of different pulses with different timescales, so that no break stands out in the total PDS, which looks like a power–law with a shallow index ($\alpha = 1.5$ in this example, thick dashed line). 40

2.3 In the figure is shown the distributions of the two populations of frequency breaks measured with the two different instruments. 41

2.4 Break frequency determined using the *BeppoSAX* light cuves on two different time intervals over which the PDS is extracted (error bars are 1σ). The $T_{5\sigma}$ interval is adopted throughout the present work; the PDS extracted over 100–s fixed duration intervals are shown for comparison purposes. Empty diamonds refer to GRBs whose PDS shows evidence for multiple break frequencies. Filled circles show the cases with a single break frequency. Equality is shown with solid line. 42

2.5 a part of the GRB 970627B light curve is illustrated in this figure. We can distinguish two different dominant time-scales. These intervals are directly related to the different frequency breaks observed in the two PDS extracted over the $T_{5\sigma}$ and the 100–s time intervals 43

2.6 Different power–law index distributions obtained for the three different energy ranges of the Fermi sample. 44

2.7 Distribution of α for both the used models. It is referred to the Fermi sample in the total energy range 44

2.8 White noise leves distribution resulting from the fitting procedure . . . 45

2.9 Relation between GRB duration $T_{5\sigma}$ and characteristic time τ for the GRBs best fitted with BPL for both *Fermi* (filled squares) and *BeppoSAX* (empty circles) sets. The dashed line shows the best proportionality model and the shaded area marks the $\pm 1\sigma$ region as estimated with the D'Agostini method. The point in the top left zone of the plot is the GRB 081028B, one of the few single–pulse GRBs for which the PDS identified the dominant timescale. 46

2.10 This picture show the average dominant timescale as a function of the energy range. The observed trend is described by the dashed line which illustrate a trend as $w \propto E^{-0.16}$ 47

2.11 Peak energy $E_{\rm p}$ of the time–averaged spectrum vs. the PDS index α for both models of *Fermi* GRBs: circles (triangles) correspond to PL (BPL). Top to bottom panels refer to the 8–40, 40–200, and 200-100 keV energy bands, respectively. Median 1–σ errors along both axes are shown in the bottom right of each panel. 49

2.12 Intrinsic peak energy $E_{\rm p,i}$ of the time–averaged spectrum vs. the PDS index α for both models of GRBs with measurable quantities. Median 1–σ errors are shown in the bottom right of each panel. 51

2.13 High–energy power–law index $\beta_{\rm B}$ of the energy spectrum modelled with the Band function vs. the PDS index α for both models of GRBs with measurable quantities out of the *Fermi* set. Error are 1σ. 52

2.14 Example of marginal posterior distributions for the pairs of parameters of the BPL model obtained from 10^4 simulated posterior simulations in the case of GRB 130504C (only 2000 points are shown for the sake of clarity). Solid lines show the contour levels. 57

3.1 This picture was taken from Stone et al. 2013.(a) Time evolution of $T_{\rm prec}$ assuming a viscously spreading disc structure given by Eq 3.4. Black dotted curves represent $\alpha = 0.1$, dashed magenta curves $\alpha = 0.03$, and solid blue curves $\alpha = 0.01$. Thick curves are for nearly equatorial disruptions with $a_{\rm BH} = 0.9$, while thin curves are for $a_{\rm BH} = 0.9$ and initial spin-orbit misalignment of 70°, or equivalently a nearly aligned disruption with $a \approx 0.5$. The dash-dotted red line is $\propto t^{4/3}$, the rough time evolution of $T_{\rm prec}$. (b) and (c) show $N_{\rm cycles}$, the accumulated number of cycles for 0.1 s $< t <$ 1 s and 0.01 s $< t <$ 1 s, respectively. 89

3.2 HR–T_{90} diagram for the three data sets: *Swift*/BAT (*top*), *Fermi*/GBM (*mid*), *CGRO*/BATSE (*bottom*). Each panel shows other catalog GRBs (crosses) for comparison. Filled circles, empty circles, and squares correspond to T–SGRBs, L–SGRBs, and P–IGRBs, respectively. Big (small) symbol sizes refer to whether each GRB can (cannot) provide useful constraints on the possible presence of pulsations using the stretched PDS technique (Section 3.4). 93

3.3 The PDS of GRB 120624A fitted using a Bayesian approach. The black solid line represents the best fit model (BPL in this case) while dashed and dotted lines give the probability thresholds at 4.5% and 0.27% to find a statistical fluctuation higher than these levels over the whole PDS, respectively. Confidence levels account for the multi–trial frequencies searched within a given PDS. 94
3.4 The two PDS are related to GRB 081209 and GRB 110705A. They show an excess above the 2σ threshold at frequency 246 Hz and 277 Hz, respectively 97
3.5 Distribution of the minimum detectable pulsation amplitude normalized to peak in the canonical PDS search. Two cases are shown: fixed time (solid) and 5σ (shaded) intervals. They refer to the 10–30 Hz frequency range. 98
3.6 Probability density function of p. 99
3.7 Minimum detectable fractional amplitude for an increasing precession period for 14 SGRBs, as determined from simulations in the stretched PDS search. Same symbols as in Figure 3.2 are used. 100
3.8 This image shows the PDS related to the simulated evolving-periodicity signal in the case of GRB 120323A. If the predicted modulation ($T_{\rm p} \propto t^{4/3}$) was hidden in the signal, I should detect it. I would be sensible to this kind of pulsations for amplitude ≥ 0.13 101
3.9 Distribution of the PDS slope as derived from the $[-3; 3]$ s interval (light shaded), and the 5σ interval (dark shaded). Also shown is the same distribution for a sample of 170 long GRBs. 103
3.10 The smoothed version of the original GRB 120323A light curve is illustrate at the top. The bottom panel exhibits how the predicted signal arises above the original one 110

4.1 This figure is taken from Warren et al. (2005). *Left*: the three-color composite Chandra image of Tychos SNR. The red, green, and blue images correspond to photon energies in the 0.95–1.26 keV, 1.63–2.26 keV, and 4.1–6.1 keV bands, respectively. *Right*: the Fe K line image with continuum (4–6 keV band) subtracted. The inner (outer) contour shows the location of the reverse shock (blast wave). 113
4.2 Sketch of the RINGO3 general configuration. The dichroic mirrors split the polarised "white light" and direct it towards the three different cameras: Red ("f"), Green ("d") and Blue ("e") 114
4.3 This image was taken from Golyandina et al. (2013). It simply describes the four main steps carried out by the SSA procedure 115
4.4 Singular values ordered from the higher to the lower ($\sqrt{\lambda_1} \geq \ldots \geq \sqrt{\lambda_K} \geq 0$) 116
4.5 Example of w–correlation matrix. Different shades of grey are related to different levels of correlation between the respective components. 117
4.6 This image was taken from Golyandina et al. (2013). The figure exhibits how the sliding window moves in the 2–dimensions 118
4.7 Classical example of 2D–SSA decomposition for a frame collected by RINGO3. The characteristic wavy components ere well identified (e.g. see 8 for low frequency and 16 for high frequency). 120

4.8 Two kinds of noises affecting the RINGO3 frames. *Left*: the linear wavy effect in the "Red" camera. *Right*: circular waves in the "Green" camera. 122
4.9 *Left*: original frame collected by the "Blue" camera. *Right*: cleaned frame in which I removed the average noise component computed for that filter. The wavy effect is not properly removed. 123
4.10 The potential of SSA method is illustrated in this figure. The wavy component is almost completely suppressed in this case. Also the vignetting effect is marginally reduced. 123
4.11 The logarithmic distributions of the S/N gain in the three cameras. The frames are collected during the optical observations of GRB 140430A. The S/N gain is expressed as the ratio between the S/N of a source in the cleaned image and the S/N of the same source in the raw frame . . 125
4.12 The S/N gain for each source is shown in comparison with the original S/N in the raw frame. 128

5.1 A world wide depiction of the Las Cumbres Observatory Global Telescope Network. 137
5.2 r'–band optical counterpart of GRB 140903A. The source lies right behind a 13.8 magnitude star and the photometry measure is heavily affected. 140
5.3 Optical counterpart of GRB 140928A. After ~ 2.8 days since the GRB I could identify the possible host galaxy $\sim 2.3''$ away from the OT. . . . 142
5.4 The lightcurve of GRB 141121A in the r' and i' filters. The first peak is followed by a second rebrightening. Solid and dashed lines show the shallow decay after the first peak ($\alpha \sim -0.8$) and the final steep decay after the rebrightening ($\alpha \sim -1.7$), respectively. 143
5.5 GRB 141121A X-ray lightcurve (XRT data) is shown with the optical ones (r' and i') to emphasise the possible common behaviour. 143
5.6 Fading GRB 141121A optical counterpart at 6.4 days (left) and at 11.4 days (right). The possible host lies in the nearby. This source lies at $\sim 2.8''$ which corresponds to a distance of ~ 23 kpc, assuming $z = 1.47$ and a standard cosmology (ΛCDM). 144
5.7 This picture was taken from Savaglio et al. (2009). R_{AB} (left plot) and K_{AB} (right plot) observed magnitudes as a function of redshift, for GRB hosts (filled circles) and Gemini Deep Deep Suvey field galaxies (crosses). The filled circles with white dots are short-GRB hosts. The red filled circle shows the GRB 141121A host candidate. 145
5.8 Processed frame collected by the SBIG camera on the south african 1–m telescope (dome C). After the reduction process the source (blue circle) disappeared leaving the ring–shaped structure on the CCD. 146
5.9 Example of 2D-SSA cleaning applied to i' frames obtained with the Spectral camera mounted on the Haleakala 2–m telescope. The fringing is completely removed using this method. 147

6.1 Example of solar X–ray flare automatic detection. The dotted line is the best fit model for the background. As soon as the transient event arises, the model exhibits trends which make the run test fail. This solar flare occurred on April 26, 2001 (UT 13:03:39). Time is expressed in terms of "Second of Day" (SOD). 152
6.2 *BeppoSAX* payload. The Sun was mostly facing GRBM unit 2. 153

6.3 Light curve of GRB 000713B in the two energy ranges $40 - 700$ kev and > 100 keV. 154
6.4 The typical emission originated from particles avalanche interaction observed just before the SAGA "gap" in the light curve. 154
6.5 Distribution of the spectral hardness ratio for our sample of solar X–ray flare candidates. 156
6.6 Solar X–ray flare of April 2, 2001. In this case the flux was so high that the ratemeter recycled. The blue line shows the recycle limit. The bottom panel shows the reconstructed light–curve. The time is referred to the start of the $T_{5\sigma}$ time. 157
6.7 Two events observed on May 4, 1998. Different light–curves are related to different GRBM units. 158
6.8 The rigidity of the solar energetic particles trapped in the Earths magnetosphere is shown in this figure taken from Adriani et al. (2015) . . . 158

List of Tables

1.1 Time and Peak count rate. *Fermi*/GBM full sample including 205 GRBs. The PDS is calculated in the time interval reported. 24
1.1 Time and Peak count rate. *Fermi*/GBM full sample including 205 GRBs. The PDS is calculated in the time interval reported. 25
1.1 Time and Peak count rate. *Fermi*/GBM full sample including 205 GRBs. The PDS is calculated in the time interval reported. 26
1.1 Time and Peak count rate. *Fermi*/GBM full sample including 205 GRBs. The PDS is calculated in the time interval reported. 27
1.2 White noise level (Leahy normalisation). *Fermi* sample. 28
1.3 Time and Peak count rate. *BeppoSAX*/GRBM HR sample including 42 GRBs. 29
1.4 White noise level (Leahy normalisation). *BeppoSAX* HR sample. . . . 30
1.5 31
1.6 Best fit parameters of the average PDS for different samples of GRBs . 32

2.1 *Fermi* sample of 398 GRBs. Each PDS is calculated in the time interval reported. 58
2.1 *Fermi* sample of 398 GRBs. Each PDS is calculated in the time interval reported. 59
2.1 *Fermi* sample of 398 GRBs. Each PDS is calculated in the time interval reported. 60
2.1 *Fermi* sample of 398 GRBs. Each PDS is calculated in the time interval reported. 61
2.1 *Fermi* sample of 398 GRBs. Each PDS is calculated in the time interval reported. 62
2.1 *Fermi* sample of 398 GRBs. Each PDS is calculated in the time interval reported. 63
2.1 *Fermi* sample of 398 GRBs. Each PDS is calculated in the time interval reported. 64
2.2 *BeppoSAX* sample of 44 GRBs. The PDS is calculated in the time interval reported. 65
2.3 Best–fitting model and parameters for each GRB of the *Fermi* sample events in the total 8–1000 keV energy band. 66
2.3 Best–fitting model and parameters for each GRB of the *Fermi* sample events in the total 8–1000 keV energy band. 67
2.3 Best–fitting model and parameters for each GRB of the *Fermi* sample events in the total 8–1000 keV energy band. 68

2.3 Best–fitting model and parameters for each GRB of the *Fermi* sample events in the total 8–1000 keV energy band. 69
2.3 Best–fitting model and parameters for each GRB of the *Fermi* sample events in the total 8–1000 keV energy band. 70
2.3 Best–fitting model and parameters for each GRB of the *Fermi* sample events in the total 8–1000 keV energy band. 71
2.4 Best–fitting model and parameters for each GRB of the *Fermi* sample events in the 8–40 keV energy band. 72
2.4 Best–fitting model and parameters for each GRB of the *Fermi* sample events in the 8–40 keV energy band. 73
2.4 Best–fitting model and parameters for each GRB of the *Fermi* sample events in the 8–40 keV energy band. 74
2.4 Best–fitting model and parameters for each GRB of the *Fermi* sample events in the 8–40 keV energy band. 75
2.5 Best–fitting model and parameters for each GRB of the *Fermi* sample in the 40–200 keV energy band. 76
2.5 Best–fitting model and parameters for each GRB of the *Fermi* sample in the 40–200 keV energy band. 77
2.5 Best–fitting model and parameters for each GRB of the *Fermi* sample in the 40–200 keV energy band. 78
2.5 Best–fitting model and parameters for each GRB of the *Fermi* sample in the 40–200 keV energy band. 79
2.5 Best–fitting model and parameters for each GRB of the *Fermi* sample in the 40–200 keV energy band. 80
2.5 Best–fitting model and parameters for each GRB of the *Fermi* sample in the 40–200 keV energy band. 81
2.6 Best–fitting model and parameters for each GRB of the *Fermi* sample in the 200–1000 keV energy band. 82
2.6 Best–fitting model and parameters for each GRB of the *Fermi* sample in the 200–1000 keV energy band. 83
2.7 Best-fitting model and parameters for each GRB of the *BeppoSAX* sample in the total 40–700 keV energy band. 84
2.8 Best-fitting model and parameters for each GRB of the *BeppoSAX* sample in the total 40–700 keV energy band. PDS are derived from a 100–s time interval. 85

3.1 2σ upper limits the amplitude obtained with the stretched synthetic light curves analysis detected by the *Fermi* and *BeppoSAX*. 102
3.2 Best-fitting model and parameters for each SGRB of the total sample. . 106
3.2 Best-fitting model and parameters for each SGRB of the total sample. . 107
3.2 Best-fitting model and parameters for each SGRB of the total sample. . 108

4.1 Source Extractor analysis results. 126

5.1 LCOGT Network Imager Characteristics. 138
5.2 Short list of optical transients re–pointed using the LCO telescopes. . 141

6.1 Comprehensive list 380 Solar X–ray flare candidates detected by *BeppoSAX*/GRBM and discovered using our algorithm. 160

6.1 Comprehensive list 380 Solar X–ray flare candidates detected by *BeppoSAX*/GRBM and discovered using our algorithm. 161
6.1 Comprehensive list 380 Solar X–ray flare candidates detected by *BeppoSAX*/GRBM and discovered using our algorithm. 162
6.1 Comprehensive list 380 Solar X–ray flare candidates detected by *BeppoSAX*/GRBM and discovered using our algorithm. 163
6.1 Comprehensive list 380 Solar X–ray flare candidates detected by *BeppoSAX*/GRBM and discovered using our algorithm. 164
6.1 Comprehensive list 380 Solar X–ray flare candidates detected by *BeppoSAX*/GRBM and discovered using our algorithm. 165
6.1 Comprehensive list 380 Solar X–ray flare candidates detected by *BeppoSAX*/GRBM and discovered using our algorithm. 166
6.1 Comprehensive list 380 Solar X–ray flare candidates detected by *BeppoSAX*/GRBM and discovered using our algorithm. 167
6.1 Comprehensive list 380 Solar X–ray flare candidates detected by *BeppoSAX*/GRBM and discovered using our algorithm. 168

To my grandfather

Giovanni Santarelli

Introduction

The interest in the field of Time Domain Astronomy (TDA) has grown considerably in the latest years thanks to the development of synoptic sky surveys which have been providing and will provide us with large data sets.

Multiwavelength transient astronomy is being revolutionised by several facilities working from the optical to the gamma–ray energy ranges. Several optical telescopes are involved in this field, such as the Palomar Transient Factory (Law et al. 2009, PTF, and intermediate PTF, iPTF), and the Panoramic Survey Telescope and Rapid Response System (Pan–STARRS), and will be the more so with advent of the Large Synoptic Survey Telescope around 2020 (Ivezic et al. 2008, LSST). LSST will image the entire Southern sky every few nights and is expected to issue $\sim 1 \times 10^6$ alerts per night, of which around $10,000$–$100,000$ will be new explosive transients. In the gamma–ray regime, the two satellite *Swift* and *Fermi* allow us to discover of several fast transient events up to the very high energies (up to 300 GeV) achieved with the *Fermi*/Large Area Space Telescope (Atwood et al 2009, LAT). Other new facilities such as the Square Kilometre Array (Carilli & Rawlings 2004, SKA) and the Cherenkov Telescope Array (Actis et al 2011, CTA) will open the temporal window on new regions of the electromagnetic spectrum.

Goals of these surveys are the identification, characterisation and monitoring of the transient sky.

The study of the temporal properties of these sources is of key importance. For example, some astrophysical phenomena such as explosion or mass accretion processes (related to strong gravity and general relativity), can be effectively explored through timing studies. TDA concerns many fields: from the Solar System to cosmology, stellar structure formation and evolution, ultra-relativistic processes. TDA was the key for the discovery of theoretically predicted phenomena: e.g., supernova shock break-outs (when a soft X–ray peak marks the final disruption of a star at the end of its life by means of a shock propagating outward), or tidal disruption events (when a star–sized object passes too close to a supermassive black hole, which then disrupts it and accretes

some of its mass). From these large data sets a wealth of new transient sources is to be expected in the near future, as is already the case for new classes of SNe.

Furthermore we usher in an era when astrophysical objects might be routinely detected through non–electromagnetic messengers. The IceCube (Karle et al. 2003) detector in Antarctica is engaged in searches for cosmic neutrinos, and this will be joined by KM3Net in the Northern hemisphere (Ulrich et al. 2014). So TDA does not exclusively concern the electromagnetic emission, but also involves the study of astrophysical neutrinos, cosmic rays, and gravitational waves (GW). In 2015 the Advanced LIGO (Harry et al. 2010) and Advanced Virgo (Degallaix et al. 2013) detectors will start operating and searching for GW emission from coalescing neutron star and black hole binaries. The challenge for astronomers will be to detect the electromagnetic counterparts of these violent events.

The possible GW detection would finally provide one of the most important confirmations of Einstein's general relativity.

In this context the study of time variability will characterise the behaviour of the transient counterparts at different energy ranges. The most common approach is based on Fourier techniques, which decompose the temporal power over different frequencies and identify possible characteristic time–scales and/or periodic/quasi-periodic signals.

The study of the temporal variability in various branches of science and engineering has propelled the development of several techniques, both in frequency and in time domains. Variability studies in the case of astronomical sources are crucial to gain insight over the dynamical and microphysical time–scales, and therefore on the size of the emitting region as well as the nature of the emission process. This is of key importance in the X–ray and γ–ray domain, where remarkable flux variations are observed over time–scales from ms to years. The Fourier spectral analysis is fundamental in the study of stationary and non–stationary processes (Guidorzi 2011), since it provides an immediate physical interpretation as a power-frequency distribution. The Fourier power density spectrum (hereafter, PDS) in particular decomposes the total variance of a given time series to the different frequencies thanks to Parseval's theorem (e.g., van der Klis 1989). PDS analysis and related tools are suitable to both search for possible periodic signals hidden in the data, and to characterise the so-called "red noise" connected with the presence of aperiodic variability.

My work was particularly focused on the study and on the characterisation of gamma–ray burst (GRB) prompt emission. GRBs are among the most energetic events in the Universe on the stellar scale. They outshine the gamma-ray sky for an interval of

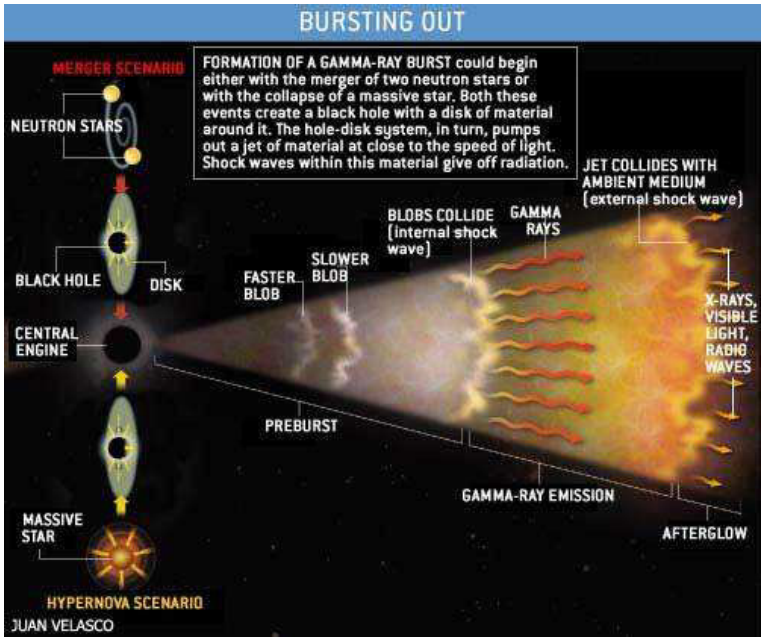

Figure 0.1 The basic features of the fireball shock model are illustrated in this figure

time between a few seconds and one thousand seconds, emitting an isotropic equivalent energy up to 10^{54} erg. A variety of physical models has been put forward to explain the nature of these explosions: the standard scenario consists of the fireball internal-external shock model (Piran 2004 and references therein), where a GRB is produced as a result of the dissipation of the kinetic energy of an ultra–relativistic flow in internal collisions. The long wavelength radiation emission, called afterglow visible up to days and weeks after the explosion instead arises when the flow is slowed down by shocks with the surrounding cirmcumburst matter (external shocks). Figure 0.1 shows an artist conception of the model.

GRBs are divided into two main families based on the duration and the hardness ratio: long GRBs ($T_{90} > 2$ s) and short GRBs ($T_{90} < 2$ s). The exact nature of the progenitor as well as the gamma-ray production mechanism are yet to be unveiled. This makes the study of the temporal properties of the associated optical transient very important. In the case of GRBs, different degrees of variability are observed over time–scales spanning from millisecond (Bhat et al. 1992; Walker et al. 2000) up to several seconds. For some GRBs, variability seems to be mostly concentrated on either a unique time scale or more distinct time scales: a fast component characterised by sub-second variability, superposed to a slow one which comprises the broad pulses and the overall temporal structure (Scargle et al. 1998; Vetere et al. 2006; Margutti 2009; Gao et al. 2012). Moreover, a better characterisation of variability can help to constrain the radiation mechanism and dissipation processes responsible for the burst itself, which

is still one of the least understood aspects of the overall GRB phenomenon (e.g., see the reviews by Ghisellini 2011; Zhang 2011). In this work I tackled these issues using two different approaches. At first, I studied the average PDS of a sample of long GRBs considering the different light-curves as different realisations of the same stochastic process. This way, one gains insight into the properties of this general process. The results of this analysis are fully expounded in Chapter 1. By contrast, in Chapter 2 each long GRB time profile was considered individually as a standalone stochastic process. In the first approach, the average PDS values and related uncertainties are the mean and standard deviation of the corresponding power distribution. While for this second analysis the statistical treatment is a bit more complex. The case of an individual PDS of a highly non–stationary, and short–lived stochastic process (Figure 0.2) was tackled properly with the aid of a Bayesian Markov Chain Monte Carlo technique.

The same approach was used in Chapter 3 to study the timing behaviour of short GRBs and to test a specific theoretical model proposed to explain their emission. A more innovative technique is Singular Spectrum Analysis (SSA), which decomposes time histories on a data-driven set of eigenvectors, and not on a predefined set such as the Fourier harmonics. This technique, introduced some 30 years ago, but still almost unknown in high–energy astrophysics, holds a great potential. It disentangles the different components possibly present within a given time series. Its broad applicability is proved in many different fields: from economy, to biology, to geophysics. In this respect, SSA turns out to be complementary to traditional Fourier-based techniques. This technique can be useful to identify and characterise the light–curve behaviour of the detected transient sources at different energy ranges. Furthermore it is suitable to study the temporal variability of the optical counterpart. In this thesis (Chapter 4) I used the two–dimensional extension of this technique for imaging analysis. Thus, I tried to suppress the noise components affecting the images collected by RINGO3, the imaging polarimeter currently deployed at the focus of 2–m robotic Liverpool Telescope.

Another part of my work concerned the real time GRBs optical followup activity. All the software development work and results are summarised in Chapter 5. The observations were achieved using the 1–m and 2–m telescopes of the Las Cumbres Observatory Global Telescope Network.

Lastly, a catalogue of all the solar X–ray flares detected by *BeppoSAX*/GRBM was produced. A complete list and a description of the detection algorithm are reported in Chapter 6. Solar X–ray flares are some of the most powerful transient energy emissions released by the Sun and a definitive explanation of their physical mechanism is still

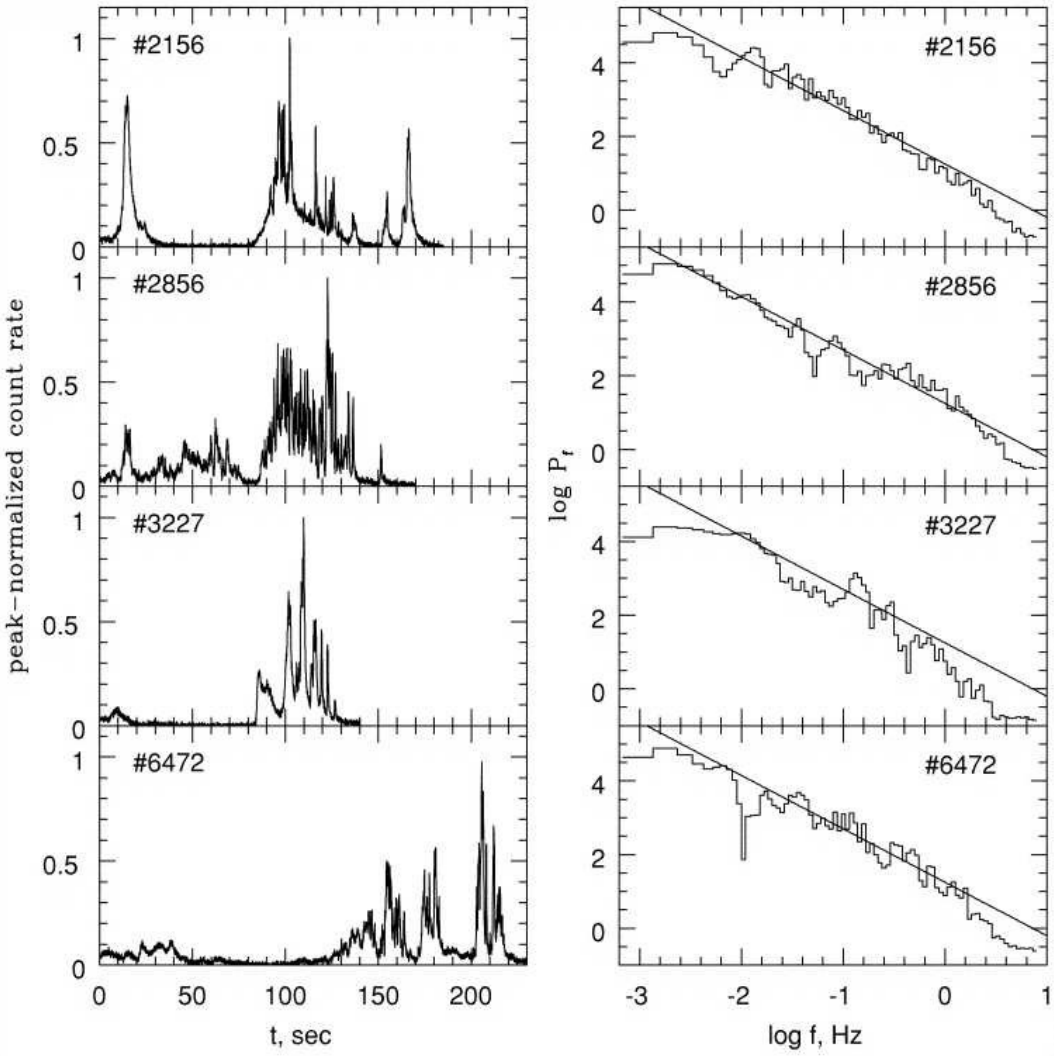

Figure 0.2 This figure was taken from Beloborodov et al. (2000). It shows four different GRB light curves (background subtracted) alongside the related individual PDS.

missing.

In this thesis I tackled different open questions of modern time domain astronomy moving from the γ to the optical waveband. Data analysis was carried out through different techniques. Last but not least, I contributed to develop several tools to carry out real–time followup activities. The work is organised in 6 chapters as described above. All the results are summarised in the Conclusions.

Chapter 1

Average power density spectrum of long GRBs detected with *BeppoSAX*/GRBM and with *Fermi*/GBM

1.1 Introduction

Together with the energy spectrum, the temporal behaviour of gamma–ray burst (GRB) light curves holds the key to both the physical mechanism responsible for the production of the prompt gamma rays and the distance from the stellar progenitor at which the energy dissipation into gamma–rays takes place. More than a decade after the first GRB afterglow discoveries, these key questions concerning the GRB prompt emission are yet to be answered. The typical observed durations of pulses span from hundreds milliseconds up to several seconds (e.g., Norris et al. 1996). A proper characterisation of the temporal properties at different energy bands is crucial to provide clues to the energy dissipation process at the origin of the gamma–rays. In this context, the average power density spectrum (PDS) provides a way to characterise the phenomenon in terms of a stochastic process starting from the null hypothesis that each long GRB is a different realisation of a general unique process. In other words, we assume that the same mechanism can explain the variability observed in different light curves, while the observed variety is due to different conditions, which may vary from different GRBs.

The question whether GRB light curves might entirely be explained in terms of

different realisations of a unique stochastic process characterised by a pure red noise, is still open. Interestingly, recent analyses have found evidence for the presence of deterministic components (as opposed to pure stochastic noise) ruling the evolution of a GRB light curve and giving rise to a chaotic behaviour (Greco et al. 2011).

In the context of a pure stochastic process entirely characterised by red noise, Beloborodov, Stern & Svensson, in 1998 and 2000 (hereafter, BSS98 and BSS00), studied the average PDS of 527 GRBs detected by the Burst and Transient Source Experiment (BATSE; Paciesas et al. 1999) aboard the *Compton Gamma Ray Observatory* (CGRO) in 25–2000 keV energy band, revealing a typical power–law behaviour spanning almost two orders of magnitude in frequency, from a few 10^{-2} to $\sim$ 1 Hz. The power–law index they found is compatible with 5/3, which is what one expects for the Kolmogorov spectrum of velocity fluctuations within a medium characterised by fully developed turbulence. They also found a sharp break around 1–2 Hz. These results were also supported by the INTEGRAL data analysis of a sample of 10 bright GRB (Ryde et al. 2003).

A recent analysis of the average PDS of the *Swift* Burst Alert Telescope (BAT; Barthelmy et al. 2005) data set in the 15–150 keV energy band was carried out for the first time in the GRB rest-frame average, thanks to the large number of GRBs detected by Swift with measured redshift. No significant differences were found between the observer and the rest-frame behaviour (Guidorzi et al. 2012; hereafter, G12). Notably, no evidence for the break around 1–2 Hz was found in the 15–150 keV band. One of the main goals of my analysis will be to verify and, possibly, to better constrain this break. The confirmation of this break would yield important informations concerning the physical process involved with respect to the different possible interpretation. For example it can be related to a characteristic time interval of the central engine emission as well as to the radial time scale. The radial time is the observed interval from the arrival of the first to the last photon (A and D in Fig. 1.1), if most of the emission takes place between R and 2R and the emitting material is an infinitely thin relativistic shell with Lorentz factor Γ (Piran 1999; Margutti 2009).

In the present work I aim to study the average PDS in two different unexplored regimes with two different data sets. The goal of this analysis is twofold: i) I address the same average PDS analysis through two additional data sets from independent satellites and detectors; ii) these data sets allow us to study the average PDS at very high frequency (up to 1 kHz) with the *BeppoSAX*/Gamma–Ray Burst Monitor (GRBM; Frontera et al. 2009 and references therein) and across a broad energy band such that

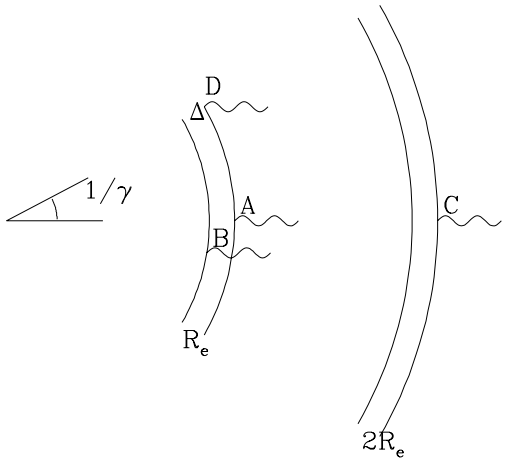

Figure 1.1 Different time scales in terms of arrival times of photons A, B, C and D. From Piran (1999).

of *Fermi*/Gamma-ray Burst Monitor (GBM; Meegan et al. 2009) from 8 keV to 1 MeV.

Uncertainties on best-fitting parameters are given at 90% confidence for one interesting parameter unless stated otherwise.

1.2 Data analysis

1.2.1 *Fermi*/GBM data selection

We initially started with 829 GRBs detected and covered by GBM from July 2008 to December 2011. For each GRB I took the two most illuminated NaI detectors, for which I extracted the corresponding light curves with 64 ms resolution, which I then added to have a single light curve. In this early stage I considered the Time Tagged Event (TTE) files, which hold information about trigger time and energy channel of each detected photon. I excluded all GRBs with no TTE file. In some cases the TTE data do not cover the whole event and thus were not considered for the present analysis. The GRBs durations were expressed in terms of T_{90} (Figure 1.2), which I estimated from the background-subtracted light curves. Background subtraction was performed through interpolation using a polynomial of either first or second order.

We excluded short duration bursts by requiring $T_{90} > 3$ s. At this stage I were left with a sample of 650 GRBs. I then rejected all the GRBs with a poor signal–to–noise ratio (S/N) excluding those with peak rate less than 50 count s^{-1}. Spikes caused by

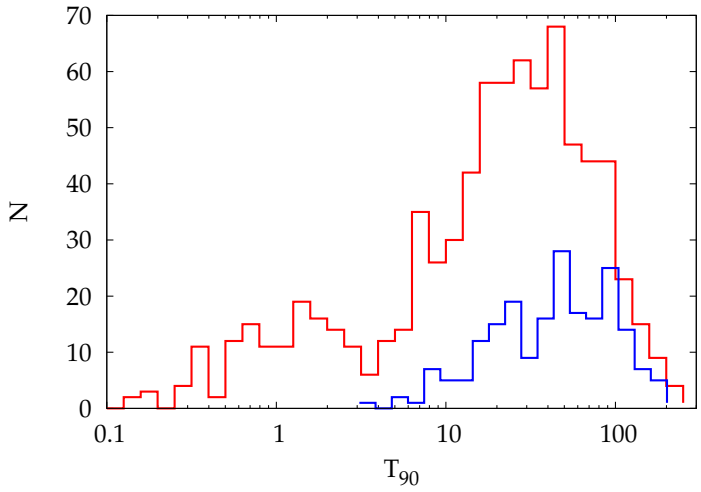

Figure 1.2 T_{90} distributions of a sample of 786 GRBs detected by *Fermi*/GBM in the 8–1000 keV energy band and of the subsample of 205 long GRBs selected for the analysis of the present work. 126 GRBs have $T_{90} < 3$ s, corresponding to $\sim 16\%$ of the whole sample.

radiative decay of some particles dragged in the Earth magnetic field that interact with the spacecraft payload were observed in 22 light curves, whose GRBs were therefore rejected from our sample (Meegan et al. 2009).

The extraction of the light curves for each GRB in different energy ranges was made retrieving the data [1] and processing them with the HEASOFT package (v6.12) following the *Fermi* team threads [2]. We selected different energy ranges using the tool `fselect`. We considered the total energy range of the NaI detectors (8–1000 keV) and three main sub-bands (8–40, 40–200, 200–1000 keV). Light curves were extracted using the `gtbin` tool. Finally I calculated the PDS for each GRB of the resulting sample in the time interval from the earliest to the latest bin whose counts exceed the 5σ signal threshold above background (hereafter, $T_{5\sigma}$). Table 1.1 reports the time interval and peak count rate for each selected GRB in the 8–1000 keV band. Moreover, I also selected a subsample of events with S/N$\geq$ 60 to better explore the high–frequency behaviour. For this sample I extracted the light curves with a time resolution of 0.5 ms (hereafter, very high resolution or VHR curves) both in the same energy band explored by the GRBM (40–700 keV) and in the total NaI energy band (8–1000 keV).

We then subtracted the white noise and checked its Poissonian nature related to the statistical fluctuations observed in light curves. To check the Poissonian character of

[1] http://legacy.gsfc.nasa.gov/fermi/data/gbm/burst
[2] http://fermi.gsfc.nasa.gov/ssc/data/analysis/scitools/gbm_grb_analysis.html

noise I estimated the mean power at $f > 6$ Hz (Table 1.2) and compared it against the value of 2, namely the expected value of a χ^2_2-distribution for pure Poissonian variance in the Leahy normalisation (Leahy et al. 1983).

Furthermore, I grouped the background-subtracted PDS along frequency so as to fulfil a 3σ significance criterion for each grouped bin. Following the same procedure by G12 for the *Swift*/BAT data, the selection excluded in each sample (total, low, middle and high energy range) the GRBs whose grouped PDS collected less than 4 grouped frequency bins.

We ended up with 205 GRBs that will be referred to as the *Fermi* sample with a 64 ms time resolution in the total energy range and, respectively, we ended up with 155, 201 and 74 in the three energy sub-bands: 8–40, 40–200, and 200–1000 keV (low, middle and high energies). The VHR sample includes 96 GRBs whose light curves were extracted in the 8–1000 keV and 40–700 keV energy bands. For each of these samples I calculated and modelled the average PDS.

1.2.2 *BeppoSAX*/GRBM data selection

For the *BeppoSAX*/GRBM GRB sample I started from the GRB catalogue (Frontera et al. 2009) by selecting the GRBs fully covered by the high time resolution mode, available only for those which triggered the GRBM on-board logic. I then excluded the GRBs whose light curves were hampered by gaps in the time profiles. Finally I selected the GRBs with the highest S/N (> 40) and ended up with a sample of 89 GRBs. This requirement was motivated by the need of having very good statistical quality even at high frequencies.

Two different kinds of time resolution are available in the GRBM data: i) light curves with 7.8125 ms resolution from -8 to 98 s from the on-board trigger time (hereafter, these curves are referred to as high-resolution or HR curves); ii) light curves with $\sim$ 0.5 ms for the first 10 s from the trigger time (VHR curves). Therefore the corresponding Nyquist frequencies are respectively 64 Hz and 1 kHz. The VHR light curve can be obtained only for a sub-sample of 74 GRBs For each GRB I extracted the PDS in two different time intervals, depending on the type of light curve: the PDS of the HR curves was extracted on the $T_{5\sigma}$, like in the case of *Fermi*/GBM data (Section 1.2.1), whereas that of the VHR curves was forcibly bound to the first 10 s from the trigger time. Table 1.3 reports the time interval and peak count rate for each selected GRB of the HR set. Also for *BeppoSAX* data the final PDS obtained for each GRB of each sub-sample was grouped according to a 3-σ significance criterion excluding the events

of the HR sample with fewer than 4 grouped bins and those with of the VHR sample with fewer than 10 bins. Consequently, the final samples include 42 GRBs with HR data and 25 GRBs with VHR data. Hereafter, the two samples are referred to as the *BeppoSAX* HR and the VHR sample, respectively.

1.2.3 PDS calculation

Each PDS was calculated through the mixed-radix FFT algorithm implemented within the GNU Scientific Library (Galassi et al. 2009),[3] which does not require the total number of bins to be a power of 2 (Temperton 1983) similarly to what was done for the *Swift*/BAT sample (G12). We calculated the PDS for each GRBs adopting the Leahy normalisation. For each individual PDS the background level, corresponding to the white noise due to counting statistics, was initially estimated by fitting with a constant the high-frequency range, where the signal is negligible with respect to the statistical noise.

Within the Leahy normalisation, a pure Poissonian noise corresponds to a power value of 2. Therefore I checked the high-frequency constant value for the power averaged out among all the PDSs. For *Fermi* sample the mean value of white noise level is estimated at 1.99 ± 0.02 for $f > 6$ Hz, fully consistent with a Poissonian variance. For the *BeppoSAX* samples the PDS shows evidence for the presence of a small, significant extra-Poissonian variance of $(3.7 \pm 1.2)\%$ and $(0.94 \pm 0.35)\%$ for the HR and the VHR samples, respectively, in addition to the statistical white noise. These values were estimated in the frequency range above 50 Hz.

The statistical noise was removed in two different way for different cases. For the *Fermi* sample, noise was assumed to be perfectly Poissonian, compatibly with what I found above. Instead, for the *BeppoSAX* samples it was obtained from fitting the PDS with a constant value estimated at sufficiently high frequencies ($f > 50$ Hz) for each event of the HR sample. The estimated background levels are reported in Table 1.4. As can be seen in Table 1.5 for VHR data, the white noise becomes dominant already at $f > 30$ Hz (at higher frequency compared to the *Fermi* case). Indeed, I did not find significantly different values for the mean power between the two following frequency ranges: $f > 30$ Hz and $f > 50$ Hz.

After calculating the white noise level for each GRB, I subtracted it and renormalised the PDS by the corresponding net variance (G12). This choice ensures that all GRBs have equal weights in the average PDS.

[3] http://www.gnu.org/s/gsl/

The binning scheme used to average the PDS is different for each considered sample. In the *Fermi* case with 64–ms binning time the Nyquist frequency is 7.8125 Hz, so I defined a uniform frequency binning scheme with a step of 0.01 Hz. At $f < 0.01$ Hz I considered two bins, 0.001 Hz $\leq f <$ 0.005 Hz and 0.005 Hz $\leq f <$ 0.01 Hz. The same step is used in the frequency grid defined for the average PDS of the HR *BeppoSAX* data. In the *BeppoSAX* case the PDS have correspondingly more frequency bins, due to the higher Nyquist frequency. I took only one single bin from 0.001 Hz and 0.01 Hz. The frequency grid changes for the VHR data: I chose a broader frequency step of 1 Hz because the total PDS extraction time is limited to 10 s for each *BeppoSAX* light curve and this implies a coarser frequency resolution. For the VHR PDS I considered 4 bins with step of 0.2 Hz at $f < 1$ Hz. For each individual GRB I calculated the average power in each frequency bin of the corresponding grid described above. Finally, for each frequency bin of the grid I determined the average power over all GRBs of a given sample after they had been renormalised. Finally the frequency bins of the average noise–subtracted PDS were grouped by requiring at least 3σ significance to reduce the uncertainties at high frequencies.

1.2.4 PDS fitting

The average PDS was modelled using a smoothly broken power-law in the same parametrisation as that adopted by G12,

$$\mathrm{PDS}(f) = 2^{1/n}\, F_0 \left[\left(\frac{f}{f_\mathrm{b}}\right)^{n\,\alpha_1} + \left(\frac{f}{f_\mathrm{b}}\right)^{n\,\alpha_2} \right]^{-1/n} \quad , \tag{1.1}$$

where the parameters left free to vary are the break frequency f_b, the two power-law indices α_1 and α_2 ($\alpha_2 > \alpha_1$) and the normalisation parameter, F_0. The smoothness parameter n could not be effectively constrained in all cases, thus it was fixed to $n = 10$, corresponding to a relatively sharp break around f_b, for all cases to ensure a more homogeneous comparison between the best-fit values obtained over different sets as well as with previous results obtained from the *Swift* data. Thanks to the central limit theorem, I can assume these variables to be normally distributed. This allowed us to determine the best-fitting model by minimising the following un-normalised negative log–likelihood function,

$$L = \frac{1}{2} \sum_{i=1}^{N_f} \left(\frac{P_i - \mathrm{PDS}(f_i)}{\sigma_i^2} \right)^2 \quad , \tag{1.2}$$

where P_i and f_i are the observed power and frequency of the i-th bin. N_f is the number of frequency bins, excluding the Nyquist frequency.

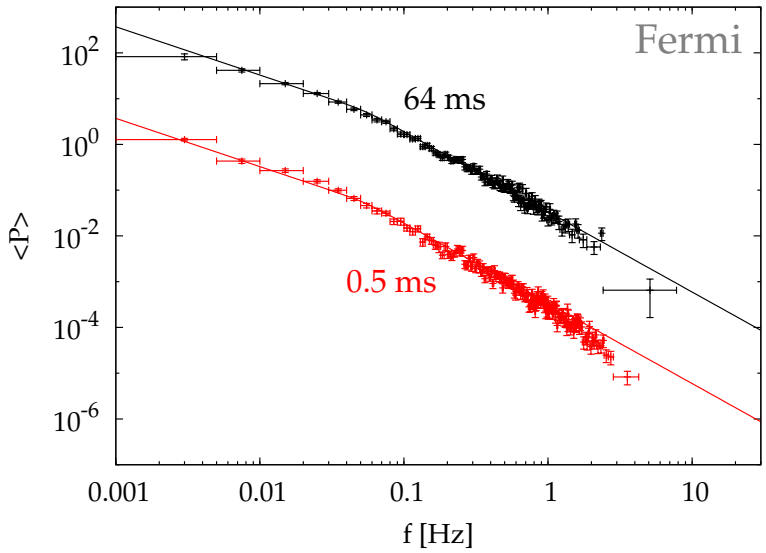

Figure 1.3 Top (bottom) data show the average PDS for a sample of 205 (96) *Fermi*/GBM GRBs in the 8–1000 keV energy range with 64–ms (0.5–ms) time resolution. Solid lines show the best–fitting model obtained on the 64–ms data set, which shows a low frequency break at 5.5×10^{-2} Hz. The same model renormalised to the 0.5–ms data set, which was shifted for the sake of clarity. The bottom data set clearly exhibits a further break at high frequencies ($f \geq 1$ Hz).

1.3 Results

1.3.1 Average PDS at different energy bands

Table 1.6 reports the best-fit parameters estimated for the average PDSs for the different GRB samples considered.

For the average *Fermi* PDS extracted in the total energy range 8–1000 keV (Figure 1.3) with 64–ms binning time the best-fitting parameters are $\alpha_1 = 1.06^{+0.05}_{-0.07}$, a break at 5.5×10^{-2} Hz above which the PDS steepens to $\alpha_2 = 1.75 \pm 0.03$. This slope of the spectra is very similar to the previous values found in the literature related to the GRBs detected with BATSE in similar energy bands (BSS98, BSS00), and in agreement with the value of 5/3 of a Kolmogorov spectrum.

Indeed BSS00 have found an index ranging from 1.50 to 1.72 in the frequency range $0.025 < f < 1$ Hz fitting the average PDS resulted from the BATSE sample (20–2000 keV) with a simple power–law. Moreover, also for the average PDS of *Swift*/BAT data (15–150 keV) I see a typical slope described with a low–frequency index $\alpha_1 = 1.03 \pm 0.05$ up to a break frequency around 3×10^{-2} Hz, followed by and an index $\alpha_2 = 1.73^{+0.04}_{-0.03}$ (G12). Since the break frequency $f_{\rm b}$ is sensitive to the average characteristic

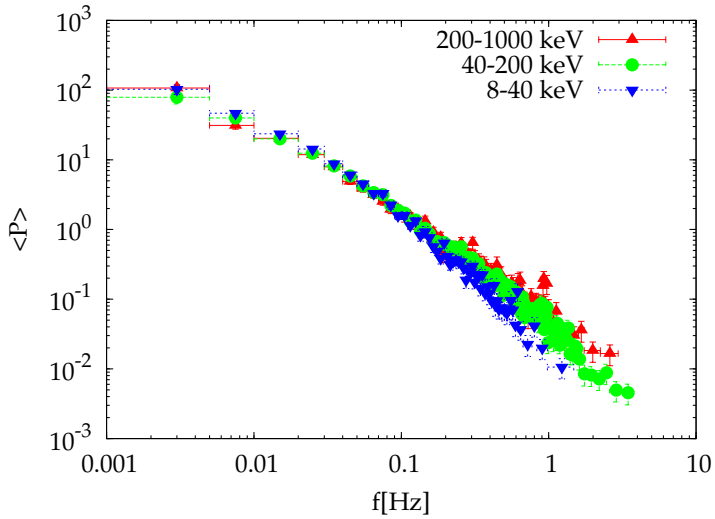

Figure 1.4 Different slopes observed in the average PDS extracted on the three main energy ranges using a time resolution of 64 ms. Upside–down triangles, circles, and triangles show the 8–40, 40–200, and 200–1000 keV energy bands, respectively. The spectrum becomes shallower moving from low to high energies.

time τ of typical individual shots roughly as $f_{\rm b} \sim 1/(2\pi\tau)$ (Frontera & Fuligni 1979; Belli 1992; Lazzati 2002), the value I found in the *Fermi* data corresponds to a mean characteristic time of about 3 s.

Comparing the average PDS of the whole Fermi sample with that of the high–quality (S/N$\geq$ 60) subsample extracted with 0.5–ms resolution, the latter data set shows evidence for a further break around 1–2 Hz with respect to the best–fitting model obtained for the former data set (bottom data in Fig. 1.3). The behaviour of the average PDS at high frequency is thoroughly discussed in Section 1.3.3 together with *BeppoSAX* data.

The analysis of the average PDS at different energy channels reveals a clear trend of the spectral shape when I move from soft to hard energy ranges. Figure 1.4 displays the average PDS corresponding to three different energy channels: 8–40, 40–200, and 200–1000 keV. The index α_2 decreases from 1.95 to 1.47 moving from 8–40 to 200–1000 keV. This reflects the known narrowing of pulses with energy, according to which the same GRB pulse appears to be narrower and spikier at higher energies (Fenimore et al. 1995; Norris et al. 1996; Piro et al. 1998). The same trend was observed in the BATSE average PDS (BSS00), for which the power–law index decreases from 1.72 in the 25–55 keV to 1.50 above 320 keV. Furthermore, a similar behaviour is observed in the *Swift* data, with α_2 varying from $1.75^{+0.05}_{-0.04}$ to $1.49^{+0.08}_{-0.07}$ passing from 15–50 to 50–150 keV.

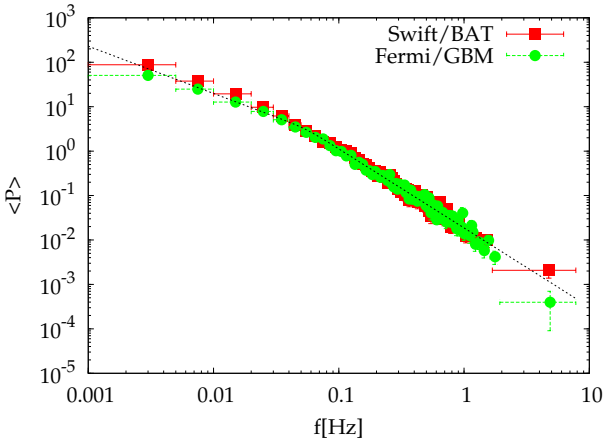

Figure 1.5 Average PDS of *Fermi* sample in the 15–150 keV energy range (circles) compared with the *Swift*/BAT result (squares) provided by G12. Both are calculated from 64–ms binned light curves. The two independent measures are compatible. The dashed line shows the best fit model for Fermi data.

We also extracted the light curves in the common energy bands with other instruments so that we can compare results limiting the systematic differences connected with different energy passbands. The average *Fermi*/GBM PDS obtained in the typical *Swift*/BAT energy range (15–150 keV) are perfectly consistent with the analogous results on *Swift*/BAT data, as shown in Fig. 1.5. The slope indices of average *Fermi*/GBM PDS for the 15–150 keV are $\alpha_1 = 1.06^{+0.06}_{-0.07}$ and $\alpha_2 = 1.78^{+0.04}_{-0.03}$, to be compared with their analogous values found with *Swift*/BAT, $\alpha_1 = 1.03 \pm 0.05$, $\alpha_2 = 1.73 \pm 0.03$. So the apparently different values at low frequencies between the two spectra in Fig. 1.5 is not statistically significant.

1.3.2 FRED sub-sample

We investigated whether the GRBs whose light curves can be described as a single fast rise exponential decay (FRED) show distinctive features in the average PDS. To this aim, I selected 10 GRB of this kind out of the *Fermi* sample by visual inspection and calculated the corresponding average PDS. The best-fit parameters in this case are $\alpha_1 = 1.32 \pm 0.10$ and $\alpha_2 = 2.53^{+0.39}_{-0.24}$ with a break at about 6×10^{-2} Hz (see Table 1.6). That the high-frequency tail of the PDS for the FRED sample is steeper than that of the whole sample of GRBs, agrees with the PDS expected for a single FRED (e.g., see Lazzati 2002). This in turns suggests that the average PDS of multiple–pulse GRBs is shallower because of the presence of various characteristic times. The sum of several PDS with different break frequencies would therefore result in a simple power–law with

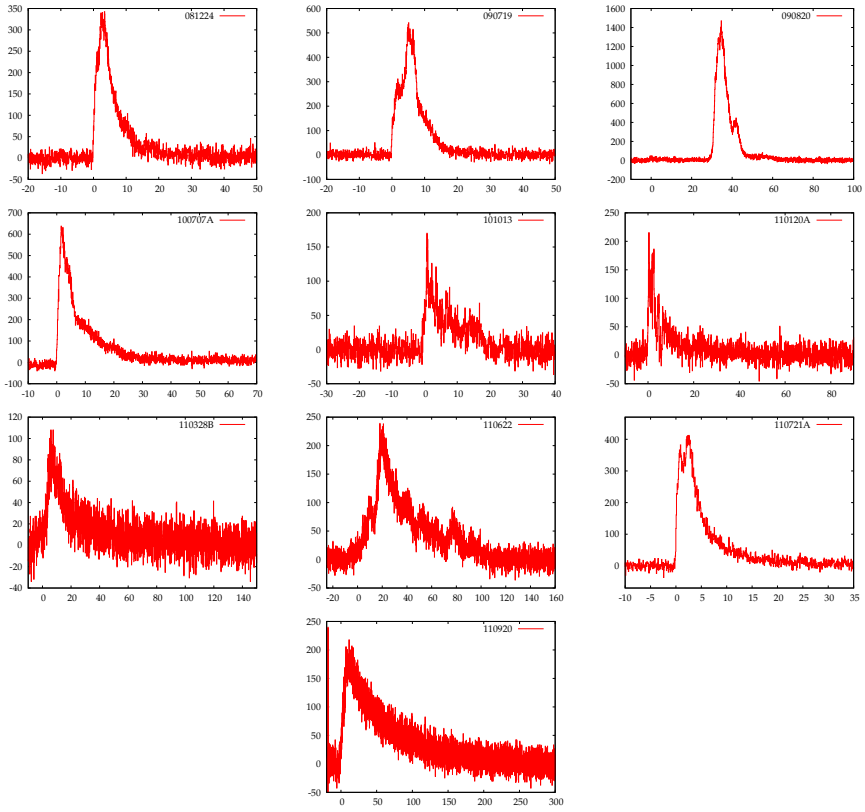

Figure 1.6 The 10 FRED used in our PDS analysis. Each curve has a 64–ms bin time and is expressed in units of counts s^{-1} as a function of time.

no dominant break in the explored frequency range.

1.3.3 Average PDS up to high frequency

The average PDS for the HR light curves provided by the *BeppoSAX*/GRBM shows a second break at high frequency ($f_{b2} = 1.91^{+0.45}_{-0.43}$ Hz). The observed slope can be parametrised with two indices, $\alpha_2 = 1.49 \pm 0.04$ and $\alpha_3 = 2.46^{+0.44}_{-0.31}$ (we did not use α_1, which has previously been used to denote the slope below a few 10^{-2} Hz). The break is likely to be real because the improvement is significant compared to the same model without it. The F–test yields a probability of 1.26% that the break is not required. The value itself of this break frequency as well as the values of the corresponding power–law indices indicate that this feature has a different origin from the other one observed at lower frequency. This motivated us to adopt a different notation for the power-law index above this break, α_3. Overall, the different slopes refer to the corresponding frequency ranges: α_1 below a few 10^{-2} Hz, α_2 holds in the range $10^{-2} < f < 1$ Hz, and α_3 for $f \geq 1$ Hz.

When I limit our PDS analysis to the first 10 s of the GRBM trigger time of each

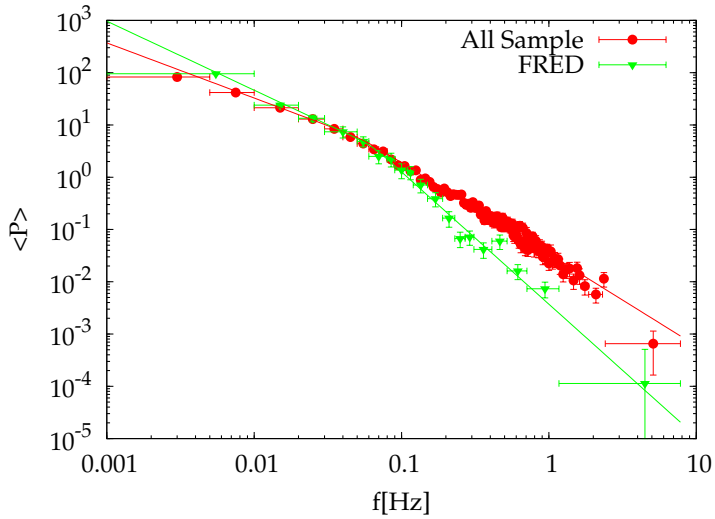

Figure 1.7 The average PDS of the FRED sample (detected with GBM) is shallower than the average PDS of the full *Fermi* sample. The energy band is 8–1000 keV for both sets with 64 ms time resolution.

GRB light curve and use the VHR data, a very similar result is found for the average PDS, which now extends up to 1 kHz. The best–fitting parameters for these data are $\alpha_2 = 1.52 \pm 0.17$, $\alpha_3 = 2.91^{+0.51}_{-0.41}$ with a clear break at $f_{\rm b2} = 2.59^{+1.04}_{-0.94}$ Hz (Fig. 1.8). Also in this case a break in the model is required to fit the data, with a probability of 0.47% that the improvement obtained with the break is due to chance according to the F–test. Furthermore in Fig. 1.3 the average PDS obtained from the *Fermi* VHR sample looks like it also requires a break at $f \geq 1$ Hz. To check the mutual compatibility of these data with a broken power–law model, I extracted the *Fermi* VHR average PDS over the same energy range covered also by GRBM, 40–700 keV. To fit these data above 0.02 Hz I used a simple power–law as well as a broken power–law and used the F–test to evaluate the improvement one obtains moving from the former to the latter. We estimate a probability of 3.4% that such improvement is just by chance. I found two different slopes, $\alpha_2 = 1.65 \pm 0.03$ and $\alpha_3 = 2.41^{+0.34}_{-0.19}$, with a break at $f_{\rm b2} = 1.1^{+0.3}_{-0.2}$ Hz ($\chi^2/dof = 1.07$). We excluded from the fit the lowest frequency point in the *BeppoSAX* HR PDS and in the *Fermi* VHR PDS (40–700 keV), because it clearly lies below the extrapolation of a double broken power–law, since it is clearly affected by the presence of the low–frequency break.

We also performed a combined analysis of the two and three samples, *BeppoSAX* (HR + VHR) (i.e., *BeppoSAX* data alone), and *BeppoSAX* (HR + VHR) plus *Fermi* VHR, fitting all the spectra simultaneously with the same model, apart from allowing each set a different normalisation term. For the *BeppoSAX* data alone, the resulting

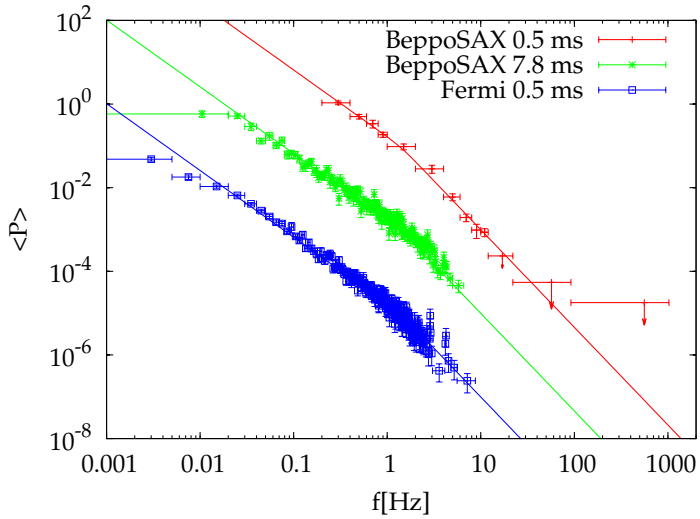

Figure 1.8 The top, mid, and bottom average PDS refer to the *BeppoSAX* 0.5–ms, 7.8–ms resolution samples and to the *Fermi* subsample with S/N$\geq$ 60, respectively, for the 40–700 keV band. The break around 1–2 Hz is present in each set. The common best–fitting model is also shown, for both the *BeppoSAX* and *Fermi* data sets. The corresponding model parameters were bound to be equal for all the data sets, except for the normalisation terms. Upper limits are given at 2σ confidence. Data were shifted vertically for the sake of clarity.

break frequency is found to be $f_{\rm b2} = 2.11^{+0.42}_{-0.33}$ Hz, while the two slopes have indices respectively $\alpha_2 = 1.50^{+0.03}_{-0.04}$ and $\alpha_3 = 2.69^{+0.27}_{-0.20}$. This treatment implicitly assumed the two data sets to be statistically independent. Although this is not completely true, since the 10 s data of the VHR curves are part of the full profile of about 100 s of HR data, on average the common data amount to 10-20% or so. Consequently, the expected correlation between the two data set affects the results within a comparable fraction. By adding the VHR sample extracted with *Fermi*, I found $\alpha_2 = 1.60^{+0.02}_{-0.03}$, $\alpha_3 = 2.33^{+0.15}_{-0.13}$ with a break at $f_{\rm b2} = 1.4 \pm 0.3$ Hz (χ^2/dof = 1.37). We tried to see whether the quality of the fit could be improved by allowing the smoothness parameter to vary (eq. 1.1), thus allowing a smooth transition from one power–law regime to the following one, with no appreciable result though.

Although the white noise subtraction was done through a careful estimation of the high frequency power (Section 1.2.3), I examined whether the break could be an artifact of a small bias in the white noise subtraction. More specifically, overestimating the white noise could mimic the appearance of an artificial break. To test this possibility, I extracted the average PDS *without* noise subtraction, keeping the same relative normalisation for each GRB as that of the noise–subtracted case. I fixed the best-fitting model

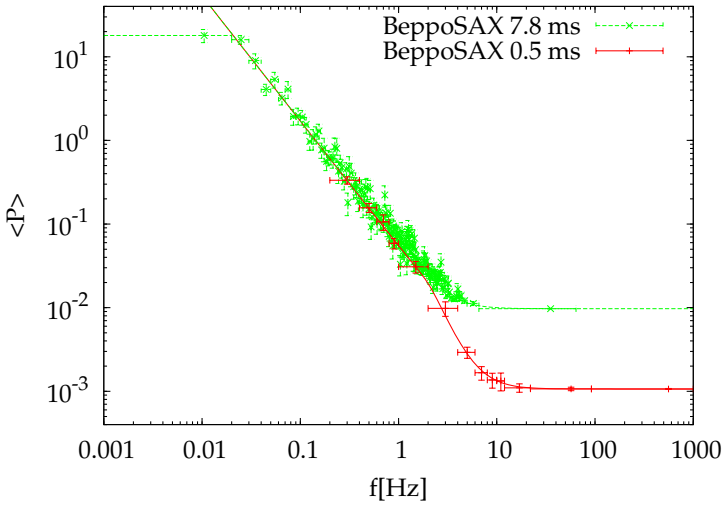

Figure 1.9 The average PDS obtained from *BeppoSAX* samples without the white noise subtraction. The break at 1–2 Hz is still evident thanks to the signal being more than one order of magnitude higher than the white noise level. This rules out any bias due to possibly wrong white noise subtraction.

of the noise-subtracted PDS obtained above and fitted the white noise with a constant. Figure 1.9 clearly shows that the break in the average PDS occurs when the average signal still dominates the white noise level (by more than one order of magnitude in the VHR data). This rules out the possibility of the break around 1–2 Hz being the result of biased white noise subtraction and suggests it to be a genuine feature of the average PDS at energies above 40 keV.

1.4 Discussion

In general, two distinct sources of time variability have been found to characterise the GRB variability: a fast component dominated by the presence of relatively short (< 1 s) pulses and a slow component linked to pulses lasting several seconds (Scargle et al. 1998; Vetere et al. 2006; Margutti 2009; Gao et al. 2012). These two kinds of dominant time scales should be produced by different mechanisms involved in the physical process, and different explanations in different scenarios are available in the literature (Morsony et al. 2010; Zhang & Yan 2011; Titarchuk et al. 2012). The simple power–law modelling the average PDS and encompassing nearly two orders of magnitude in frequency is suggestive of some kind of scale invariance within the same frequency range, thus confirming the coexistence of multiple characteristic timescales.

The study of the average PDS in different energy ranges made possible by *Fermi*/GBM

provides clues to better characterise the different aspects of GRB time variability. The observed energy dependence of the power–law index of the average PDS, α_2, in the frequency range $10^{-2} < f < 1$ Hz confirms and extends the results found with previous work and data sets. Indeed, in the 8–1000 keV band the average PDS of long GRBs detected with GBM show a broken power–law behaviour ($\alpha_1 = 1.06^{+0.05}_{-0.07}$, $\alpha_2 = 1.73^{+0.04}_{-0.03}$ and $f_\mathrm{b} = 5.5 \times 10^{-2}$ Hz) with α_2 very close to the slope of average PDS observed in the BATSE analysis ($\alpha \approx 1.67$).

More specifically, the average PDS slope undergoes a steep–to–shallow evolution passing from soft to hard energy channels, as shown in Fig. 1.10. This behaviour is consistent with the narrowing of pulses with energy: Fenimore et al. (1995) found a dependence of the average pulse width w on energy E as $w \propto E^{-0.4}$, estimated by measuring the average auto-correlation function (ACF) width for a sample of BATSE bursts as a function of the energy channel. In addition to the energy dependence of the average pulse width, also the shape itself and, in particular, the peakedness of the average ACF depends on energy (BSS00). Indeed, the energy dependence of the shape of the pulse profile explains the energy dependence of the power–law index: if the shapes of a given pulse at different energies were the same, only the break frequency in the average PDS should change correspondingly, while the slope should remain unaffected. Since this is not what is observed, the evolution with energy of the average power–law index in the PDS confirms the change in the shape itself of the energy pulse as a function of energy.

Another important result that emerged from the present analysis is the break revealed around 1–2 Hz in the *BeppoSAX* average PDS. Although the evidence for it in the *Fermi* data alone is less compelling because of the lower S/N in that frequency range, the *Fermi* average PDS is fully compatible with it. The joint *BeppoSAX–Fermi* analysis of such high–frequency break shows that this may significantly vary between 1 and 2 Hz, depending on the GRB sample and on its average S/N. Together with results obtained on *Swift* data by G12, this break becomes evident at harder energies.

This feature in the average PDS and its possible dependence on energy provides an important clue to constraining theoretical models proposed to explain the physical mechanism involved in GRBs and confirms and strengthens the analogous result obtained by BSS00 on BATSE data. The break could be related to an average intrinsic variability time scale, $\Delta\ t \leq 0.1$ s, below which the temporal power changes regime. This may link directly to the central engine. Alternatively, it could be related to the variation of the outflow Lorentz factor, or it could depend on the radius at which

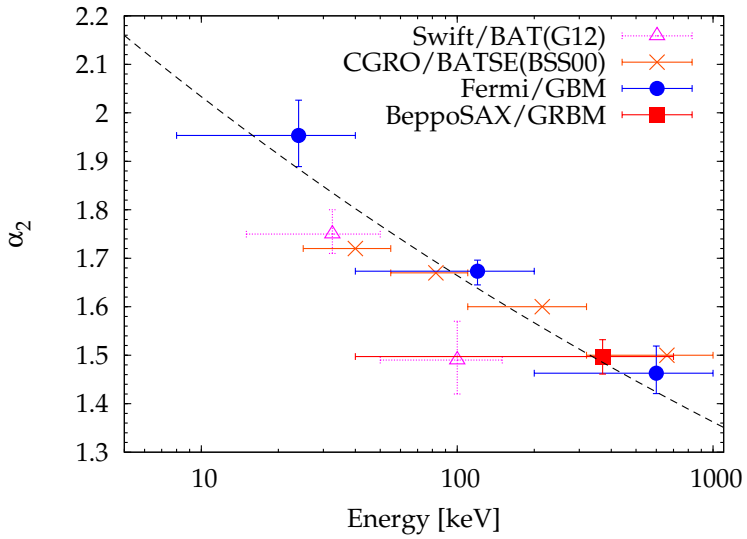

Figure 1.10 The power–law index of the average PDS in the frequency range $10^{-2} < f/\mathrm{Hz} < 1$ obtained from different data sets as a function of energy. Dashed line ($\alpha_2 \propto E^{-0.09}$) illustrates the α_2 dependence on energy as estimated from Fermi data.

the expanding shell becomes optically thin R_*. In this latter scenario I could observe variability only on time scales longer than a characteristic time $t_* = R_*/c\Gamma^2$ (BSS00).

A number of theoretical interpretations of the power–law PDS with an index compatible with 5/3 have been put forward in the literature. This is what is expected for a Kolmogorov spectrum within a medium with fully developed turbulence. For instance, in the internal shock model, the parameters of the wind of relativistic shells can be constrained so as to reproduce the observed average PDS (Panaitescu et al. 1999; Spada et al. 2000); or in the context of a relativistic jet making its way out through the stellar envelope of the progenitor star (Zhang et al. 2009; Morsony et al. 2010). Within other scenarios, in which the dissipation into gamma–rays is magnetically driven, the observed features of the average PDS in the frequency range from a few 0.01 to 1–2 Hz can also be explained (e.g., Zhang & Yan 2011). Again, alternatively the observed temporal properties could be driven by instabilities in the accretion disc of potentially different origins: erratic episodic accretion (e.g., Kumar et al. 2008); hydrodynamical or magnetic origin (e.g., Perna et al. 2006; Proga & Zhang 2006; Margutti et al. 2011); magneto–rotational origin, in which neutrino cooling is the dominant process (Carballido & Lee 2011). The reader is referred to G12 for a more detailed discussion of the predictions of the various theoretical models with reference to the average PDS properties.

1.5 Conclusions

We studied the properties of the average PDS of GRBs in two unexplored regimes: across a broadband energy range from 8 keV to 1 MeV using *Fermi*/GBM data and up to very high frequencies (up to 1 kHz) using *BeppoSAX*/GRBM data.

In agreement with previous results obtained from an analogous analysis of *CGRO*/BATSE and of *Swift*/BAT data, I also found a clear relation between the average PDS slope from ~ 0.01 to ~ 1 Hz range and energy, with the index spanning the range from 1.5 to 1.9 from 8 keV through 1 MeV in three channels (8–40, 40–200, and 200–1000 keV). The slope of the average PDS carries information about the spikiness of light curve as well as the multiple presence of several characteristic time scales (scale invariance within the two decades of the aforementioned frequency range).

For the first time I extended the study of PDS up to 1 kHz in frequency with the very high time resolution provided by *BeppoSAX*/GRBM. In this case, the average PDS pinned down a clear break at 1–2 Hz. This provides a strong clue to the dominant minimum variability time, potentially connected with either the intrinsic inner engine variability, or with the dispersion of the bulk Lorentz factor distribution for a wind of relativistic shells, or with the average distance at which internal collisions dissipate energy into gamma–rays. Combining our results with those obtained from the *Swift* data set, the presence of this break emerges only in the harder energy channels (≥ 100 keV).

The average slope is broadly consistent with the theoretically appealing value of 5/3 expected for a Kolmogorov spectrum of velocities within a fully turbulent medium, as suggested in previous works (BSS98, BSS00). Our results in the frequency range $\sim 10^{-2}$ to ~ 1 Hz are in broad agreement with a number of theoretical interpretations within different alternative contexts, encompassing the classical internal shock scenario as well as the magnetically–dominated outflows models. Instead, still missing is a detailed theoretical explanation for the other two properties: i) the presence of the 1–2 Hz break and its energy dependence; ii) the energy dependence of the average power–law index.

Table 1.1. Time and Peak count rate. *Fermi*/GBM full sample including 205 GRBs. The PDS is calculated in the time interval reported.

Trigger	$t_{\rm start}$ [a] (s)	$t_{\rm stop}$ [a] (s)	Peak rate (count s^{-1})	T_{90} (s)
080714745	−1.76	31.77	69.31 ± 4.81	38.7
080723557	−0.13	119.42	460.31 ± 16.96	77.1
080723985	−0.29	52.89	127.58 ± 8.09	42.8
080724401	−0.11	48.34	268.31 ± 20.20	41.5
080730786	−0.91	18.54	233.28 ± 13.66	18.1
080806896	−6.98	40.63	113.13 ± 7.88	43.8
080807993	0.01	49.86	266.82 ± 20.00	20.2
080810549	−10.59	102.31	49.99 ± 4.54	57.7
080816503	−0.47	69.35	122.05 ± 10.74	64.6
080816989	0.04	29.10	98.06 ± 10.64	6.1
080817161	−4.42	87.36	188.76 ± 6.22	69.2
080818579	−0.40	36.72	82.44 ± 8.35	43.9
080824909	−4.56	17.32	177.18 ± 12.34	23.9
080825593	−0.04	31.84	395.63 ± 17.22	22.5
080904886	−4.06	20.96	201.32 ± 7.34	18.4
080906212	−19.30	3.87	326.10 ± 12.35	21.9
080913735	−0.40	26.48	60.08 ± 6.40	26.4
080916009	−3.83	86.34	199.50 ± 6.88	66.0
080925775	−2.38	31.80	212.74 ± 6.63	25.3
081009140	−0.09	54.69	1568.85 ± 29.29	44.9
081025349	−0.37	44.69	54.34 ± 8.06	40.7
081028538	−4.50	6.44	88.16 ± 6.33	13.4
081101532	−0.07	27.45	171.97 ± 18.49	24.7
081110601	0.01	19.59	288.82 ± 14.48	23.3
081121858	−3.74	21.09	94.06 ± 10.61	19.8
081122520	−0.75	97.24	263.60 ± 14.20	24.8
081124060	−1.98	29.58	185.77 ± 7.59	20.5
081126899	−18.52	37.99	90.13 ± 3.88	55.5
081129161	−0.79	33.83	218.42 ± 13.47	43.1
081130629	−28.04	7.35	138.37 ± 16.43	7.9
081206275	−5.99	42.78	20.83 ± 1.75	44.8
081215784	−1.64	24.60	1839.88 ± 44.40	7.9
081221681	−0.53	78.57	347.30 ± 9.60	32.4
081222204	−0.31	36.30	175.78 ± 7.81	27.6
081224887	0.04	34.98	322.82 ± 8.70	27.4
081231140	−3.25	45.83	212.43 ± 10.69	35.8
090101758	−1.20	120.02	149.47 ± 6.78	112.6
090102122	−0.01	54.78	252.16 ± 19.13	32.2
090112332	−1.72	38.03	104.59 ± 15.23	43.3
090112729	−4.35	17.54	192.91 ± 10.50	13.9
090117640	−5.33	12.40	177.79 ± 12.10	14.7
090131090	−0.18	55.88	658.13 ± 28.42	35.9
090202347	−10.18	42.36	111.00 ± 9.88	42.9
090217206	−0.19	37.12	204.05 ± 18.25	30.5
090310189	−0.23	125.47	37.32 ± 3.82	226.8
090323002	−2.15	147.42	172.94 ± 8.83	132.7
090328401	−3.81	80.10	302.23 ± 14.74	62.4
090419997	−2.32	101.62	54.42 ± 3.94	100.1
090424592	0.00	62.08	1607.18 ± 41.86	47.4
090425377	−0.56	86.10	184.72 ± 10.57	78.5
090502777	−11.11	58.53	87.56 ± 7.99	67.7
090514006	−0.40	54.70	96.32 ± 6.91	102.0
090516137	1.31	190.17	44.44 ± 3.46	116.6
090516353	−15.68	89.85	43.18 ± 3.82	92.9
090519462	−18.61	229.64	52.15 ± 6.39	34.6
090524346	−0.54	62.82	153.03 ± 7.63	56.1
090528516	−0.94	118.93	207.70 ± 13.84	92.4
090529564	−1.01	10.76	412.16 ± 23.77	10.4
090530760	−0.23	201.37	122.56 ± 3.24	155.2
090618353	−0.58	190.91	335.42 ± 7.09	119.8
090620400	−0.24	19.28	265.40 ± 13.88	14.8

Table 1.1 (cont'd)

Trigger	$t_{\rm start}$[a] (s)	$t_{\rm stop}$[a] (s)	Peak rate (count s^{-1})	T_{90} (s)
090623107	−1.10	78.38	111.36 ± 15.59	62.0
090626189	−1.53	72.59	559.95 ± 18.71	52.7
090711850	−15.15	45.58	43.81 ± 3.93	44.9
090717034	−0.42	81.63	186.37 ± 8.76	69.8
090718762	−0.04	31.83	355.05 ± 11.24	25.7
090719063	0.03	25.69	505.01 ± 10.44	14.7
090813174	−0.14	8.69	303.00 ± 20.37	18.8
090814950	−2.25	108.09	54.52 ± 4.29	108.5
090815438	−4.51	24.68	129.32 ± 6.04	24.6
090820027	−0.26	67.26	1407.34 ± 22.80	18.9
090820509	−0.05	15.43	151.95 ± 16.70	15.4
090828099	−2.16	103.06	175.59 ± 7.70	78.3
090829672	−2.44	117.17	736.87 ± 29.85	74.6
090831317	0.06	68.03	413.85 ± 23.47	61.6
090902462	0.00	55.94	1286.20 ± 37.76	20.7
090910812	−2.05	74.56	62.85 ± 5.60	72.1
090922539	−0.23	98.97	188.93 ± 5.70	93.8
090926181	−0.52	48.44	1414.03 ± 39.42	15.0
090928646	−0.13	14.97	56.17 ± 5.40	13.3
090929190	−0.16	81.57	233.98 ± 13.47	8.8
091003191	−0.06	24.39	588.51 ± 27.39	21.8
091010113	−0.17	13.91	1104.80 ± 35.83	7.8
091020977	0.01	37.71	88.56 ± 6.54	48.8
091031500	−0.28	37.03	143.44 ± 16.85	36.4
091101143	−0.07	79.93	156.59 ± 7.57	74.0
091103912	−3.89	18.45	86.19 ± 4.72	21.9
091109895	−0.09	25.25	128.79 ± 12.10	26.4
091120191	−0.17	56.28	324.78 ± 15.58	51.6
091127976	−0.01	15.61	1107.30 ± 35.38	10.2
091128285	−1.90	72.15	123.28 ± 8.40	55.8
091208410	−0.01	13.24	419.94 ± 24.25	11.9
091227294	−0.50	64.20	58.69 ± 6.15	29.9
100116897	−4.24	115.50	212.57 ± 5.81	112.3
100122616	−1.54	38.14	516.55 ± 12.93	25.9
100130729	−6.61	95.66	74.09 ± 4.39	93.3
100131730	0.01	9.86	460.33 ± 24.70	8.8
100224112	−10.04	71.75	168.51 ± 9.19	89.6
100225580	−16.90	8.32	197.31 ± 13.24	29.6
100304004	−2.47	180.89	31.16 ± 3.88	127.4
100322045	−0.40	76.97	250.00 ± 11.48	39.8
100324172	0.05	63.34	495.75 ± 18.02	61.8
100326402	−21.23	97.61	38.13 ± 3.80	48.9
100401297	−2.77	134.96	68.99 ± 6.73	134.8
100414097	0.02	62.55	342.92 ± 15.71	23.7
100424876	−8.93	209.63	65.77 ± 5.20	199.3
100502356	−9.50	100.00	74.76 ± 4.95	129.8
100503554	−2.58	146.29	115.81 ± 11.42	139.8
100511035	−4.35	86.08	330.81 ± 21.95	55.3
100515467	−0.32	14.84	227.52 ± 11.14	14.8
100517072	−0.34	64.23	210.98 ± 13.54	52.0
100517154	−0.02	31.53	131.02 ± 9.67	30.9
100519204	−2.09	82.52	82.85 ± 4.10	70.9
100522157	−0.09	38.31	167.20 ± 17.61	40.7
100527795	−2.92	95.77	104.48 ± 8.07	92.8
100528075	−9.03	53.62	187.81 ± 4.80	47.5
100612726	−0.45	24.96	292.80 ± 8.29	17.0
100615083	−0.20	40.05	114.93 ± 6.66	37.0
100701490	−0.03	30.82	584.93 ± 26.81	35.1
100704149	−7.76	183.86	94.55 ± 5.51	23.7
100707032	0.07	97.41	621.67 ± 14.04	64.6
100709602	−3.27	100.80	49.37 ± 3.88	101.6

Table 1.1 (cont'd)

Trigger	$t_{\rm start}$ [a] (s)	$t_{\rm stop}$ [a] (s)	Peak rate (count s^{-1})	T_{90} (s)
100719989	−1.14	41.22	782.37 ± 30.10	22.0
100722096	−1.12	47.97	589.90 ± 27.40	8.3
100724029	−4.29	221.95	317.48 ± 10.45	119.8
100725475	−4.08	216.14	39.64 ± 2.78	150.6
100728095	−2.54	204.56	167.28 ± 12.45	162.1
100804104	−0.65	12.53	307.42 ± 24.17	9.0
100805845	−0.07	59.45	75.30 ± 4.62	81.7
100820373	−1.06	3.81	232.22 ± 14.27	6.5
100826957	−0.13	133.37	466.15 ± 17.64	90.6
100829374	−3.55	82.47	70.27 ± 4.12	94.8
100829876	−0.14	12.59	952.40 ± 33.29	11.0
100906576	0.07	118.60	214.97 ± 11.13	107.1
100910818	−0.14	20.79	397.57 ± 16.32	15.6
100918863	−0.40	127.86	143.28 ± 4.02	94.3
100923844	−0.13	52.48	81.81 ± 4.72	53.8
101013412	−0.31	17.68	152.36 ± 8.72	16.7
101021009	−2.37	75.64	93.93 ± 7.50	63.7
101023951	−1.31	112.54	373.13 ± 11.75	85.5
101113483	−0.57	136.07	72.65 ± 6.59	130.0
101123952	−2.23	154.64	608.23 ± 27.22	105.3
101126198	−3.98	66.81	249.77 ± 6.30	54.0
101201418	−2.13	112.04	85.87 ± 5.30	102.7
101207536	−2.23	70.22	92.24 ± 10.76	69.1
101208498	−1.11	6.31	598.25 ± 19.92	3.1
101224578	−20.90	96.03	70.41 ± 6.07	54.3
101225377	−3.00	101.83	52.39 ± 3.35	21.7
101227406	−1.61	161.40	123.44 ± 16.79	63.2
101227536	0.14	27.21	134.29 ± 11.65	26.6
101231067	0.09	41.75	254.35 ± 14.31	24.2
110102788	−16.37	149.19	240.07 ± 14.06	137.3
110118857	−1.47	30.85	114.26 ± 7.48	36.6
110120666	−0.06	42.69	188.86 ± 13.22	41.2
110207470	−0.16	38.69	105.34 ± 15.10	91.9
110213220	−2.36	38.09	193.95 ± 8.39	34.9
110227420	−111.98	11.86	42.47 ± 3.52	134.5
110301214	−0.01	12.22	1357.59 ± 38.56	6.5
110302043	−14.78	42.18	82.39 ± 5.59	51.5
110304071	−1.36	51.05	76.42 ± 5.61	50.2
110318552	−4.38	16.30	154.76 ± 6.90	15.0
110328520	−5.03	114.46	80.87 ± 3.50	101.8
110402009	0.09	36.82	221.70 ± 19.57	55.7
110415541	−0.11	166.23	60.59 ± 5.25	122.5
110421757	−3.82	125.46	75.85 ± 3.99	99.6
110428338	−4.44	99.05	149.04 ± 11.00	44.8
110517573	−3.23	27.94	155.00 ± 12.18	24.1
110528624	−4.65	111.89	26.29 ± 2.24	113.8
110529262	−0.84	49.40	199.71 ± 13.14	48.6
110605183	−0.81	77.85	97.50 ± 3.89	89.4
110610640	−8.49	39.06	85.44 ± 5.76	45.3
110622158	−6.18	106.01	210.66 ± 5.19	80.1
110625881	−0.85	128.37	964.50 ± 19.45	51.6
110702187	−9.41	25.53	57.92 ± 5.10	46.7
110705364	−2.03	25.23	95.07 ± 7.58	22.9
110709463	−0.33	27.96	234.28 ± 10.96	27.3
110709642	−1.55	60.66	173.33 ± 11.57	52.5
110710954	−10.12	19.45	246.31 ± 14.47	17.9
110717319	−0.47	112.75	218.88 ± 9.55	94.8
110721200	0.05	48.30	399.42 ± 10.09	34.8
110725236	−0.52	25.08	68.06 ± 7.15	35.8
110729142	−11.20	198.21	124.94 ± 8.16	188.2
110731465	−0.25	13.83	287.43 ± 14.92	9.5

Table 1.1 (cont'd)

Trigger	$t_{\rm start}$[a] (s)	$t_{\rm stop}$[a] (s)	Peak rate (count s^{-1})	T_{90} (s)
110806934	−1.63	36.84	80.02 ± 5.38	34.5
110825102	0.02	92.75	958.77 ± 33.38	69.4
110903009	−6.48	39.79	472.66 ± 14.46	34.0
110904124	−8.81	100.11	119.64 ± 11.42	84.7
110904163	−1.54	44.86	73.25 ± 8.58	47.1
110919634	−4.93	67.78	163.79 ± 7.22	44.5
110920546	−1.91	254.67	239.90 ± 20.69	170.4
110921912	−0.14	92.66	597.84 ± 27.06	18.8
110926107	−4.26	88.80	72.30 ± 4.08	99.1
110928180	−132.73	44.42	130.22 ± 15.26	167.9
111003465	−0.05	25.04	225.39 ± 8.41	20.6
111009282	−0.58	277.75	161.89 ± 4.57	262.3
111012456	−1.21	30.02	139.62 ± 8.18	27.1
111012811	0.06	7.29	274.10 ± 14.17	23.0
111015427	−4.46	174.29	101.84 ± 7.10	92.4
111017657	−2.14	28.45	228.81 ± 8.41	15.5
111024722	−11.15	70.26	176.85 ± 12.88	75.6
111107076	−0.57	106.69	41.93 ± 3.75	103.7
111127810	−2.33	21.67	224.30 ± 7.85	18.1
111216389	−11.32	98.12	163.01 ± 12.14	88.6
111228453	−0.97	51.57	260.09 ± 10.04	4.9
111228657	−14.04	61.36	304.71 ± 14.41	66.3

Note. — The PDS is calculated in the time interval reported.

[a]Referred to the *Fermi*/GBM trigger time.

Table 1.2. White noise level (Leahy normalisation). *Fermi* sample.

Trigger	$\langle P \rangle$ ($f > 6$ Hz)	Trigger	$\langle P \rangle$ ($f > 6$ Hz)	Trigger	$\langle P \rangle$ ($f > 6$ Hz)	Trigger	$\langle P \rangle$ ($f > 6$ Hz)
080714745	1.63 ± 0.42	090514006	1.64 ± 0.33	100401297	2.08 ± 0.22	110207470	2.74 ± 0.47
080723557	2.00 ± 0.24	090516137	2.14 ± 0.19	100414097	1.88 ± 0.32	110213220	1.71 ± 0.39
080723985	2.50 ± 0.38	090516353	1.96 ± 0.25	100424876	1.85 ± 0.17	110227420	1.87 ± 0.23
080724401	2.26 ± 0.39	090519462	2.02 ± 0.16	100502356	2.04 ± 0.25	110301214	1.97 ± 0.73
080730786	2.44 ± 0.63	090524346	2.07 ± 0.33	100503554	1.76 ± 0.20	110302043	2.15 ± 0.35
080806896	1.67 ± 0.35	090528516	2.00 ± 0.24	100511035	1.91 ± 0.27	110304071	2.12 ± 0.37
080807993	2.05 ± 0.24	090529564	2.48 ± 0.86	100515467	2.18 ± 0.68	110318552	2.51 ± 0.61
080810549	1.98 ± 0.24	090530760	1.86 ± 0.18	100517072	2.35 ± 0.34	110328520	1.88 ± 0.23
080816503	2.09 ± 0.31	090618353	1.98 ± 0.19	100517154	2.00 ± 0.46	110402009	2.76 ± 0.48
080816989	2.31 ± 0.51	090620400	1.75 ± 0.56	100519204	2.13 ± 0.29	110415541	1.92 ± 0.20
080817161	2.39 ± 0.29	090623107	2.07 ± 0.29	100522157	2.02 ± 0.42	110421757	1.88 ± 0.22
080818579	2.02 ± 0.43	090626189	2.18 ± 0.31	100527795	1.96 ± 0.26	110428338	2.11 ± 0.26
080824909	2.20 ± 0.57	090711850	2.11 ± 0.34	100528075	1.62 ± 0.30	110517573	2.04 ± 0.46
080825593	1.89 ± 0.45	090717034	2.09 ± 0.29	100612726	1.67 ± 0.48	110528624	1.86 ± 0.23
080904886	2.00 ± 0.52	090718762	2.44 ± 0.49	100615083	2.12 ± 0.41	110529262	1.67 ± 0.34
080906212	1.69 ± 0.51	090719063	2.34 ± 0.55	100701490	2.10 ± 0.18	110605183	1.91 ± 0.29
080913735	2.02 ± 0.50	090813174[a]	1.98 ± 0.59	100704149	2.01 ± 0.19	110610640	2.13 ± 0.38
080916009	2.14 ± 0.28	090815438	1.95 ± 0.48	100707032	2.01 ± 0.26	110622158	2.04 ± 0.24
080925775	1.55 ± 0.41	090820027	1.82 ± 0.30	100709602	1.96 ± 0.25	110625881	2.30 ± 0.24
081009140	1.73 ± 0.33	090820509	2.28 ± 0.70	100719989	1.65 ± 0.37	110702187	2.60 ± 0.48
081025349	1.98 ± 0.38	090828099	1.84 ± 0.24	100722096	1.91 ± 0.36	110705364	1.88 ± 0.48
081028538	1.95 ± 0.14	090829672	2.03 ± 0.24	100724029	2.00 ± 0.17	110709463	2.04 ± 0.49
081101532	1.76 ± 0.47	090831317	2.64 ± 0.34	100725475	1.94 ± 0.17	110709642	1.98 ± 0.33
081110601	1.70 ± 0.55	090902462	2.07 ± 0.16	100728095	2.05 ± 0.18	110710954	2.15 ± 0.49
081121858	1.89 ± 0.51	090910812	1.51 ± 0.27	100804104	1.64 ± 0.67	110717319	2.04 ± 0.24
081122520	1.97 ± 0.26	090922539	1.80 ± 0.25	100805845	2.01 ± 0.34	110721200	1.84 ± 0.36
081124060	2.02 ± 0.46	090926181	2.88 ± 0.42	100820373	2.54 ± 1.27	110725236	1.98 ± 0.51
081126899	2.35 ± 0.36	090928646	1.98 ± 0.68	100826957	1.94 ± 0.22	110729142	1.95 ± 0.18
081129161	2.12 ± 0.45	090929190	2.06 ± 0.29	100829374	1.76 ± 0.27	110731465	2.01 ± 0.69
081130629	1.73 ± 0.41	091003191	1.93 ± 0.52	100829876	2.13 ± 0.19	110806934	1.80 ± 0.40
081206275	2.18 ± 0.17	091010113	4.48 ± 0.92	100906576	2.14 ± 0.24	110825102	2.61 ± 0.29
081215784	1.91 ± 0.50	091020977	1.57 ± 0.39	100910818	2.33 ± 0.59	110903009	2.08 ± 0.39
081221681	1.91 ± 0.29	091031500	2.05 ± 0.42	100918863	2.08 ± 0.23	110904124	2.04 ± 0.25
081222204	1.91 ± 0.42	091101143	1.88 ± 0.28	100923844	1.66 ± 0.34	110904163	1.92 ± 0.37
081224887	1.89 ± 0.43	091103912	2.35 ± 0.58	101013412	1.87 ± 0.60	110919634	1.73 ± 0.29
081231140	1.69 ± 0.35	091109895	1.99 ± 0.51	101021009	2.16 ± 0.30	110920546	2.01 ± 0.16
090101758	2.00 ± 0.23	091120191	1.88 ± 0.34	101023951	1.81 ± 0.23	110921912	2.14 ± 0.27
090102122	1.99 ± 0.35	091127976	2.99 ± 0.76	101113483	2.05 ± 0.22	110926107	2.01 ± 0.27
090112332	1.87 ± 0.40	091128285	2.15 ± 0.31	101123952	1.96 ± 0.20	110928180	1.78 ± 0.19
090112729	1.84 ± 0.54	091208410	1.90 ± 0.72	101126198	1.81 ± 0.30	111003465	1.95 ± 0.51
090117640	2.34 ± 0.64	091227294	2.23 ± 0.34	101201418	2.07 ± 0.24	111009282	1.93 ± 0.15
090131090	1.89 ± 0.34	100116897	1.88 ± 0.23	101207536	2.10 ± 0.31	111012456	1.91 ± 0.45
090202347	2.12 ± 0.36	100122616	1.81 ± 0.40	101208498	1.99 ± 0.94	111012811	2.38 ± 1.02
090217206	2.37 ± 0.45	100130729	1.93 ± 0.25	101224578	2.10 ± 0.24	111015427	1.94 ± 0.19
090310189	1.76 ± 0.22	100131730	2.09 ± 0.18	101225377	1.77 ± 0.24	111017657	2.42 ± 0.50
090323002	2.03 ± 0.21	100224112	2.06 ± 0.29	101227406	2.08 ± 0.20	111024722	1.91 ± 0.28
090328401	2.08 ± 0.28	100225580	2.18 ± 0.53	101227536	2.33 ± 0.54	111107076	2.00 ± 0.25
090419997	2.13 ± 0.26	100304004	2.03 ± 0.19	101231067	1.82 ± 0.39	111127810	1.65 ± 0.49
090424592	2.07 ± 0.18	100322045	1.86 ± 0.29	110102788	1.93 ± 0.20	111216389	1.88 ± 0.24
090425377	2.01 ± 0.28	100324172	1.87 ± 0.32	110118857	1.87 ± 0.44	111228453	2.14 ± 0.36
090502777	2.18 ± 0.32	100326402	1.90 ± 0.23	110120666	1.88 ± 0.39	111228657	1.97 ± 0.30

[a] Too low statistic at $f > 6$ Hz. In this case white noise start at lower frequency, so we have estimated the $\langle P \rangle$ level above 4 Hz.

Table 1.3. Time and Peak count rate. *BeppoSAX*/GRBM HR sample including 42 GRBs.

GRB	$t_{\rm start}$[a] (s)	$t_{\rm stop}$[a] (s)	Peak rate (count s^{-1})	T_{90} (s)
970111	−0.34	40.02	46.53 ± 1.26	31.00
970117B	−0.25	19.00	61.63 ± 1.38	13.00
970315A	−0.41	20.97	116.87 ± 8.15	15.00
970517B	−0.75	3.61	139.11 ± 5.09	5.00
970601	6.99	41.75	74.83 ± 3.13	30.00
970612B	−0.89	37.71	14.53 ± 2.49	38.00
970625B	−1.35	48.98	178.88 ± 9.79	15.00
970627B	−0.73	15.86	100.03 ± 7.58	15.00
970706	−9.01	72.25	15.69 ± 0.61	59.00
970816	−0.06	6.61	51.43 ± 2.74	6.00
971027A	−1.66	12.20	26.89 ± 1.46	11.00
971223C	−6.22	50.18	52.58 ± 4.13	47.00
980203B	0.38	48.75	217.07 ± 8.81	23.00
980306C	0.62	28.25	79.07 ± 1.95	21.00
980329A	−1.06	36.93	73.26 ± 4.15	19.00
980428	−5.05	88.46	21.72 ± 1.34	100.00
980615B	0.94	97.48	85.10 ± 5.01	64.00
980827C	0.33	87.24	158.30 ± 5.36	51.00
981111	−6.39	48.81	35.91 ± 2.67	34.00
990128	0.67	11.30	121.88 ± 3.11	8.00
990620	0.42	13.97	38.68 ± 1.72	16.00
990705	−0.23	41.19	63.92 ± 3.93	32.00
990913A	0.03	44.54	183.03 ± 8.08	40.00
991124B	−1.65	25.31	8.01 ± 0.62	28.00
991216B	0.46	25.42	416.88 ± 11.96	15.00
000115	0.04	25.71	200.84 ± 8.42	15.00
000214A	0.37	8.75	58.66 ± 3.60	8.00
000218B	0.26	23.70	258.43 ± 11.67	20.00
000419	0.72	20.70	21.65 ± 0.82	20.00
000630	0.94	44.55	21.76 ± 2.02	26.00
000718B	−0.19	97.05	67.51 ± 2.98	34.00
001004	1.10	11.20	191.46 ± 8.26	9.00
001011C	0.94	31.62	29.67 ± 1.42	24.00
001212B	0.64	72.46	45.83 ± 3.10	67.00
010109	0.90	22.17	293.48 ± 6.62	7.00
010317	0.87	31.03	210.87 ± 8.65	30.00
010408B	0.23	6.40	199.33 ± 8.39	3.81
010412	−1.49	65.48	24.62 ± 2.47	60.00
010504	−0.12	19.84	42.79 ± 4.07	15.00
010710B	1.06	27.05	53.73 ± 4.50	20.00
010922	0.60	41.52	19.20 ± 1.30	40.00
011003	−0.94	45.41	36.72 ± 1.81	34.00

Note. — The PDS is calculated in the time interval reported.

[a]Referred to the *BeppoSAX*/GRBM trigger time.

Table 1.4. White noise level (Leahy normalisation). *BeppoSAX* HR sample.

GRB	$\langle P \rangle$ ($f > 30$ Hz)	$\langle P \rangle$ ($f > 50$ Hz)
970111	2.13 ± 0.09	2.11 ± 0.15
970117B	2.11 ± 0.14	2.17 ± 0.22
970315A	2.09 ± 0.13	2.09 ± 0.20
970517B	2.50 ± 0.31	2.19 ± 0.46
970601	2.18 ± 0.10	2.24 ± 0.16
970612B	2.15 ± 0.10	2.14 ± 0.15
970625B	2.10 ± 0.08	2.04 ± 0.13
970627B	2.02 ± 0.15	1.94 ± 0.26
970706	2.09 ± 0.07	2.13 ± 0.10
970816	1.75 ± 0.22	1.88 ± 0.35
971027A	1.98 ± 0.16	1.95 ± 0.25
971223C	2.13 ± 0.08	2.22 ± 0.13
980203B	2.07 ± 0.09	2.04 ± 0.13
980306C	1.96 ± 0.11	1.97 ± 0.17
980329A	2.06 ± 0.10	1.98 ± 0.15
980428	2.08 ± 0.06	2.14 ± 0.10
980615B	2.10 ± 0.06	2.08 ± 0.09
980827C	2.08 ± 0.06	2.18 ± 0.10
981111	2.16 ± 0.08	2.19 ± 0.13
990128	2.11 ± 0.19	2.08 ± 0.29
990620	2.13 ± 0.16	2.12 ± 0.26
990705	2.07 ± 0.09	1.97 ± 0.14
990913A	1.94 ± 0.09	1.95 ± 0.14
991124B	2.11 ± 0.12	2.14 ± 0.18
991216B	2.01 ± 0.12	2.01 ± 0.19
000115	2.06 ± 0.12	2.03 ± 0.18
000214A	2.12 ± 0.21	1.91 ± 0.32
000218B	2.44 ± 0.13	1.81 ± 0.18
000419	2.12 ± 0.13	2.05 ± 0.21
000630	2.03 ± 0.09	2.03 ± 0.14
000718B	2.10 ± 0.06	2.05 ± 0.09
001004	2.05 ± 0.19	1.99 ± 0.29
001011C	2.07 ± 0.11	2.00 ± 0.18
001212B	2.04 ± 0.07	2.12 ± 0.11
010109	1.93 ± 0.13	1.87 ± 0.20
010317	2.29 ± 0.11	2.05 ± 0.17
010408B	1.76 ± 0.23	1.4 ± 0.34
010412	2.01 ± 0.07	2.07 ± 0.11
010504	2.03 ± 0.14	1.98 ± 0.25
010710B	2.07 ± 0.12	2.00 ± 0.18
010922	2.06 ± 0.09	2.09 ± 0.15
011003	2.10 ± 0.09	2.17 ± 0.14

Note. — Table of white noise level at $f > 30$ Hz and at $f > 50$ Hz related to the sub-sample of 42 GRBs detected by *BeppoSAX*/GRBM with 7.8 ms time resolution. Uncertainties at 1σ

Table 1.5.

GRB	$\langle P \rangle$ ($f > 30$ Hz)	$\langle P \rangle$ ($f > 50$ Hz)
970315A	2.00 ± 0.03	2.00 ± 0.03
970517B	2.03 ± 0.03	2.03 ± 0.03
970601	2.12 ± 0.03	2.10 ± 0.04
970625B	2.02 ± 0.03	2.01 ± 0.03
970627B	2.02 ± 0.03	2.02 ± 0.03
970816	1.97 ± 0.04	1.98 ± 0.04
980203B	2.01 ± 0.03	2.01 ± 0.03
990128	2.04 ± 0.03	2.04 ± 0.03
990620	2.06 ± 0.03	2.06 ± 0.03
990705	2.04 ± 0.03	2.04 ± 0.03
990913A	1.97 ± 0.03	1.97 ± 0.03
991216B	1.91 ± 0.03	1.91 ± 0.03
000115	2.01 ± 0.03	2.01 ± 0.03
000214A	2.03 ± 0.03	2.03 ± 0.03
000630	2.05 ± 0.03	2.05 ± 0.03
001004	1.99 ± 0.03	1.98 ± 0.03
001212B	2.06 ± 0.03	2.06 ± 0.03
010109	1.94 ± 0.03	1.94 ± 0.03
010317	2.04 ± 0.03	2.03 ± 0.03
010408B	1.99 ± 0.03	1.99 ± 0.03
010504	2.01 ± 0.04	2.01 ± 0.04

Note. — Table of white noise level at $f > 30$ Hz and at $f > 50$ Hz related to the sub sample of 25 GRBs detected by *BeppoSAX*/GRBM with 0.5 ms time resolution. Uncertainties at 1σ

Table 1.6. Best fit parameters of the average PDS for different samples of GRBs

Sample	Size	Norm	α_1	$f_{\rm b}$ (10^{-2} Hz)	α_2	$f_{\rm b2}$ (Hz)	α_3	χ^2/dof
Fermi/GBM (8–1000 keV)[a]	205	$5.0^{+1.2}_{-0.9}$	$1.06^{+0.05}_{-0.07}$	$5.5^{+0.8}_{-0.7}$	$1.75^{+0.03}_{-0.03}$	–	–	110/100
Fermi/GBM (8–40 keV)[a]	155	$3.9^{+1.5}_{-1.1}$	$1.20^{+0.07}_{-0.08}$	$6.4^{+1.4}_{-1.2}$	$1.95^{+0.07}_{-0.06}$	–	–	78/54
Fermi/GBM (40–200 keV)[a]	201	$5.1^{+0.7}_{-1.1}$	$1.03^{+0.06}_{-0.04}$	$5.5^{+1.0}_{-0.5}$	$1.67^{+0.02}_{-0.03}$	–	–	130/115
Fermi/GBM (200–1000 keV)[a]	74	$7.3^{+5.8}_{-4.2}$	$1.05^{+0.08}_{-0.09}$	$3.8^{+3.4}_{-1.5}$	$1.47^{+0.06}_{-0.04}$	–	–	79/72
Fermi/GBM FRED (8–1000 keV)[a]	10	$3.8^{+3.0}_{-1.9}$	$1.32^{+0.10}_{-0.10}$	$6.3^{+3.1}_{-1.9}$	$2.53^{+0.39}_{-0.24}$	–	–	16/14
BeppoSAX/GRBM HR (40–700 keV)[b]	42	$0.021^{+0.011}_{-0.006}$	–	–	$1.49^{+0.04}_{-0.04}$	$1.9^{+0.4}_{-0.4}$	$2.46^{+0.44}_{-0.31}$	145/143
BeppoSAX/GRBM VHR (40–700 keV)[b]	25	$0.040^{+0.048}_{-0.022}$	–	–	$1.52^{+0.17}_{-0.17}$	$2.6^{+1.0}_{-0.9}$	$2.91^{+0.51}_{-0.41}$	4/7
BeppoSAX/GRBM HR+VHR (40–700 keV)[b,c]	42+25	$0.016^{+0.006}_{-0.005}$; $0.053^{+0.017}_{-0.014}$	–	–	$1.50^{+0.03}_{-0.04}$	$2.1^{+0.4}_{-0.3}$	$2.69^{+0.27}_{-0.20}$	165/161
Fermi/GBM VHR (40–700 keV)[b,d]	96	$0.029^{+0.015}_{-0.011}$	–	–	$1.65^{+0.03}_{-0.03}$	$1.1^{+0.3}_{-0.2}$	$2.41^{+0.34}_{-0.19}$	213/200
BeppoSAX/GRBM HR+VHR + *Fermi*/GBM VHR (40–700 keV))[b,e]	42+25+96	$0.027^{+0.014}_{-0.008}$; $0.088^{+0.042}_{-0.025}$; $0.019^{+0.010}_{-0.006}$	–	–	$1.60^{+0.02}_{-0.03}$	$1.4^{+0.3}_{-0.3}$	$2.33^{+0.15}_{-0.13}$	502/365
Fermi/GBM (15–150 keV)[a]	200	$5.1^{+1.2}_{-1.0}$	$1.06^{+0.06}_{-0.07}$	$5.5^{+0.9}_{-0.7}$	$1.78^{+0.04}_{-0.03}$	–	–	95/91

Note. — Best–fitting parameters of the average PDS of each sample within different energy bands (*Fermi*) and time resolution (*BeppoSAX*).

[a]Low frequency break

[b]High frequency break

[c]Joint fitting of two samples with different time resolutions obtained through the minimization of the joint likelihood. The normalisation parameters refer to 7.8 and 0.5–ms time resolution, respectively.

[d]In this case, the best–fitting parameters were found by fitting the average spectra in the same frequency range considered for *BeppoSAX* from 0.02 to 1000 Hz.

[e]Joint fitting of three samples with different time resolutions obtained through the minimization of the joint likelihood. The normalisation parameters refer to 7.8 and 0.5 ms time resolution for *BeppoSAX* and 0.5 ms for the *Fermi*, respectively.

Chapter 2

Clues on the GRBs prompt emission from the power density spectra. The *BeppoSAX* and *Fermi* samples

2.1 Introduction

Although many progress was achieved in the exploration of long GRBa physical nature, several are the issues which still remain unsolved. The nature of the hard X–and gamma–ray signal emitted in the first seconds, the so–called prompt emission, remains one of the most elusive aspects of GRBs. The energy spectrum is highly non–thermal and is usually described empirically by the Band function (Band et al. 1993), a smoothly joined broken power–law whose νF_ν spectrum peaks at $E_{\rm p}$ of a few hundreds keV (Preece et al. 2000; Kaneko et al. 2006; Guidorzi et al. 2011; Goldstein et al. 2012; Gruber et al. 2014).

Generally, two kinds of dissipation processes have been proposed: i) the so–called internal shock (IS) model (Rees & Mészáros 1994; Narayan et al. 1992), in which the dissipation into gamma–rays takes place well above the Thomson photosphere; ii) the photospheric models, in which the dissipation occurs near the photosphere, and where a blackbody–like spectrum is distorted by additional heating and Compton scattering. In either case the dissipation details depend on the ejecta magnetisation, $\sigma = B^2/4\pi\Gamma\rho c^2$, defined as the ratio between the magnetic field and matter energy densities, because it affects the dynamic evolution of the outflow. In models i) a fraction of the kinetic energy

is dissipated into radiation directly through internal shock (IS), or through magnetic reconnection as a consequence of the distortion of the magnetic field lines entrained in the ejecta caused by IS (Zhang & Yan 2011). For models ii), energy dissipation takes place at or below the photosphere, either for baryonic–dominated outflows (Rees & Mészáros 2005; Peer et al. 2006; Thompson et al. 2007; Derishev & Kocharovsky 1999; Rossi et al. 2006; Beloborodov 2010; Titarchuk et al. 2012), or for magnetically-dominated outflows (Giannios 2008; Mészáros & ReesJ. 2011; Giannios 2012).

In this context, timing analysis and its spectral characterisation can provide some insight into the physical processes and geometry of the prompt emission. A classical way of characterising time variability of stochastic processes is offered by Fourier analysis, and astrophysical time series are no exception (e.g., see van der Klis 1989; Vaughan 2013 for reviews). The study of the continuum of the power density spectrum (PDS), corresponding to the Fourier transform of the auto–correlation function (ACF) of a time series, and the possible presence of periodic features in it can constrain the spatial distribution of sources contributing to the observed flux (e.g., Titarchuk et al. 2007). The average PDS of long GRBs is described by a power–law extending over two frequency decades, from a few 10^{-2} to 1–2 Hz. The power–law index lies in the range 1.5–2 with a small but significant dependence on photon energy, with steeper slopes corresponding to softer energy bands. This was found in several independent data sets (Beloborodov et al. 2000; Ryde et al. 2003; Guidorzi et al. 2012; Dichiara et al. 2013) (see also Chapter 1), with evidence for a break around 1–2 Hz for the harder ($\geq$ 100 keV) energy channels. Whilst the average PDS over a large number of GRB exhibits small fluctuations and is easier to characterise in terms of a general stochastic process, it provides no clues on the variety of properties of individual GRBs.

In this work I study the individual PDS of a sample of bright GRBs detected with the *Fermi*/GBM within the 8–1000 keV energy band, and with the *BeppoSAX*/GRBM within the 40–700 keV band.

The difficulty of a proper statistical treatment of the PDS of an individual, highly non–stationary, and short–lived stochastic process such as that given by a GRB time series, is properly overcome with the aid of a Bayesian Markov Chain Monte Carlo technique (see Craiu & Rosenthal 2014 for a review), which is essentially the same as that outlined by Vaughan (2010; hereafter, V10), except for a few minor changes. The same technique has recently been adopted for studying a selected sample of bright short GRBs (Dichiara et al. 2013, see Chapter 3), and outbursts from soft–gamma ray repeaters (Huppenkothen et al. 2013), for which Fourier analysis faces the same formal

problems of short–lived, non–stationary time series.

The main advantage of studying individual vs. averaged PDS is threefold: i) we directly probe the variety of stochastic processes taking place during the γ–ray prompt emission; ii) I search for possible connections between PDS and other key properties of the prompt emission, such as the intrinsic (i.e., source–rest frame) peak energy $E_{\rm p,i}$, and the isotropic–equivalent radiated energy, $E_{\rm iso}$, involved in the eponymous correlation (Amati et al. 2002); iii) I search for occasional features emerging from the PDS continuum, such as coherent pulsations or quasi–periodic oscillations (QPO), which, if any, would be completely washed out by averaging the PDS of many different GRBs. A very similar technique has recently been successfully employed to reveal QPOs in short bursts from Galactic magnetars (Huppenkothen et al. 2014).

In a companion paper (Guidorzi et al. in prep) we carry out the same analysis in the 15–150 keV energy band with the *Swift*/BAT. Using these data sets I explore different energy ranges and provide independent analyses on the timing properties and their possible relations with the energy spectral parameters.

Uncertainties on the best–fitting parameters are given at 90% confidence for one parameter of interest, unless stated otherwise.

2.2 Data analysis

2.2.1 Data selection

We started from 1281 GRBs detected and covered by GBM from July 2008 to December 2013. For each GRB I took the two most illuminated NaI detectors, for which I extracted the corresponding light curves with 64 ms resolution, which I then summed to have a single light curve with the best signal–to–noise ratio (S/N). At this stage I considered the time tagged event (TTE) files, which hold information about trigger time and energy channel of each detected photon. I excluded all the GRBs with no TTE file. In some cases TTE data did not cover the whole event and thus were not considered for the present analysis. We excluded short duration bursts by requiring $T_{90} > 3$ s, and I made sure not to include the short GRBs with extended emission. I then rejected all the GRBs with poor S/N (peak rate fainter than 50 count s^{-1}). We further excluded GRBs with light curves affected by the presence of spikes caused by high–energy particles interacting with the spacecraft (Meegan et al. 2009).

The light curve extraction in different energy bands was made after the data re-

trieval.[1] We processed them with the HEASOFT package (v6.12) following the *Fermi* team threads[2]. We selected different energy ranges using the tool `fselect`. We considered the total energy range of the NaI detectors (8–1000 keV) and three main sub-bands (8–40, 40–200, 200–1000 keV). Light curves were extracted using the `gtbin` tool. For the sigle case of GRB130427A I extract the light curves in the different bands with a time resolution of 10 ms I since the very high S/N observed for this special event. Finally I calculated the PDS for each GRB of the resulting sample in the time interval from the earliest to the latest bin whose counts exceed the 5σ signal threshold above background (hereafter, $T_{5\sigma}$). The PDS were calculated adopting the Leahy normalisation, in which the constant power due to uncorrelated statistical noise has an expected value of 2, namely the expected value of a χ^2_2-distribution in the absence of any extra–Poissonian component (Leahy et al. 1983). To check the Poissonian character of white noise I estimated the mean power at $f > 6$ Hz. Furthermore, I grouped the background-subtracted PDS along frequency so as to fulfil a 3σ significance criterion for each grouped bin. Following the same procedure by Guidorzi et al. (2012) for the *Swift*/BAT data, the selection excluded the GRB whose grouped PDS collected less than 4 grouped frequency bins.

We ended up with 398 GRBs that will be referred to as the *Fermi* sample in the total energy range and with 261, 380 and 134 in the three (soft, mid, and hard) energy channels mentioned above.

Likewise, for the *BeppoSAX*/GRBM sample I started from the GRB catalogue (Frontera et al. 2009) by selecting the GRBs fully covered by the high–time resolution mode, available only for those which triggered the GRBM on–board logic and which did not last longer than ~ 100 s. I then excluded the GRBs whose light curves were hampered by gaps in the time profiles. Finally, I selected the GRBs with the highest S/N (> 40) and ended up with a sample of 89 GRBs. This requirement was motivated by the need of having very good statistical quality even at high frequencies.

In our analysis I selected the light curves with 7.8125 ms time resolution from -8 to 98 s from the on-board trigger time. Therefore the corresponding Nyquist frequency is 64 Hz. The corresponding PDS was extracted over the $T_{5\sigma}$ interval, as in the case of *Fermi*. Tables 2.1 and 2.2 report the $T_{5\sigma}$ interval for each selected GRB. The same procedure was adopted for the *BeppoSAX* data: the final PDS obtained for each GRB of each sub–sample was grouped according to a 3–σ significance criterion excluding the events which collected less than 4 grouped bins. Consequently, the final sample consists

[1] http://legacy.gsfc.nasa.gov/fermi/data/gbm/burst

[2] http://fermi.gsfc.nasa.gov/ssc/data/analysis/scitools/gbm_grb_analysis.html

of 44 GRBs.

2.2.2 PDS modelling

In order to fit the observed PDS with a given model, it is crucial to know how power values fluctuate around it, i.e. the statistical distribution followed by the PDS at each frequency. For instance, adopting standard χ^2 minimisation techniques is conceptually wrong in the case of an unbinned PDS, because power fluctuates according to a χ^2, i.e. more wildly than a Gaussian variable. I chose the proper treatment outlined by V10 with some minor changes.

We considered two different models. The simpler one is a mere power–law (PL) plus the white noise constant,

$$S_{\rm PL}(f) = N\, f^{-\alpha} + B \qquad . \tag{2.1}$$

For each PDS I adopted the following fitting procedure. First, I tried to fit the PDS with eq. (2.1), where the following parameters were left free to vary: the normalisation constant N, the power–law index α (> 0), and the white noise level B. In practice, the logarithm of the normalisation was left free to vary, $\log N$, instead of N itself, because of the reasons explained in AppendixA 2.5.

However, for a sizeable fraction of GRBs of our sample the PDS clearly showed evidence for a break in the power–law. For such cases, I considered a model of a power–law with a break, below which the slope is constant, which will be hereafter called bent power–law (BPL) model,

$$S_{\rm BPL}(f) = N\left[1 + \left(\frac{f}{f_{\rm b}}\right)^{\alpha}\right]^{-1} + B \qquad , \tag{2.2}$$

which reduces to the simple PL model of eq. (2.1) in the limit $f \gg f_{\rm b}$. $f_{\rm b}$ is the break frequency, below which the power density flattens. Our preference for this model over the broken power–law model, such as that of eq.(1) of G12 used for the average PDS of sets of GRBs, which instead allows an additional power–law index for the low–frequency range, is justified by the following reason: the PDS of individual GRBs fluctuate more wildly around the model than the average PDS of a sample of GRBs, simply because the fewer the degrees of freedom of a χ^2 distribution, the larger the ratio between variance and expected value. This makes the fit with a broken power–law very poorly constrained for most PDS of our sample, due to the presence of an extra free parameter, five instead of four. A justification for the specific choice of eq. (2.2) resides in that it provides a good description of the typical PDS of a fast rise exponential decay (FRED) pulse (e.g., Lazzati 2002).

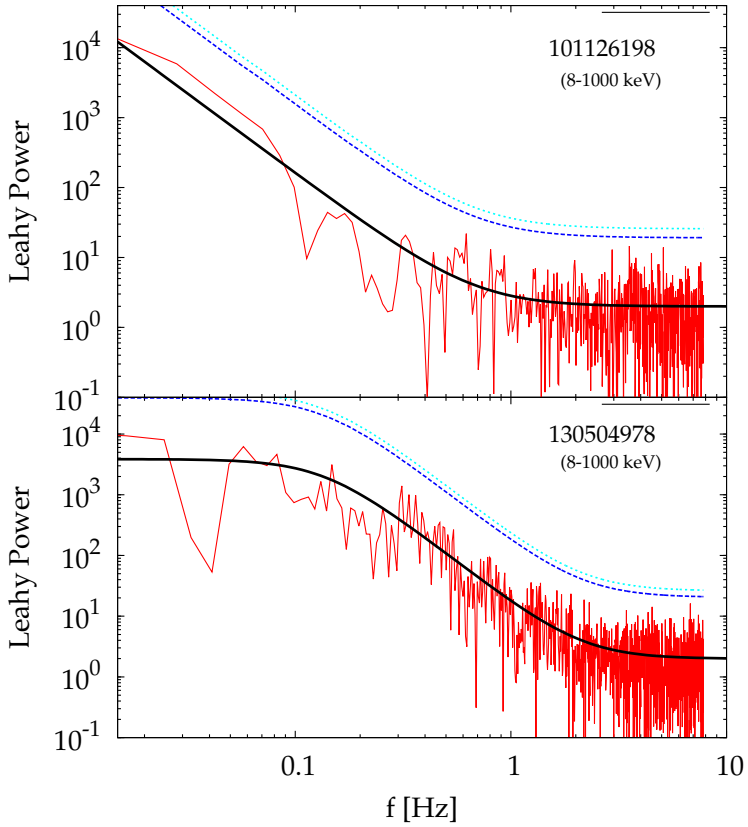

Figure 2.1 Examples of individual PDS. Dashed lines show the corresponding best–fitting model. Blue and cyan dotted lines show the 2σ and 3σ threshold for possible periodic pulsations. *Top*: the PDS of GRB 101126A can be fitted with a simple PL model and background. *Bottom*:fitting the PDS of GRB 130504C significantly improves with a BPL model.

To establish whether a BPL provides a statistically significant improvement in the fit of a given PDS of a GRB with respect to a PL, I used the likelihood ratio test (LRT) in the Bayesian implementation described by V10 (see eq. 2.9 and AppendixA 2.5 for details). For the LRT test, I accepted the BPL model when the probability of chance improvement was lower than 1%. Figure 2.1 illustrates two examples of PDS and their best–fitting models, one for each model.

The choice of 1% for the LRT test significance was the result of a trade–off between Type I and Type II errors. For lower values, a number of PDS which display a clear–cut break by visual inspection, and for which fitting with BPL constrained the parameters reasonably well, did not pass the test (too many Type II errors). On the other side, adopting significance values higher than 1% turned into too many BPL–modelled PDS with very poorly constrained parameters (Type I errors). The final choice of 1% in our sample gave only a handful of GRBs, for which I had to force the PL model, although

the LRT test had formally rejected it. The reason was that the BPL parameters could not be constrained (Type I errors). Just a few is also consistent with what one would expect from a 398–sized sample with 1% probability that BPL is mistakenly preferred to PL.

2.3 Results

We found 88 *Fermi* GRBs whose PDS are best fitted with BPL (∼22%) in the total full passband 8–1000 keV. This fraction becomes 14%, 27%, and 23% in the soft, mid, and hard channels, respectively. I then selected the break frequency values with a logarithmic uncertainty $\sigma(\log(f_{\rm b})) < 0.3$. This constraint shrank the samples to 70, 23, 71 and 23 GRBs for the total, soft, mid, and soft channels, respectively. The detection of a break reflects the presence of a timescale which predominantly contributes to the total variance over the others, while the PL best–fitted PDS is the result of the superposition of several characteristic time scales with comparable contributions to the total variance of the light curve.

In order to show this, in Figure 2.2 we illustrate the difference between the two groups of PDS best fitted with either BPL or PL and the meaning of dominant timescale, wherever there exists one. Whenever the total variance is mostly dominated by some specific timescale, this stands out and determines the break in the PDS, which is best fitted with BPL (top panel of Fig. 2.2). Differently, when several different timescales have comparable weights in the total variance, the resulting PDS exhibits no clear break, and appears to be remarkably shallower ($\alpha_{\rm pl} \leq 2$) than the case with similar pulses.

The same procedure was applied to the *BeppoSAX* sample. BPL best fits the PDS of 21 GRBs (∼48%). Adopting the same accuracy constraint on the break frequency, 4 GRBs out of 21 were discarded, thus leaving us with 17. A Kolmogorov–Smirnov (KS) test applied to the different break frequency sets obtained from *Fermi* (total energy range) and *BeppoSAX* samples rejects the assumption of a common distribution with a p–value of 4.4×10^{-5} (see Figure 2.3).

Actually it is likely to be due to a combination of several factors: different time resolution in the light curve (and consequently a different Nyquist frequency), different S/N distribution, different time interval distributions (the HR light curves could not last longer than 106 s for the *BeppoSAX*/GRBM). We investigated the weight of the latter effect and picked up the *Fermi* GRBs with $T_{5\sigma} < 100$ s. The chance probability

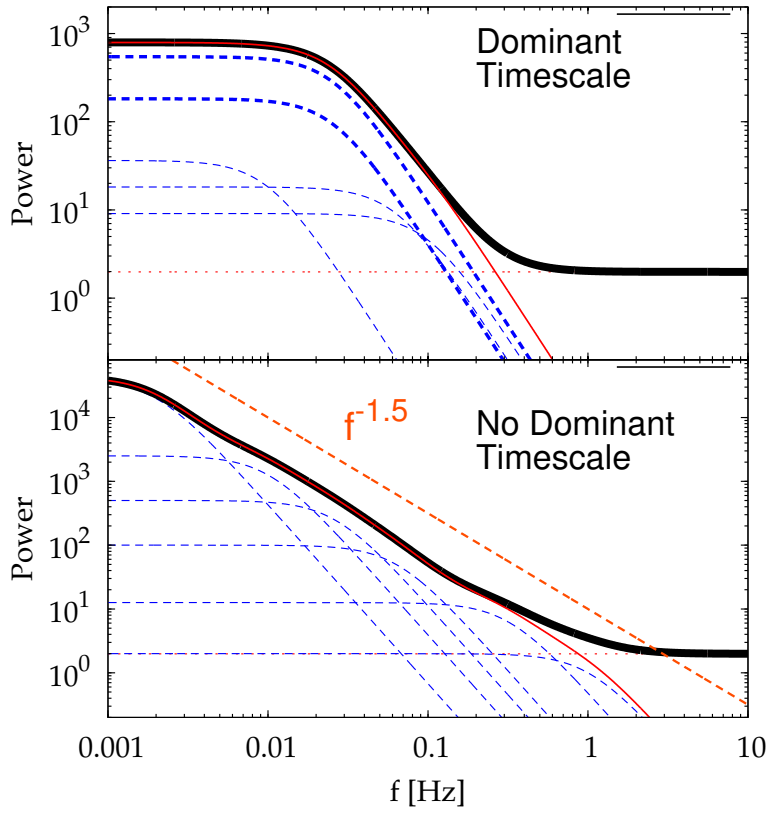

Figure 2.2 *Top panel*: sketch of a BPL PDS (thick solid line) as the result of the superposition of PDS of different pulses (thin dashed lines). The overall variance is dominated by pulses with similar timescales (thick dashed lines), whose frequency break there corresponds to the dominant time. The white noise level is also shown (dotted line). *Bottom panel*: the PL PDS is the result of the superposition of different pulses with different timescales, so that no break stands out in the total PDS, which looks like a power–law with a shallow index ($\alpha = 1.5$ in this example, thick dashed line).

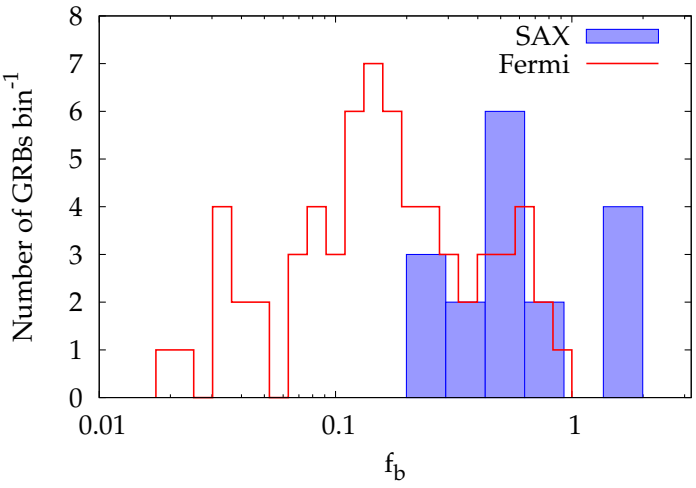

Figure 2.3 In the figure is shown the distributions of the two populations of frequency breaks measured with the two different instruments.

of a common distribution for the sets of break frequency values remarkably increased to 7.4×10^{-4}, i.e. not enough to make it plausible though.

We then re-extracted the PDS on a fixed time interval of 100 s in the 8–1000 keV band. For this analysis I considered the *BeppoSAX* sample and all the *Fermi* GRBs with a $T_{5\sigma} < 100$ s, thus ending up with 292 GRBs. This interval was centred either in the middle of the $T_{5\sigma}$ one wherever it was possible, or starting from the beginning of the light curve. For this further analysis the number of PDS best fitted with BPL increased because, on average, lower frequencies can be explored more effectively and the resulting PDS begins to be affected by the overall duration of the event. 39% (60%) of these PDS are best fitted with BPL for the *Fermi* (*BeppoSAX*) sample, whereas for the PDS extracted on the $T_{5\sigma}$ interval the same fractions were 22% and 48%. Passing from extracting the PDS on the $T_{5\sigma}$ to the 100–s long interval, only 63% of the *Fermi* PDS fitted with BPL in the former case are still best fitted with the same model. This consideration emphasises the importance of the $T_{5\sigma}$ interval for providing an optimal estimate of the break in PDS.

Noteworthy is that some *BeppoSAX* PDS seem to show more than one break in the spectral shape. This may be due to the presence of just a few, distinct characteristic times in the light curve. Indeed, in these cases, I found systematically higher break frequency values for the $T_{5\sigma}$ PDS than those extracted on the 100–s interval. The comparison between the break frequencies as determined in both cases is shown in Fig. 2.4; in particular, five *BeppoSAX* GRBs exhibiting this behaviour (970315A, 970517B, 970627B, 990705 and 010408B) show a significant dependence of the break

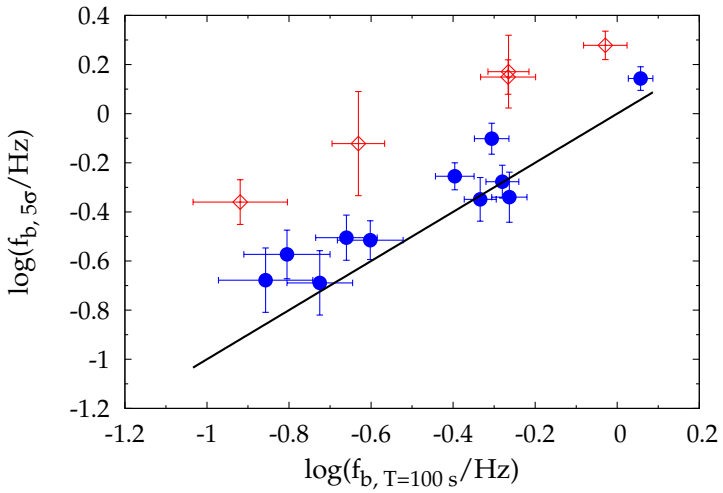

Figure 2.4 Break frequency determined using the *BeppoSAX* light cuves on two different time intervals over which the PDS is extracted (error bars are 1σ). The $T_{5\sigma}$ interval is adopted throughout the present work; the PDS extracted over 100–s fixed duration intervals are shown for comparison purposes. Empty diamonds refer to GRBs whose PDS shows evidence for multiple break frequencies. Filled circles show the cases with a single break frequency. Equality is shown with solid line.

on the time interval choice (Fig. 2.4), whereas for the remaining GRBs the estimate remains unaffected within uncertainties. We can also note that generally the frequency break is slightly shifted at higher values for PDS extracted on the 100–s time interval. This is simply connected with a better expansion to the low frequency region of the PDS. Just to give an example I can point out the case of GRB 970627B for which I found two well separated frequency breaks related to the two PDS extraction time intervals. In this case I found $f_b = 0.93 \pm 0.12$ Hz and $f_b = 1.90 \pm 0.27$ Hz for 100–s and $T_{5\sigma}$ time interval, respectively. These frequencies correspond to $\tau = 0.08 \pm 0.01$ and $\tau = 0.17 \pm 0.02$ in terms of dominant time scale. We can distinguish this kind of pulsation in the light curve shown in Figure 2.5.

Lastly, I further restricted to the sample of GRBs also with a minimum accuracy on the power–law index α, $|\sigma(\alpha)| < 0.5$, for both models. This way I were left with 40 GRBs for the *BeppoSAX* sample and with 342, 225, 311, and 115 GRBs for the *Fermi* sample in the total, soft, mid, and hard energy channels, respectively. Tables 2.3–2.8 report the best–fitting parameters for each PDS of the different samples. In agreement with previous results obtained from the study of average PDS, (Beloborodov et al. 2000; Guidorzi et al. 2012; Dichiara et al. 2013), the average power–law index has a slight but significant dependence on energy. This mean value is 2.32, 2.12, and 1.83 for

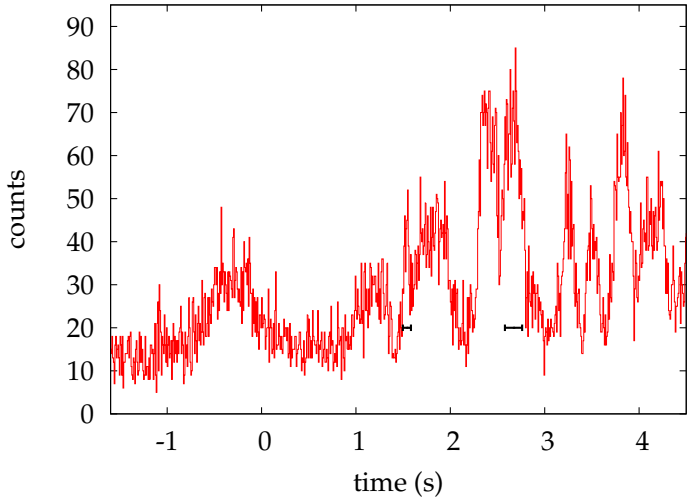

Figure 2.5 a part of the GRB 970627B light curve is illustrated in this figure. We can distinguish two different dominant time-scales. These intervals are directly related to the different frequency breaks observed in the two PDS extracted over the $T_{5\sigma}$ and the 100–s time intervals

increasing energies. The α distributions of the selected samples in the three different energy ranges are shown in Figure 2.6. A KS-test between the three distributions turn out with the following p-value: $P_{low-mid} = 3.3 \times 10^{-4}$, $P_{mid-high} = 9.1 \times 10^{-7}$ and $P_{low-high} = 3.3 \times 10^{-14}$. Therefore I can surely assert that the high energy α population is completely different than the lower energy values and it is intrinsically connected with the shallower PDS.

The contrast between the power–law index distributions obtained with the two models is illustrated in Figure 2.7 in the case of Fermi data.

2.3.1 White noise level

In a first preliminary run over the total band (8-1000 keV) PDS, I assumed a uniform prior distribution for B. The resulting values were approximately normally distributed around $\langle B \rangle = 1.993$ with $\sigma = 0.020$. Therefore in the next set of run I assume a Gaussian distribution with the same values. I then reapplied the fitting procedure to each GRB. The resulting distribution is shown in Figure 2.8.

From this I computed the average value of B obtaining $\langle B \rangle = 1.991 \pm 0.001$. Compared with the pure Poissonian noise, it is equivalent to $99.6 \pm 0.1)\%$ The suppression effect is due to the dead time. Indeed the average counts rate in our light curves is The white noise suppressed power is described as:

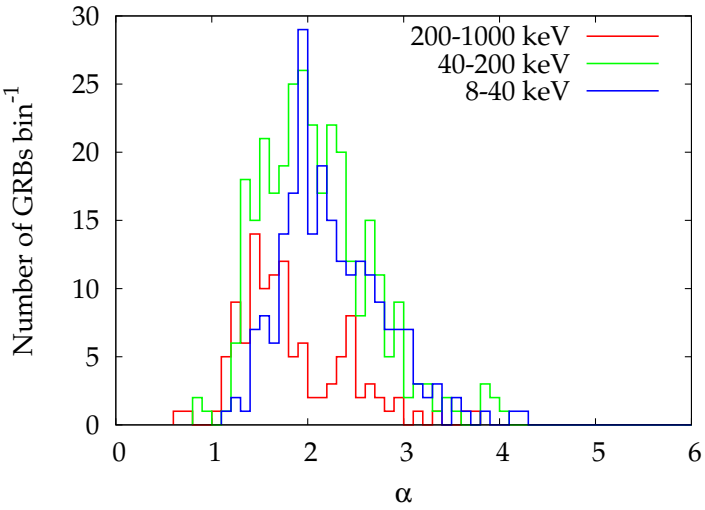

Figure 2.6 Different power–law index distributions obtained for the three different energy ranges of the Fermi sample.

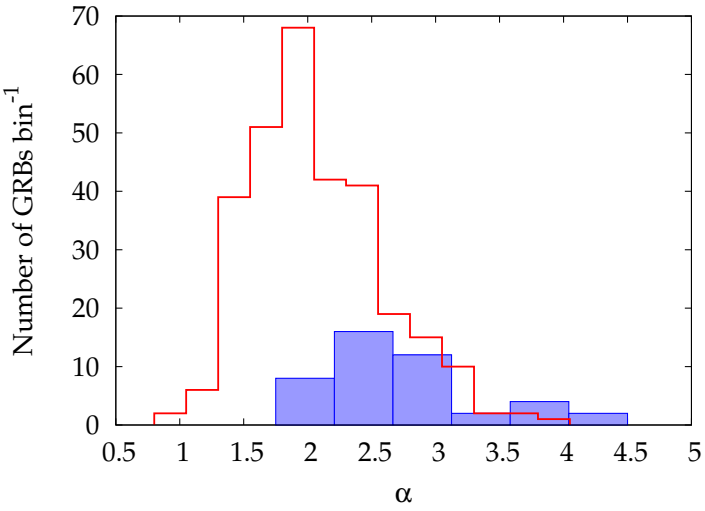

Figure 2.7 Distribution of α for both the used models. It is referred to the Fermi sample in the total energy range

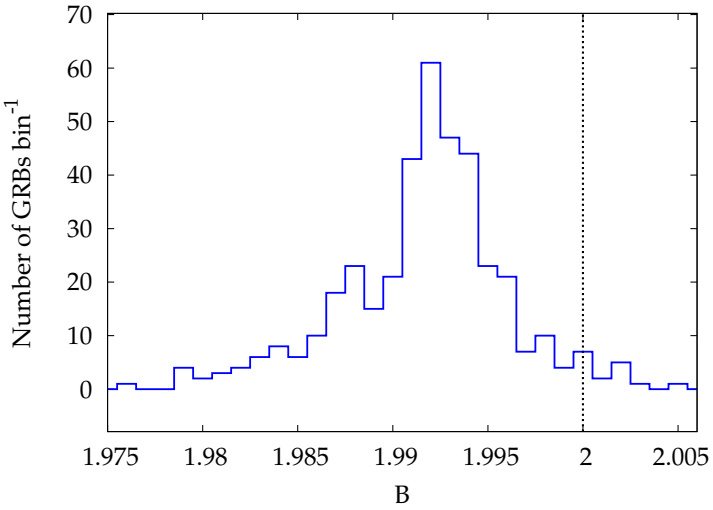

Figure 2.8 White noise leves distribution resulting from the fitting procedure

$$WN = 2(1 - \mu\tau)^2 \tag{2.3}$$

where μ is the mean counts rate and τ is the dead time. Since that $\tau \sim 2$ μs in case of *Fermi*/GBM, we can estimate the value of μ able to generate such suppression ($\mu \sim 70$ counts over 64 ms). The average counts rate in the used light curves is 87.66 ± 23.41 which is consistent with the observed suppression factor. Since the dead time acts in same way independently of the energy band I adopted the same prior as for the total energy band and finally obtained equal estimates within uncertainties.

2.3.2 Dominant timescale vs. duration

For the 70 *Fermi* and 17 *BeppoSAX* GRBs , whose PDS are best fitted with BPL (we did not include restriction on the α uncertainty at this stage to keep a good statistic), we observed a relation between the dominant timescale $\tau = 1/(2\pi f_{\rm b})$ and the total duration of each event as measured by the $T_{5\sigma}$ interval. Modelling it with a power–law using the D'Agostini method, which is suitable to account for a non–null extrinsic scatter (D'Agostini 2005), the power–law index turns out to be consistent with unity ($m = 0.9 \pm 0.2$) i.e. with a simple proportionality relationship. We therefore fitted assuming $m = 1$ both data sets simultaneously in the total energy range I find:

$$\tau = 10^{-1.77 \pm 0.05}\, T_{5\sigma} \qquad , \tag{2.4}$$

with an extrinsic scatter $\sigma(\log \tau) = 0.25 \pm 0.04$. Hence, on average the characteristic time, whenever this can be identified, it is ~ 60 times as short as the overall duration

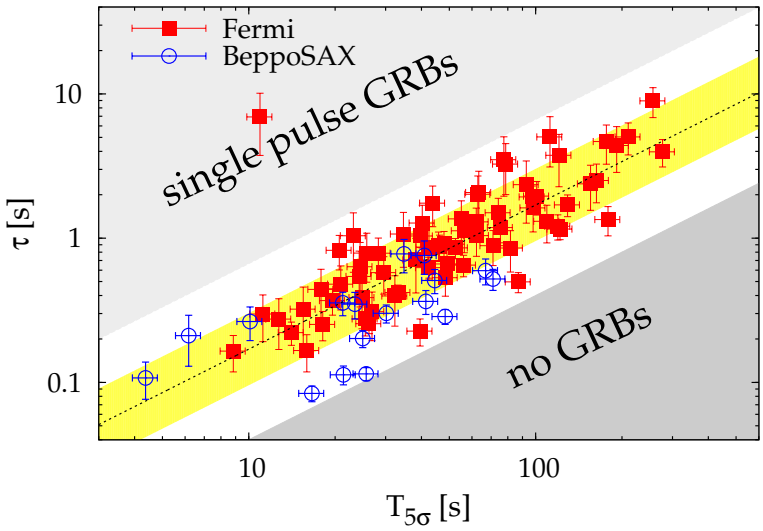

Figure 2.9 Relation between GRB duration $T_{5\sigma}$ and characteristic time τ for the GRBs best fitted with BPL for both *Fermi* (filled squares) and *BeppoSAX* (empty circles) sets. The dashed line shows the best proportionality model and the shaded area marks the $\pm 1\sigma$ region as estimated with the D'Agostini method. The point in the top left zone of the plot is the GRB 081028B, one of the few single–pulse GRBs for which the PDS identified the dominant timescale.

of the burst, with a scatter of about 80%. The result is displayed in Figure 2.9. For the *Fermi* GRBs alone, thus excluding in particular the three aforementioned *BeppoSAX* GRBs with evidence for multiple characteristic times, the proportionality constant remains unchanged within uncertainties, while the extrinsic scatter slightly decreases to $\sigma(\log \tau) = 0.22 \pm 0.05$.

A very similar result is also found within the analogous and independent *Swift* data set. The top left portion of the $T_{5\sigma}$–τ space in Fig. 2.9 is known to be populated by the GRBs whose light curves merely consist of a single, smooth pulse. This is the case of most fast–rise exponential–decay (FRED) GRBs, for which the unique characteristic time scale coincides with the duration itself of the pulse. This kind of simple events are under sampled in our set, which collects the best S/N events and, as such, disfavours the GRBs with few pulses. Furthermore, the procedure I set up for the PDS fitting is not efficient in detecting the break due to the finite duration of the GRBs, for which one would need much longer time intervals at the cost of worse S/N. This explains why there is only one such GRB (081028B).

Instead, there is no a priori reason why one should not observe GRBs in the bottom right part of the $T_{5\sigma}$–τ space, i.e. with short dominant timescale and long duration. To make sure that possible GRBs populating this region had not accidentally been either

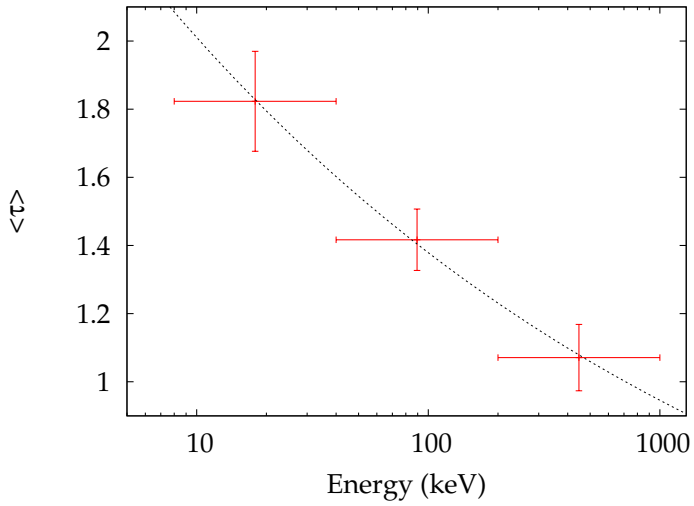

Figure 2.10 This picture show the average dominant timescale as a function of the energy range. The observed trend is described by the dashed line which illustrate a trend as $w \propto E^{-0.16}$

discarded or misclassified by our procedure, I simulated a light curve by replicating and appending a real GRB profile with a short dominant timescale, and ended up with an arbitrarily long GRB. Indeed, our procedure did identify the same short dominant timescale within uncertainties, with no appreciable bias in the estimates of both quantities. We are therefore led to conclude that the lack of long GRBs with short dominant timescales ($T_{5\sigma}/\tau \geq 60$) is not an artifact, but a genuine property of GRB samples.

2.3.3 Dominant timescale vs. Energy

We then compared the average dominant timescales found for the different energy ranges (low, middle and high band). Therefore I estimated the average value for τ from the BPL selected samples in each band. The result is shown in Figure 2.10

Fitting these values I found a tight relation between the average width of the pulses with respect to the energy channel. I found $w = 2.9 \times E^{-0.16}$. This kind of study provide a completely different approach to study how the pulses width change with energy compared with analysis reported by (Fenimore et al. 1995). Despite the completely different technique and the independent sample, I found similar results.

2.3.4 PDS and peak energy $E_{\rm p}$

We searched for possible relations between PDS and spectral properties such as the peak energy of the time–averaged νF_ν spectrum, $E_{\rm p}$. I used the values for $E_{\rm p}$ published

in the official *Fermi* catalogue (Goldstein et al. 2012; Gruber et al. 2014) by selecting GRBs with a peak energy with $\leq 40\%$ uncertainty and with a high–energy power–law index $\beta_{\rm B} < -2$ as parametrised in the Band function (Band et al. 1993), so as to ensure a finite maximum in the νF_ν spectrum. Moreover I excluded from the following analysis the GRB 080810. Indeed this event occurred in the middle of a solar flare and an unambiguous measure of $E_{\rm p}$ has still to be found.

I considered only the cases in which the best fit model is indicated as Band function, cut–off power–law or smoothly broken power–law. The Band model's parameters were considered even when the smoothly broken power law model was the best fit.

No relation stood out between the characteristic time τ and peak energy. We instead found a clear link between the PDS power–law index α (for the BPL best model cases, α is the slope above the break) and $E_{\rm p}$. Figure 2.11 displays $E_{\rm p}$ vs. α for *Fermi*/GBM data, with the latter being estimated separately for the PDS of the light curves in the three energy channels. Unfortunately, the *BeppoSAX*/GRBM limited energy range prevented us from deriving a statistically sound sample with both measured quantities.

For the soft energy channel, Pearson's, Spearman's, and Kendall's correlation coefficients between $\log E_{\rm p}$ and α have p–values of 5.0×10^{-3}, 6.4×10^{-5}, and 4.5×10^{-5}, respectively. The significance of the correlation improves when one applies the same tests to the mid energy channel: the same p–values become 6.8×10^{-4}, 7.4×10^{-6}, and 9.3×10^{-6}. Instead, the correlation is no more significant for the hard energy channels, with the few GRB with the required statistical quality showing no evident link between the two quantities. The full passband case has significance values between those of the soft and the mid energy channels. The above correlation coefficients do not account for the uncertainties affecting each points along both axes. When one does it through MC simulations, the significance intervals for each correlation tests do not change in essence the previous results. For instance, the intervals comprising the second and third quartiles of each significance distribution of Pearson's test, i.e. from 25% to 75% of simulated values, are $[4.3 \times 10^{-3}$–$1.2 \times 10^{-2}]$ and $[5.3 \times 10^{-4}$–$2.3 \times 10^{-3}]$ for the soft and mid energy channels, respectively.

The correlation might also be due to the existence of two classes, depending on whether $\alpha < 2$ or $\alpha > 2$. I split the sample of $E_{\rm p}$ values in two such classes and performed a KS test to see whether the two resulting $E_{\rm p}$ sets could possibly originate from a common distribution. As a result, only for the energy channel with the most significant correlation, the 40–200 keV, which also has the best S/N, I found a p–value

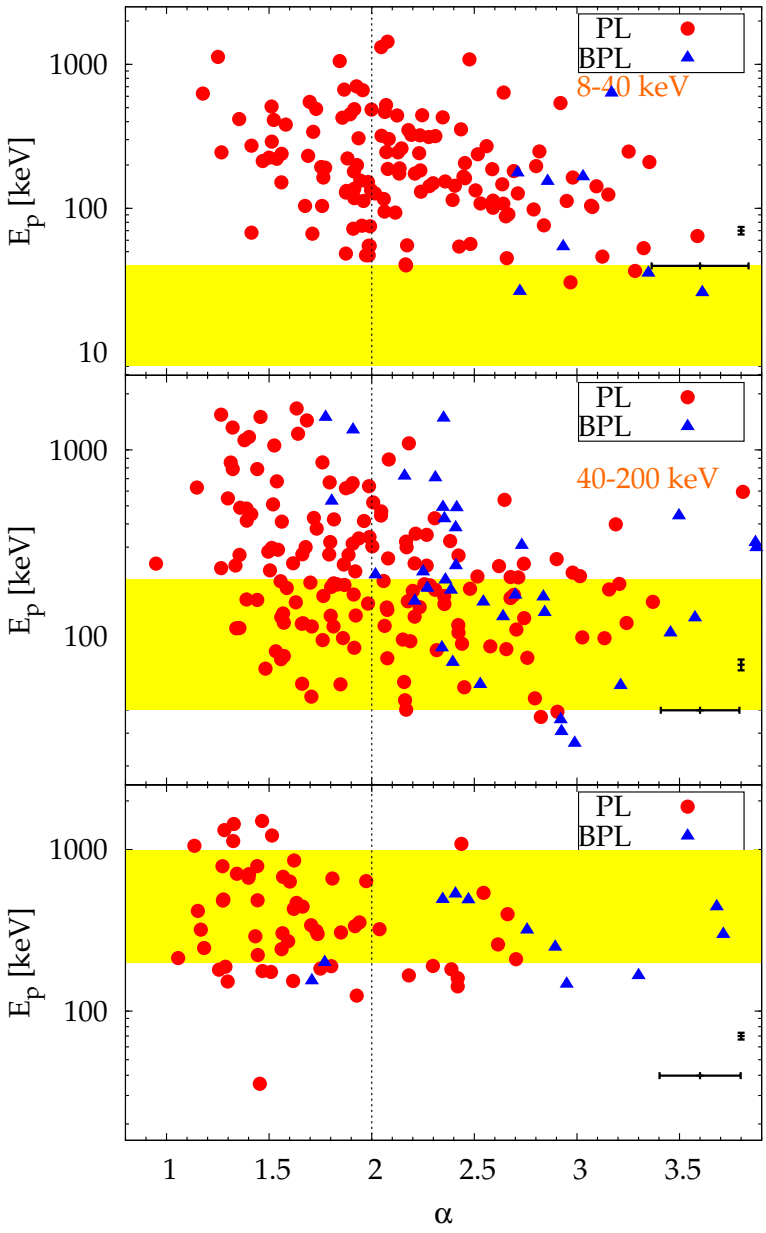

Figure 2.11 Peak energy $E_{\rm p}$ of the time–averaged spectrum vs. the PDS index α for both models of *Fermi* GRBs: circles (triangles) correspond to PL (BPL). Top to bottom panels refer to the 8–40, 40–200, and 200-100 keV energy bands, respectively. Median 1–σ errors along both axes are shown in the bottom right of each panel.

of 1.1×10^{-3}. In spite of the different detectors, energy bands and possibly different GRB populations, these results are similar to what I found with the *Swift*/BAT data, with the correlation being stronger when the PDS refer to the light curves extracted in the best–S/N energy channel. Hence, the correlation significance is likely to be more sensitive to the S/N rather than the energy channel itself.

2.3.5 GRBs with redshift

While the *Fermi* data set allowed us to better explore the dependence on energy, for a large fraction of *Swift* data I could study the $E_{\rm p}$–α correlation in the intrinsic (i.e., source–rest frame) space. This requires the knowledge of redshift z, by which one can estimate the intrinsic peak energy $E_{\rm p,i} = E_{\rm p}\,(1+z)$. The power–law index α is invariant.

In the *Fermi* and *BeppoSAX* samples I could nonetheless determine $E_{\rm p,i}$ for a sub–sample of 22 GRBs from the former and 4 GRBs from the latter set. I didn't apply the uncertainty selection on α and $\log(f_{\rm b})$ for the rest-frame analysis to have a good statistic.

I retrived the values of redshift from the literature (Gruber et al. 2011) and from the web [3]. As shown in Fig. 2.12, the property that GRB with high values of $E_{\rm p}$ tend to exhibit shallower PDS than what softer GRBs mostly do is also confirmed in the intrinsic plane as far as these GRBs are considered. Pearson's, Spearman's, and Kendall's tests yield p–values respectively of $(1.8, 1.4, 2.9) \times 10^{-5}$. The corresponding intervals from MC simulations accounting for uncertainties give the following 25%–75% p–value intervals: $[3.1 \times 10^{-5}$–$3.3 \times 10^{-4}]$, $[2.6 \times 10^{-5}$–$2.4 \times 10^{-4}]$, and $[5.7 \times 10^{-5}$–$5.4 \times 10^{-4}]$ for the same tests.

According to the *Swift* results, the correlation between $E_{\rm p,i}$ and α in not only confirmed, but it is more significant in the GRB source rest frame.

2.3.6 PDS and energy spectrum slope

Another interesting result derived from the joint analysis of energy spectrum and PDS comes from the behaviour observed in α–$\beta_{\rm B}$ plane.

The spectral parameter $\beta_{\rm B}$ was taken from the official catalogue (Goldstein et al. 2012; Gruber et al. 2014). We excluded the GRBs for which the quality of the spectral fitting, as reported in the official catalogue (Goldstein et al. 2012; Gruber et al. 2014),

[3] http://www.mpe.mpg.de/ jcg/grbgen.html

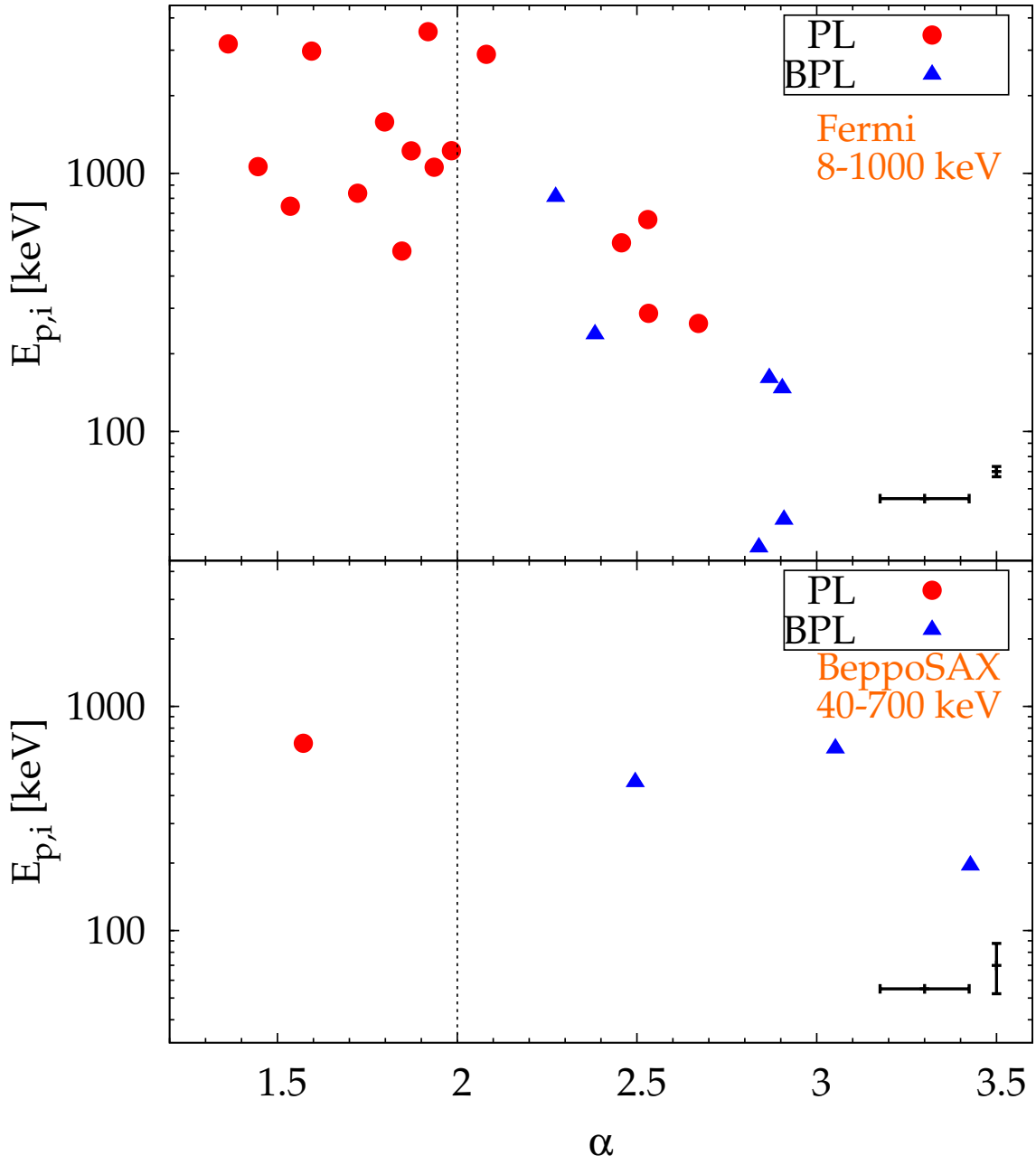

Figure 2.12 Intrinsic peak energy $E_{\rm p,i}$ of the time–averaged spectrum vs. the PDS index α for both models of GRBs with measurable quantities. Median 1–σ errors are shown in the bottom right of each panel.

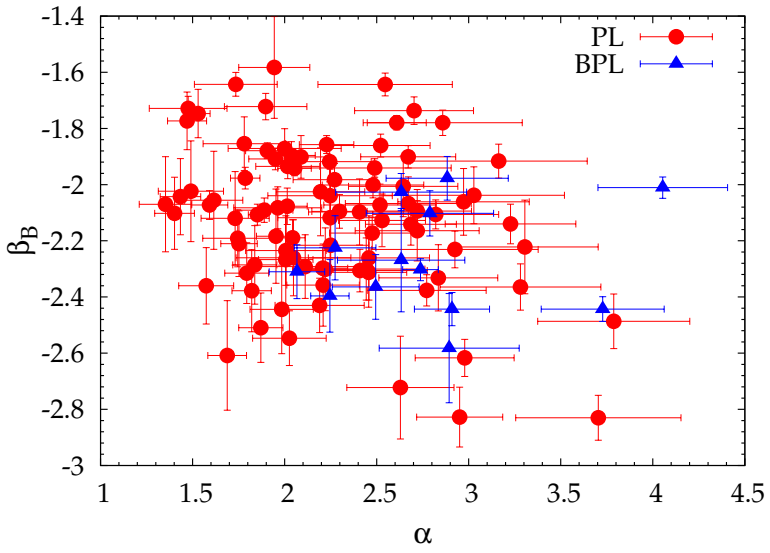

Figure 2.13 High–energy power–law index $\beta_{\rm B}$ of the energy spectrum modelled with the Band function vs. the PDS index α for both models of GRBs with measurable quantities out of the *Fermi* set. Error are 1σ.

was incompatible with a good fit criteria, i.e. with $\chi^2/\mathrm{dof} > 1.3$ or $\chi^2/\mathrm{dof} < 0.7$. In addition, I restricted to the sample of GRBs for which the high energy spectral index had reasonably small uncertainties by requiring $|\sigma(\beta_{\rm B})| \leq 0.2$. In this selection I include also the cases with $\beta_{\rm B} \geq -2$ differently than before. This on purpose to test possible link between the high energy emission (in terms of spectral high energy tail) with respect to timing behaviour. With this analysis I want to probe if, even for relatively low value of $E_{\rm p}$, the presence of an hard energy tail can influence the observed PDS shape. Therefore we required also $E_{\rm p} \leq 500$. Otherwise I already know that higher is the peak-energies value flatter is PDS slope (Section 2.3.4). The result is displayed in Figure 2.13. Despite the large dispersion, there is a hint for correlation. Performing the aforementioned tests, the associated p–values are 0.5%, 3.1%, and 2.7% for the linear (Pearson's), and non–parametric Spearman's and Kendall's statistics, respectively. Not surprisingly, evaluating the same values upon accounting for the uncertainties makes it worse, although MC simulations are a conservative approach. The corresponding 25%–75% intervals for the p–value distributions are (0.5–4.9)%, (2.1–12.2)%, and (2.1–12.3)% for the three tests, respectively. The correlation, if real, is mostly hampered by the difficulty of accurately measuring the high–energy slope of the spectrum, so that with the relatively poor significance being mostly due to the large scatter and low number of points with both measurable quantities. In this regard the present data set clearly do not allow us to make any statement, apart from suggesting it. In Figure 2.13

α refers to the PDS of the full *Fermi*/GBM energy passband. This hint for correlation disappears when one repeats the same analysis assuming the α values as derived from the extreme energy channels, whereas the mid channel, 40–200 keV still shows evidence for it. That this channels is also characterised by the best S/N suggests that the strength of this result as well as of those previously discussed is likely to be a mere effect of a better statistical quality of the sample, rather than a genuine dependence on energy.

2.4 Conclusions

We studied the behaviour of the PDS of individual GRBs in a systematic way. We identified the cases which show a characteristic time scale in the light curve and studied the slope of the PDS related to the different GRBs. Furthermore, keeping on consider the light curve with dominant time scale associated, I have found a strict relation between the characteristic pulse time and the overall duration of GRB. Indeed the ratio $\frac{T_{5\sigma}}{\tau}$ turn out to be quite constant, around the value of 60. This same behaviour it's also followed by the *BeppoSAX* sample. For this sample I found same cases which don't fit with the simple model used to describe the shape of the PDS. Indeed, the lower instrumental threshold of GRBM and the finest time resolution allow us to explore the PDS shape up to very high frequency. I have found that some PDS model need more than one break to provide a better description of the shape. Another important confirm came from the combined analysis between PDS and energy spectral properties. I have seen that the PDS best fit model is always the PL model for high peak energy value and the average value of these power–law indices seems settle around 1.7, similarly to the index found for the average PDS. Moreover, the multi-band analysis results show that most of the PDS extracted in the lowest energy range (large part of the $E_{\rm p}$ are above the upper limit of this energy band) are best fit using a simple PL ($\sim 92\%$). This effect leads one to think that no characteristic time can be found for energy smaller than the peak energy observed in the energy spectra. As seen in the previous analysis made on the *Swift* data, I have found different classes related to the value of the PDS slope, α, and the peak energy, $E_{\rm p}$. Taking in consideration the 40–200 keV channel, which perform the best S/N ratio, we can see that for α less than 2, the mean value of $E_{\rm p}$ tend to be substantially higher than the other one found for α greater than 2. This effect becomes clearly evident in the rest–frame. Actually a kind of correlation is observable in the $E_{p,i}$–α plane (the Pearson's correlation coefficient has a p–value of 1.8×10^{-5}). At the end, also another dependence was found among timing and

spectral energy properties. Generically the GRBs related to shallower PDS have flatter behaviour at high energy in the energy spectrum. If we fit the energy spectra using a Band law, we have steeper value of $\beta_{\rm B}$ index in correspondence to the steeper PDS. All together this indication seem to suggest that the timing features are strictly tied with some spectral parameter. Therefore the models suggested to explain this kind of phenomena should provide an interpretation able to expect this joint behaviour.

2.5 AppendixA

2.5.1 PDS modelling: details

Under the general assumption that a time series is the outcome of a stochastic process, the power in each frequency bin distributes like a χ^2_{2M}, where the degrees of freedom, $2\,M$, is given by 2 times M, i.e. the number of original spectra that are summed (van der Klis 1989). Let P_j be the observed power at frequency bin j and S_j its model value. The corresponding probability density function for P_j given the expected value S_j is given by

$$\begin{aligned} p(P_j|S_j) &= \frac{2M}{S_j}\,\chi^2_{2M}\Big(2M\,\frac{P_j}{S_j}\Big) \\ &= \frac{M}{S_j\Gamma(M)}\,\Big(M\,\frac{P_j}{S_j}\Big)^{M-1}\,\exp\left(-MP_j/S_j\right), \end{aligned} \tag{2.5}$$

where $\Gamma()$ is the gamma function.

The joint likelihood function, $p(\boldsymbol{P}|\boldsymbol{S},H)$, for a given PDS $\boldsymbol{P}$, given a generic model H with expected values $\boldsymbol{S}$, is given by

$$p(\boldsymbol{P}|\boldsymbol{S},H) = \prod_{j=1}^{j=N/2-1} p(P_j|S_j) \qquad , \tag{2.6}$$

where N is the number of bins in the light curves. We excluded the Nyquist frequency bin ($j = N/2$), since this follows a different distribution, $\chi^2_M(MP_{N/2}/S_{N/2})$ (van der Klis 1989).

Maximising eq.(2.6) is equivalent to minimising the corresponding un–normalised negative log–likelihood, $L(\boldsymbol{P},\boldsymbol{S},H)$,

$$L(\boldsymbol{P},\boldsymbol{S},H) = \sum_{j=1}^{j=N/2-1} \Big(M\,\log S_j + M\,\frac{P_j}{S_j} - (M-1)\,\log P_j\Big). \tag{2.7}$$

So far, the dependence of the joint log–likelihood in eq. (2.7) on model H is implicit through the model values, S_j.

We determine the best–fitting model and the relative best–fitting parameters in the Bayesian context. From Bayes' theorem, the posterior probability density function of the parameters of a given model H and for a given observed PDS $\boldsymbol{P}$, is

$$p(\boldsymbol{S}|\boldsymbol{P}, H) = \frac{p(\boldsymbol{P}|\boldsymbol{S}, H)\, p(\boldsymbol{S}, H)}{p(\boldsymbol{P}|H)}, \tag{2.8}$$

where the first term in the numerator of the right-hand side of eq. (3.11) is the likelihood function of eq. (2.6), $p(\boldsymbol{S}, H)$ is the prior distribution of the model parameters, in addition to the normalising term at the denominator.

Initially I assumed a uniform prior distribution, as is customary when no a priori information is available to usefully constrain the parameter space. Finding the mode of the posterior probability of eq. (3.11) is therefore equivalent to minimising the negative log–likelihood (2.7).

For each PDS I adopted the following fitting procedure. First, I tried to fit the PDS with a simple PL model described by eq. (2.1) where the free parameters are the normalisation constant N, the power–law index α (> 0), and the white noise level B. The logarithm of the normalisation was used instead of N itself, because its posterior is more symmetric and easier to handle.

For a sizable part of our sample the PDS required the more complex model described by BPL (eq. 2.2). The reasons for the choice of this particular models are explained in Section 2.2.2.

We adopted the Bayesian procedure presented by V10 for estimating the posterior density of the model parameters through a Markov Chain Monte Carlo (MCMC) algorithm such as the random–walk Metropolis–Hastings in the implementation of the R package `MHadaptive`[4] (v.1.1-2). V10 treated the case $M = 1$, whereas I considered a more general $M \geq 1$. We started approximating the posterior using a multivariate normal distribution centred on the mode and whose covariance matrix is that obtained by minimisation of eq. (2.7). For a given PDS, I generated 5.1×10^4 sets of simulated parameters and retained one every 5 MCMC iterations after excluding the first 1000. I kept these out to remove any dependence on the starting condition. The remaining 10^4 sets of parameters were therefore used to approximate the posterior density. To check the quality of the fit results and search for interesting features, such as QPO or periodic signatures superposed to the continuum spectrum, I used each set of simulated parameters of the PDS model to generate as many synthetic PDS from the the posterior predictive distribution. Hence for a given observed PDS, this procedure allowed us

[4]http://cran.r-project.org/web/packages/MHadaptive/index.html.

to directly calculate 10^4 simulated PDS and use them to infer the probability density function of all the statistics we are interested in.

Let $\hat{S}_j$ be the model value at frequency bin j obtained with the best-fit parameters at the mode of the posterior. Following V10, I define the following quantity, $R_j = 2MP_j/\hat{S}_j$. If the true model S_j were known, R_j would be exactly χ^2_{2M}-distributed. However, estimating it through $\hat{S}_j$ affects its distribution. The advantage of using the posterior predictive distribution is that no assumption on the nature of the distribution of R_j is required when I need to determine the corresponding p–values, since its probability density function (hereafter pdf) is sampled through the simulated spectra and the uncertainties in the model are automatically included. Let $\tilde{P}_{j,k}$ be the j-th bin power of the k-th simulated PDS. Correspondingly, we also define $\tilde{R}_{j,k} = 2M\tilde{P}_{j,k}/\hat{S}_j$. We chose three different statistics:

- $\tilde{T}_{R,k}$ =max$_j(\tilde{R}_{j,k})$ ($k = 1, \ldots, 10^4$). This statistic picks up the maximum deviation from the continuum spectrum for each simulated PDS. The observed value T_R =max$_j(2MP_j/\hat{S}_j)$ is then compared with the simulated distribution and the significance is evaluated directly. By construction, it implicitly accounts for the multitrial search performed all over the frequencies.

- A_k is the Anderson–Darling (AD) statistic (Anderson & Darling 1952) obtained for the k-th set of $\tilde{R}_{j,k}$ compared with a χ^2_{2M} distribution.

- Analogously, KS$_k$ is the Kolmogorov–Smirnov (KS) statistic obtained for the k-th set of $\tilde{R}_{j,k}$ compared with a χ^2_{2M} distribution.

For each of the three statistics, comparing the values obtained from the observed PDS with the corresponding distribution of simulated values immediately yields the significance of possible deviations such as that of a QPO, or the goodness of the fit, as indicated by the AD and KS statistics. As in G12, in addition to the KS, I chose the AD statistic because it is sensitive to the presence of a few outliers from the expected distribution.

For each GRB the choice between the two competing models was determined by the likelihood ratio test (LRT) in the Bayesian implementation described by V10. As for the aforementioned statistics, from the posterior predictive distribution I sampled the pdf of the T_{LRT} statistic defined as

$$T_{LRT} = -\log \frac{p(\boldsymbol{P}|\hat{\boldsymbol{S}}_{\rm PL}, {\rm PL})}{p(\boldsymbol{P}|\hat{\boldsymbol{S}}_{\rm BPL}, {\rm BPL})}$$

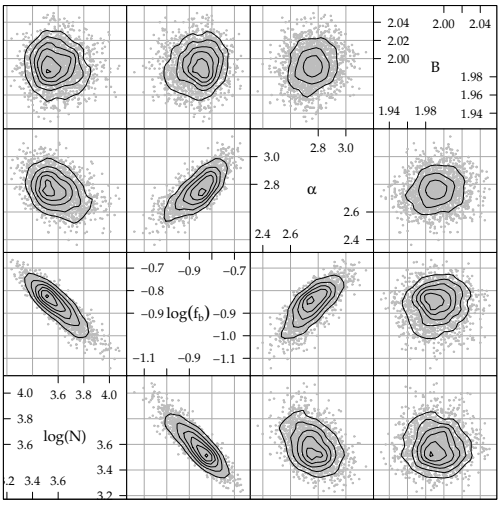

Figure 2.14 Example of marginal posterior distributions for the pairs of parameters of the BPL model obtained from 10^4 simulated posterior simulations in the case of GRB 130504C (only 2000 points are shown for the sake of clarity). Solid lines show the contour levels.

$$= \quad L(\boldsymbol{P}, \hat{\boldsymbol{S}}_{\rm PL}, {\rm PL}) - L(\boldsymbol{P}, \hat{\boldsymbol{S}}_{\rm BPL}, {\rm BPL}) \qquad , \tag{2.9}$$

where $\hat{\boldsymbol{S}}_{\rm H}$ denotes the model obtained with the parameters at the mode of the posterior distribution of a generic model H. Asymptotic theory shows that, given certain regularity conditions are met, The statistic in eq. (2.9) should be distributed as a χ^2_ν variable, where ν is the difference between the number of free parameters in the two used models. The T_{LRT} value is then sampled using the simulated PDS $\tilde{\boldsymbol{P}}_k$ ($k = 1, \ldots, 10^4$) and compared with the observed value. For the LRT test, I performed 10^3 simulations, and accepted the BPL model when the probability of chance improvement was lower than 1% (see Section 2.2.2).

Finally, once the best–fitting model is determined, through the MCMC simulations above described one samples the joint posterior distribution of the model parameters and provides expected value and confidence intervals for each of them. As an example, Figure 2.14

The goodness of fit is established by the p–values associated to the AD and KS statistics. In addition, I also compare the distribution of R_j of the observed PDS against the expected χ^2_{2M} distribution,

Table 2.1. *Fermi* sample of 398 GRBs. Each PDS is calculated in the time interval reported.

Trigger Name	$t_{\rm start}$ [a] (s)	$t_{\rm stop}$ [a] (s)	T_{90} (s)	$E_{\rm p}$ [b] (keV)	$\beta_{\rm B}$ [c]	Redshift
080714745	−1.76	31.77	38.6	-	-	-
080715950	−0.14	108.02	8.8	272.47 ± 33.343	-	-
080723557	−0.13	119.42	76.0	199.72 ± 8.04	-	-
080723985	−0.29	52.89	42.9	428.71 ± 21.37	-	-
080724401	−0.11	48.34	43.6	103.80 ± 10.32	−2.10 ± 0.08	-
080730786	−0.91	18.54	17.5	133.23 ± 5.36	-	-
080806896	−6.98	40.63	43.6	45.07 ± 3.18	−2.31 ± 0.08	-
080807993	0.01	49.86	46.8	626.77 ± 103.69	-	-
080810549	−10.59	102.31	70.9	-	-	3.35
080816503	−0.47	69.35	65.1	136.76 ± 5.25	−2.61 ± 0.20	-
080816989	0.04	29.10	5.7	1544.88 ± 286.27	-	-
080817161	−4.42	87.36	69.4	353.97 ± 18.85	−2.10 ± 0.06	-
080818579	−0.40	36.72	46.3	225.46 ± 72.62	-	-
080824909	−4.56	17.32	24.1	181.02 ± 24.12	-	-
080825593	−0.04	31.84	22.3	174.47 ± 6.50	−2.30 ± 0.07	-
080830368	−1.15	30.66	46.9	272.29 ± 43.89	-	-
080904886	−4.06	20.96	18.7	40.14 ± 1.93	-	-
080906212	−19.30	3.87	22.0	-	-	-
080913735	−0.40	26.48	26.3	-	-	-
080916009	−3.83	86.34	66.6	661.59 ± 45.17	-	4.35
080916406	−0.48	52.51	50.4	-	−1.78 ± 0.04	-
080925775	−2.38	31.80	25.2	163.63 ± 13.62	−2.09 ± 0.08	-
081003644	−1.52	89.56	95.6	-	−1.73 ± 0.04	-
081009140	−0.09	54.69	44.9	30.63 ± 0.45	-	-
081025349	−0.37	44.69	40.7	300.02 ± 31.35	-	-
081028538	−4.50	6.44	13.3	70.67 ± 4.76	-	-
081101532	−0.07	27.45	21.8	521.38 ± 32.23	-	-
081110601	0.01	19.59	23.3	-	-	-
081121858	−3.74	21.09	19.5	-	-	2.51
081122520	−0.75	97.24	24.6	220.99 ± 15.43	-	-
081124060	−1.98	29.58	20.7	-	−2.83 ± 0.08	-
081126899	−18.52	37.99	55.7	323.63 ± 24.73	-	-
081129161	−0.79	33.83	44.0	306.69 ± 27.38	-	-
081130629	−28.04	7.35	8.3	166.78 ± 23.16	-	-
081206275	−5.99	42.78	45.4	-	−1.75 ± 0.09	-
081207680	−3.04	125.28	99.2	414.79 ± 24.00	−2.08 ± 0.07	-
081215784	−1.64	24.60	7.5	441.99 ± 13.18	-	-
081215880	−0.38	82.31	83.5	126.11 ± 11.00	-	-
081221681	−0.53	78.57	32.4	87.96 ± 1.19	-	2.26
081222204	−0.31	36.30	27.6	142.72 ± 9.58	−2.31 ± 0.12	2.77
081224887	0.04	34.98	26.0	397.50 ± 12.24	-	-
081231140	−3.25	45.83	35.8	-	−1.98 ± 0.08	-
090101758	−1.20	120.02	112.6	-	-	-
090102122	−0.01	54.78	32.3	416.73 ± 17.20	-	1.55
090112332	−1.72	38.03	50.5	274.10 ± 71.71	-	-
090112729	−4.35	17.54	14.0	149.32 ± 6.94	-	-
090117640	−5.33	12.40	14.8	-	−2.43 ± 0.10	-
090131090	−0.18	55.88	35.4	54.18 ± 3.62	-	-
090202347	−10.18	42.36	42.4	-	−1.72 ± 0.05	-
090217206	−0.19	37.12	30.3	677.46 ± 38.66	-	-
090310189	−0.23	125.47	121.7	128.33 ± 11.72	-	-
090323002	−2.15	147.42	132.7	632.90 ± 40.83	-	3.57
090328401	−3.81	80.10	60.9	704.12 ± 41.34	-	0.74
090419997	−2.32	101.62	100.2	-	-	-
090424592	0.00	62.08	47.2	153.96 ± 3.83	-	0.54
090425377	−0.56	86.10	78.3	191.62 ± 32.86	−1.88 ± 0.03	-
090502777	−11.11	58.53	67.8	66.65 ± 5.03	−2.36 ± 0.14	-
090514006	−0.40	54.70	102.0	-	-	-
090516137	1.31	190.17	117.6	430.60 ± 37.06	−2.12 ± 0.17	-
090516353	−15.68	89.85	93.0	163.85 ± 19.55	-	4.11
090516853	−0.16	14.81	14.7	-	-	-

Table 2.1 (cont'd)

Trigger Name	$t_{\rm start}$ [a] (s)	$t_{\rm stop}$ [a] (s)	T_{90} (s)	$E_{\rm p}$ [b] (keV)	$\beta_{\rm B}$ [c]	Redshift
090519462	−18.61	229.64	18.8	-	-	-
090524346	−0.54	62.82	56.4	-	-	-
090528516	−0.94	118.93	92.2	222.28 ± 9.61	-	-
090529564	−1.01	10.76	10.4	-	−1.90 ± 0.08	-
090530760	−0.23	201.37	154.8	-	-	-
090618353	−0.58	190.91	119.6	-	-	0.54
090620400	−0.24	19.28	15.9	159.83 ± 6.21	−2.72 ± 0.18	-
090623107	−1.10	78.38	61.4	483.26 ± 44.53	−2.04 ± 0.14	-
090626189	−1.53	72.59	52.5	176.25 ± 9.96	-	-
090711850	−15.15	45.58	46.3	-	−1.64 ± 0.04	-
090717034	−0.42	81.63	69.8	104.23 ± 5.59	−2.17 ± 0.06	-
090718762	−0.04	31.83	25.9	181.32 ± 6.98	-	-
090719063	0.03	25.69	15.1	258.66 ± 5.28	-	-
090720710	0.03	15.96	22.5	1481.154 ± 236.3743	-	-
090804940	−0.01	9.53	8.0	-	-	-
090809978	−1.12	20.45	13.4	-	-	-
090810659	−1.00	132.25	120.3	414.79 ± 24.00	−2.36 ± 0.08	-
090813174	−0.14	8.69	18.6	-	-	-
090814950	−2.25	108.09	108.5	411.12 ± 55.90	-	-
090815438	−4.51	24.68	25.2	36.70 ± 1.70	-	-
090820027	−0.26	67.26	18.7	209.45 ± 2.82	-	-
090820509	−0.05	15.43	15.4	-	-	-
090828099	−2.16	103.06	78.3	189.52 ± 11.52	−2.30 ± 0.15	-
090829672	−2.44	117.17	74.5	187.89 ± 10.68	−2.19 ± 0.06	-
090831317	0.06	68.03	62.2	244.66 ± 33.14	-	-
090902462	0.00	55.94	20.9	1054.71 ± 17.43	-	1.82
090904058	−3.87	62.88	57.7	112.42 ± 11.04	−2.29 ± 0.11	-
090910812	−2.05	74.56	72.6	297.12 ± 20.45	-	-
090922539	−0.23	98.97	93.8	-	-	-
090926181	−0.52	48.44	15.8	339.83 ± 5.75	-	2.11
090928646	−0.13	14.97	13.2	-	-	-
090929190	−0.16	81.57	8.8	530.42 ± 40.27	-	-
091003191	−0.06	24.39	23.3	426.30 ± 20.94	−2.23 ± 0.11	0.90
091010113	−0.17	13.91	7.7	-	-	-
091020900	−5.55	34.51	40.4	244.31 ± 32.26	-	1.71
091020977	0.01	37.71	48.7	1220.94 ± 203.38	-	-
091031500	−0.28	37.03	37.6	548.40 ± 42.91	−2.10 ± 0.13	-
091101143	−0.07	79.93	75.1	151.57 ± 9.25	−2.21 ± 0.12	-
091103912	−3.89	18.45	21.4	245.49 ± 26.56	−2.12 ± 0.19	-
091109895	−0.09	25.25	39.3	103.85 ± 1.07	-	-
091120191	−0.17	56.28	51.6	126.84 ± 3.26	-	-
091127976	−0.01	15.61	9.9	-	-	0.49
091128285	−1.90	72.15	56.2	193.49 ± 8.46	-	-
091208410	−0.01	13.24	12.1	127.01 ± 12.95	−1.90 ± 0.04	1.06
091221870	−6.80	91.89	32.3	164.43 ± 16.73	−2.04 ± 0.09	-
091227294	−0.50	64.20	29.3	283.84 ± 30.43	-	-
100116897	−4.24	115.50	113.6	1083.37 ± 80.30	-	-
100122616	−1.54	38.14	13.8	-	-	-
100130729	−6.61	95.66	94.8	237.28 ± 34.45	-	-
100131730	0.01	9.86	8.8	176.92 ± 8.92	−2.36 ± 0.15	-
100211440	−2.36	27.34	26.9	121.55 ± 5.06	-	-
100224112	−10.04	71.75	89.5	174.24 ± 22.88	-	-
100225580	−16.90	8.32	31.9	334.18 ± 37.46	-	-
100301223	−1.22	29.12	29.2	110.28 ± 7.43	-	-
100304004	−2.47	180.89	127.4	621.41 ± 122.42	-	-
100322045	−0.40	76.97	40.1	-	−1.94 ± 0.03	-
100324172	0.05	63.34	61.8	443.36 ± 13.08	-	-
100326402	−21.23	97.61	48.6	274.79 ± 28.82	−2.06 ± 0.17	-
100401297	−2.77	134.96	134.2	-	−2.07 ± 0.17	-
100414097	0.02	62.55	24.2	668.18 ± 15.11	-	1.37
100424876	−8.93	209.63	199.8	231.38 ± 19.57	-	-

Table 2.1 (cont'd)

Trigger Name	t_{start} [a] (s)	t_{stop} [a] (s)	T_{90} (s)	E_p [b] (keV)	β_B [c]	Redshift
100502356	−9.50	10−	129.7	509.15 ± 80.24	-	-
100503554	−2.58	146.29	139.6	239.00 ± 18.27	-	-
100511035	−4.35	86.08	51.2	1438.43 ± 255.93	-	-
100515467	−0.32	14.84	14.9	177.81 ± 14.60	−2.22 ± 0.17	-
100517072	−0.34	64.23	51.6	128.66 ± 17.92	−1.91 ± 0.04	-
100517154	−0.02	31.53	30.8	48.46 ± 2.65	-	-
100517639	−1.44	6.43	7.0	86.38 ± 3.03	-	-
100519204	−2.09	82.52	70.3	108.18 ± 3.22	-	-
100522157	−0.09	38.31	55.0	155.97 ± 25.67	-	-
100527795	−2.92	95.77	93.7	131.97 ± 9.22	-	-
100528075	−9.03	53.62	44.9	-	−1.90 ± 0.05	-
100612726	−0.45	24.96	17.0	-	−2.49 ± 0.10	-
100615083	−0.20	40.05	36.8	-	-	-
100701490	−0.03	30.82	34.1	1127.64 ± 113.32	-	-
100704149	−7.76	183.86	27.6	-	-	-
100707032	0.07	97.41	64.0	248.58 ± 11.56	−2.01 ± 0.04	-
100709602	−3.27	100.80	102.0	188.96 ± 21.20	-	-
100718160	−23.06	13.87	35.5	109.92 ± 13.13	-	-
100719989	−1.14	41.22	23.0	317.53 ± 11.73	-	-
100722096	−1.12	47.97	8.3	-	-	-
100724029	−4.29	221.95	119.5	-	-	-
100725475	−4.08	216.14	151.7	117.73 ± 17.55	-	-
100728095	−2.54	204.56	162.1	290.37 ± 7.82	-	1.57
100804104	−0.65	12.53	11.1	138.08 ± 4.08	-	-
100805845	−0.07	59.45	79.6	71.42 ± 6.12	−2.07 ± 0.07	-
100820373	−1.06	3.81	8.7	95.58 ± 8.58	−2.26 ± 0.14	-
100826957	−0.13	133.37	90.8	-	-	-
100829374	−3.55	82.47	94.8	90.82 ± 13.24	−2.07 ± 0.09	-
100829876	−0.14	12.59	10.9	133.59 ± 12.29	−2.03 ± 0.07	-
100906576	0.07	118.60	106.8	-	−1.86 ± 0.03	-
100910818	−0.14	20.79	16.3	152.27 ± 8.91	−2.36 ± 0.12	-
100918863	−0.40	127.86	94.1	538.69 ± 12.61	-	-
100923844	−0.13	52.48	53.4	55.32 ± 3.47	−1.58 ± 0.18	-
101013412	−0.31	17.68	16.5	156.96 ± 9.85	-	-
101021009	−2.37	75.64	63.5	260.85 ± 24.62	-	-
101023951	−1.31	112.54	86.6	-	-	-
101113483	−0.57	136.07	129.9	450.75 ± 95.90	−1.77 ± 0.10	-
101123952	−2.23	154.64	105.7	484.97 ± 16.78	−2.11 ± 0.04	-
101126198	−3.98	66.81	53.5	142.12 ± 5.12	-	-
101201418	−2.13	112.04	102.7	-	−1.86 ± 0.04	-
101206036	−0.79	32.10	54.0	423.16 ± 91.46	-	-
101207536	−2.23	70.22	69.9	225.01 ± 26.28	-	-
101208498	−1.11	6.31	3.1	84.95 ± 8.60	−2.14 ± 0.07	-
101224578	−20.90	96.03	54.4	54.89 ± 3.00	-	-
101225377	−3.00	101.83	58.6	208.72 ± 15.25	−2.16 ± 0.11	-
101227406	−1.61	161.40	63.0	722.92 ± 197.95	-	-
101227536	0.14	27.21	86.7	787.88 ± 120.59	-	-
101231067	0.09	41.75	24.1	180.41 ± 10.85	−2.38 ± 0.15	-
110102788	−16.37	149.19	137.4	466.90 ± 37.45	−2.18 ± 0.17	-
110118857	−1.47	30.85	36.7	93.47 ± 7.79	−2.26 ± 0.15	-
110120666	−0.06	42.69	41.2	855.61 ± 74.27	-	-
110207470	−0.16	38.69	88.4	-	-	-
110213220	−2.36	38.09	35.5	113.17 ± 12.16	−2.13 ± 0.09	-
110227420	−111.98	11.86	204.5	-	-	-
110301214	−0.01	12.22	6.5	-	-	-
110302043	−14.78	42.18	51.5	54.21 ± 2.68	−2.23 ± 0.07	-
110304071	−1.36	51.05	50.4	97.41 ± 6.64	-	-
110318552	−4.38	16.30	15.2	116.24 ± 4.82	-	-
110328520	−5.03	114.46	101.8	-	−1.74 ± 0.05	-
110402009	0.09	36.82	55.7	-	-	-
110415541	−0.11	166.23	122.5	-	-	-

Table 2.1 (cont'd)

Trigger Name	t_{start} [a] (s)	t_{stop} [a] (s)	T_{90} (s)	E_p [b] (keV)	β_B [c]	Redshift
110421757	−3.82	125.46	100.0	47.19 ± 4.32	−2.09 ± 0.04	-
110428338	−4.44	99.05	44.8	47.17 ± 3.15	−2.51 ± 0.12	-
110517573	−3.23	27.94	25.5	116.88 ± 4.06	-	-
110522633	−0.06	23.05	22.5	888.18 ± 152.74	-	-
110528624	−4.65	111.89	130.9	196.72 ± 37.74	-	-
110529262	−0.84	49.40	50.7	72.14 ± 7.00	−2.32 ± 0.11	-
110601681	−2.64	59.51	92.5	1668.45 ± 336.76	-	-
110605183	−0.81	77.85	90.4	-	-	-
110610640	−8.49	39.06	46.5	-	−1.85 ± 0.10	-
110622158	−6.18	106.01	79.4	98.21 ± 2.15	−2.62 ± 0.07	-
110625881	−0.85	128.37	50.4	165.78 ± 4.02	−2.30 ± 0.04	-
110702187	−9.41	25.53	97.0	77.94 ± 3.10	-	-
110705364	−2.03	25.23	22.4	377.18 ± 36.41	-	-
110706728	−0.02	17.84	29.9	-	-	-
110709463	−0.33	27.96	27.2	-	-	-
110709642	−1.55	60.66	51.8	488.99 ± 20.81	-	-
110710954	−10.12	19.45	18.9	86.35 ± 3.45	−2.58 ± 0.19	-
110717319	−0.47	112.75	94.5	302.97 ± 19.06	−2.08 ± 0.06	-
110721200	0.05	48.30	33.5	-	−1.78 ± 0.03	-
110725236	−0.52	25.08	36.5	190.66 ± 53.97	-	-
110729142	−11.20	198.21	188.3	313.05 ± 14.46	−2.29 ± 0.14	-
110730660	−13.89	28.99	37.8	93.59 ± 14.26	−1.94 ± 0.03	-
110731465	−0.25	13.83	9.4	319.32 ± 19.69	−2.44 ± 0.16	2.83
110806934	−1.63	36.84	34.8	83.85 ± 3.57	-	-
110809461	−3.99	30.12	35.4	238.66 ± 28.63	−1.92 ± 0.06	-
110813237	−4.34	23.18	36.6	-	-	-
110824009	0.08	71.12	81.4	1496.35 ± 324.82	-	-
110825102	0.02	92.75	69.2	245.54 ± 7.12	-	-
110831282	−0.37	23.38	76.9	-	-	-
110903009	−6.48	39.79	31.4	25.99 ± 1.10	−2.44 ± 0.04	-
110904124	−8.81	100.11	83.8	-	−1.94 ± 0.04	-
110904163	−1.54	44.86	46.9	94.94 ± 5.72	−2.23 ± 0.12	-
110919634	−4.93	67.78	44.3	241.78 ± 14.59	−2.27 ± 0.18	-
110920546	−1.91	254.67	170.0	-	-	-
110921912	−0.14	92.66	18.8	491.03 ± 25.42	−2.40 ± 0.13	-
110926107	−4.26	88.80	101.3	-	−1.98 ± 0.06	-
110928180	−132.73	44.42	167.7	-	−1.92 ± 0.07	-
111003465	−0.05	25.04	20.9	190.21 ± 11.73	−2.14 ± 0.07	-
111009282	−0.33	43.19	34.9	-	-	-
111010709	−1.20	61.71	76.5	-	-	-
111012456	−1.21	30.02	27.0	114.33 ± 7.72	−2.11 ± 0.05	-
111012811	0.06	7.29	22.8	187.05 ± 20.93	−2.03 ± 0.16	-
111015427	−4.46	174.29	92.9	238.69 ± 19.29	−2.27 ± 0.18	-
111017657	−2.14	28.45	15.8	594.75 ± 37.03	-	-
111024722	−11.15	70.26	75.9	75.01 ± 6.35	−2.07 ± 0.05	-
111107076	−0.57	106.69	105.0	197.32 ± 15.52	-	-
111127810	−2.33	21.67	18.0	46.21 ± 2.61	−2.38 ± 0.06	-
111216389	−11.32	98.12	88.7	212.94 ± 7.54	−2.31 ± 0.10	-
111221739	0.01	24.26	23.6	1279.25 ± 314.78	-	-
111228453	−0.97	51.57	4.9	-	-	-
111228657	−14.04	61.36	66.2	26.51 ± 1.25	−2.44 ± 0.06	0.71
120102095	−0.15	19.37	14.7	335.60 ± 29.14	−2.06 ± 0.12	-
120107384	−0.15	25.33	23.2	-	-	-
120118898	−0.08	18.04	28.8	-	-	-
120119170	−8.50	74.06	57.8	183.25 ± 7.96	-	1.73
120119229	−0.04	48.35	59.2	1171.60 ± 163.30	-	-
120121251	−3.00	37.90	43.7	200.08 ± 23.56	−2.04 ± 0.10	-
120129580	0.04	33.19	30.8	298.12 ± 8.75	-	-
120130699	−0.11	27.93	27.7	82.68 ± 5.40	−2.19 ± 0.10	-
120130938	−8.56	41.68	41.6	-	-	-
120204054	−9.49	145.01	65.1	166.22 ± 3.39	-	-

Table 2.1 (cont'd)

Trigger Name	$t_{\rm start}$ [a] (s)	$t_{\rm stop}$ [a] (s)	T_{90} (s)	$E_{\rm p}$ [b] (keV)	$\beta_{\rm B}$ [c]	Redshift
120206949	-0.62	12.50	16.1	270.38 ± 18.38	-2.10 ± 0.12	-
120213606	-3.52	13.51	16.6	112.39 ± 10.31	-	-
120217904	-0.04	4.06	15.5	299.47 ± 26.29	-2.01 ± 0.11	-
120223933	-0.59	46.00	73.1	207.28 ± 15.97	-	-
120224282	-2.88	70.72	100.6	-	-1.87 ± 0.07	-
120226447	-3.57	11.79	24.0	488.45 ± 51.23	-	-
120226871	-12.44	138.09	81.4	-	-1.98 ± 0.04	-
120227725	-0.67	31.58	19.6	128.31 ± 7.09	-2.55 ± 0.10	-
120304061	-0.12	9.10	9.9	-	-	-
120304248	0.06	5.05	10.4	1502.03 ± 99.89	-	-
120308588	-21.67	4.12	26.6	-	-	-
120316008	-2.90	29.42	28.2	707.86 ± 45.33	-	-
120328268	-0.87	114.71	64.8	-	-	-
120402669	-2.04	18.63	17.3	-	-	-
120412920	-0.25	94.79	94.3	75.80 ± 7.05	-2.22 ± 0.09	-
120420858	-1.73	136.57	180.5	-	-1.64 ± 0.04	-
120426090	-0.05	8.40	5.9	124.58 ± 3.20	-2.83 ± 0.11	-
120427054	-0.09	32.10	31.4	-	-	-
120429484	-0.64	60.04	91.1	-	-	-
120512112	-1.77	27.86	36.8	568.16 ± 57.35	-	-
120522361	-4.47	18.25	18.3	56.56 ± 8.04	-2.00 ± 0.05	-
120526303	-0.66	68.66	53.2	788.83 ± 30.93	-	-
120528442	-0.82	45.71	114.9	-	-	-
120530121	0.01	91.14	85.2	196.31 ± 20.02	-	-
120605453	-24.07	18.43	42.6	-	-	-
120611108	-15.28	43.48	54.4	-	-	-
120618919	-20.62	12.47	32.6	190.13 ± 34.22	-2.02 ± 0.18	-
120624933	-1.64	32.80	22.6	637.65 ± 24.51	-	-
120625119	-0.89	8.32	7.9	179.24 ± 14.79	-2.30 ± 0.11	-
120703417	-3.95	70.93	62.6	76.21 ± 6.92	-2.33 ± 0.12	-
120703726	-1.74	26.16	21.8	321.39 ± 28.43	-	-
120707800	-7.71	63.14	45.1	153.55 ± 7.82	-	-
120709883	0.03	38.30	95.2	490.54 ± 42.76	-	-
120711115	-0.48	117.28	41.2	1318.66 ± 45.86	-	1.41
120716712	0.03	235.11	228.7	-	-	-
120719146	-0.26	89.08	82.0	-	-	-
120728434	-26.74	183.50	96.1	-	-	-
120729456	-1.49	49.20	102.0	-	-	-
120806007	-0.60	30.51	87.4	-	-	-
120819048	-6.45	59.92	133.6	-	-	-
120830212	-0.43	17.87	20.3	-	-	-
120830702	-0.85	35.12	42.6	-	-	-
120905657	-2.60	155.61	148.1	-	-	-
120909070	-5.40	136.49	123.5	-	-	-
120913997	-8.39	96.51	93.7	-	-	-
120919052	-0.06	126.66	119.0	-	-	-
120919309	0.01	32.08	21.8	-	-	-
120921877	0.00	9.67	33.4	-	-	-
120926335	-0.27	4.08	6.1	-	-	-
120926426	-4.41	57.35	94.7	-	-	-
121005340	-9.90	144.21	142.3	-	-	-
121029350	-2.75	16.39	16.0	-	-	-
121031949	-5.49	224.91	226.0	-	-	-
121113544	-3.25	109.32	94.2	-	-	-
121117018	-43.81	60.13	100.1	-	-	-
121118576	-2.78	36.78	39.4	-	-	-
121119579	-8.01	2.23	9.6	-	-	-
121122870	-1.02	129.80	125.6	-	-	-
121122885	0.04	15.15	14.6	-	-	-
121123442	-0.02	51.24	50.1	-	-	-
121125356	-6.59	46.34	47.4	-	-	-

Table 2.1 (cont'd)

Trigger Name	t_{start} [a] (s)	t_{stop} [a] (s)	T_{90} (s)	E_p [b] (keV)	β_B [c]	Redshift
121128212	−13.28	25.82	73.6	-	-	-
121225417	−2.15	116.77	80.7	-	-	-
130104721	−10.72	45.09	107.6	-	-	-
130106829	−2.66	70.43	107.9	-	-	-
130106995	−2.72	74.78	73.9	-	-	-
130112286	−29.60	4.77	5.4	-	-	-
130114019	−71.07	5.15	9.2	-	-	-
130121835	−1.06	187.68	182.5	-	-	-
130131511	−3.81	177.44	145.9	-	-	-
130206482	−12.71	85.47	110.1	-	-	-
130209961	−0.23	10.97	30.3	-	-	-
130215649	−6.43	70.11	190.6	-	-	-
130216790	−7.01	9.25	28.4	-	-	-
130216927	−2.53	6.49	21.0	-	-	-
130218261	−9.95	34.53	57.3	-	-	-
130219775	−0.03	107.42	102.4	-	-	-
130220964	−1.25	8.22	6.7	-	-	-
130224370	−33.38	31.97	65.3	-	-	-
130228111	−13.47	98.40	176.9	-	-	-
130304410	−0.03	75.10	94.1	-	-	-
130305486	−0.67	55.39	35.4	-	-	-
130306991	−39.52	95.20	106.8	-	-	-
130307238	−12.32	51.36	67.3	-	-	-
130314147	−0.99	99.04	122.2	-	-	-
130318456	−2.59	118.81	154.2	-	-	-
130320560	−6.47	239.86	331.4	-	-	-
130325203	−0.23	12.64	23.7	-	-	-
130327350	−18.40	34.78	31.6	-	-	-
130331566	−1.63	14.37	14.7	-	-	-
130406288	−0.80	8.29	19.9	-	-	-
130406334	−4.71	86.37	90.5	-	-	-
130409960	−0.74	28.89	27.3	-	-	-
130418844	−51.04	107.36	150.4	-	-	-
130420422	−1.25	29.34	55.0	-	-	-
130425327	−1.83	69.60	66.9	-	-	-
130427324	−0.03	332.19	154.4	-	-	-
130502327	−0.87	86.17	39.4	-	-	-
130504978	−4.07	117.60	87.9	-	-	-
130509078	−1.06	275.87	200.8	-	-	-
130514560	−0.29	18.59	17.9	-	-	-
130517781	−4.39	41.57	35.4	-	-	-
130518551	0.00	4.16	34.4	-	-	-
130518580	−9.25	102.17	57.0	-	-	-
130522510	−0.67	25.95	24.1	-	-	-
130523095	−0.61	206.69	23.7	-	-	-
130528695	−0.23	69.79	64.8	-	-	-
130530719	−0.48	58.27	57.8	-	-	-
130604033	−5.03	34.65	33.8	-	-	-
130606316	−1.76	28.25	38.9	-	-	-
130606497	−0.43	214.35	111.4	-	-	-
130609902	−0.35	207.71	37.5	-	-	-
130612456	0.00	11.07	10.2	-	-	-
130614997	−17.38	61.15	87.6	-	-	-
130623790	−0.61	372.64	369.9	-	-	-
130626596	−24.99	42.14	60.2	-	-	-
130627372	−5.35	133.15	108.4	-	-	-
130628531	−9.63	24.35	31.4	-	-	-
130630272	−0.35	18.85	19.0	-	-	-
130702004	−0.61	175.84	159.4	-	-	-
130704560	−0.99	11.42	7.0	-	-	-
130707505	−0.54	170.27	122.1	-	-	-

Table 2.1 (cont'd)

Trigger Name	t_{start} [a] (s)	t_{stop} [a] (s)	T_{90} (s)	E_p [b] (keV)	β_B [c]	Redshift
130715906	−1.95	60.96	50.8	-	-	-
130725527	−0.23	6.24	7.7	-	-	-
130727698	−2.15	13.47	18.4	-	-	-
130803419	−59.04	41.82	87.6	-	-	-
130815420	−29.22	233.05	247.4	-	-	-
130815660	−0.29	43.49	39.1	-	-	-
130818941	−72.93	9.69	81.1	-	-	-
130821674	−79.59	226.78	206.6	-	-	-
130828306	−0.48	154.91	139.5	-	-	-
130928537	−0.93	117.85	128.1	-	-	-
131011741	−12.45	79.26	94.6	-	-	-
131014215	−0.03	47.90	4.7	-	-	-
131014513	−21.79	7.07	30.9	-	-	-
131021352	0.03	10.65	25.4	-	-	-
131028076	−0.35	36.96	17.8	-	-	-
131029973	−1.25	122.72	118.9	-	-	-
131030791	−68.83	22.94	25.3	-	-	-
131031482	−1.57	7.65	7.7	-	-	-
131105087	−1.76	118.88	112.6	-	-	-
131108024	−0.99	285.92	14.7	-	-	-
131108862	0.03	32.67	19.3	-	-	-
131113483	−0.48	88.35	71.7	-	-	-
131118958	−0.93	133.73	92.4	-	-	-
131122490	−2.79	40.03	28.0	-	-	-
131127592	−4.07	41.82	20.2	-	-	-
131209547	−2.02	69.15	83.2	-	-	-
131214705	−0.42	111.77	79.0	-	-	-
131215298	−0.16	28.83	25.7	-	-	-
131216081	0.03	30.88	30.0	-	-	-
131217183	−8.45	10.30	37.8	-	-	-
131229277	0.00	18.69	14.2	-	-	-
131231198	−3.10	95.78	35.3	-	-	-

[a] Times are referred to the *Fermi*/GBM trigger time.

[b] E_p is the observed peak energy of the time–averaged spectrum (just the values selected for our analysis). Uncertainties are 1σ (Goldstein et al. 2012; Gruber et al. 2014).

[c] β_B is the high–energy power–law index of the energy spectrum modelled with the Band function (selected only). Uncertainties are 1σ (Goldstein et al. 2012; Gruber et al. 2014).

Table 2.2. *BeppoSAX* sample of 44 GRBs. The PDS is calculated in the time interval reported.

Trigger Name	$t_{\rm start}$ [a] (s)	$t_{\rm stop}$ [a] (s)	T_{90} (s)	$E_{\rm p}$ [b] (keV)	Redshift
970111	−0.34	40.02	31.00	159^{+6}_{-6}	-
970117B	−0.25	19.00	13.00	224^{+43}_{-31}	-
970228	−0.14	70.91	56.00	157^{+24}_{-19}	0.695
970315A	−0.41	20.97	15.00	348^{+89}_{-59}	-
970517B	−0.75	3.61	5.00	381^{+159}_{-86}	-
970601	6.99	41.75	30.00	-	-
970612B	−0.89	37.71	38.00	-	-
970625B	−1.35	48.98	15.00	286^{+19}_{-17}	-
970627B	−0.73	15.86	15.00	-	-
970706	−9.01	72.25	59.00	168^{+18}_{-22}	-
970816	−0.06	6.61	6.00	-	-
971027A	−1.66	12.20	11.00	167^{+35}_{-27}	-
971214B	−2.02	30.93	30.00	208^{+54}_{-31}	3.42
971223C	−6.22	50.18	47.00	186^{+37}_{-30}	-
980203B	0.38	48.75	23.00	285^{+10}_{-11}	-
980306C	0.62	28.25	21.00	258^{+95}_{-54}	-
980329A	−1.06	36.93	19.00	269^{+30}_{-25}	-
980428	−5.05	88.46	100.00	314^{+334}_{-68}	-
980615B	0.94	97.48	64.00	168^{+17}_{-15}	-
980827C	0.33	87.24	51.00	202^{+40}_{-58}	-
981111	−6.39	48.81	34.00	376^{+53}_{-41}	-
990128	0.67	11.30	8.00	152^{+20}_{-11}	-
990620	0.42	13.97	16.00	-	-
990705	−0.23	41.19	32.00	276^{+15}_{-13}	0.842
990913A	0.03	44.54	40.00	340^{+93}_{-59}	-
991124B	−1.65	25.31	28.00	-	-
991216B	0.46	25.42	15.00	324^{+60}_{-46}	1.02
000115	0.04	25.71	15.00	214^{+25}_{-21}	-
000214A	0.37	8.75	8.00	271^{+50}_{-33}	-
000218B	0.26	23.70	20.00	-	-
000419	0.72	20.70	20.00	241^{+46}_{-27}	-
000630	0.94	44.55	26.00	216^{+42}_{-56}	-
000718B	−0.19	97.05	34.00	406^{+39}_{-31}	-
001004	1.10	11.20	9.00	187^{+72}_{-40}	-
001011C	0.94	31.62	24.00	345^{+57}_{-53}	-
001212B	0.64	72.46	67.00	208^{+65}_{-37}	-
010109	0.90	22.17	7.00	338^{+72}_{-50}	-
010317	0.87	31.03	30.00	218^{+114}_{-94}	-
010408B	0.23	6.40	3.81	147^{+32}_{-25}	-
010412	−1.49	65.48	60.00	216^{+20}_{-17}	-
010504	−0.12	19.84	15.00	404^{+184}_{-87}	-
010710B	1.06	27.05	20.00	175^{+11}_{-11}	-
010922	0.60	41.52	40.00	204^{+17}_{-15}	-
011003	−0.94	45.41	34.00	288^{+44}_{-34}	-

[a] Times are referred to the *BeppoSAX*/GRBM trigger time.

[b] $E_{\rm p}$ is the observed peak energy of the time-averaged spectrum (Guidorzi et al. 2011).

[c] T_{90} is taken from Guidorzi et al. (2011).

Table 2.3. Best–fitting model and parameters for each GRB of the *Fermi* sample events in the total 8–1000 keV energy band.

GRB	Model	$\log N$	$\log f_{\rm b}$ (Hz)	α	B	$p(T_R)$[a]	$p_{\rm AD}$[b]	$p_{\rm KS}$[c]	$N_{\rm peak}$
080715950	PL	$0.360^{+0.080}_{-0.085}$	-	$1.406^{+0.156}_{-0.139}$	$1.992^{+0.033}_{-0.033}$	0.631	0.828	0.701	2
080723557	BPL	$3.523^{+0.263}_{-0.221}$	$-0.881^{+0.144}_{-0.168}$	$2.326^{+0.163}_{-0.155}$	$1.982^{+0.033}_{-0.033}$	0.957	0.378	0.460	23
080723985	PL	$0.174^{+0.165}_{-0.185}$	-	$2.250^{+0.320}_{-0.288}$	$1.996^{+0.032}_{-0.032}$	0.331	0.834	0.745	7
080724401	BPL	$2.546^{+0.310}_{-0.246}$	$-0.524^{+0.188}_{-0.231}$	$2.789^{+0.612}_{-0.498}$	$1.993^{+0.032}_{-0.033}$	0.862	0.780	0.647	4
080730786	PL	$0.958^{+0.135}_{-0.142}$	-	$2.514^{+0.441}_{-0.385}$	$1.994^{+0.033}_{-0.033}$	0.533	0.510	0.232	4
080806896	PL	$-0.739^{+0.481}_{-0.588}$	-	$2.409^{+0.654}_{-0.534}$	$1.995^{+0.032}_{-0.032}$	0.276	0.867	0.611	3
080807993	PL	$0.917^{+0.069}_{-0.066}$	-	$1.171^{+0.137}_{-0.134}$	$1.993^{+0.033}_{-0.033}$	0.623	0.829	0.735	6
080810549	PL	$-0.211^{+0.163}_{-0.192}$	-	$1.434^{+0.235}_{-0.207}$	$1.992^{+0.032}_{-0.032}$	0.686	0.984	0.971	4
080816503	PL	$0.552^{+0.083}_{-0.083}$	-	$1.688^{+0.177}_{-0.166}$	$1.988^{+0.033}_{-0.032}$	0.771	0.535	0.615	10
080816989	PL	$0.377^{+0.146}_{-0.168}$	-	$1.254^{+0.329}_{-0.280}$	$1.995^{+0.033}_{-0.033}$	0.609	0.420	0.405	1
080817161	PL	$-0.116^{+0.171}_{-0.185}$	-	$2.298^{+0.259}_{-0.234}$	$1.999^{+0.033}_{-0.032}$	0.030	0.162	0.310	3
080818579	PL	$-0.007^{+0.212}_{-0.252}$	-	$1.847^{+0.452}_{-0.384}$	$1.992^{+0.033}_{-0.032}$	0.124	0.655	0.668	2
080824909	PL	$0.624^{+0.141}_{-0.155}$	-	$1.873^{+0.361}_{-0.313}$	$1.992^{+0.033}_{-0.033}$	0.356	0.961	0.948	2
080825593	PL	$1.152^{+0.089}_{-0.086}$	-	$2.207^{+0.233}_{-0.218}$	$1.991^{+0.033}_{-0.033}$	0.948	0.349	0.478	9
080830368	PL	$-0.150^{+0.286}_{-0.359}$	-	$1.965^{+0.516}_{-0.417}$	$1.992^{+0.033}_{-0.033}$	0.947	0.926	0.953	2
080904886	PL	$0.657^{+0.136}_{-0.148}$	-	$2.260^{+0.354}_{-0.315}$	$1.990^{+0.032}_{-0.032}$	0.925	0.299	0.702	4
080916009	PL	$0.250^{+0.119}_{-0.132}$	-	$1.919^{+0.181}_{-0.166}$	$1.996^{+0.033}_{-0.033}$	0.074	0.795	0.839	7
080916406	PL	$-1.423^{+0.615}_{-0.762}$	-	$2.859^{+0.784}_{-0.629}$	$1.988^{+0.033}_{-0.031}$	0.734	0.235	0.554	2
080925775	PL	$0.009^{+0.270}_{-0.327}$	-	$2.720^{+0.528}_{-0.434}$	$1.990^{+0.033}_{-0.033}$	0.332	0.173	0.262	2
081003644	PL	$-0.572^{+0.282}_{-0.358}$	-	$1.476^{+0.375}_{-0.299}$	$1.991^{+0.033}_{-0.032}$	0.296	0.803	0.852	3
081009140	PL	$1.117^{+0.079}_{-0.082}$	-	$2.860^{+0.178}_{-0.167}$	$1.988^{+0.033}_{-0.033}$	0.202	0.110	0.176	2
081025349	PL	$-0.040^{+0.215}_{-0.262}$	-	$1.689^{+0.385}_{-0.315}$	$1.995^{+0.033}_{-0.033}$	0.859	0.761	0.539	4
081028538	BPL	$2.181^{+0.572}_{-0.364}$	$-1.639^{+0.317}_{-0.486}$	$1.893^{+0.435}_{-0.346}$	$2.000^{+0.029}_{-0.030}$	0.079	0.600	0.410	1
081101532	PL	$0.229^{+0.211}_{-0.240}$	-	$2.052^{+0.403}_{-0.340}$	$1.995^{+0.033}_{-0.033}$	0.684	0.573	0.608	4
081122520	BPL	$2.686^{+0.401}_{-0.303}$	$-1.008^{+0.234}_{-0.294}$	$2.085^{+0.271}_{-0.243}$	$1.983^{+0.032}_{-0.033}$	0.535	0.357	0.295	5
081124060	PL	$-0.965^{+0.484}_{-0.548}$	-	$3.704^{+0.793}_{-0.677}$	$1.992^{+0.032}_{-0.033}$	0.603	0.650	0.770	2
081126899	PL	$-0.190^{+0.239}_{-0.273}$	-	$2.181^{+0.365}_{-0.318}$	$1.995^{+0.033}_{-0.033}$	0.723	0.864	0.585	2
081129161	BPL	$2.854^{+0.702}_{-0.441}$	$-0.827^{+0.272}_{-0.417}$	$2.981^{+0.888}_{-0.701}$	$1.995^{+0.033}_{-0.033}$	0.679	0.771	0.702	3
081130629	PL	$-0.344^{+0.318}_{-0.391}$	-	$2.119^{+0.519}_{-0.429}$	$1.991^{+0.032}_{-0.032}$	0.557	0.633	0.513	1
081206275	PL	$0.230^{+0.062}_{-0.062}$	-	$1.530^{+0.110}_{-0.103}$	$1.984^{+0.031}_{-0.032}$	0.114	0.545	0.819	1
081207680	PL	$-1.246^{+0.484}_{-0.625}$	-	$1.963^{+0.431}_{-0.345}$	$2.002^{+0.032}_{-0.032}$	0.785	0.117	0.168	2
081215784	BPL	$3.715^{+0.242}_{-0.204}$	$-0.205^{+0.105}_{-0.121}$	$3.686^{+0.407}_{-0.377}$	$1.991^{+0.033}_{-0.033}$	0.517	0.268	0.426	4
081215880	PL	$-1.223^{+0.626}_{-0.887}$	-	$1.939^{+0.722}_{-0.541}$	$1.997^{+0.032}_{-0.033}$	0.707	0.254	0.183	1
081221681	PL	$0.054^{+0.146}_{-0.158}$	-	$2.532^{+0.259}_{-0.228}$	$1.987^{+0.032}_{-0.033}$	0.841	0.409	0.314	5
081222204	PL	$0.058^{+0.203}_{-0.226}$	-	$2.457^{+0.361}_{-0.317}$	$1.989^{+0.032}_{-0.033}$	0.865	0.597	0.772	1
081224887	PL	$-0.103^{+0.265}_{-0.293}$	-	$3.175^{+0.461}_{-0.407}$	$1.992^{+0.033}_{-0.032}$	0.885	0.992	0.937	1
081231140	BPL	$2.524^{+0.345}_{-0.270}$	$-0.619^{+0.183}_{-0.225}$	$2.883^{+0.588}_{-0.493}$	$1.987^{+0.034}_{-0.033}$	0.993	0.240	0.172	10
090102122	PL	$1.145^{+0.065}_{-0.062}$	-	$1.446^{+0.133}_{-0.123}$	$1.988^{+0.033}_{-0.033}$	0.798	0.157	0.118	11
090112332	PL	$-0.326^{+0.262}_{-0.318}$	-	$1.964^{+0.470}_{-0.399}$	$1.988^{+0.032}_{-0.031}$	0.870	0.441	0.448	2
090112729	PL	$0.448^{+0.199}_{-0.220}$	-	$2.163^{+0.376}_{-0.326}$	$1.994^{+0.033}_{-0.032}$	0.456	0.999	0.999	2
090117640	PL	$0.681^{+0.162}_{-0.177}$	-	$2.190^{+0.427}_{-0.370}$	$1.992^{+0.033}_{-0.033}$	0.362	0.744	0.789	1
090131090	BPL	$3.319^{+0.268}_{-0.227}$	$-0.611^{+0.123}_{-0.140}$	$3.073^{+0.312}_{-0.285}$	$1.988^{+0.032}_{-0.033}$	0.637	0.596	0.678	5
090202347	PL	$-0.392^{+0.286}_{-0.348}$	-	$1.897^{+0.397}_{-0.327}$	$1.994^{+0.032}_{-0.032}$	0.319	0.691	0.563	1
090217206	PL	$0.758^{+0.094}_{-0.098}$	-	$1.615^{+0.190}_{-0.173}$	$1.992^{+0.032}_{-0.032}$	0.458	0.530	0.472	9
090310189	PL	$-0.718^{+0.269}_{-0.335}$	-	$1.528^{+0.336}_{-0.280}$	$1.984^{+0.032}_{-0.032}$	0.796	0.307	0.349	2
090323002	PL	$-0.054^{+0.134}_{-0.142}$	-	$2.081^{+0.192}_{-0.177}$	$1.986^{+0.032}_{-0.032}$	0.521	0.391	0.304	14
090328401	PL	$0.785^{+0.063}_{-0.065}$	-	$1.872^{+0.157}_{-0.147}$	$1.988^{+0.033}_{-0.032}$	0.979	0.256	0.363	9
090424592	BPL	$4.458^{+0.407}_{-0.312}$	$-0.911^{+0.169}_{-0.212}$	$2.383^{+0.131}_{-0.125}$	$1.991^{+0.033}_{-0.034}$	0.988	0.097	0.045	9
090425377	PL	$0.339^{+0.100}_{-0.105}$	-	$1.906^{+0.198}_{-0.187}$	$1.988^{+0.032}_{-0.033}$	0.191	0.313	0.192	5
090502777	PL	$0.007^{+0.155}_{-0.175}$	-	$1.574^{+0.257}_{-0.233}$	$1.991^{+0.032}_{-0.033}$	0.913	0.942	0.984	3
090516137	PL	$-1.078^{+0.346}_{-0.437}$	-	$1.731^{+0.332}_{-0.275}$	$1.996^{+0.031}_{-0.031}$	0.211	0.828	0.822	4
090516353	PL	$-0.589^{+0.272}_{-0.341}$	-	$1.723^{+0.349}_{-0.280}$	$1.990^{+0.032}_{-0.031}$	0.460	0.899	0.757	5
090516853	PL	$0.247^{+0.289}_{-0.342}$	-	$2.384^{+0.719}_{-0.586}$	$1.994^{+0.033}_{-0.033}$	0.349	0.666	0.339	2
090519462	PL	$-0.657^{+0.201}_{-0.242}$	-	$1.126^{+0.231}_{-0.193}$	$1.991^{+0.031}_{-0.031}$	0.995	0.959	0.959	3
090528516	PL	$0.148^{+0.100}_{-0.107}$	-	$1.864^{+0.182}_{-0.165}$	$1.984^{+0.032}_{-0.033}$	0.946	0.302	0.389	12
090529564	PL	$1.693^{+0.130}_{-0.126}$	-	$2.089^{+0.261}_{-0.249}$	$1.993^{+0.033}_{-0.033}$	0.889	0.889	0.917	4
090620400	PL	$0.307^{+0.230}_{-0.261}$	-	$2.629^{+0.513}_{-0.424}$	$1.993^{+0.033}_{-0.032}$	0.993	0.705	0.920	1
090623107	PL	$0.270^{+0.104}_{-0.112}$	-	$1.434^{+0.191}_{-0.173}$	$1.994^{+0.032}_{-0.032}$	0.352	0.898	0.764	8
090626189	BPL	$3.727^{+0.401}_{-0.307}$	$-0.974^{+0.184}_{-0.231}$	$2.326^{+0.173}_{-0.163}$	$1.988^{+0.033}_{-0.034}$	0.894	0.797	0.968	11
090711850	PL	$-0.303^{+0.272}_{-0.344}$	-	$1.735^{+0.403}_{-0.332}$	$1.994^{+0.033}_{-0.033}$	0.583	0.567	0.644	3
090717034	PL	$-0.372^{+0.287}_{-0.336}$	-	$2.476^{+0.404}_{-0.350}$	$2.002^{+0.033}_{-0.032}$	0.593	0.236	0.273	4

Table 2.3 (cont'd)

GRB	Model	$\log N$	$\log f_{\rm b}$ (Hz)	α	B	$p(T_R)$[a]	$p_{\rm AD}$[b]	$p_{\rm KS}$[c]	$N_{\rm peak}$
090718762	PL	$0.159^{+0.227}_{-0.255}$	-	$3.085^{+0.463}_{-0.404}$	$1.994^{+0.032}_{-0.032}$	0.867	0.521	0.394	2
090719063	PL	$0.245^{+0.250}_{-0.273}$	-	$3.153^{+0.520}_{-0.446}$	$1.998^{+0.032}_{-0.033}$	0.426	0.096	0.076	1
090720710	BPL	$2.293^{+0.308}_{-0.246}$	$-0.019^{+0.200}_{-0.263}$	$2.422^{+0.617}_{-0.528}$	$1.994^{+0.033}_{-0.032}$	0.692	0.187	0.063	1
090810659	PL	$-2.929^{+0.883}_{-1.062}$	-	$3.281^{+0.779}_{-0.649}$	$1.983^{+0.031}_{-0.031}$	0.254	0.300	0.332	2
090814950	PL	$-0.136^{+0.150}_{-0.169}$	-	$1.528^{+0.229}_{-0.206}$	$1.992^{+0.033}_{-0.032}$	0.653	0.658	0.636	7
090815438	PL	$-0.756^{+0.469}_{-0.521}$	-	$3.377^{+0.754}_{-0.670}$	$1.993^{+0.032}_{-0.032}$	0.431	0.995	0.996	1
090820027	PL	$0.399^{+0.127}_{-0.133}$	-	$3.227^{+0.225}_{-0.214}$	$1.992^{+0.032}_{-0.032}$	0.155	0.420	0.357	2
090828099	PL	$-0.187^{+0.188}_{-0.214}$	-	$2.221^{+0.269}_{-0.246}$	$1.998^{+0.032}_{-0.032}$	0.599	0.687	0.524	4
090829672	PL	$1.133^{+0.044}_{-0.044}$	-	$2.043^{+0.113}_{-0.110}$	$1.980^{+0.033}_{-0.032}$	0.571	0.079	0.073	15
090831317	PL	$0.945^{+0.059}_{-0.057}$	-	$1.123^{+0.116}_{-0.108}$	$1.992^{+0.033}_{-0.034}$	0.946	0.802	0.511	6
090902462	PL	$1.951^{+0.056}_{-0.053}$	-	$1.595^{+0.095}_{-0.090}$	$1.993^{+0.032}_{-0.033}$	0.534	0.679	0.631	25
090904058	PL	$-0.954^{+0.437}_{-0.561}$	-	$2.112^{+0.537}_{-0.444}$	$1.993^{+0.031}_{-0.032}$	0.862	0.802	0.806	4
090910812	PL	$-0.203^{+0.181}_{-0.210}$	-	$1.747^{+0.273}_{-0.232}$	$1.985^{+0.032}_{-0.032}$	0.885	0.353	0.145	5
090926181	PL	$1.771^{+0.063}_{-0.058}$	-	$1.936^{+0.112}_{-0.105}$	$1.992^{+0.034}_{-0.034}$	1.000	0.173	0.175	8
090929190	BPL	$2.182^{+0.321}_{-0.254}$	$-0.730^{+0.235}_{-0.294}$	$1.931^{+0.322}_{-0.285}$	$1.991^{+0.033}_{-0.033}$	0.906	0.714	0.717	3
091003191	BPL	$3.166^{+0.643}_{-0.415}$	$-0.600^{+0.300}_{-0.426}$	$2.274^{+0.382}_{-0.350}$	$1.991^{+0.033}_{-0.033}$	0.406	0.976	0.992	8
091020900	PL	$-0.920^{+0.624}_{-0.807}$	-	$2.530^{+0.806}_{-0.638}$	$2.002^{+0.032}_{-0.033}$	0.159	0.007	0.006	1
091020977	PL	$0.290^{+0.137}_{-0.150}$	-	$1.657^{+0.288}_{-0.256}$	$1.987^{+0.033}_{-0.033}$	0.804	0.152	0.119	4
091031500	PL	$0.737^{+0.092}_{-0.094}$	-	$1.402^{+0.185}_{-0.167}$	$1.991^{+0.032}_{-0.033}$	0.515	0.086	0.126	8
091101143	PL	$0.594^{+0.078}_{-0.080}$	-	$1.752^{+0.166}_{-0.158}$	$1.987^{+0.033}_{-0.032}$	0.312	0.193	0.224	5
091103912	PL	$0.082^{+0.246}_{-0.277}$	-	$2.247^{+0.499}_{-0.425}$	$1.991^{+0.033}_{-0.033}$	0.896	0.726	0.740	2
091109895	PL	$0.498^{+0.134}_{-0.144}$	-	$1.545^{+0.343}_{-0.294}$	$1.992^{+0.033}_{-0.033}$	0.942	0.989	0.967	2
091120191	BPL	$3.013^{+0.435}_{-0.327}$	$-0.849^{+0.212}_{-0.268}$	$2.482^{+0.346}_{-0.298}$	$1.989^{+0.033}_{-0.032}$	0.760	0.944	0.994	12
091128285	PL	$0.072^{+0.140}_{-0.156}$	-	$1.756^{+0.231}_{-0.207}$	$1.992^{+0.032}_{-0.033}$	0.356	0.903	0.583	5
091208410	PL	$1.293^{+0.145}_{-0.139}$	-	$2.671^{+0.452}_{-0.396}$	$1.993^{+0.033}_{-0.033}$	0.763	0.162	0.209	1
091221870	PL	$-1.309^{+0.606}_{-0.762}$	-	$2.247^{+0.604}_{-0.484}$	$1.993^{+0.032}_{-0.032}$	0.273	0.514	0.579	1
091227294	PL	$-0.275^{+0.250}_{-0.302}$	-	$1.685^{+0.363}_{-0.300}$	$1.997^{+0.032}_{-0.033}$	0.303	0.492	0.367	1
100116897	PL	$-0.202^{+0.164}_{-0.178}$	-	$2.291^{+0.225}_{-0.203}$	$1.988^{+0.031}_{-0.032}$	0.838	0.412	0.595	3
100130729	PL	$-1.370^{+0.539}_{-0.681}$	-	$2.436^{+0.576}_{-0.461}$	$1.992^{+0.032}_{-0.033}$	0.134	0.383	0.645	2
100131730	PL	$1.774^{+0.144}_{-0.136}$	-	$2.209^{+0.337}_{-0.302}$	$1.994^{+0.033}_{-0.033}$	0.630	0.967	0.989	2
100211440	PL	$-0.541^{+0.455}_{-0.541}$	-	$2.454^{+0.707}_{-0.571}$	$1.996^{+0.032}_{-0.033}$	0.935	0.284	0.124	2
100224112	PL	$0.103^{+0.147}_{-0.172}$	-	$1.866^{+0.257}_{-0.225}$	$1.994^{+0.032}_{-0.033}$	0.695	0.540	0.281	5
100225580	PL	$0.103^{+0.393}_{-0.570}$	-	$2.383^{+0.815}_{-0.546}$	$2.000^{+0.033}_{-0.032}$	0.440	0.037	0.016	1
100301223	PL	$0.205^{+0.171}_{-0.191}$	-	$1.568^{+0.350}_{-0.306}$	$1.992^{+0.032}_{-0.033}$	0.711	0.976	0.963	3
100304004	PL	$-1.299^{+0.454}_{-0.579}$	-	$1.741^{+0.427}_{-0.348}$	$1.989^{+0.031}_{-0.031}$	0.768	0.101	0.115	2
100322045	PL	$0.829^{+0.068}_{-0.071}$	-	$2.054^{+0.157}_{-0.143}$	$1.989^{+0.032}_{-0.033}$	0.883	0.699	0.703	10
100324172	PL	$0.983^{+0.068}_{-0.071}$	-	$2.114^{+0.167}_{-0.155}$	$1.988^{+0.033}_{-0.033}$	0.171	0.347	0.393	3
100326402	PL	$-0.627^{+0.243}_{-0.285}$	-	$1.615^{+0.280}_{-0.240}$	$1.989^{+0.031}_{-0.032}$	0.519	0.736	0.814	3
100401297	PL	$-0.378^{+0.199}_{-0.246}$	-	$1.353^{+0.252}_{-0.215}$	$1.994^{+0.031}_{-0.032}$	0.503	0.711	0.612	2
100414097	PL	$0.795^{+0.074}_{-0.076}$	-	$1.798^{+0.158}_{-0.145}$	$1.992^{+0.033}_{-0.033}$	0.900	0.334	0.234	6
100424876	PL	$-0.352^{+0.128}_{-0.142}$	-	$1.381^{+0.148}_{-0.135}$	$1.979^{+0.032}_{-0.032}$	0.407	0.304	0.347	8
100502356	PL	$0.050^{+0.116}_{-0.129}$	-	$1.562^{+0.201}_{-0.185}$	$1.992^{+0.032}_{-0.032}$	0.947	0.629	0.668	8
100503554	PL	$-0.048^{+0.103}_{-0.111}$	-	$1.498^{+0.159}_{-0.148}$	$1.980^{+0.032}_{-0.032}$	0.618	0.091	0.029	12
100511035	PL	$0.695^{+0.065}_{-0.067}$	-	$1.784^{+0.139}_{-0.130}$	$1.986^{+0.032}_{-0.033}$	0.104	0.203	0.245	7
100515467	PL	$0.209^{+0.289}_{-0.321}$	-	$3.305^{+0.708}_{-0.609}$	$1.994^{+0.032}_{-0.033}$	0.656	0.948	0.638	1
100517072	PL	$0.349^{+0.130}_{-0.144}$	-	$1.950^{+0.253}_{-0.225}$	$1.998^{+0.033}_{-0.032}$	0.721	0.465	0.471	2
100517154	PL	$0.462^{+0.134}_{-0.146}$	-	$1.881^{+0.331}_{-0.296}$	$1.991^{+0.033}_{-0.034}$	0.931	0.788	0.890	2
100517639	PL	$1.064^{+0.192}_{-0.194}$	-	$2.086^{+0.588}_{-0.489}$	$1.994^{+0.033}_{-0.033}$	0.505	0.608	0.471	2
100519204	PL	$-1.464^{+0.513}_{-0.608}$	-	$2.713^{+0.609}_{-0.505}$	$1.993^{+0.033}_{-0.032}$	0.519	0.942	0.985	4
100522157	PL	$0.633^{+0.110}_{-0.116}$	-	$1.683^{+0.231}_{-0.207}$	$1.992^{+0.033}_{-0.032}$	0.947	0.525	0.739	3
100527795	PL	$-0.180^{+0.159}_{-0.183}$	-	$1.703^{+0.264}_{-0.228}$	$1.984^{+0.032}_{-0.033}$	0.668	0.066	0.010	5
100528075	PL	$0.154^{+0.145}_{-0.158}$	-	$2.037^{+0.228}_{-0.198}$	$1.993^{+0.032}_{-0.032}$	0.331	0.580	0.448	3
100612726	PL	$-0.545^{+0.403}_{-0.456}$	-	$3.788^{+0.739}_{-0.625}$	$1.990^{+0.033}_{-0.033}$	0.579	0.270	0.350	1
100701490	PL	$1.894^{+0.079}_{-0.076}$	-	$1.374^{+0.144}_{-0.139}$	$1.993^{+0.033}_{-0.033}$	0.867	0.834	0.755	8
100707032	BPL	$4.037^{+0.372}_{-0.299}$	$-1.084^{+0.136}_{-0.159}$	$4.054^{+0.618}_{-0.524}$	$1.992^{+0.032}_{-0.032}$	0.856	0.129	0.079	1
100709602	PL	$-0.970^{+0.350}_{-0.408}$	-	$2.078^{+0.383}_{-0.338}$	$1.990^{+0.032}_{-0.032}$	0.711	0.503	0.387	2
100718160	PL	$0.353^{+0.127}_{-0.142}$	-	$1.462^{+0.286}_{-0.257}$	$1.991^{+0.033}_{-0.033}$	0.937	0.577	0.406	4
100719989	BPL	$3.695^{+0.306}_{-0.260}$	$-0.594^{+0.132}_{-0.148}$	$3.832^{+0.540}_{-0.469}$	$1.985^{+0.034}_{-0.033}$	0.986	0.181	0.305	5
100724029	PL	$0.322^{+0.066}_{-0.069}$	-	$1.972^{+0.111}_{-0.104}$	$1.984^{+0.032}_{-0.032}$	0.650	0.388	0.540	19
100725475	PL	$-1.138^{+0.334}_{-0.400}$	-	$1.893^{+0.310}_{-0.261}$	$1.987^{+0.031}_{-0.031}$	0.201	0.389	0.528	3
100728095	PL	$0.318^{+0.060}_{-0.063}$	-	$1.536^{+0.102}_{-0.096}$	$1.981^{+0.032}_{-0.032}$	0.743	0.153	0.197	24

Table 2.3 (cont'd)

GRB	Model	$\log N$	$\log f_{\rm b}$ (Hz)	α	B	$p(T_R)$[a]	$p_{\rm AD}$[b]	$p_{\rm KS}$[c]	$N_{\rm peak}$
100804104	PL	$0.698^{+0.206}_{-0.236}$	-	$2.335^{+0.482}_{-0.410}$	$1.992^{+0.033}_{-0.032}$	0.603	0.658	0.689	2
100805845	PL	$-0.865^{+0.374}_{-0.446}$	-	$2.518^{+0.541}_{-0.462}$	$1.991^{+0.032}_{-0.032}$	0.327	0.723	0.723	1
100820373	PL	$1.426^{+0.231}_{-0.215}$	-	$2.048^{+0.559}_{-0.461}$	$1.993^{+0.033}_{-0.032}$	0.537	0.956	0.909	2
100826957	PL	$0.647^{+0.059}_{-0.061}$	-	$1.887^{+0.115}_{-0.110}$	$1.986^{+0.032}_{-0.032}$	0.168	0.127	0.233	20
100829374	PL	$-1.449^{+0.538}_{-0.640}$	-	$2.672^{+0.607}_{-0.513}$	$1.987^{+0.032}_{-0.033}$	0.727	0.424	0.553	1
100829876	BPL	$3.405^{+0.548}_{-0.362}$	$-0.237^{+0.272}_{-0.390}$	$2.633^{+0.636}_{-0.537}$	$1.994^{+0.032}_{-0.032}$	0.987	0.434	0.379	5
100906576	PL	$-0.327^{+0.186}_{-0.210}$	-	$2.228^{+0.255}_{-0.227}$	$1.998^{+0.032}_{-0.031}$	0.052	0.901	0.824	4
100910818	BPL	$3.085^{+0.517}_{-0.358}$	$-0.479^{+0.236}_{-0.315}$	$2.495^{+0.415}_{-0.359}$	$1.993^{+0.032}_{-0.032}$	0.894	0.350	0.271	6
100918863	PL	$-1.330^{+0.400}_{-0.471}$	-	$2.682^{+0.403}_{-0.353}$	$1.995^{+0.032}_{-0.031}$	0.319	0.669	0.579	3
100923844	PL	$-0.174^{+0.215}_{-0.246}$	-	$1.944^{+0.336}_{-0.291}$	$1.987^{+0.032}_{-0.033}$	0.626	0.299	0.516	2
101013412	PL	$0.610^{+0.159}_{-0.175}$	-	$1.649^{+0.373}_{-0.315}$	$1.995^{+0.033}_{-0.032}$	0.753	0.824	0.648	2
101021009	PL	$-0.293^{+0.216}_{-0.247}$	-	$2.054^{+0.310}_{-0.274}$	$1.992^{+0.031}_{-0.032}$	0.099	0.880	0.889	3
101113483	PL	$-0.092^{+0.126}_{-0.141}$	-	$1.470^{+0.183}_{-0.162}$	$1.992^{+0.032}_{-0.032}$	0.038	0.968	0.803	5
101123952	PL	$1.215^{+0.038}_{-0.038}$	-	$1.852^{+0.081}_{-0.078}$	$1.981^{+0.033}_{-0.033}$	0.545	0.270	0.425	14
101126198	PL	$-0.075^{+0.187}_{-0.209}$	-	$2.280^{+0.248}_{-0.221}$	$1.995^{+0.033}_{-0.033}$	0.384	0.973	0.916	2
101201418	PL	$-1.269^{+0.413}_{-0.477}$	-	$2.522^{+0.464}_{-0.410}$	$1.997^{+0.032}_{-0.031}$	0.568	0.531	0.508	4
101206036	PL	$-0.626^{+0.481}_{-0.621}$	-	$2.317^{+0.826}_{-0.663}$	$1.993^{+0.033}_{-0.032}$	0.967	0.639	0.661	1
101207536	PL	$0.079^{+0.130}_{-0.146}$	-	$1.526^{+0.239}_{-0.210}$	$1.990^{+0.033}_{-0.032}$	0.663	0.975	0.996	5
101208498	PL	$1.925^{+0.172}_{-0.159}$	-	$2.686^{+0.421}_{-0.384}$	$1.994^{+0.032}_{-0.033}$	0.984	0.281	0.180	1
101224578	PL	$-0.541^{+0.236}_{-0.261}$	-	$1.956^{+0.296}_{-0.271}$	$2.000^{+0.031}_{-0.031}$	0.209	0.595	0.412	3
101225377	PL	$-1.916^{+0.616}_{-0.742}$	-	$2.720^{+0.593}_{-0.505}$	$1.990^{+0.032}_{-0.032}$	0.673	0.941	0.885	2
101227406	BPL	$2.307^{+0.378}_{-0.287}$	$-1.198^{+0.220}_{-0.284}$	$2.449^{+0.554}_{-0.446}$	$1.987^{+0.031}_{-0.031}$	0.921	0.643	0.836	5
101227536	PL	$0.748^{+0.105}_{-0.110}$	-	$1.377^{+0.231}_{-0.208}$	$1.992^{+0.033}_{-0.033}$	0.692	0.491	0.455	5
101231067	PL	$1.052^{+0.078}_{-0.077}$	-	$1.821^{+0.182}_{-0.168}$	$1.989^{+0.033}_{-0.033}$	0.611	0.222	0.121	8
110102788	PL	$-0.118^{+0.139}_{-0.151}$	-	$1.953^{+0.183}_{-0.165}$	$1.998^{+0.032}_{-0.032}$	0.423	0.531	0.452	6
110118857	PL	$-0.298^{+0.323}_{-0.391}$	-	$2.458^{+0.573}_{-0.483}$	$1.991^{+0.033}_{-0.033}$	0.969	0.804	0.758	1
110120666	PL	$0.633^{+0.108}_{-0.113}$	-	$1.791^{+0.235}_{-0.214}$	$1.994^{+0.033}_{-0.033}$	0.487	0.583	0.857	3
110207470	PL	$0.537^{+0.097}_{-0.098}$	-	$0.920^{+0.183}_{-0.172}$	$1.992^{+0.032}_{-0.032}$	0.503	0.677	0.730	6
110213220	PL	$-0.081^{+0.221}_{-0.243}$	-	$2.529^{+0.416}_{-0.361}$	$1.984^{+0.033}_{-0.033}$	0.724	0.016	0.029	1
110302043	PL	$-1.465^{+0.637}_{-0.768}$	-	$2.925^{+0.803}_{-0.669}$	$1.993^{+0.032}_{-0.032}$	0.410	0.845	0.877	1
110304071	PL	$-0.302^{+0.250}_{-0.296}$	-	$1.970^{+0.387}_{-0.328}$	$1.993^{+0.033}_{-0.033}$	0.605	0.948	0.980	2
110318552	PL	$0.622^{+0.167}_{-0.183}$	-	$1.949^{+0.350}_{-0.302}$	$1.995^{+0.034}_{-0.033}$	0.875	0.386	0.348	3
110328520	PL	$-1.600^{+0.555}_{-0.659}$	-	$2.703^{+0.572}_{-0.488}$	$1.986^{+0.032}_{-0.031}$	0.183	0.498	0.490	1
110402009	PL	$0.784^{+0.084}_{-0.082}$	-	$0.884^{+0.162}_{-0.151}$	$1.993^{+0.034}_{-0.033}$	0.502	0.849	0.741	3
110421757	PL	$-0.731^{+0.247}_{-0.276}$	-	$1.889^{+0.269}_{-0.239}$	$1.986^{+0.031}_{-0.031}$	0.171	0.714	0.931	4
110428338	PL	$0.095^{+0.113}_{-0.124}$	-	$1.871^{+0.207}_{-0.189}$	$1.988^{+0.032}_{-0.033}$	0.187	0.729	0.837	7
110517573	PL	$0.483^{+0.147}_{-0.168}$	-	$1.913^{+0.309}_{-0.271}$	$1.994^{+0.033}_{-0.033}$	0.810	0.966	0.950	4
110522633	PL	$-0.026^{+0.261}_{-0.314}$	-	$1.934^{+0.580}_{-0.475}$	$1.992^{+0.033}_{-0.032}$	0.741	0.876	0.541	1
110528624	PL	$-0.609^{+0.267}_{-0.332}$	-	$1.461^{+0.322}_{-0.273}$	$1.992^{+0.033}_{-0.033}$	0.799	0.742	0.265	2
110529262	PL	$0.639^{+0.090}_{-0.092}$	-	$1.794^{+0.203}_{-0.186}$	$1.987^{+0.033}_{-0.033}$	0.893	0.330	0.232	5
110601681	PL	$-0.454^{+0.283}_{-0.355}$	-	$1.674^{+0.383}_{-0.326}$	$1.992^{+0.033}_{-0.032}$	0.787	0.705	0.607	1
110610640	PL	$-0.158^{+0.260}_{-0.320}$	-	$1.781^{+0.399}_{-0.332}$	$1.995^{+0.032}_{-0.033}$	0.979	0.525	0.321	3
110622158	PL	$-1.328^{+0.413}_{-0.469}$	-	$2.978^{+0.471}_{-0.407}$	$1.991^{+0.032}_{-0.032}$	0.279	0.646	0.469	6
110625881	BPL	$4.012^{+0.284}_{-0.237}$	$-1.029^{+0.121}_{-0.141}$	$2.738^{+0.165}_{-0.154}$	$1.996^{+0.031}_{-0.033}$	0.475	0.128	0.105	9
110702187	PL	$0.205^{+0.174}_{-0.208}$	-	$1.516^{+0.320}_{-0.269}$	$1.995^{+0.033}_{-0.032}$	0.862	0.340	0.303	3
110705364	PL	$0.321^{+0.175}_{-0.200}$	-	$1.817^{+0.425}_{-0.351}$	$1.992^{+0.033}_{-0.033}$	0.438	0.968	0.951	5
110709642	BPL	$2.653^{+0.392}_{-0.297}$	$-0.816^{+0.195}_{-0.260}$	$2.578^{+0.456}_{-0.393}$	$1.992^{+0.032}_{-0.032}$	0.705	0.808	0.879	9
110710954	BPL	$2.745^{+0.405}_{-0.316}$	$-0.559^{+0.213}_{-0.265}$	$2.894^{+0.684}_{-0.553}$	$1.993^{+0.034}_{-0.032}$	0.448	0.998	0.980	8
110717319	PL	$0.326^{+0.086}_{-0.093}$	-	$2.014^{+0.189}_{-0.168}$	$1.986^{+0.032}_{-0.032}$	0.377	0.314	0.336	9
110721200	PL	$0.684^{+0.124}_{-0.134}$	-	$2.609^{+0.275}_{-0.247}$	$1.994^{+0.033}_{-0.033}$	0.259	0.861	0.920	1
110725236	PL	$0.071^{+0.230}_{-0.276}$	-	$2.017^{+0.525}_{-0.435}$	$1.991^{+0.032}_{-0.033}$	0.466	0.532	0.509	2
110729142	PL	$-0.573^{+0.191}_{-0.208}$	-	$1.838^{+0.207}_{-0.189}$	$1.996^{+0.030}_{-0.030}$	0.580	0.854	0.715	5
110730660	PL	$-0.979^{+0.533}_{-0.707}$	-	$2.489^{+0.747}_{-0.590}$	$1.993^{+0.032}_{-0.032}$	0.972	0.805	0.595	2
110731465	PL	$1.311^{+0.129}_{-0.122}$	-	$1.984^{+0.299}_{-0.265}$	$1.992^{+0.033}_{-0.033}$	0.620	0.760	0.703	3
110806934	PL	$-0.913^{+0.516}_{-0.634}$	-	$2.812^{+0.777}_{-0.638}$	$1.991^{+0.032}_{-0.032}$	0.908	0.693	0.344	2
110809461	PL	$-0.578^{+0.487}_{-0.634}$	-	$2.405^{+0.776}_{-0.589}$	$1.994^{+0.033}_{-0.032}$	0.696	0.560	0.804	1
110813237	PL	$-0.915^{+0.562}_{-0.712}$	-	$3.163^{+0.858}_{-0.685}$	$1.991^{+0.033}_{-0.032}$	0.976	0.938	0.942	1
110824009	BPL	$2.575^{+0.313}_{-0.247}$	$-0.746^{+0.198}_{-0.248}$	$1.944^{+0.250}_{-0.221}$	$2.001^{+0.033}_{-0.033}$	0.401	0.113	0.083	5
110825102	PL	$1.633^{+0.044}_{-0.042}$	-	$1.666^{+0.081}_{-0.078}$	$1.988^{+0.033}_{-0.033}$	0.605	0.056	0.021	11
110831282	PL	$-0.116^{+0.322}_{-0.437}$	-	$1.933^{+0.675}_{-0.521}$	$1.993^{+0.032}_{-0.033}$	0.551	0.572	0.662	1
110903009	BPL	$3.475^{+0.362}_{-0.295}$	$-0.740^{+0.143}_{-0.169}$	$3.728^{+0.589}_{-0.502}$	$1.989^{+0.032}_{-0.032}$	0.843	0.161	0.265	3

Table 2.3 (cont'd)

GRB	Model	$\log N$	$\log f_{\rm b}$ (Hz)	α	B	$p(T_R)$[a]	$p_{\rm AD}$[b]	$p_{\rm KS}$[c]	$N_{\rm peak}$
110904124	PL	$-0.317^{+0.216}_{-0.243}$	-	$2.017^{+0.304}_{-0.270}$	$1.999^{+0.032}_{-0.032}$	0.592	0.662	0.955	4
110904163	PL	$-0.229^{+0.221}_{-0.244}$	-	$2.007^{+0.388}_{-0.335}$	$1.984^{+0.032}_{-0.033}$	0.378	0.091	0.173	3
110919634	PL	$-0.144^{+0.179}_{-0.204}$	-	$2.006^{+0.259}_{-0.225}$	$1.988^{+0.033}_{-0.032}$	0.616	0.567	0.610	4
110921912	BPL	$3.784^{+0.521}_{-0.393}$	$-1.169^{+0.227}_{-0.296}$	$2.246^{+0.175}_{-0.167}$	$1.998^{+0.033}_{-0.033}$	0.104	0.318	0.317	5
110926107	PL	$-0.851^{+0.328}_{-0.386}$	-	$2.271^{+0.390}_{-0.331}$	$1.986^{+0.032}_{-0.032}$	0.417	0.484	0.692	3
110928180	PL	$-1.529^{+0.444}_{-0.508}$	-	$2.245^{+0.387}_{-0.347}$	$1.990^{+0.031}_{-0.031}$	0.195	0.225	0.078	1
111003465	PL	$-0.179^{+0.314}_{-0.372}$	-	$3.227^{+0.635}_{-0.530}$	$1.990^{+0.033}_{-0.032}$	0.879	0.167	0.357	2
111012456	PL	$-0.280^{+0.329}_{-0.391}$	-	$2.821^{+0.607}_{-0.510}$	$1.990^{+0.033}_{-0.032}$	0.503	0.385	0.245	3
111012811	PL	$1.721^{+0.171}_{-0.161}$	-	$2.195^{+0.421}_{-0.370}$	$1.993^{+0.033}_{-0.034}$	0.952	0.641	0.539	1
111015427	BPL	$2.063^{+0.250}_{-0.206}$	$-0.927^{+0.167}_{-0.202}$	$2.633^{+0.630}_{-0.494}$	$1.990^{+0.031}_{-0.031}$	0.114	0.812	0.754	10
111017657	PL	$-1.079^{+0.513}_{-0.573}$	-	$3.945^{+0.828}_{-0.708}$	$1.992^{+0.032}_{-0.032}$	0.636	0.327	0.290	1
111024722	PL	$0.342^{+0.087}_{-0.092}$	-	$1.592^{+0.174}_{-0.154}$	$1.983^{+0.032}_{-0.032}$	0.746	0.086	0.100	6
111107076	PL	$-1.558^{+0.552}_{-0.665}$	-	$2.348^{+0.574}_{-0.488}$	$1.991^{+0.032}_{-0.031}$	0.478	0.950	0.820	1
111127810	PL	$0.045^{+0.294}_{-0.352}$	-	$2.772^{+0.578}_{-0.474}$	$1.992^{+0.033}_{-0.033}$	0.690	0.883	0.953	3
111216389	BPL	$2.687^{+0.347}_{-0.271}$	$-0.915^{+0.217}_{-0.268}$	$2.067^{+0.263}_{-0.228}$	$1.982^{+0.032}_{-0.032}$	0.178	0.140	0.182	27
111221739	BPL	$2.337^{+0.588}_{-0.393}$	$-0.533^{+0.355}_{-0.528}$	$1.786^{+0.398}_{-0.329}$	$1.994^{+0.033}_{-0.033}$	0.813	0.107	0.074	2
111228657	BPL	$3.244^{+0.352}_{-0.268}$	$-0.872^{+0.152}_{-0.188}$	$2.909^{+0.354}_{-0.320}$	$1.989^{+0.032}_{-0.033}$	0.802	0.387	0.255	6
120102095	PL	$0.371^{+0.248}_{-0.271}$	-	$2.972^{+0.624}_{-0.536}$	$1.996^{+0.033}_{-0.032}$	0.824	0.152	0.069	1
120119170	PL	$0.233^{+0.110}_{-0.119}$	-	$1.846^{+0.177}_{-0.157}$	$1.988^{+0.033}_{-0.033}$	0.387	0.201	0.157	5
120119229	PL	$0.179^{+0.135}_{-0.147}$	-	$1.579^{+0.281}_{-0.250}$	$1.991^{+0.032}_{-0.033}$	0.869	0.634	0.744	1
120121251	PL	$-1.658^{+0.753}_{-0.923}$	-	$3.028^{+0.894}_{-0.702}$	$1.991^{+0.033}_{-0.033}$	0.600	0.399	0.621	1
120129580	BPL	$4.225^{+0.267}_{-0.219}$	$-0.421^{+0.091}_{-0.103}$	$4.458^{+0.523}_{-0.469}$	$2.003^{+0.032}_{-0.033}$	0.484	0.003	0.000	2
120130699	PL	$0.268^{+0.189}_{-0.227}$	-	$1.745^{+0.330}_{-0.285}$	$1.991^{+0.032}_{-0.032}$	0.730	0.183	0.394	2
120204054	PL	$-0.339^{+0.144}_{-0.157}$	-	$2.628^{+0.220}_{-0.201}$	$1.986^{+0.031}_{-0.031}$	0.767	0.430	0.444	4
120206949	PL	$1.166^{+0.154}_{-0.159}$	-	$2.407^{+0.492}_{-0.410}$	$1.995^{+0.033}_{-0.033}$	0.624	0.849	0.822	1
120213606	PL	$0.545^{+0.171}_{-0.184}$	-	$2.038^{+0.465}_{-0.395}$	$1.990^{+0.033}_{-0.032}$	0.980	0.526	0.522	4
120217904	PL	$2.267^{+0.231}_{-0.216}$	-	$2.644^{+0.509}_{-0.462}$	$1.994^{+0.033}_{-0.033}$	0.623	0.438	0.345	1
120223933	PL	$-0.890^{+0.505}_{-0.617}$	-	$2.336^{+0.726}_{-0.587}$	$1.996^{+0.033}_{-0.033}$	0.887	0.426	0.558	1
120224282	PL	$-0.979^{+0.457}_{-0.561}$	-	$2.000^{+0.546}_{-0.453}$	$1.995^{+0.033}_{-0.032}$	0.114	0.908	0.939	2
120226447	PL	$0.573^{+0.161}_{-0.169}$	-	$1.265^{+0.328}_{-0.282}$	$1.993^{+0.033}_{-0.033}$	0.579	0.852	0.636	2
120226871	PL	$0.228^{+0.081}_{-0.087}$	-	$1.786^{+0.137}_{-0.125}$	$1.984^{+0.032}_{-0.033}$	0.386	0.370	0.524	9
120227725	PL	$0.401^{+0.152}_{-0.174}$	-	$2.026^{+0.351}_{-0.306}$	$1.991^{+0.033}_{-0.033}$	0.927	0.778	0.828	3
120304248	PL	$1.654^{+0.214}_{-0.199}$	-	$1.394^{+0.411}_{-0.383}$	$1.993^{+0.033}_{-0.033}$	0.615	0.579	0.536	3
120316008	BPL	$2.030^{+0.424}_{-0.295}$	$-0.397^{+0.279}_{-0.394}$	$2.461^{+0.862}_{-0.648}$	$1.992^{+0.032}_{-0.032}$	0.057	0.821	0.778	8
120412920	PL	$-0.430^{+0.229}_{-0.259}$	-	$2.250^{+0.366}_{-0.317}$	$2.000^{+0.032}_{-0.032}$	0.577	0.425	0.500	3
120420858	PL	$-2.098^{+0.683}_{-0.823}$	-	$2.546^{+0.646}_{-0.535}$	$1.996^{+0.031}_{-0.032}$	0.926	0.656	0.428	1
120426090	PL	$1.918^{+0.158}_{-0.149}$	-	$2.951^{+0.405}_{-0.360}$	$1.993^{+0.033}_{-0.033}$	0.227	0.928	0.518	1
120429484	PL	$-1.037^{+0.474}_{-0.591}$	-	$2.335^{+0.660}_{-0.528}$	$1.987^{+0.032}_{-0.032}$	0.898	0.178	0.209	1
120512112	PL	$-0.405^{+0.442}_{-0.663}$	-	$2.338^{+0.703}_{-0.496}$	$1.996^{+0.032}_{-0.032}$	0.675	0.872	0.756	2
120522361	PL	$0.390^{+0.186}_{-0.204}$	-	$2.480^{+0.494}_{-0.416}$	$1.991^{+0.032}_{-0.032}$	0.963	0.693	0.693	4
120526303	PL	$0.129^{+0.138}_{-0.155}$	-	$1.429^{+0.191}_{-0.166}$	$1.994^{+0.032}_{-0.032}$	0.961	0.853	0.951	6
120530121	PL	$-1.115^{+0.389}_{-0.458}$	-	$2.526^{+0.479}_{-0.409}$	$1.981^{+0.032}_{-0.032}$	0.273	0.011	0.058	1
120618919	PL	$0.218^{+0.156}_{-0.180}$	-	$1.491^{+0.308}_{-0.272}$	$1.991^{+0.033}_{-0.033}$	0.056	0.102	0.217	3
120624933	PL	$0.674^{+0.122}_{-0.130}$	-	$2.199^{+0.282}_{-0.255}$	$1.993^{+0.032}_{-0.033}$	0.965	0.237	0.261	3
120625119	PL	$1.076^{+0.186}_{-0.188}$	-	$2.443^{+0.571}_{-0.475}$	$1.993^{+0.033}_{-0.032}$	0.860	0.582	0.528	2
120703417	PL	$-1.134^{+0.443}_{-0.510}$	-	$2.835^{+0.577}_{-0.489}$	$1.993^{+0.032}_{-0.032}$	0.184	0.617	0.840	5
120703726	PL	$0.816^{+0.125}_{-0.134}$	-	$2.322^{+0.316}_{-0.284}$	$1.994^{+0.032}_{-0.033}$	0.627	0.512	0.419	2
120707800	PL	$0.310^{+0.125}_{-0.135}$	-	$2.195^{+0.238}_{-0.215}$	$1.995^{+0.032}_{-0.032}$	0.293	0.843	0.875	6
120709883	BPL	$2.792^{+0.522}_{-0.347}$	$-0.647^{+0.305}_{-0.407}$	$2.066^{+0.385}_{-0.316}$	$1.989^{+0.033}_{-0.033}$	0.453	0.183	0.221	9
120711115	PL	$0.874^{+0.049}_{-0.048}$	-	$1.363^{+0.077}_{-0.073}$	$1.993^{+0.034}_{-0.033}$	0.759	0.989	0.934	15
120716712	PL	$0.074^{+0.075}_{-0.079}$	-	$1.421^{+0.111}_{-0.107}$	$1.989^{+0.031}_{-0.032}$	0.319	0.294	0.324	2
120719146	PL	$-0.248^{+0.199}_{-0.238}$	-	$1.728^{+0.281}_{-0.243}$	$1.992^{+0.032}_{-0.032}$	0.780	0.620	0.754	4
120728434	BPL	$4.337^{+0.439}_{-0.337}$	$-1.500^{+0.166}_{-0.204}$	$2.801^{+0.212}_{-0.194}$	$1.992^{+0.031}_{-0.032}$	0.498	0.724	0.707	21
120806007	PL	$0.114^{+0.210}_{-0.238}$	-	$2.334^{+0.465}_{-0.390}$	$1.989^{+0.033}_{-0.032}$	0.902	0.247	0.114	3
120830212	PL	$0.542^{+0.169}_{-0.189}$	-	$1.487^{+0.322}_{-0.276}$	$1.994^{+0.033}_{-0.033}$	0.047	0.931	0.699	1
120830702	PL	$0.079^{+0.189}_{-0.223}$	-	$1.530^{+0.380}_{-0.331}$	$1.995^{+0.033}_{-0.032}$	0.846	0.132	0.105	4
120909070	PL	$-0.707^{+0.259}_{-0.307}$	-	$1.676^{+0.309}_{-0.264}$	$1.988^{+0.031}_{-0.031}$	0.969	0.910	0.932	6
120913997	PL	$-1.293^{+0.432}_{-0.505}$	-	$2.371^{+0.465}_{-0.402}$	$1.995^{+0.031}_{-0.032}$	0.437	0.369	0.437	2
120919052	PL	$0.418^{+0.068}_{-0.070}$	-	$1.607^{+0.132}_{-0.125}$	$1.982^{+0.032}_{-0.032}$	0.230	0.318	0.291	9
120919309	PL	$0.437^{+0.165}_{-0.178}$	-	$2.612^{+0.338}_{-0.303}$	$1.991^{+0.032}_{-0.032}$	0.105	0.655	0.784	1
120921877	PL	$0.834^{+0.213}_{-0.236}$	-	$2.400^{+0.615}_{-0.500}$	$1.992^{+0.033}_{-0.033}$	0.623	0.880	0.898	1

Table 2.3 (cont'd)

GRB	Model	$\log N$	$\log f_{\rm b}$ (Hz)	α	B	$p(T_R)$[a]	$p_{\rm AD}$[b]	$p_{\rm KS}$[c]	$N_{\rm peak}$
120926335	PL	$1.574^{+0.261}_{-0.234}$	-	$2.443^{+0.736}_{-0.612}$	$1.993^{+0.033}_{-0.034}$	0.858	0.992	0.997	2
120926426	PL	$-0.185^{+0.217}_{-0.255}$	-	$1.650^{+0.339}_{-0.294}$	$1.997^{+0.033}_{-0.032}$	0.478	0.696	0.812	3
121005340	PL	$-0.860^{+0.291}_{-0.361}$	-	$1.631^{+0.307}_{-0.263}$	$1.983^{+0.032}_{-0.031}$	0.453	0.431	0.183	4
121029350	PL	$1.175^{+0.111}_{-0.109}$	-	$1.904^{+0.277}_{-0.251}$	$1.991^{+0.033}_{-0.033}$	0.084	0.654	0.514	3
121031949	PL	$-1.242^{+0.340}_{-0.400}$	-	$2.009^{+0.324}_{-0.277}$	$1.987^{+0.030}_{-0.030}$	0.982	0.591	0.386	3
121113544	PL	$0.067^{+0.117}_{-0.127}$	-	$1.782^{+0.183}_{-0.169}$	$1.990^{+0.032}_{-0.032}$	0.877	0.433	0.423	10
121117018	PL	$-1.009^{+0.381}_{-0.471}$	-	$1.989^{+0.446}_{-0.357}$	$1.987^{+0.032}_{-0.032}$	0.693	0.539	0.728	2
121118576	BPL	$2.000^{+0.222}_{-0.183}$	$-0.154^{+0.152}_{-0.188}$	$2.936^{+0.751}_{-0.609}$	$1.992^{+0.032}_{-0.033}$	0.146	0.097	0.016	5
121119579	PL	$0.594^{+0.218}_{-0.246}$	-	$1.989^{+0.602}_{-0.490}$	$1.993^{+0.033}_{-0.033}$	0.926	0.600	0.586	1
121122870	PL	$-0.452^{+0.200}_{-0.228}$	-	$1.904^{+0.260}_{-0.234}$	$1.991^{+0.033}_{-0.032}$	0.299	0.774	0.613	3
121122885	PL	$0.334^{+0.281}_{-0.329}$	-	$2.596^{+0.605}_{-0.496}$	$1.992^{+0.032}_{-0.033}$	0.186	0.552	0.469	1
121123442	PL	$-0.608^{+0.354}_{-0.432}$	-	$2.349^{+0.524}_{-0.433}$	$1.992^{+0.033}_{-0.033}$	0.298	0.876	0.747	2
121125356	PL	$-0.175^{+0.216}_{-0.255}$	-	$1.748^{+0.360}_{-0.309}$	$1.991^{+0.033}_{-0.033}$	0.939	0.627	0.741	6
121128212	PL	$0.815^{+0.091}_{-0.092}$	-	$1.834^{+0.212}_{-0.195}$	$1.991^{+0.033}_{-0.033}$	0.946	0.725	0.833	5
130104721	PL	$0.184^{+0.147}_{-0.157}$	-	$1.877^{+0.272}_{-0.243}$	$1.991^{+0.032}_{-0.032}$	0.923	0.753	0.804	5
130106829	PL	$-0.141^{+0.170}_{-0.191}$	-	$1.566^{+0.280}_{-0.245}$	$1.988^{+0.032}_{-0.033}$	0.975	0.407	0.603	3
130112286	PL	$0.184^{+0.167}_{-0.192}$	-	$1.617^{+0.319}_{-0.283}$	$1.992^{+0.033}_{-0.032}$	0.773	0.694	0.726	3
130114019	PL	$-1.477^{+0.696}_{-0.885}$	-	$2.235^{+0.780}_{-0.631}$	$1.992^{+0.032}_{-0.032}$	0.633	0.584	0.515	1
130121835	PL	$-0.124^{+0.117}_{-0.128}$	-	$1.815^{+0.163}_{-0.147}$	$1.992^{+0.031}_{-0.031}$	0.965	0.776	0.724	7
130131511	PL	$-0.020^{+0.102}_{-0.108}$	-	$1.781^{+0.163}_{-0.150}$	$1.986^{+0.032}_{-0.032}$	0.900	0.584	0.539	15
130206482	PL	$0.112^{+0.127}_{-0.144}$	-	$1.908^{+0.199}_{-0.175}$	$1.991^{+0.032}_{-0.032}$	0.607	0.565	0.492	1
130209961	BPL	$2.387^{+0.569}_{-0.382}$	$-0.272^{+0.242}_{-0.352}$	$2.782^{+0.832}_{-0.640}$	$1.994^{+0.032}_{-0.033}$	0.411	0.949	0.950	7
130215649	PL	$-1.338^{+0.488}_{-0.570}$	-	$2.507^{+0.518}_{-0.446}$	$1.991^{+0.032}_{-0.031}$	0.488	0.667	0.133	3
130216790	PL	$0.834^{+0.147}_{-0.152}$	-	$2.602^{+0.497}_{-0.435}$	$1.990^{+0.033}_{-0.034}$	0.555	0.226	0.254	3
130216927	PL	$1.118^{+0.165}_{-0.152}$	-	$1.408^{+0.307}_{-0.278}$	$1.994^{+0.034}_{-0.033}$	0.240	0.992	0.897	2
130218261	PL	$-0.249^{+0.236}_{-0.277}$	-	$1.977^{+0.421}_{-0.363}$	$1.985^{+0.033}_{-0.033}$	0.391	0.043	0.055	3
130219775	PL	$0.097^{+0.126}_{-0.136}$	-	$2.115^{+0.218}_{-0.201}$	$1.995^{+0.032}_{-0.032}$	0.026	0.809	0.584	3
130220964	PL	$0.900^{+0.231}_{-0.238}$	-	$3.289^{+0.838}_{-0.694}$	$1.993^{+0.033}_{-0.034}$	0.820	0.910	0.978	2
130224370	PL	$-0.443^{+0.279}_{-0.340}$	-	$1.705^{+0.357}_{-0.308}$	$1.994^{+0.033}_{-0.032}$	0.844	0.233	0.138	2
130228111	PL	$-0.995^{+0.376}_{-0.435}$	-	$1.988^{+0.441}_{-0.375}$	$1.988^{+0.032}_{-0.031}$	0.188	0.500	0.594	3
130304410	PL	$0.175^{+0.129}_{-0.142}$	-	$1.436^{+0.202}_{-0.175}$	$1.996^{+0.032}_{-0.032}$	0.927	0.810	0.686	1
130305486	PL	$-0.081^{+0.209}_{-0.229}$	-	$2.853^{+0.358}_{-0.326}$	$1.994^{+0.033}_{-0.032}$	0.771	0.171	0.247	3
130306991	PL	$-1.271^{+0.469}_{-0.573}$	-	$2.149^{+0.485}_{-0.399}$	$2.001^{+0.031}_{-0.032}$	0.812	0.228	0.307	3
130307238	PL	$-0.410^{+0.256}_{-0.320}$	-	$1.414^{+0.357}_{-0.306}$	$1.994^{+0.033}_{-0.032}$	0.250	0.978	0.993	3
130318456	PL	$-1.299^{+0.514}_{-0.668}$	-	$1.954^{+0.540}_{-0.426}$	$1.992^{+0.031}_{-0.032}$	0.876	0.945	0.666	1
130320560	PL	$-2.409^{+0.574}_{-0.689}$	-	$2.891^{+0.500}_{-0.417}$	$1.996^{+0.029}_{-0.030}$	0.042	0.825	0.894	1
130325203	PL	$0.760^{+0.188}_{-0.201}$	-	$2.395^{+0.441}_{-0.393}$	$1.993^{+0.033}_{-0.033}$	0.460	0.474	0.369	2
130327350	PL	$0.824^{+0.081}_{-0.084}$	-	$1.948^{+0.184}_{-0.174}$	$1.990^{+0.033}_{-0.033}$	0.869	0.522	0.395	8
130331566	PL	$0.057^{+0.314}_{-0.359}$	-	$2.862^{+0.791}_{-0.663}$	$1.992^{+0.033}_{-0.033}$	0.891	0.690	0.883	1
130406288	PL	$1.060^{+0.195}_{-0.216}$	-	$2.067^{+0.557}_{-0.429}$	$1.996^{+0.032}_{-0.033}$	0.589	0.272	0.143	2
130406334	PL	$-1.150^{+0.500}_{-0.606}$	-	$1.849^{+0.521}_{-0.434}$	$1.999^{+0.031}_{-0.031}$	0.946	0.377	0.285	1
130409960	PL	$-0.736^{+0.481}_{-0.587}$	-	$3.090^{+0.766}_{-0.645}$	$1.994^{+0.032}_{-0.032}$	0.235	0.968	0.944	2
130418844	PL	$-1.227^{+0.397}_{-0.468}$	-	$1.907^{+0.384}_{-0.327}$	$1.990^{+0.031}_{-0.032}$	0.491	0.883	0.611	1
130420422	PL	$-0.516^{+0.444}_{-0.646}$	-	$2.027^{+0.766}_{-0.558}$	$1.992^{+0.032}_{-0.033}$	0.913	0.934	0.841	1
130425327	PL	$0.282^{+0.103}_{-0.110}$	-	$1.502^{+0.199}_{-0.179}$	$1.988^{+0.033}_{-0.033}$	0.304	0.316	0.330	8
130502327	BPL	$3.609^{+0.196}_{-0.167}$	$-0.495^{+0.115}_{-0.130}$	$2.502^{+0.178}_{-0.168}$	$1.989^{+0.032}_{-0.032}$	0.003	0.045	0.064	25
130504978	BPL	$3.586^{+0.240}_{-0.204}$	$-0.861^{+0.112}_{-0.128}$	$2.762^{+0.199}_{-0.183}$	$1.993^{+0.032}_{-0.033}$	0.354	0.964	0.893	12
130509078	BPL	$2.968^{+0.331}_{-0.267}$	$-1.397^{+0.157}_{-0.185}$	$3.433^{+0.671}_{-0.563}$	$1.996^{+0.030}_{-0.030}$	0.532	0.588	0.605	2
130514560	PL	$0.005^{+0.296}_{-0.374}$	-	$2.009^{+0.638}_{-0.503}$	$1.992^{+0.033}_{-0.031}$	0.656	0.821	0.644	1
130517781	PL	$-0.178^{+0.260}_{-0.291}$	-	$2.247^{+0.460}_{-0.390}$	$1.997^{+0.032}_{-0.032}$	0.653	0.392	0.595	6
130518551	PL	$1.772^{+0.271}_{-0.244}$	-	$1.713^{+0.529}_{-0.489}$	$1.993^{+0.033}_{-0.033}$	0.568	0.991	0.969	1
130518580	PL	$0.251^{+0.097}_{-0.103}$	-	$2.501^{+0.172}_{-0.160}$	$1.979^{+0.031}_{-0.032}$	0.981	0.085	0.110	4
130522510	PL	$-0.108^{+0.304}_{-0.354}$	-	$2.686^{+0.635}_{-0.528}$	$1.992^{+0.034}_{-0.033}$	0.968	0.849	0.897	1
130523095	PL	$-0.222^{+0.119}_{-0.130}$	-	$1.750^{+0.176}_{-0.161}$	$1.979^{+0.031}_{-0.032}$	0.468	0.122	0.037	5
130528695	PL	$-0.333^{+0.241}_{-0.280}$	-	$2.010^{+0.338}_{-0.300}$	$1.995^{+0.032}_{-0.032}$	0.543	0.584	0.668	4
130530719	PL	$-1.320^{+0.661}_{-0.871}$	-	$2.389^{+0.790}_{-0.602}$	$1.996^{+0.032}_{-0.032}$	0.155	0.160	0.187	1
130604033	PL	$0.913^{+0.085}_{-0.085}$	-	$1.818^{+0.210}_{-0.194}$	$1.991^{+0.032}_{-0.032}$	0.495	0.688	0.856	8
130606316	PL	$-0.334^{+0.399}_{-0.510}$	-	$2.402^{+0.633}_{-0.513}$	$1.994^{+0.033}_{-0.033}$	0.738	0.637	0.745	3
130606497	PL	$1.032^{+0.036}_{-0.036}$	-	$1.850^{+0.069}_{-0.065}$	$1.989^{+0.033}_{-0.033}$	0.952	0.358	0.241	15
130609902	PL	$-0.404^{+0.158}_{-0.176}$	-	$2.150^{+0.206}_{-0.182}$	$1.994^{+0.031}_{-0.031}$	0.040	0.988	0.873	4
130612456	PL	$0.554^{+0.335}_{-0.450}$	-	$3.164^{+0.895}_{-0.676}$	$1.996^{+0.033}_{-0.033}$	0.471	0.189	0.130	1

Table 2.3 (cont'd)

GRB	Model	$\log N$	$\log f_{\rm b}$ (Hz)	α	B	$p(T_R)$[a]	$p_{\rm AD}$[b]	$p_{\rm KS}$[c]	$N_{\rm peak}$
130623790	PL	$-0.432^{+0.105}_{-0.113}$	-	$1.512^{+0.122}_{-0.114}$	$1.982^{+0.030}_{-0.029}$	0.819	0.841	0.659	9
130626596	PL	$0.165^{+0.120}_{-0.130}$	-	$1.449^{+0.221}_{-0.190}$	$1.989^{+0.032}_{-0.033}$	0.171	0.731	0.690	6
130627372	PL	$-0.675^{+0.267}_{-0.329}$	-	$1.259^{+0.294}_{-0.249}$	$1.996^{+0.032}_{-0.031}$	0.658	0.995	0.991	2
130628531	PL	$0.506^{+0.146}_{-0.161}$	-	$1.958^{+0.281}_{-0.246}$	$1.995^{+0.033}_{-0.034}$	0.767	0.782	0.721	4
130630272	PL	$0.454^{+0.165}_{-0.189}$	-	$1.553^{+0.378}_{-0.317}$	$1.993^{+0.033}_{-0.033}$	0.107	0.829	0.639	2
130704560	PL	$2.030^{+0.135}_{-0.128}$	-	$2.457^{+0.311}_{-0.285}$	$1.992^{+0.032}_{-0.033}$	0.845	0.582	0.399	6
130707505	PL	$-1.069^{+0.304}_{-0.344}$	-	$2.130^{+0.288}_{-0.250}$	$1.987^{+0.032}_{-0.031}$	0.818	0.140	0.076	5
130715906	PL	$-0.293^{+0.244}_{-0.291}$	-	$2.005^{+0.352}_{-0.298}$	$1.995^{+0.033}_{-0.032}$	0.223	0.504	0.530	6
130725527	PL	$1.269^{+0.213}_{-0.205}$	-	$2.712^{+0.822}_{-0.642}$	$1.992^{+0.032}_{-0.033}$	0.614	0.351	0.136	2
130727698	PL	$0.501^{+0.195}_{-0.217}$	-	$2.211^{+0.609}_{-0.512}$	$1.993^{+0.033}_{-0.033}$	0.693	0.888	0.762	4
130815420	PL	$-0.525^{+0.172}_{-0.191}$	-	$1.794^{+0.189}_{-0.171}$	$1.991^{+0.031}_{-0.031}$	0.592	0.408	0.363	9
130815660	BPL	$3.820^{+0.659}_{-0.450}$	$-1.041^{+0.204}_{-0.280}$	$3.636^{+0.681}_{-0.580}$	$1.994^{+0.033}_{-0.033}$	0.626	0.430	0.351	2
130818941	PL	$0.187^{+0.104}_{-0.110}$	-	$1.491^{+0.184}_{-0.171}$	$1.987^{+0.033}_{-0.033}$	0.976	0.422	0.337	5
130821674	PL	$0.496^{+0.041}_{-0.043}$	-	$1.633^{+0.074}_{-0.071}$	$1.976^{+0.032}_{-0.032}$	0.248	0.203	0.135	8
130828306	BPL	$2.511^{+0.388}_{-0.297}$	$-1.175^{+0.234}_{-0.292}$	$1.986^{+0.260}_{-0.233}$	$1.986^{+0.032}_{-0.031}$	0.114	0.437	0.259	16
130928537	PL	$-1.588^{+0.626}_{-0.804}$	-	$2.060^{+0.616}_{-0.497}$	$2.002^{+0.032}_{-0.031}$	0.229	0.363	0.406	1
131014215	BPL	$5.054^{+0.379}_{-0.294}$	$-0.758^{+0.158}_{-0.189}$	$2.604^{+0.163}_{-0.153}$	$1.992^{+0.034}_{-0.033}$	0.997	0.695	0.603	5
131014513	PL	$0.117^{+0.221}_{-0.284}$	-	$1.400^{+0.383}_{-0.304}$	$1.996^{+0.033}_{-0.034}$	0.209	0.674	0.633	1
131021352	PL	$0.735^{+0.188}_{-0.196}$	-	$1.705^{+0.488}_{-0.407}$	$1.993^{+0.033}_{-0.033}$	0.064	0.193	0.147	1
131028076	PL	$0.826^{+0.110}_{-0.114}$	-	$2.605^{+0.273}_{-0.244}$	$1.990^{+0.033}_{-0.033}$	0.708	0.496	0.382	2
131029973	PL	$-0.674^{+0.291}_{-0.346}$	-	$1.852^{+0.319}_{-0.275}$	$1.998^{+0.032}_{-0.032}$	0.424	0.082	0.057	5
131030791	PL	$-1.143^{+0.473}_{-0.540}$	-	$2.344^{+0.547}_{-0.491}$	$2.005^{+0.032}_{-0.031}$	0.749	0.144	0.155	1
131031482	PL	$1.162^{+0.174}_{-0.169}$	-	$2.246^{+0.505}_{-0.444}$	$1.993^{+0.032}_{-0.032}$	0.878	0.692	0.482	3
131105087	BPL	$3.248^{+0.626}_{-0.425}$	$-1.373^{+0.272}_{-0.371}$	$2.266^{+0.273}_{-0.234}$	$1.983^{+0.032}_{-0.032}$	0.850	0.490	0.615	8
131108024	PL	$-0.487^{+0.145}_{-0.155}$	-	$1.526^{+0.178}_{-0.161}$	$1.987^{+0.031}_{-0.031}$	0.952	0.783	0.472	5
131108862	PL	$1.713^{+0.082}_{-0.077}$	-	$1.639^{+0.158}_{-0.149}$	$1.991^{+0.034}_{-0.033}$	0.241	0.483	0.504	13
131113483	PL	$-1.796^{+0.611}_{-0.794}$	-	$2.899^{+0.674}_{-0.533}$	$1.988^{+0.032}_{-0.031}$	0.233	0.071	0.035	1
131118958	PL	$0.274^{+0.074}_{-0.080}$	-	$1.460^{+0.145}_{-0.132}$	$1.983^{+0.032}_{-0.033}$	0.190	0.276	0.297	16
131122490	PL	$0.656^{+0.104}_{-0.106}$	-	$2.170^{+0.277}_{-0.258}$	$1.990^{+0.033}_{-0.032}$	0.880	0.227	0.336	6
131127592	BPL	$3.712^{+0.389}_{-0.306}$	$-0.750^{+0.163}_{-0.193}$	$2.857^{+0.306}_{-0.267}$	$1.992^{+0.032}_{-0.033}$	0.936	0.858	0.754	7
131209547	PL	$-0.177^{+0.184}_{-0.209}$	-	$2.102^{+0.313}_{-0.272}$	$1.991^{+0.032}_{-0.032}$	0.752	0.820	0.867	3
131214705	BPL	$4.699^{+0.848}_{-0.519}$	$-1.500^{+0.222}_{-0.324}$	$3.362^{+0.418}_{-0.361}$	$1.992^{+0.031}_{-0.032}$	0.570	0.767	0.731	4
131215298	PL	$0.579^{+0.118}_{-0.124}$	-	$1.508^{+0.260}_{-0.236}$	$1.992^{+0.033}_{-0.033}$	0.962	0.953	0.979	5
131216081	PL	$0.015^{+0.276}_{-0.330}$	-	$2.502^{+0.554}_{-0.472}$	$1.996^{+0.032}_{-0.032}$	0.144	0.235	0.435	1
131217183	PL	$0.384^{+0.193}_{-0.227}$	-	$1.616^{+0.401}_{-0.331}$	$1.994^{+0.033}_{-0.033}$	0.394	0.468	0.570	3
131229277	PL	$1.812^{+0.103}_{-0.096}$	-	$1.615^{+0.193}_{-0.176}$	$1.993^{+0.033}_{-0.033}$	0.597	0.400	0.336	12
131231198	PL	$0.421^{+0.101}_{-0.105}$	-	$2.845^{+0.221}_{-0.204}$	$1.985^{+0.032}_{-0.032}$	0.558	0.181	0.066	6

[a] $p(T_R)$ is the significance associated to statistic T_R.

[b] $p_{\rm AD}$ is the significance of the Anderson–Darling test.

[c] $p_{\rm KS}$ is the significance of the Kolmogorov–Smirnov test.

Table 2.4. Best–fitting model and parameters for each GRB of the *Fermi* sample events in the 8–40 keV energy band.

GRB	Model	$\log N$	$\log f_{\rm b}$ (Hz)	α	B	$p(T_R)^{\rm a}$	$p_{\rm AD}{}^{\rm b}$	$p_{\rm KS}{}^{\rm c}$	$N_{\rm peak}$
080715950	PL	$-0.230^{+0.174}_{-0.204}$	-	$1.414^{+0.259}_{-0.223}$	$1.996^{+0.032}_{-0.033}$	0.366	0.398	0.172	1
080723557	PL	$0.452^{+0.073}_{-0.076}$	-	$1.928^{+0.147}_{-0.138}$	$1.985^{+0.032}_{-0.032}$	0.702	0.519	0.391	12
080723985	PL	$-0.829^{+0.387}_{-0.491}$	-	$2.346^{+0.548}_{-0.450}$	$1.987^{+0.032}_{-0.032}$	0.998	0.375	0.271	2
080724401	PL	$0.425^{+0.110}_{-0.118}$	-	$1.758^{+0.244}_{-0.219}$	$1.988^{+0.033}_{-0.033}$	0.443	0.078	0.079	4
080730786	PL	$0.225^{+0.257}_{-0.303}$	-	$2.506^{+0.658}_{-0.533}$	$1.992^{+0.033}_{-0.033}$	0.836	0.376	0.554	3
080806896	PL	$-1.277^{+0.634}_{-0.758}$	-	$2.658^{+0.785}_{-0.658}$	$1.996^{+0.033}_{-0.033}$	0.659	0.953	0.847	1
080807993	PL	$-0.100^{+0.194}_{-0.236}$	-	$1.177^{+0.347}_{-0.294}$	$1.995^{+0.033}_{-0.033}$	0.716	0.676	0.533	1
080816503	PL	$-0.196^{+0.213}_{-0.240}$	-	$1.915^{+0.335}_{-0.298}$	$1.998^{+0.031}_{-0.032}$	0.198	0.319	0.243	6
080817161	PL	$-1.080^{+0.384}_{-0.435}$	-	$2.435^{+0.447}_{-0.389}$	$1.997^{+0.031}_{-0.032}$	0.663	0.060	0.064	3
080825593	PL	$0.182^{+0.196}_{-0.218}$	-	$2.210^{+0.392}_{-0.338}$	$1.990^{+0.032}_{-0.032}$	0.671	0.658	0.884	5
080904886	PL	$0.542^{+0.152}_{-0.162}$	-	$2.167^{+0.349}_{-0.312}$	$1.989^{+0.033}_{-0.033}$	0.725	0.255	0.376	4
080916009	PL	$-0.403^{+0.244}_{-0.281}$	-	$1.956^{+0.326}_{-0.281}$	$1.994^{+0.032}_{-0.032}$	0.900	0.822	0.635	4
080925775	PL	$-0.872^{+0.506}_{-0.599}$	-	$2.980^{+0.795}_{-0.651}$	$1.989^{+0.032}_{-0.033}$	0.978	0.429	0.310	2
081009140	PL	$0.658^{+0.125}_{-0.131}$	-	$2.969^{+0.220}_{-0.203}$	$1.993^{+0.033}_{-0.033}$	0.416	0.602	0.640	2
081110601	PL	$0.386^{+0.199}_{-0.230}$	-	$2.070^{+0.536}_{-0.445}$	$1.994^{+0.033}_{-0.032}$	0.606	0.869	0.872	1
081122520	PL	$-0.090^{+0.152}_{-0.178}$	-	$1.537^{+0.225}_{-0.200}$	$1.989^{+0.032}_{-0.033}$	0.922	0.566	0.709	3
081124060	PL	$-0.866^{+0.510}_{-0.572}$	-	$3.574^{+0.818}_{-0.696}$	$1.997^{+0.032}_{-0.032}$	0.721	0.229	0.317	2
081126899	PL	$-0.974^{+0.556}_{-0.738}$	-	$2.193^{+0.745}_{-0.579}$	$1.994^{+0.032}_{-0.032}$	0.924	0.870	0.977	2
081129161	PL	$-0.091^{+0.240}_{-0.284}$	-	$1.936^{+0.459}_{-0.391}$	$1.991^{+0.033}_{-0.032}$	0.719	0.637	0.550	2
081215784	PL	$1.221^{+0.096}_{-0.093}$	-	$2.124^{+0.254}_{-0.238}$	$1.991^{+0.032}_{-0.032}$	0.259	0.628	0.555	2
081221681	PL	$-0.684^{+0.286}_{-0.321}$	-	$2.653^{+0.337}_{-0.304}$	$1.991^{+0.032}_{-0.032}$	0.122	0.845	0.687	3
081222204	PL	$-0.239^{+0.281}_{-0.330}$	-	$2.281^{+0.434}_{-0.366}$	$1.993^{+0.032}_{-0.033}$	0.433	0.794	0.814	1
090101758	PL	$-1.502^{+0.461}_{-0.528}$	-	$2.641^{+0.475}_{-0.421}$	$1.992^{+0.032}_{-0.032}$	0.029	0.480	0.417	1
090102122	PL	$0.288^{+0.116}_{-0.128}$	-	$1.354^{+0.207}_{-0.178}$	$1.992^{+0.033}_{-0.033}$	0.286	0.535	0.525	5
090112729	PL	$-0.166^{+0.354}_{-0.440}$	-	$2.299^{+0.642}_{-0.508}$	$1.993^{+0.033}_{-0.033}$	0.846	0.971	0.908	1
090117640	PL	$0.402^{+0.222}_{-0.265}$	-	$2.368^{+0.580}_{-0.467}$	$1.992^{+0.033}_{-0.033}$	0.912	0.505	0.488	1
090131090	BPL	$3.265^{+0.313}_{-0.256}$	$-0.709^{+0.139}_{-0.160}$	$2.933^{+0.328}_{-0.284}$	$1.991^{+0.032}_{-0.032}$	0.667	0.785	0.584	5
090323002	BPL	$2.618^{+0.456}_{-0.326}$	$-1.302^{+0.206}_{-0.270}$	$3.169^{+0.922}_{-0.688}$	$1.984^{+0.032}_{-0.032}$	0.859	0.365	0.227	9
090328401	PL	$-0.216^{+0.193}_{-0.216}$	-	$1.926^{+0.297}_{-0.268}$	$1.994^{+0.033}_{-0.033}$	0.647	0.309	0.161	3
090419997	BPL	$2.281^{+0.000}_{0.000}$	$-1.312^{+0.000}_{0.000}$	$7.572^{+0.000}_{0.000}$	$1.993^{+0.000}_{0.000}$	0.529	0.690	0.561	1
090424592	BPL	$3.991^{+0.393}_{-0.301}$	$-0.889^{+0.150}_{-0.182}$	$2.857^{+0.234}_{-0.212}$	$1.990^{+0.033}_{-0.033}$	0.999	0.879	0.964	6
090425377	PL	$0.139^{+0.126}_{-0.139}$	-	$1.773^{+0.218}_{-0.196}$	$1.994^{+0.033}_{-0.032}$	0.021	0.928	0.937	5
090502777	PL	$-0.424^{+0.270}_{-0.328}$	-	$1.711^{+0.393}_{-0.332}$	$1.992^{+0.032}_{-0.032}$	0.086	0.699	0.769	3
090516353	PL	$-0.978^{+0.417}_{-0.536}$	-	$1.764^{+0.471}_{-0.379}$	$1.986^{+0.033}_{-0.033}$	0.206	0.267	0.232	2
090524346	PL	$-0.846^{+0.384}_{-0.436}$	-	$2.591^{+0.519}_{-0.444}$	$1.994^{+0.032}_{-0.032}$	0.715	0.855	0.878	2
090528516	PL	$-0.549^{+0.237}_{-0.276}$	-	$1.882^{+0.304}_{-0.260}$	$1.996^{+0.032}_{-0.032}$	0.866	0.850	0.764	7
090529564	PL	$0.577^{+0.268}_{-0.310}$	-	$3.067^{+0.814}_{-0.705}$	$1.993^{+0.033}_{-0.033}$	0.897	0.573	0.499	3
090530760	PL	$-3.844^{+1.019}_{-1.192}$	-	$3.587^{+0.801}_{-0.691}$	$1.996^{+0.030}_{-0.030}$	0.991	0.943	0.976	2
090618353	PL	$-0.870^{+0.209}_{-0.225}$	-	$2.636^{+0.234}_{-0.222}$	$1.991^{+0.031}_{-0.031}$	0.671	0.984	0.967	4
090626189	BPL	$3.330^{+0.529}_{-0.382}$	$-1.081^{+0.215}_{-0.283}$	$2.711^{+0.379}_{-0.327}$	$1.993^{+0.032}_{-0.032}$	0.461	0.953	0.668	10
090717034	PL	$-1.499^{+0.516}_{-0.581}$	-	$3.069^{+0.581}_{-0.521}$	$1.995^{+0.032}_{-0.032}$	0.370	0.873	0.778	2
090718762	PL	$-0.245^{+0.346}_{-0.428}$	-	$2.692^{+0.589}_{-0.492}$	$1.995^{+0.032}_{-0.033}$	0.062	0.915	0.962	2
090810659	PL	$-3.127^{+0.983}_{-1.214}$	-	$3.325^{+0.844}_{-0.693}$	$1.985^{+0.031}_{-0.032}$	0.557	0.160	0.212	2
090813174	PL	$0.948^{+0.191}_{-0.195}$	-	$2.240^{+0.555}_{-0.476}$	$1.992^{+0.032}_{-0.033}$	0.979	0.446	0.644	2
090814950	PL	$-0.810^{+0.327}_{-0.410}$	-	$1.523^{+0.399}_{-0.336}$	$1.989^{+0.033}_{-0.032}$	0.286	0.475	0.340	2
090815438	PL	$-0.841^{+0.523}_{-0.612}$	-	$3.283^{+0.827}_{-0.701}$	$1.995^{+0.032}_{-0.032}$	0.939	0.272	0.440	1
090820027	PL	$-0.470^{+0.305}_{-0.348}$	-	$3.353^{+0.413}_{-0.365}$	$1.998^{+0.032}_{-0.032}$	0.423	0.515	0.458	2
090820509	PL	$0.554^{+0.179}_{-0.201}$	-	$2.165^{+0.526}_{-0.445}$	$1.992^{+0.032}_{-0.032}$	0.585	0.385	0.370	1
090828099	PL	$-0.587^{+0.254}_{-0.289}$	-	$2.136^{+0.319}_{-0.281}$	$1.990^{+0.032}_{-0.031}$	0.959	0.957	0.977	3
090829672	PL	$0.492^{+0.071}_{-0.074}$	-	$2.078^{+0.163}_{-0.148}$	$1.977^{+0.033}_{-0.033}$	0.617	0.001	0.001	13
090831317	PL	$0.340^{+0.093}_{-0.099}$	-	$1.268^{+0.176}_{-0.157}$	$1.988^{+0.033}_{-0.033}$	0.964	0.386	0.477	4
090902462	PL	$1.150^{+0.064}_{-0.063}$	-	$1.844^{+0.137}_{-0.123}$	$1.994^{+0.033}_{-0.032}$	0.016	0.703	0.315	6
090922539	PL	$-0.877^{+0.338}_{-0.388}$	-	$2.455^{+0.420}_{-0.365}$	$1.999^{+0.031}_{-0.031}$	0.794	0.124	0.046	3
090926181	PL	$1.363^{+0.063}_{-0.061}$	-	$1.715^{+0.121}_{-0.113}$	$1.991^{+0.034}_{-0.032}$	0.907	0.114	0.137	5
091003191	PL	$0.505^{+0.155}_{-0.170}$	-	$1.857^{+0.367}_{-0.319}$	$1.992^{+0.033}_{-0.032}$	0.279	0.752	0.519	3
091031500	PL	$-0.232^{+0.285}_{-0.370}$	-	$1.698^{+0.450}_{-0.367}$	$1.992^{+0.033}_{-0.032}$	0.967	0.925	0.965	2
091101143	PL	$0.059^{+0.133}_{-0.146}$	-	$1.560^{+0.211}_{-0.184}$	$1.988^{+0.033}_{-0.033}$	0.755	0.220	0.267	3
091109895	PL	$-0.086^{+0.260}_{-0.319}$	-	$1.675^{+0.492}_{-0.416}$	$1.992^{+0.033}_{-0.034}$	0.588	0.817	0.472	2
091120191	PL	$0.289^{+0.139}_{-0.154}$	-	$2.016^{+0.280}_{-0.252}$	$1.994^{+0.033}_{-0.034}$	0.839	0.948	0.966	7
091127976	BPL	$3.696^{+0.600}_{-0.407}$	$-0.498^{+0.208}_{-0.276}$	$3.348^{+0.678}_{-0.542}$	$1.996^{+0.033}_{-0.033}$	0.456	0.513	0.523	4
091128285	PL	$-0.679^{+0.313}_{-0.389}$	-	$1.754^{+0.395}_{-0.323}$	$1.989^{+0.032}_{-0.032}$	0.245	0.728	0.789	2

Table 2.4 (cont'd)

GRB	Model	$\log N$	$\log f_{\rm b}$ (Hz)	α	B	$p(T_R)$[a]	$p_{\rm AD}$[b]	$p_{\rm KS}$[c]	$N_{\rm peak}$
091208410	PL	$0.691^{+0.217}_{-0.240}$	-	$2.712^{+0.634}_{-0.527}$	$1.992^{+0.033}_{-0.032}$	0.928	0.962	0.638	1
100116897	PL	$-1.153^{+0.433}_{-0.499}$	-	$2.476^{+0.482}_{-0.421}$	$1.995^{+0.031}_{-0.032}$	0.148	0.392	0.580	2
100130729	PL	$-1.972^{+0.772}_{-0.959}$	-	$2.517^{+0.737}_{-0.588}$	$1.997^{+0.032}_{-0.031}$	0.941	0.452	0.083	1
100224112	PL	$-0.785^{+0.413}_{-0.349}$	-	$2.134^{+0.469}_{-0.393}$	$1.992^{+0.032}_{-0.032}$	0.476	0.739	0.791	4
100322045	PL	$0.114^{+0.145}_{-0.163}$	-	$2.131^{+0.263}_{-0.238}$	$1.992^{+0.032}_{-0.032}$	0.514	0.726	0.621	5
100324172	PL	$-0.344^{+0.245}_{-0.290}$	-	$2.246^{+0.346}_{-0.297}$	$1.990^{+0.032}_{-0.032}$	0.479	0.405	0.672	1
100401297	PL	$-0.955^{+0.467}_{-0.617}$	-	$1.666^{+0.522}_{-0.415}$	$2.001^{+0.031}_{-0.032}$	0.145	0.572	0.686	2
100414097	PL	$-0.185^{+0.230}_{-0.266}$	-	$1.866^{+0.329}_{-0.288}$	$1.996^{+0.032}_{-0.032}$	0.123	0.770	0.909	2
100424876	PL	$-1.378^{+0.516}_{-0.787}$	-	$1.690^{+0.474}_{-0.325}$	$1.989^{+0.031}_{-0.031}$	0.192	0.641	0.682	2
100502356	PL	$-0.568^{+0.270}_{-0.323}$	-	$1.512^{+0.341}_{-0.289}$	$1.996^{+0.032}_{-0.032}$	0.761	0.765	0.761	5
100503554	PL	$-0.778^{+0.255}_{-0.302}$	-	$1.561^{+0.282}_{-0.252}$	$1.988^{+0.032}_{-0.033}$	0.411	0.368	0.275	3
100511035	PL	$-0.338^{+0.222}_{-0.255}$	-	$2.077^{+0.329}_{-0.295}$	$1.990^{+0.033}_{-0.032}$	0.804	0.540	0.323	5
100517072	PL	$0.255^{+0.139}_{-0.154}$	-	$1.874^{+0.259}_{-0.236}$	$1.996^{+0.032}_{-0.033}$	0.996	0.043	0.028	2
100517154	PL	$0.034^{+0.222}_{-0.264}$	-	$1.874^{+0.418}_{-0.354}$	$1.990^{+0.033}_{-0.033}$	0.329	0.837	0.588	2
100519204	PL	$-1.476^{+0.558}_{-0.674}$	-	$2.530^{+0.621}_{-0.507}$	$1.986^{+0.033}_{-0.032}$	0.844	0.320	0.641	3
100522157	PL	$0.122^{+0.179}_{-0.211}$	-	$1.944^{+0.386}_{-0.332}$	$1.988^{+0.032}_{-0.033}$	0.377	0.440	0.379	2
100527795	PL	$-0.933^{+0.338}_{-0.404}$	-	$1.877^{+0.433}_{-0.365}$	$1.979^{+0.032}_{-0.033}$	0.990	0.131	0.230	6
100528075	PL	$-0.528^{+0.326}_{-0.415}$	-	$2.107^{+0.369}_{-0.308}$	$1.995^{+0.032}_{-0.032}$	0.470	0.589	0.415	2
100615083	PL	$-0.235^{+0.300}_{-0.358}$	-	$2.405^{+0.521}_{-0.436}$	$1.994^{+0.032}_{-0.032}$	0.194	0.291	0.297	3
100701490	PL	$0.868^{+0.092}_{-0.091}$	-	$1.251^{+0.202}_{-0.190}$	$1.992^{+0.033}_{-0.032}$	0.451	0.675	0.480	3
100704149	PL	$-1.812^{+0.603}_{-0.726}$	-	$2.128^{+0.536}_{-0.447}$	$2.004^{+0.030}_{-0.030}$	0.662	0.572	0.665	1
100707032	PL	$-1.150^{+0.369}_{-0.411}$	-	$2.817^{+0.432}_{-0.384}$	$1.992^{+0.032}_{-0.031}$	0.176	0.139	0.308	1
100719989	PL	$0.577^{+0.112}_{-0.115}$	-	$2.310^{+0.280}_{-0.249}$	$1.986^{+0.032}_{-0.032}$	0.791	0.122	0.203	3
100722096	PL	$0.752^{+0.087}_{-0.089}$	-	$1.990^{+0.193}_{-0.176}$	$1.989^{+0.033}_{-0.033}$	0.340	0.350	0.382	3
100724029	PL	$-0.384^{+0.134}_{-0.147}$	-	$1.926^{+0.162}_{-0.154}$	$1.991^{+0.031}_{-0.031}$	0.866	0.684	0.504	8
100725475	PL	$-1.430^{+0.453}_{-0.605}$	-	$1.915^{+0.412}_{-0.320}$	$1.988^{+0.031}_{-0.032}$	0.211	0.732	0.602	3
100728095	PL	$-0.544^{+0.208}_{-0.254}$	-	$1.513^{+0.229}_{-0.199}$	$1.997^{+0.031}_{-0.031}$	0.153	0.811	0.544	7
100826957	PL	$-0.102^{+0.123}_{-0.132}$	-	$2.008^{+0.183}_{-0.168}$	$1.984^{+0.032}_{-0.032}$	0.514	0.394	0.463	8
100829374	PL	$-1.916^{+0.841}_{-1.048}$	-	$2.666^{+0.880}_{-0.715}$	$1.993^{+0.032}_{-0.032}$	0.473	0.810	0.795	1
100829876	PL	$1.377^{+0.135}_{-0.131}$	-	$1.997^{+0.293}_{-0.267}$	$1.993^{+0.033}_{-0.034}$	0.903	0.933	0.895	3
100906576	PL	$-0.950^{+0.348}_{-0.404}$	-	$2.218^{+0.376}_{-0.324}$	$1.994^{+0.032}_{-0.031}$	0.089	0.316	0.292	3
100910818	PL	$1.025^{+0.112}_{-0.115}$	-	$1.982^{+0.319}_{-0.278}$	$1.994^{+0.032}_{-0.033}$	0.777	0.948	0.662	4
100918863	PL	$-2.558^{+0.842}_{-1.102}$	-	$2.920^{+0.803}_{-0.627}$	$1.996^{+0.032}_{-0.031}$	0.533	0.509	0.580	2
100923844	PL	$-0.418^{+0.285}_{-0.339}$	-	$2.172^{+0.430}_{-0.361}$	$1.989^{+0.032}_{-0.032}$	0.749	0.457	0.192	1
101021009	PL	$-1.034^{+0.433}_{-0.542}$	-	$2.145^{+0.527}_{-0.436}$	$1.990^{+0.033}_{-0.032}$	0.104	0.421	0.329	3
101023951	PL	$-0.725^{+0.232}_{-0.253}$	-	$2.376^{+0.307}_{-0.272}$	$1.982^{+0.031}_{-0.032}$	0.473	0.177	0.136	2
101113483	PL	$-1.342^{+0.474}_{-0.574}$	-	$1.895^{+0.474}_{-0.396}$	$1.989^{+0.032}_{-0.032}$	0.900	0.843	0.815	2
101123952	PL	$0.255^{+0.084}_{-0.089}$	-	$1.999^{+0.150}_{-0.139}$	$1.986^{+0.032}_{-0.032}$	0.951	0.816	0.934	7
101126198	PL	$-1.423^{+0.494}_{-0.587}$	-	$3.095^{+0.550}_{-0.465}$	$1.984^{+0.032}_{-0.032}$	0.219	0.255	0.405	1
101201418	PL	$-1.681^{+0.575}_{-0.695}$	-	$2.535^{+0.627}_{-0.524}$	$2.000^{+0.032}_{-0.031}$	0.088	0.480	0.382	3
101207536	PL	$-0.406^{+0.231}_{-0.292}$	-	$1.499^{+0.352}_{-0.297}$	$1.987^{+0.032}_{-0.033}$	0.924	0.605	0.787	4
101208498	BPL	$2.895^{+0.000}_{0.000}$	$-0.178^{+0.000}_{0.000}$	$11.397^{+0.000}_{0.000}$	$1.995^{+0.000}_{0.000}$	0.184	0.491	0.582	2
101224578	PL	$-0.688^{+0.255}_{-0.288}$	-	$1.985^{+0.296}_{-0.271}$	$1.995^{+0.032}_{-0.032}$	0.992	0.609	0.176	3
101231067	PL	$0.306^{+0.154}_{-0.169}$	-	$1.913^{+0.310}_{-0.272}$	$1.994^{+0.032}_{-0.033}$	0.815	0.988	0.923	2
110102788	PL	$-0.798^{+0.270}_{-0.305}$	-	$2.064^{+0.296}_{-0.261}$	$2.003^{+0.031}_{-0.031}$	0.441	0.252	0.284	4
110118857	PL	$-0.474^{+0.393}_{-0.509}$	-	$2.115^{+0.633}_{-0.499}$	$1.991^{+0.032}_{-0.033}$	0.581	0.913	0.917	1
110213220	PL	$-0.406^{+0.293}_{-0.338}$	-	$2.591^{+0.494}_{-0.431}$	$1.986^{+0.033}_{-0.033}$	0.970	0.017	0.055	1
110301214	PL	$1.508^{+0.139}_{-0.134}$	-	$3.075^{+0.501}_{-0.430}$	$1.991^{+0.033}_{-0.033}$	0.619	0.392	0.162	2
110302043	PL	$-0.999^{+0.597}_{-0.796}$	-	$2.426^{+0.809}_{-0.601}$	$1.998^{+0.033}_{-0.033}$	0.693	0.097	0.114	1
110318552	PL	$0.114^{+0.260}_{-0.320}$	-	$2.059^{+0.490}_{-0.395}$	$1.992^{+0.033}_{-0.033}$	0.760	0.988	0.992	1
110328520	PL	$-1.800^{+0.686}_{-0.834}$	-	$2.342^{+0.652}_{-0.529}$	$1.990^{+0.032}_{-0.031}$	0.968	0.513	0.345	1
110415541	PL	$-0.927^{+0.322}_{-0.403}$	-	$1.581^{+0.350}_{-0.291}$	$1.990^{+0.031}_{-0.031}$	0.995	0.632	0.399	2
110421757	PL	$-1.203^{+0.409}_{-0.494}$	-	$1.985^{+0.393}_{-0.333}$	$1.990^{+0.032}_{-0.032}$	0.897	0.571	0.623	3
110428338	PL	$-0.263^{+0.181}_{-0.199}$	-	$1.972^{+0.256}_{-0.234}$	$1.998^{+0.032}_{-0.032}$	0.568	0.568	0.568	7
110529262	PL	$-0.023^{+0.201}_{-0.234}$	-	$1.910^{+0.325}_{-0.271}$	$1.989^{+0.033}_{-0.032}$	0.793	0.646	0.660	3
110622158	PL	$-1.553^{+0.483}_{-0.563}$	-	$2.789^{+0.509}_{-0.434}$	$1.993^{+0.031}_{-0.032}$	0.380	0.896	0.898	4
110625881	BPL	$3.559^{+0.362}_{-0.282}$	$-1.146^{+0.156}_{-0.186}$	$3.030^{+0.370}_{-0.324}$	$1.992^{+0.032}_{-0.032}$	0.878	0.647	0.322	6
110709463	PL	$-0.064^{+0.282}_{-0.316}$	-	$2.950^{+0.580}_{-0.496}$	$1.991^{+0.033}_{-0.033}$	0.915	0.739	0.833	2
110709642	PL	$-0.415^{+0.282}_{-0.348}$	-	$1.915^{+0.439}_{-0.373}$	$1.990^{+0.033}_{-0.033}$	0.166	0.701	0.532	4
110717319	PL	$-0.796^{+0.291}_{-0.348}$	-	$2.083^{+0.320}_{-0.276}$	$1.989^{+0.032}_{-0.033}$	0.818	0.771	0.641	4
110721200	PL	$-0.161^{+0.221}_{-0.240}$	-	$2.744^{+0.372}_{-0.335}$	$1.988^{+0.033}_{-0.033}$	0.045	0.266	0.311	1

Table 2.4 (cont'd)

GRB	Model	$\log N$	$\log f_{\rm b}$ (Hz)	α	B	$p(T_R)$[a]	$p_{\rm AD}$[b]	$p_{\rm KS}$[c]	$N_{\rm peak}$
110729142	PL	$-1.901^{+0.580}_{-0.678}$	-	$2.278^{+0.507}_{-0.430}$	$1.995^{+0.031}_{-0.030}$	0.731	0.923	0.783	2
110731465	PL	$0.731^{+0.175}_{-0.190}$	-	$2.048^{+0.438}_{-0.370}$	$1.992^{+0.033}_{-0.031}$	0.693	0.993	0.997	3
110825102	PL	$0.591^{+0.083}_{-0.087}$	-	$2.071^{+0.166}_{-0.150}$	$1.992^{+0.033}_{-0.033}$	0.039	0.621	0.421	5
110903009	BPL	$3.645^{+0.473}_{-0.354}$	$-0.876^{+0.164}_{-0.201}$	$3.611^{+0.554}_{-0.482}$	$1.991^{+0.033}_{-0.032}$	0.624	0.471	0.390	4
110904124	PL	$-0.643^{+0.307}_{-0.357}$	-	$1.925^{+0.376}_{-0.324}$	$1.998^{+0.031}_{-0.032}$	0.159	0.644	0.726	3
110904163	PL	$-0.770^{+0.402}_{-0.516}$	-	$2.062^{+0.570}_{-0.468}$	$1.987^{+0.033}_{-0.032}$	0.441	0.208	0.330	1
110919634	PL	$-0.975^{+0.427}_{-0.522}$	-	$2.231^{+0.469}_{-0.396}$	$1.991^{+0.032}_{-0.032}$	0.495	0.387	0.507	1
110920546	PL	$-3.676^{+0.907}_{-1.064}$	-	$3.252^{+0.693}_{-0.589}$	$1.998^{+0.030}_{-0.030}$	0.510	0.564	0.571	1
110926107	PL	$-1.293^{+0.452}_{-0.543}$	-	$2.339^{+0.503}_{-0.430}$	$1.987^{+0.032}_{-0.032}$	0.914	0.539	0.568	3
110928180	PL	$-2.634^{+1.062}_{-1.420}$	-	$2.510^{+0.905}_{-0.683}$	$1.999^{+0.031}_{-0.031}$	0.047	0.264	0.215	1
111010709	PL	$-1.175^{+0.569}_{-0.652}$	-	$2.454^{+0.677}_{-0.584}$	$2.003^{+0.032}_{-0.032}$	0.878	0.040	0.020	4
111012456	PL	$-0.613^{+0.438}_{-0.553}$	-	$2.394^{+0.722}_{-0.577}$	$1.993^{+0.033}_{-0.032}$	0.819	0.837	0.741	3
111012811	PL	$1.025^{+0.218}_{-0.224}$	-	$2.587^{+0.855}_{-0.674}$	$1.993^{+0.033}_{-0.033}$	0.626	0.609	0.656	1
111024722	PL	$-0.660^{+0.330}_{-0.412}$	-	$1.992^{+0.403}_{-0.330}$	$1.989^{+0.032}_{-0.032}$	0.631	0.824	0.758	4
111127810	PL	$-0.500^{+0.439}_{-0.514}$	-	$3.124^{+0.745}_{-0.626}$	$1.992^{+0.032}_{-0.033}$	0.761	0.921	0.935	2
111216389	PL	$0.159^{+0.092}_{-0.098}$	-	$1.469^{+0.171}_{-0.154}$	$1.981^{+0.032}_{-0.032}$	0.678	0.093	0.169	12
111228657	BPL	$3.326^{+0.436}_{-0.331}$	$-1.028^{+0.195}_{-0.244}$	$2.722^{+0.386}_{-0.338}$	$1.996^{+0.032}_{-0.033}$	0.483	0.704	0.500	6
120119170	PL	$-0.878^{+0.355}_{-0.413}$	-	$2.237^{+0.380}_{-0.330}$	$1.993^{+0.032}_{-0.032}$	0.613	0.983	0.993	2
120129580	BPL	$3.712^{+0.387}_{-0.304}$	$-0.622^{+0.144}_{-0.173}$	$4.124^{+0.757}_{-0.637}$	$1.991^{+0.033}_{-0.032}$	0.777	0.130	0.223	2
120204054	PL	$-0.826^{+0.246}_{-0.272}$	-	$2.447^{+0.275}_{-0.245}$	$1.997^{+0.031}_{-0.031}$	0.964	0.426	0.725	4
120206949	PL	$-0.027^{+0.363}_{-0.448}$	-	$2.560^{+0.904}_{-0.714}$	$1.992^{+0.033}_{-0.033}$	0.261	0.274	0.205	1
120213606	PL	$0.095^{+0.245}_{-0.287}$	-	$1.960^{+0.595}_{-0.485}$	$1.990^{+0.032}_{-0.032}$	0.486	0.024	0.058	2
120224282	PL	$-1.090^{+0.531}_{-0.690}$	-	$1.877^{+0.602}_{-0.491}$	$1.993^{+0.032}_{-0.032}$	0.290	0.780	0.593	1
120226871	PL	$-0.542^{+0.233}_{-0.270}$	-	$1.810^{+0.244}_{-0.215}$	$1.999^{+0.032}_{-0.032}$	0.262	0.703	0.818	7
120308588	PL	$-0.025^{+0.243}_{-0.284}$	-	$2.179^{+0.536}_{-0.463}$	$1.988^{+0.033}_{-0.033}$	0.975	0.273	0.230	1
120328268	PL	$-0.205^{+0.196}_{-0.209}$	-	$2.276^{+0.257}_{-0.235}$	$2.000^{+0.032}_{-0.031}$	0.452	0.563	0.422	4
120412920	PL	$-0.377^{+0.228}_{-0.256}$	-	$1.952^{+0.338}_{-0.285}$	$1.997^{+0.032}_{-0.032}$	0.393	0.591	0.423	3
120426090	PL	$1.127^{+0.246}_{-0.282}$	-	$3.153^{+0.634}_{-0.518}$	$1.995^{+0.033}_{-0.033}$	0.754	0.667	0.516	1
120429484	PL	$-1.126^{+0.519}_{-0.647}$	-	$2.216^{+0.656}_{-0.519}$	$1.990^{+0.032}_{-0.032}$	0.395	0.452	0.326	1
120522361	PL	$0.094^{+0.247}_{-0.283}$	-	$2.481^{+0.578}_{-0.479}$	$1.990^{+0.033}_{-0.034}$	0.999	0.574	0.610	2
120530121	PL	$-2.030^{+0.839}_{-1.091}$	-	$2.801^{+0.877}_{-0.689}$	$1.989^{+0.032}_{-0.032}$	0.817	0.747	0.655	2
120605453	PL	$-0.389^{+0.286}_{-0.339}$	-	$2.108^{+0.476}_{-0.407}$	$1.988^{+0.033}_{-0.033}$	0.058	0.183	0.125	1
120611108	PL	$-0.013^{+0.173}_{-0.204}$	-	$1.414^{+0.325}_{-0.275}$	$1.995^{+0.032}_{-0.031}$	0.595	0.331	0.244	6
120624933	PL	$-0.550^{+0.352}_{-0.399}$	-	$2.643^{+0.616}_{-0.525}$	$1.996^{+0.032}_{-0.032}$	0.760	0.314	0.164	2
120703417	PL	$-1.483^{+0.500}_{-0.568}$	-	$2.839^{+0.594}_{-0.518}$	$1.989^{+0.032}_{-0.032}$	0.212	0.770	0.665	5
120703726	PL	$-0.046^{+0.277}_{-0.322}$	-	$2.235^{+0.553}_{-0.455}$	$1.994^{+0.032}_{-0.033}$	0.965	0.350	0.530	2
120707800	PL	$-0.515^{+0.259}_{-0.292}$	-	$2.358^{+0.370}_{-0.325}$	$1.989^{+0.032}_{-0.032}$	0.456	0.337	0.231	3
120709883	PL	$0.296^{+0.153}_{-0.172}$	-	$1.729^{+0.279}_{-0.253}$	$1.990^{+0.033}_{-0.033}$	0.936	0.633	0.757	3
120711115	PL	$-0.871^{+0.343}_{-0.435}$	-	$2.046^{+0.358}_{-0.288}$	$1.995^{+0.032}_{-0.032}$	0.300	0.436	0.423	2
120716712	PL	$-0.461^{+0.169}_{-0.189}$	-	$1.450^{+0.180}_{-0.162}$	$2.003^{+0.031}_{-0.031}$	0.176	0.392	0.327	2
120719146	PL	$-0.784^{+0.403}_{-0.536}$	-	$1.759^{+0.505}_{-0.392}$	$1.996^{+0.032}_{-0.032}$	0.622	0.248	0.102	3
120728434	BPL	$4.001^{+0.404}_{-0.307}$	$-1.469^{+0.163}_{-0.199}$	$3.090^{+0.344}_{-0.307}$	$1.997^{+0.031}_{-0.030}$	0.734	0.414	0.790	15
120806007	PL	$-0.104^{+0.267}_{-0.313}$	-	$2.308^{+0.507}_{-0.429}$	$1.988^{+0.033}_{-0.033}$	0.427	0.071	0.027	4
120913997	PL	$-1.586^{+0.709}_{-1.000}$	-	$2.119^{+0.780}_{-0.579}$	$1.996^{+0.032}_{-0.032}$	0.556	0.446	0.329	2
120919052	PL	$-0.530^{+0.219}_{-0.244}$	-	$1.650^{+0.247}_{-0.221}$	$1.993^{+0.031}_{-0.032}$	0.108	0.978	0.951	3
120919309	PL	$-0.379^{+0.299}_{-0.341}$	-	$2.689^{+0.502}_{-0.425}$	$1.990^{+0.032}_{-0.033}$	0.636	0.111	0.235	1
121029350	PL	$0.125^{+0.271}_{-0.360}$	-	$2.050^{+0.578}_{-0.455}$	$1.992^{+0.033}_{-0.033}$	0.634	0.494	0.484	2
121031949	PL	$-2.065^{+0.650}_{-0.799}$	-	$2.203^{+0.551}_{-0.447}$	$1.990^{+0.031}_{-0.030}$	0.606	0.812	0.811	2
121113544	PL	$-0.471^{+0.244}_{-0.291}$	-	$1.788^{+0.296}_{-0.253}$	$1.994^{+0.032}_{-0.032}$	0.267	0.477	0.371	6
121117018	PL	$-1.217^{+0.490}_{-0.629}$	-	$1.928^{+0.529}_{-0.414}$	$1.986^{+0.032}_{-0.031}$	0.154	0.320	0.161	3
121122870	PL	$-0.869^{+0.317}_{-0.356}$	-	$2.014^{+0.368}_{-0.326}$	$1.995^{+0.031}_{-0.031}$	0.010	0.326	0.603	2
121123442	PL	$-1.255^{+0.624}_{-0.760}$	-	$2.455^{+0.786}_{-0.648}$	$1.998^{+0.033}_{-0.032}$	0.102	0.461	0.380	2
121128212	PL	$0.135^{+0.198}_{-0.231}$	-	$1.959^{+0.386}_{-0.330}$	$1.994^{+0.033}_{-0.033}$	0.074	0.397	0.379	5
121225417	PL	$0.303^{+0.087}_{-0.091}$	-	$1.750^{+0.140}_{-0.131}$	$1.985^{+0.032}_{-0.032}$	0.979	0.590	0.564	10
130104721	PL	$-0.546^{+0.298}_{-0.342}$	-	$2.306^{+0.467}_{-0.414}$	$1.991^{+0.033}_{-0.033}$	0.526	0.946	0.856	3
130106829	PL	$-0.575^{+0.308}_{-0.402}$	-	$1.497^{+0.379}_{-0.302}$	$1.989^{+0.033}_{-0.033}$	0.316	0.343	0.340	1
130106995	PL	$-1.524^{+0.577}_{-0.689}$	-	$2.726^{+0.674}_{-0.560}$	$1.993^{+0.031}_{-0.032}$	0.203	0.832	0.736	2
130121835	PL	$-0.894^{+0.263}_{-0.302}$	-	$1.803^{+0.280}_{-0.249}$	$1.990^{+0.031}_{-0.031}$	0.359	0.376	0.493	4
130131511	PL	$-0.763^{+0.226}_{-0.263}$	-	$1.799^{+0.255}_{-0.231}$	$1.991^{+0.031}_{-0.031}$	0.959	0.709	0.518	9
130216790	PL	$0.553^{+0.177}_{-0.183}$	-	$2.332^{+0.499}_{-0.420}$	$1.990^{+0.032}_{-0.033}$	0.767	0.227	0.512	2
130219775	PL	$-0.402^{+0.220}_{-0.243}$	-	$1.965^{+0.281}_{-0.254}$	$1.999^{+0.031}_{-0.032}$	0.815	0.323	0.243	2

Table 2.4 (cont'd)

GRB	Model	$\log N$	$\log f_{\rm b}$ (Hz)	α	B	$p(T_R)$[a]	$p_{\rm AD}$[b]	$p_{\rm KS}$[c]	$N_{\rm peak}$
130220964	PL	$0.455^{+0.300}_{-0.341}$	-	$2.891^{+0.866}_{-0.714}$	$1.994^{+0.032}_{-0.033}$	0.677	0.913	0.607	2
130305486	PL	$-1.161^{+0.485}_{-0.565}$	-	$2.810^{+0.599}_{-0.525}$	$1.992^{+0.032}_{-0.032}$	0.242	0.308	0.509	1
130318456	PL	$-1.444^{+0.592}_{-0.762}$	-	$1.967^{+0.591}_{-0.474}$	$1.991^{+0.031}_{-0.031}$	0.909	0.640	0.425	1
130320560	PL	$-1.908^{+0.528}_{-0.663}$	-	$2.451^{+0.458}_{-0.379}$	$1.992^{+0.030}_{-0.030}$	0.015	0.500	0.597	2
130327350	PL	$-0.199^{+0.234}_{-0.265}$	-	$1.996^{+0.383}_{-0.330}$	$1.990^{+0.033}_{-0.032}$	0.551	0.739	0.911	4
130418844	PL	$-1.313^{+0.481}_{-0.606}$	-	$1.830^{+0.446}_{-0.373}$	$1.995^{+0.031}_{-0.031}$	0.656	0.647	0.535	1
130427324	PL	$1.567^{+0.024}_{-0.025}$	-	$1.866^{+0.037}_{-0.036}$	$1.526^{+0.022}_{-0.022}$	0.219	0.000	0.000	15
130502327	BPL	$3.547^{+0.513}_{-0.369}$	$-1.157^{+0.243}_{-0.325}$	$2.150^{+0.200}_{-0.180}$	$1.987^{+0.032}_{-0.032}$	0.746	0.685	0.882	15
130504978	BPL	$2.976^{+0.290}_{-0.236}$	$-0.940^{+0.152}_{-0.179}$	$2.872^{+0.426}_{-0.366}$	$1.993^{+0.031}_{-0.032}$	0.253	0.693	0.332	9
130509078	BPL	$3.107^{+0.521}_{-0.370}$	$-1.651^{+0.219}_{-0.290}$	$2.794^{+0.502}_{-0.432}$	$1.988^{+0.031}_{-0.030}$	0.478	0.485	0.601	2
130517781	PL	$-0.596^{+0.355}_{-0.420}$	-	$2.280^{+0.536}_{-0.451}$	$1.994^{+0.032}_{-0.033}$	0.068	0.261	0.231	3
130518580	PL	$-0.800^{+0.298}_{-0.348}$	-	$2.648^{+0.354}_{-0.302}$	$1.986^{+0.032}_{-0.031}$	0.984	0.608	0.597	1
130522510	PL	$-0.210^{+0.343}_{-0.412}$	-	$2.521^{+0.663}_{-0.555}$	$1.993^{+0.033}_{-0.032}$	0.440	0.894	0.700	1
130523095	PL	$-0.541^{+0.169}_{-0.188}$	-	$1.749^{+0.212}_{-0.191}$	$1.987^{+0.031}_{-0.031}$	0.921	0.222	0.285	5
130604033	PL	$0.240^{+0.156}_{-0.173}$	-	$1.870^{+0.320}_{-0.280}$	$1.994^{+0.032}_{-0.032}$	0.489	0.961	0.848	3
130606497	PL	$-0.015^{+0.111}_{-0.122}$	-	$2.124^{+0.162}_{-0.148}$	$2.010^{+0.031}_{-0.031}$	0.528	0.054	0.042	8
130609902	PL	$-1.476^{+0.408}_{-0.483}$	-	$2.217^{+0.404}_{-0.343}$	$1.986^{+0.031}_{-0.031}$	0.653	0.509	0.415	3
130614997	BPL	$3.460^{+0.815}_{-0.488}$	$-1.267^{+0.270}_{-0.429}$	$2.668^{+0.404}_{-0.355}$	$1.992^{+0.032}_{-0.033}$	0.477	0.877	0.684	2
130623790	PL	$-0.737^{+0.179}_{-0.201}$	-	$1.606^{+0.180}_{-0.163}$	$1.992^{+0.030}_{-0.030}$	0.194	0.846	0.854	7
130626596	PL	$-0.400^{+0.236}_{-0.278}$	-	$1.542^{+0.320}_{-0.278}$	$1.990^{+0.033}_{-0.032}$	0.024	0.214	0.249	2
130628531	PL	$-0.743^{+0.503}_{-0.582}$	-	$2.781^{+0.727}_{-0.619}$	$1.997^{+0.032}_{-0.033}$	0.266	0.270	0.129	2
130702004	PL	$-1.308^{+0.440}_{-0.540}$	-	$1.923^{+0.447}_{-0.367}$	$1.986^{+0.031}_{-0.032}$	0.668	0.754	0.957	1
130704560	PL	$1.410^{+0.137}_{-0.131}$	-	$2.550^{+0.407}_{-0.349}$	$1.993^{+0.034}_{-0.033}$	0.750	0.444	0.646	4
130707505	PL	$-2.435^{+0.570}_{-0.683}$	-	$2.944^{+0.474}_{-0.399}$	$1.970^{+0.031}_{-0.032}$	0.862	0.006	0.025	2
130715906	PL	$-1.218^{+0.591}_{-0.766}$	-	$2.167^{+0.708}_{-0.557}$	$1.999^{+0.032}_{-0.032}$	0.176	0.364	0.464	1
130803419	BPL	$1.906^{+0.000}_{0.000}$	$-1.138^{+0.000}_{0.000}$	$4.224^{+0.000}_{0.000}$	$1.985^{+0.000}_{0.000}$	0.976	0.438	0.567	2
130815420	PL	$-1.207^{+0.324}_{-0.374}$	-	$1.882^{+0.300}_{-0.261}$	$1.986^{+0.030}_{-0.030}$	0.583	0.736	0.723	4
130815660	PL	$-0.110^{+0.240}_{-0.259}$	-	$2.991^{+0.435}_{-0.393}$	$1.996^{+0.032}_{-0.032}$	0.411	0.148	0.263	2
130818941	PL	$-0.742^{+0.362}_{-0.441}$	-	$1.838^{+0.444}_{-0.358}$	$1.995^{+0.031}_{-0.033}$	0.305	0.066	0.062	2
130821674	PL	$-0.517^{+0.152}_{-0.163}$	-	$1.880^{+0.168}_{-0.156}$	$1.991^{+0.030}_{-0.030}$	0.786	0.780	0.639	4
131014215	PL	$1.531^{+0.065}_{-0.066}$	-	$2.431^{+0.153}_{-0.141}$	$1.987^{+0.033}_{-0.033}$	1.000	0.568	0.797	3
131028076	PL	$-0.121^{+0.251}_{-0.292}$	-	$2.310^{+0.403}_{-0.346}$	$1.993^{+0.032}_{-0.032}$	0.610	0.870	0.970	2
131029973	PL	$-2.216^{+0.930}_{-1.262}$	-	$2.559^{+0.880}_{-0.671}$	$1.998^{+0.032}_{-0.031}$	0.553	0.510	0.697	1
131030791	PL	$-1.482^{+0.605}_{-0.728}$	-	$2.174^{+0.649}_{-0.551}$	$1.995^{+0.032}_{-0.032}$	0.375	0.050	0.032	1
131108024	PL	$-0.941^{+0.265}_{-0.307}$	-	$1.462^{+0.258}_{-0.225}$	$1.986^{+0.030}_{-0.030}$	0.746	0.458	0.403	2
131108862	PL	$0.735^{+0.101}_{-0.106}$	-	$1.775^{+0.248}_{-0.220}$	$1.989^{+0.033}_{-0.033}$	0.047	0.172	0.225	6
131113483	PL	$-2.019^{+0.826}_{-1.080}$	-	$2.684^{+0.870}_{-0.673}$	$1.992^{+0.031}_{-0.032}$	0.390	0.671	0.874	1
131122490	PL	$-0.113^{+0.212}_{-0.244}$	-	$1.902^{+0.346}_{-0.303}$	$1.991^{+0.033}_{-0.033}$	0.971	0.583	0.646	2
131127592	BPL	$3.333^{+0.477}_{-0.345}$	$-0.839^{+0.202}_{-0.265}$	$3.068^{+0.564}_{-0.466}$	$1.989^{+0.033}_{-0.032}$	0.968	0.651	0.470	5
131214705	BPL	$4.346^{+0.473}_{-0.360}$	$-1.284^{+0.164}_{-0.198}$	$3.819^{+0.545}_{-0.469}$	$1.990^{+0.032}_{-0.031}$	0.323	0.387	0.601	3
131229277	PL	$0.637^{+0.154}_{-0.162}$	-	$1.777^{+0.340}_{-0.304}$	$1.993^{+0.034}_{-0.033}$	0.191	0.962	0.931	3
131231198	PL	$-0.206^{+0.149}_{-0.156}$	-	$2.732^{+0.249}_{-0.230}$	$1.987^{+0.031}_{-0.031}$	0.838	0.363	0.512	6

[a] $p(T_R)$ is the significance associated to statistic T_R.

[b] $p_{\rm AD}$ is the significance of the Anderson–Darling test.

[c] $p_{\rm KS}$ is the significance of the Kolmogorov–Smirnov test.

Table 2.5. Best–fitting model and parameters for each GRB of the *Fermi* sample in the 40–200 keV energy band.

GRB	Model	$\log N$	$\log f_{\rm b}$ (Hz)	α	B	$p(T_R)$[a]	$p_{\rm AD}$[b]	$p_{\rm KS}$[c]	$N_{\rm peak}$
080714745	PL	$-1.113^{+0.532}_{-0.629}$	-	$2.979^{+0.823}_{-0.678}$	$1.994^{+0.033}_{-0.033}$	0.660	0.576	0.621	1
080715950	PL	$0.458^{+0.069}_{-0.073}$	-	$1.356^{+0.135}_{-0.126}$	$1.991^{+0.033}_{-0.033}$	0.128	0.368	0.277	2
080723557	BPL	$3.318^{+0.221}_{-0.189}$	$-0.731^{+0.131}_{-0.144}$	$2.359^{+0.177}_{-0.161}$	$1.985^{+0.033}_{-0.032}$	0.876	0.432	0.204	24
080723985	PL	$0.166^{+0.170}_{-0.186}$	-	$2.307^{+0.328}_{-0.286}$	$1.993^{+0.032}_{-0.033}$	0.219	0.532	0.302	6
080724401	BPL	$2.313^{+0.229}_{-0.186}$	$-0.310^{+0.130}_{-0.154}$	$3.456^{+0.820}_{-0.650}$	$1.994^{+0.032}_{-0.033}$	0.481	0.841	0.817	5
080806896	PL	$-0.577^{+0.382}_{-0.523}$	-	$2.162^{+0.567}_{-0.436}$	$1.995^{+0.032}_{-0.033}$	0.280	0.811	0.905	1
080807993	PL	$0.868^{+0.071}_{-0.071}$	-	$1.148^{+0.141}_{-0.136}$	$1.992^{+0.033}_{-0.033}$	0.604	0.785	0.901	6
080810549	PL	$-0.108^{+0.140}_{-0.159}$	-	$1.313^{+0.192}_{-0.171}$	$1.990^{+0.033}_{-0.033}$	0.558	0.432	0.364	5
080816989	PL	$0.411^{+0.135}_{-0.149}$	-	$1.266^{+0.294}_{-0.256}$	$1.993^{+0.033}_{-0.034}$	0.904	0.988	0.987	1
080817161	PL	$-0.091^{+0.161}_{-0.180}$	-	$2.214^{+0.247}_{-0.221}$	$1.993^{+0.031}_{-0.032}$	0.910	0.496	0.474	4
080824909	PL	$0.797^{+0.121}_{-0.120}$	-	$1.586^{+0.282}_{-0.257}$	$1.993^{+0.033}_{-0.033}$	0.308	0.775	0.854	2
080825593	PL	$1.226^{+0.086}_{-0.086}$	-	$2.200^{+0.239}_{-0.219}$	$1.991^{+0.033}_{-0.033}$	0.895	0.278	0.418	8
080830368	PL	$-0.192^{+0.279}_{-0.352}$	-	$1.887^{+0.489}_{-0.390}$	$1.989^{+0.032}_{-0.033}$	0.582	0.197	0.078	1
080904886	PL	$0.307^{+0.186}_{-0.214}$	-	$2.168^{+0.465}_{-0.399}$	$1.992^{+0.033}_{-0.033}$	0.384	0.836	0.937	2
080906212	BPL	$3.523^{+0.663}_{-0.446}$	$-0.739^{+0.224}_{-0.306}$	$3.575^{+0.879}_{-0.681}$	$1.991^{+0.032}_{-0.033}$	0.873	0.773	0.739	1
080916009	PL	$0.193^{+0.132}_{-0.148}$	-	$1.907^{+0.191}_{-0.179}$	$1.995^{+0.033}_{-0.033}$	0.541	0.887	0.883	7
080916406	PL	$-0.962^{+0.450}_{-0.558}$	-	$2.630^{+0.622}_{-0.527}$	$1.989^{+0.032}_{-0.033}$	0.232	0.741	0.641	1
080925775	PL	$0.314^{+0.202}_{-0.237}$	-	$2.353^{+0.399}_{-0.332}$	$1.992^{+0.032}_{-0.033}$	0.504	0.987	0.985	3
081003644	PL	$-0.567^{+0.334}_{-0.455}$	-	$1.460^{+0.443}_{-0.340}$	$2.000^{+0.033}_{-0.033}$	0.342	0.311	0.340	2
081009140	BPL	$4.334^{+0.525}_{-0.384}$	$-1.006^{+0.185}_{-0.241}$	$2.925^{+0.259}_{-0.243}$	$1.991^{+0.032}_{-0.032}$	0.737	0.486	0.627	3
081025349	PL	$0.139^{+0.162}_{-0.181}$	-	$1.678^{+0.298}_{-0.266}$	$1.991^{+0.033}_{-0.032}$	0.755	0.683	0.745	5
081101532	PL	$0.410^{+0.170}_{-0.194}$	-	$2.007^{+0.357}_{-0.300}$	$1.993^{+0.032}_{-0.032}$	0.519	0.859	0.951	2
081122520	BPL	$2.576^{+0.320}_{-0.256}$	$-0.855^{+0.198}_{-0.238}$	$2.250^{+0.335}_{-0.281}$	$1.986^{+0.031}_{-0.031}$	0.030	0.539	0.457	4
081126899	PL	$-0.315^{+0.242}_{-0.288}$	-	$2.382^{+0.384}_{-0.337}$	$1.989^{+0.033}_{-0.032}$	0.600	0.459	0.202	2
081129161	BPL	$2.806^{+0.624}_{-0.422}$	$-0.794^{+0.258}_{-0.375}$	$2.731^{+0.631}_{-0.513}$	$1.993^{+0.033}_{-0.032}$	0.918	0.973	0.711	3
081130629	PL	$-0.178^{+0.279}_{-0.346}$	-	$1.912^{+0.480}_{-0.400}$	$1.993^{+0.033}_{-0.033}$	0.390	0.946	0.887	2
081207680	PL	$-1.295^{+0.520}_{-0.685}$	-	$1.962^{+0.455}_{-0.356}$	$1.996^{+0.031}_{-0.032}$	0.873	0.657	0.458	1
081215784	BPL	$3.691^{+0.259}_{-0.216}$	$-0.240^{+0.112}_{-0.127}$	$3.497^{+0.404}_{-0.355}$	$1.992^{+0.033}_{-0.033}$	0.756	0.259	0.333	4
081215880	PL	$-0.660^{+0.353}_{-0.481}$	-	$1.559^{+0.447}_{-0.341}$	$1.996^{+0.032}_{-0.033}$	0.195	0.690	0.474	1
081221681	PL	$0.106^{+0.135}_{-0.144}$	-	$2.578^{+0.269}_{-0.246}$	$1.985^{+0.032}_{-0.032}$	0.997	0.164	0.110	2
081222204	PL	$0.092^{+0.251}_{-0.292}$	-	$2.234^{+0.391}_{-0.327}$	$1.996^{+0.032}_{-0.031}$	0.495	0.714	0.734	1
081224887	PL	$-0.126^{+0.291}_{-0.337}$	-	$3.189^{+0.486}_{-0.428}$	$1.992^{+0.033}_{-0.033}$	0.189	0.885	0.772	1
081231140	BPL	$2.419^{+0.320}_{-0.261}$	$-0.564^{+0.185}_{-0.227}$	$2.797^{+0.575}_{-0.494}$	$1.990^{+0.033}_{-0.033}$	0.756	0.532	0.269	9
090102122	PL	$1.262^{+0.062}_{-0.061}$	-	$1.391^{+0.124}_{-0.116}$	$1.990^{+0.032}_{-0.033}$	0.958	0.735	0.770	13
090112332	PL	$-0.407^{+0.292}_{-0.367}$	-	$1.793^{+0.482}_{-0.404}$	$1.989^{+0.033}_{-0.033}$	0.597	0.412	0.611	1
090112729	PL	$0.590^{+0.156}_{-0.168}$	-	$1.982^{+0.316}_{-0.279}$	$1.991^{+0.032}_{-0.032}$	0.704	0.659	0.828	3
090117640	PL	$0.510^{+0.180}_{-0.212}$	-	$1.643^{+0.507}_{-0.404}$	$1.994^{+0.033}_{-0.033}$	0.775	0.538	0.686	1
090131090	BPL	$2.862^{+0.247}_{-0.210}$	$-0.522^{+0.121}_{-0.136}$	$3.213^{+0.428}_{-0.372}$	$1.986^{+0.033}_{-0.033}$	0.457	0.306	0.389	5
090202347	PL	$-0.252^{+0.224}_{-0.258}$	-	$1.943^{+0.332}_{-0.286}$	$1.987^{+0.033}_{-0.033}$	0.895	0.554	0.599	1
090217206	PL	$0.832^{+0.091}_{-0.091}$	-	$1.538^{+0.174}_{-0.160}$	$1.992^{+0.033}_{-0.033}$	0.728	0.354	0.225	8
090323002	PL	$0.059^{+0.119}_{-0.131}$	-	$1.893^{+0.173}_{-0.157}$	$1.999^{+0.032}_{-0.032}$	0.926	0.780	0.894	12
090419997	PL	$-1.478^{+0.613}_{-0.782}$	-	$2.354^{+0.657}_{-0.530}$	$1.996^{+0.031}_{-0.031}$	0.290	0.975	0.996	2
090424592	BPL	$4.245^{+0.353}_{-0.281}$	$-0.822^{+0.170}_{-0.210}$	$2.210^{+0.133}_{-0.126}$	$1.991^{+0.034}_{-0.033}$	0.972	0.316	0.632	8
090425377	PL	$0.163^{+0.117}_{-0.126}$	-	$1.815^{+0.218}_{-0.195}$	$1.990^{+0.033}_{-0.032}$	0.961	0.571	0.296	4
090502777	PL	$0.030^{+0.141}_{-0.163}$	-	$1.482^{+0.256}_{-0.233}$	$1.990^{+0.033}_{-0.032}$	0.380	0.895	0.985	3
090516137	PL	$-1.127^{+0.412}_{-0.531}$	-	$1.718^{+0.377}_{-0.300}$	$1.998^{+0.032}_{-0.031}$	0.335	0.553	0.355	4
090516353	PL	$-0.742^{+0.327}_{-0.411}$	-	$1.764^{+0.393}_{-0.323}$	$1.991^{+0.032}_{-0.032}$	0.961	0.384	0.627	4
090516853	PL	$0.494^{+0.217}_{-0.255}$	-	$2.171^{+0.590}_{-0.467}$	$1.994^{+0.033}_{-0.033}$	0.182	0.976	0.971	2
090528516	PL	$0.151^{+0.099}_{-0.105}$	-	$1.920^{+0.185}_{-0.168}$	$1.980^{+0.032}_{-0.033}$	0.800	0.154	0.085	8
090529564	PL	$1.837^{+0.134}_{-0.124}$	-	$1.938^{+0.264}_{-0.240}$	$1.994^{+0.032}_{-0.033}$	0.405	0.997	0.973	3
090620400	PL	$0.374^{+0.219}_{-0.239}$	-	$2.676^{+0.502}_{-0.423}$	$1.991^{+0.033}_{-0.033}$	0.223	0.463	0.687	1
090623107	PL	$0.318^{+0.100}_{-0.108}$	-	$1.390^{+0.180}_{-0.160}$	$1.994^{+0.033}_{-0.032}$	0.503	0.822	0.940	7
090626189	BPL	$3.512^{+0.318}_{-0.254}$	$-0.807^{+0.162}_{-0.192}$	$2.386^{+0.194}_{-0.177}$	$1.986^{+0.033}_{-0.033}$	0.393	0.337	0.251	12
090711850	PL	$-0.173^{+0.217}_{-0.266}$	-	$1.634^{+0.344}_{-0.281}$	$1.990^{+0.033}_{-0.032}$	0.453	0.587	0.609	5
090717034	PL	$-0.367^{+0.254}_{-0.280}$	-	$2.423^{+0.374}_{-0.329}$	$1.998^{+0.031}_{-0.032}$	0.542	0.334	0.274	3
090719063	PL	$0.353^{+0.219}_{-0.246}$	-	$2.901^{+0.470}_{-0.393}$	$1.997^{+0.033}_{-0.033}$	0.846	0.344	0.401	1
090720710	BPL	$2.191^{+0.321}_{-0.241}$	$0.048^{+0.228}_{-0.330}$	$2.350^{+0.745}_{-0.657}$	$1.994^{+0.034}_{-0.033}$	0.988	0.220	0.090	2
090804940	PL	$0.731^{+0.276}_{-0.313}$	-	$3.134^{+0.807}_{-0.634}$	$1.994^{+0.031}_{-0.033}$	0.623	0.395	0.369	1
090810659	PL	$-2.133^{+0.917}_{-1.288}$	-	$2.451^{+0.923}_{-0.670}$	$1.995^{+0.031}_{-0.032}$	0.246	0.626	0.824	2
090814950	PL	$-0.070^{+0.129}_{-0.144}$	-	$1.562^{+0.212}_{-0.187}$	$1.984^{+0.032}_{-0.032}$	0.386	0.420	0.800	7
090815438	PL	$-0.680^{+0.448}_{-0.537}$	-	$2.824^{+0.765}_{-0.630}$	$1.990^{+0.033}_{-0.033}$	0.789	0.598	0.477	1

Table 2.5 (cont'd)

GRB	Model	$\log N$	$\log f_{\rm b}$ (Hz)	α	B	$p(T_R)$[a]	$p_{\rm AD}$[b]	$p_{\rm KS}$[c]	$N_{\rm peak}$
090820027	PL	$0.542^{+0.114}_{-0.122}$	-	$3.015^{+0.204}_{-0.190}$	$1.994^{+0.032}_{-0.032}$	0.009	0.543	0.294	3
090828099	PL	$-0.275^{+0.203}_{-0.233}$	-	$2.256^{+0.297}_{-0.265}$	$1.998^{+0.032}_{-0.032}$	0.248	0.585	0.590	3
090829672	PL	$1.190^{+0.042}_{-0.043}$	-	$1.867^{+0.108}_{-0.104}$	$1.985^{+0.033}_{-0.033}$	0.458	0.317	0.163	13
090831317	PL	$0.900^{+0.056}_{-0.055}$	-	$0.949^{+0.107}_{-0.102}$	$1.993^{+0.032}_{-0.033}$	0.924	0.103	0.030	6
090902462	PL	$1.935^{+0.054}_{-0.054}$	-	$1.525^{+0.096}_{-0.094}$	$1.993^{+0.033}_{-0.033}$	0.584	0.857	0.630	22
090904058	PL	$-0.550^{+0.300}_{-0.379}$	-	$1.814^{+0.390}_{-0.337}$	$1.993^{+0.032}_{-0.032}$	0.112	0.696	0.492	5
090910812	PL	$0.072^{+0.134}_{-0.151}$	-	$1.513^{+0.207}_{-0.180}$	$1.989^{+0.032}_{-0.032}$	0.378	0.516	0.523	6
090922539	BPL	$3.390^{+0.820}_{-0.494}$	$-1.341^{+0.264}_{-0.410}$	$2.836^{+0.509}_{-0.415}$	$1.991^{+0.033}_{-0.033}$	0.670	0.591	0.602	3
090926181	PL	$1.641^{+0.061}_{-0.060}$	-	$1.989^{+0.117}_{-0.114}$	$1.994^{+0.033}_{-0.033}$	0.844	0.227	0.178	6
090929190	BPL	$2.310^{+0.396}_{-0.291}$	$-0.800^{+0.273}_{-0.361}$	$1.805^{+0.292}_{-0.258}$	$1.992^{+0.034}_{-0.034}$	0.088	0.439	0.397	3
091003191	BPL	$3.048^{+0.467}_{-0.339}$	$-0.485^{+0.240}_{-0.325}$	$2.354^{+0.380}_{-0.340}$	$1.992^{+0.032}_{-0.032}$	0.506	0.233	0.135	11
091020900	PL	$-1.146^{+0.657}_{-0.811}$	-	$2.741^{+0.838}_{-0.681}$	$1.997^{+0.032}_{-0.032}$	0.360	0.446	0.523	1
091020977	PL	$0.422^{+0.123}_{-0.128}$	-	$1.641^{+0.268}_{-0.240}$	$1.989^{+0.032}_{-0.032}$	0.803	0.573	0.555	4
091031500	PL	$0.868^{+0.082}_{-0.083}$	-	$1.299^{+0.164}_{-0.154}$	$1.991^{+0.033}_{-0.033}$	0.874	0.703	0.541	8
091101143	PL	$0.712^{+0.068}_{-0.067}$	-	$1.630^{+0.149}_{-0.140}$	$1.988^{+0.032}_{-0.032}$	0.116	0.404	0.309	7
091103912	PL	$0.274^{+0.186}_{-0.203}$	-	$2.209^{+0.408}_{-0.367}$	$1.986^{+0.033}_{-0.033}$	0.835	0.020	0.019	3
091120191	BPL	$2.756^{+0.318}_{-0.249}$	$-0.638^{+0.174}_{-0.212}$	$2.640^{+0.399}_{-0.338}$	$1.986^{+0.032}_{-0.033}$	0.791	0.297	0.365	13
091127976	BPL	$3.582^{+0.540}_{-0.390}$	$-0.445^{+0.207}_{-0.286}$	$2.921^{+0.421}_{-0.381}$	$1.991^{+0.033}_{-0.033}$	0.845	0.987	0.998	3
091128285	PL	$0.186^{+0.126}_{-0.138}$	-	$1.701^{+0.211}_{-0.188}$	$1.992^{+0.033}_{-0.032}$	0.679	0.477	0.511	7
091208410	PL	$1.373^{+0.133}_{-0.129}$	-	$2.209^{+0.357}_{-0.323}$	$1.993^{+0.034}_{-0.033}$	0.333	0.665	0.800	1
091227294	PL	$0.019^{+0.153}_{-0.177}$	-	$1.496^{+0.244}_{-0.209}$	$1.988^{+0.034}_{-0.032}$	0.193	0.501	0.530	1
100116897	PL	$-0.077^{+0.141}_{-0.153}$	-	$2.181^{+0.206}_{-0.188}$	$1.992^{+0.031}_{-0.031}$	0.600	0.767	0.875	3
100130729	PL	$-1.692^{+0.609}_{-0.757}$	-	$2.620^{+0.637}_{-0.531}$	$1.997^{+0.032}_{-0.032}$	0.462	0.016	0.009	2
100131730	PL	$1.949^{+0.160}_{-0.146}$	-	$2.309^{+0.352}_{-0.323}$	$1.992^{+0.033}_{-0.033}$	0.474	0.564	0.581	3
100225580	PL	$0.519^{+0.167}_{-0.191}$	-	$1.937^{+0.294}_{-0.262}$	$1.993^{+0.033}_{-0.033}$	0.410	0.939	0.997	1
100301223	PL	$0.413^{+0.132}_{-0.146}$	-	$1.355^{+0.283}_{-0.246}$	$1.992^{+0.032}_{-0.032}$	0.533	0.924	0.962	4
100304004	PL	$-1.607^{+0.682}_{-0.939}$	-	$1.874^{+0.627}_{-0.468}$	$1.996^{+0.031}_{-0.031}$	0.960	0.061	0.059	1
100322045	PL	$0.921^{+0.063}_{-0.063}$	-	$1.936^{+0.145}_{-0.133}$	$1.990^{+0.032}_{-0.032}$	0.977	0.534	0.549	12
100324172	PL	$1.073^{+0.065}_{-0.065}$	-	$2.045^{+0.149}_{-0.141}$	$1.992^{+0.034}_{-0.032}$	0.882	0.989	0.818	3
100326402	PL	$-0.730^{+0.277}_{-0.318}$	-	$1.662^{+0.312}_{-0.267}$	$1.986^{+0.032}_{-0.032}$	0.264	0.241	0.257	4
100414097	PL	$0.859^{+0.073}_{-0.073}$	-	$1.795^{+0.153}_{-0.139}$	$1.991^{+0.033}_{-0.033}$	0.966	0.981	0.991	9
100424876	PL	$-0.248^{+0.116}_{-0.127}$	-	$1.266^{+0.142}_{-0.126}$	$1.982^{+0.031}_{-0.031}$	0.867	0.333	0.146	8
100502356	PL	$0.177^{+0.092}_{-0.100}$	-	$1.519^{+0.175}_{-0.163}$	$1.983^{+0.032}_{-0.032}$	0.915	0.310	0.264	8
100503554	PL	$0.143^{+0.080}_{-0.086}$	-	$1.336^{+0.130}_{-0.122}$	$1.982^{+0.032}_{-0.033}$	0.356	0.296	0.503	12
100511035	PL	$0.794^{+0.061}_{-0.062}$	-	$1.684^{+0.130}_{-0.124}$	$1.987^{+0.033}_{-0.032}$	0.346	0.597	0.898	7
100515467	PL	$0.308^{+0.274}_{-0.300}$	-	$3.157^{+0.663}_{-0.581}$	$1.993^{+0.033}_{-0.033}$	0.247	0.984	0.821	1
100517072	PL	$0.048^{+0.191}_{-0.225}$	-	$1.922^{+0.333}_{-0.289}$	$1.997^{+0.033}_{-0.033}$	0.195	0.673	0.870	2
100517639	PL	$1.150^{+0.186}_{-0.179}$	-	$1.915^{+0.494}_{-0.422}$	$1.993^{+0.033}_{-0.034}$	0.764	0.971	0.982	3
100519204	PL	$-1.622^{+0.561}_{-0.651}$	-	$2.705^{+0.621}_{-0.521}$	$1.984^{+0.032}_{-0.032}$	0.977	0.266	0.267	2
100522157	PL	$0.727^{+0.093}_{-0.096}$	-	$1.442^{+0.189}_{-0.171}$	$1.993^{+0.032}_{-0.033}$	0.860	0.621	0.697	1
100527795	PL	$-0.061^{+0.134}_{-0.145}$	-	$1.568^{+0.228}_{-0.202}$	$1.984^{+0.033}_{-0.033}$	0.973	0.103	0.115	4
100528075	PL	$0.084^{+0.158}_{-0.176}$	-	$2.033^{+0.220}_{-0.201}$	$1.987^{+0.033}_{-0.033}$	0.574	0.304	0.407	3
100612726	PL	$-0.812^{+0.466}_{-0.509}$	-	$4.029^{+0.795}_{-0.698}$	$1.991^{+0.032}_{-0.032}$	0.687	0.242	0.071	1
100701490	PL	$1.831^{+0.080}_{-0.075}$	-	$1.380^{+0.138}_{-0.135}$	$1.993^{+0.033}_{-0.033}$	0.813	0.965	0.889	7
100707032	BPL	$4.142^{+0.383}_{-0.301}$	$-1.100^{+0.129}_{-0.151}$	$3.986^{+0.530}_{-0.462}$	$1.995^{+0.032}_{-0.033}$	0.929	0.909	0.936	1
100709602	PL	$-0.686^{+0.296}_{-0.340}$	-	$1.833^{+0.336}_{-0.305}$	$2.000^{+0.032}_{-0.032}$	0.552	0.262	0.491	2
100718160	PL	$0.401^{+0.116}_{-0.123}$	-	$1.340^{+0.263}_{-0.239}$	$1.991^{+0.032}_{-0.032}$	0.533	0.232	0.240	3
100719989	BPL	$3.706^{+0.333}_{-0.262}$	$-0.611^{+0.135}_{-0.160}$	$3.870^{+0.563}_{-0.497}$	$1.989^{+0.032}_{-0.032}$	0.671	0.559	0.464	4
100722096	BPL	$2.855^{+0.271}_{-0.226}$	$-0.445^{+0.172}_{-0.206}$	$2.529^{+0.368}_{-0.327}$	$1.988^{+0.033}_{-0.033}$	0.974	0.379	0.173	4
100724029	PL	$0.228^{+0.076}_{-0.080}$	-	$1.952^{+0.118}_{-0.110}$	$1.984^{+0.031}_{-0.032}$	0.626	0.688	0.752	14
100725475	PL	$-0.809^{+0.264}_{-0.322}$	-	$1.572^{+0.263}_{-0.222}$	$1.995^{+0.031}_{-0.031}$	0.658	0.495	0.519	4
100728095	PL	$0.379^{+0.055}_{-0.057}$	-	$1.543^{+0.097}_{-0.094}$	$1.980^{+0.031}_{-0.031}$	0.972	0.121	0.058	24
100804104	PL	$1.066^{+0.148}_{-0.150}$	-	$2.076^{+0.366}_{-0.316}$	$1.993^{+0.033}_{-0.032}$	0.223	0.936	0.973	3
100820373	PL	$1.381^{+0.244}_{-0.226}$	-	$2.152^{+0.571}_{-0.495}$	$1.993^{+0.033}_{-0.033}$	0.534	0.796	0.537	2
100826957	PL	$0.636^{+0.059}_{-0.060}$	-	$1.818^{+0.110}_{-0.102}$	$1.982^{+0.032}_{-0.032}$	0.816	0.279	0.374	16
100829374	PL	$-1.237^{+0.542}_{-0.660}$	-	$2.440^{+0.645}_{-0.533}$	$1.996^{+0.031}_{-0.031}$	0.944	0.827	0.893	1
100829876	BPL	$3.256^{+0.381}_{-0.287}$	$-0.083^{+0.212}_{-0.281}$	$2.843^{+0.681}_{-0.589}$	$1.993^{+0.033}_{-0.033}$	0.988	0.473	0.485	6
100906576	PL	$-0.287^{+0.197}_{-0.228}$	-	$2.207^{+0.277}_{-0.243}$	$2.002^{+0.031}_{-0.031}$	0.225	0.039	0.032	4
100910818	BPL	$2.951^{+0.391}_{-0.306}$	$-0.367^{+0.207}_{-0.254}$	$2.544^{+0.423}_{-0.364}$	$1.993^{+0.034}_{-0.033}$	0.335	0.983	0.907	7
100918863	PL	$-1.345^{+0.461}_{-0.557}$	-	$2.647^{+0.475}_{-0.391}$	$1.989^{+0.031}_{-0.031}$	0.889	0.705	0.722	3
100923844	PL	$-0.454^{+0.297}_{-0.364}$	-	$1.661^{+0.409}_{-0.349}$	$1.995^{+0.033}_{-0.033}$	0.356	0.278	0.459	2

Table 2.5 (cont'd)

GRB	Model	$\log N$	$\log f_{\rm b}$ (Hz)	α	B	$p(T_R)$[a]	$p_{\rm AD}$[b]	$p_{\rm KS}$[c]	$N_{\rm peak}$
101013412	PL	$0.831^{+0.127}_{-0.126}$	-	$1.390^{+0.290}_{-0.259}$	$1.993^{+0.033}_{-0.032}$	0.951	0.714	0.652	3
101021009	PL	$-0.446^{+0.255}_{-0.307}$	-	$2.080^{+0.351}_{-0.303}$	$1.992^{+0.033}_{-0.032}$	0.196	0.664	0.597	4
101113483	PL	$0.108^{+0.096}_{-0.102}$	-	$1.413^{+0.147}_{-0.137}$	$1.985^{+0.032}_{-0.033}$	0.746	0.051	0.069	6
101126198	PL	$0.060^{+0.159}_{-0.177}$	-	$2.073^{+0.226}_{-0.201}$	$1.993^{+0.033}_{-0.032}$	0.361	0.899	0.663	2
101201418	PL	$-1.151^{+0.402}_{-0.469}$	-	$2.317^{+0.451}_{-0.387}$	$1.989^{+0.032}_{-0.032}$	0.915	0.631	0.334	3
101206036	PL	$-0.214^{+0.313}_{-0.399}$	-	$1.816^{+0.583}_{-0.462}$	$1.994^{+0.032}_{-0.033}$	0.883	0.762	0.841	1
101207536	PL	$0.066^{+0.130}_{-0.148}$	-	$1.504^{+0.232}_{-0.207}$	$1.988^{+0.032}_{-0.033}$	0.538	0.866	0.822	4
101208498	PL	$1.987^{+0.170}_{-0.156}$	-	$2.656^{+0.445}_{-0.402}$	$1.993^{+0.032}_{-0.033}$	0.959	0.406	0.513	1
101224578	PL	$-0.805^{+0.314}_{-0.358}$	-	$1.848^{+0.370}_{-0.322}$	$1.996^{+0.031}_{-0.032}$	0.734	0.849	0.768	4
101225377	PL	$-1.543^{+0.467}_{-0.542}$	-	$2.515^{+0.473}_{-0.407}$	$1.994^{+0.032}_{-0.032}$	0.518	0.767	0.645	2
101227406	BPL	$2.625^{+0.575}_{-0.390}$	$-1.385^{+0.285}_{-0.415}$	$2.160^{+0.401}_{-0.338}$	$1.980^{+0.031}_{-0.032}$	0.832	0.305	0.288	6
101227536	PL	$0.754^{+0.106}_{-0.107}$	-	$1.442^{+0.232}_{-0.212}$	$1.991^{+0.033}_{-0.032}$	0.882	0.261	0.174	5
101231067	BPL	$2.943^{+0.513}_{-0.354}$	$-0.749^{+0.263}_{-0.364}$	$2.271^{+0.387}_{-0.323}$	$1.990^{+0.033}_{-0.033}$	0.721	0.239	0.199	11
110102788	PL	$-0.265^{+0.160}_{-0.178}$	-	$2.046^{+0.204}_{-0.186}$	$1.989^{+0.032}_{-0.032}$	0.342	0.951	0.953	6
110120666	PL	$0.696^{+0.100}_{-0.106}$	-	$1.760^{+0.212}_{-0.191}$	$1.989^{+0.033}_{-0.033}$	0.584	0.430	0.435	3
110207470	PL	$0.494^{+0.096}_{-0.100}$	-	$0.866^{+0.183}_{-0.175}$	$1.992^{+0.033}_{-0.032}$	0.624	0.675	0.534	5
110213220	PL	$-0.008^{+0.231}_{-0.268}$	-	$2.063^{+0.403}_{-0.342}$	$1.994^{+0.032}_{-0.032}$	0.679	0.486	0.431	1
110227420	BPL	$1.651^{+0.000}_{0.000}$	$-1.119^{+0.000}_{0.000}$	$11.102^{+0.000}_{0.000}$	$1.989^{+0.000}_{0.000}$	0.978	0.788	0.860	1
110304071	PL	$-0.104^{+0.204}_{-0.247}$	-	$1.860^{+0.355}_{-0.302}$	$1.992^{+0.032}_{-0.032}$	0.495	0.699	0.436	2
110318552	PL	$0.812^{+0.133}_{-0.141}$	-	$1.659^{+0.253}_{-0.222}$	$1.994^{+0.033}_{-0.033}$	0.584	0.951	0.909	3
110328520	PL	$-1.566^{+0.565}_{-0.668}$	-	$2.677^{+0.586}_{-0.492}$	$1.982^{+0.032}_{-0.032}$	0.876	0.326	0.483	1
110402009	PL	$0.825^{+0.083}_{-0.079}$	-	$0.832^{+0.153}_{-0.148}$	$1.993^{+0.033}_{-0.032}$	0.415	0.961	0.947	4
110415541	BPL	$1.999^{+0.462}_{-0.334}$	$-1.259^{+0.278}_{-0.379}$	$2.409^{+0.766}_{-0.581}$	$1.999^{+0.031}_{-0.031}$	0.895	0.142	0.110	2
110421757	PL	$-0.558^{+0.227}_{-0.269}$	-	$1.706^{+0.262}_{-0.227}$	$1.987^{+0.032}_{-0.032}$	0.855	0.738	0.589	3
110517573	PL	$0.758^{+0.108}_{-0.115}$	-	$1.666^{+0.227}_{-0.209}$	$1.994^{+0.033}_{-0.033}$	0.574	0.776	0.569	5
110522633	PL	$0.033^{+0.239}_{-0.285}$	-	$2.083^{+0.571}_{-0.475}$	$1.990^{+0.033}_{-0.033}$	0.862	0.590	0.418	1
110528624	PL	$-0.858^{+0.340}_{-0.421}$	-	$1.556^{+0.378}_{-0.319}$	$1.996^{+0.032}_{-0.032}$	0.403	0.743	0.509	3
110529262	BPL	$2.309^{+0.374}_{-0.283}$	$-0.606^{+0.244}_{-0.320}$	$2.395^{+0.590}_{-0.476}$	$1.989^{+0.033}_{-0.033}$	0.882	0.861	0.846	5
110601681	PL	$-0.322^{+0.239}_{-0.293}$	-	$1.634^{+0.342}_{-0.290}$	$1.990^{+0.031}_{-0.032}$	0.776	0.227	0.224	1
110610640	PL	$-0.274^{+0.305}_{-0.396}$	-	$1.886^{+0.455}_{-0.365}$	$1.994^{+0.033}_{-0.033}$	0.485	0.486	0.348	3
110622158	PL	$-1.478^{+0.430}_{-0.498}$	-	$3.026^{+0.490}_{-0.422}$	$1.990^{+0.031}_{-0.032}$	0.822	0.898	0.763	5
110625881	BPL	$3.918^{+0.249}_{-0.208}$	$-0.938^{+0.109}_{-0.125}$	$2.700^{+0.149}_{-0.144}$	$1.993^{+0.032}_{-0.033}$	0.115	0.681	0.695	9
110702187	PL	$0.248^{+0.157}_{-0.180}$	-	$1.572^{+0.294}_{-0.260}$	$1.992^{+0.033}_{-0.033}$	0.958	0.782	0.566	3
110705364	PL	$0.470^{+0.139}_{-0.150}$	-	$1.732^{+0.334}_{-0.297}$	$1.990^{+0.033}_{-0.033}$	0.806	0.871	0.955	5
110706728	BPL	$1.878^{+0.000}_{0.000}$	$-0.298^{+0.000}_{0.000}$	$3.965^{+0.000}_{0.000}$	$1.993^{+0.000}_{0.000}$	0.713	0.640	0.468	3
110709642	BPL	$2.926^{+0.423}_{-0.308}$	$-0.879^{+0.207}_{-0.264}$	$2.414^{+0.349}_{-0.308}$	$1.992^{+0.033}_{-0.033}$	0.275	0.898	0.984	10
110710954	BPL	$2.565^{+0.464}_{-0.334}$	$-0.551^{+0.259}_{-0.341}$	$2.342^{+0.563}_{-0.439}$	$1.995^{+0.033}_{-0.032}$	0.260	0.899	0.690	7
110717319	PL	$0.411^{+0.078}_{-0.083}$	-	$2.003^{+0.183}_{-0.167}$	$1.987^{+0.032}_{-0.032}$	0.336	0.218	0.349	8
110721200	PL	$0.694^{+0.121}_{-0.132}$	-	$2.472^{+0.264}_{-0.237}$	$1.997^{+0.032}_{-0.032}$	0.364	0.606	0.383	1
110729142	PL	$-0.647^{+0.197}_{-0.211}$	-	$1.907^{+0.210}_{-0.193}$	$2.001^{+0.031}_{-0.031}$	0.981	0.268	0.118	6
110730660	PL	$-0.844^{+0.530}_{-0.704}$	-	$2.188^{+0.746}_{-0.596}$	$1.993^{+0.033}_{-0.032}$	0.663	0.348	0.302	1
110731465	PL	$1.380^{+0.127}_{-0.122}$	-	$1.798^{+0.273}_{-0.247}$	$1.993^{+0.032}_{-0.033}$	0.752	0.780	0.741	4
110806934	PL	$-0.631^{+0.487}_{-0.640}$	-	$2.317^{+0.747}_{-0.593}$	$1.995^{+0.033}_{-0.032}$	0.381	0.493	0.323	2
110809461	PL	$-0.378^{+0.422}_{-0.567}$	-	$2.268^{+0.704}_{-0.530}$	$1.995^{+0.032}_{-0.032}$	0.795	0.350	0.172	1
110824009	BPL	$2.667^{+0.361}_{-0.292}$	$-0.809^{+0.233}_{-0.292}$	$1.775^{+0.194}_{-0.181}$	$1.999^{+0.033}_{-0.033}$	0.846	0.111	0.051	6
110825102	PL	$1.752^{+0.044}_{-0.043}$	-	$1.617^{+0.079}_{-0.076}$	$1.988^{+0.033}_{-0.033}$	0.806	0.024	0.043	12
110904124	PL	$-0.398^{+0.236}_{-0.278}$	-	$2.023^{+0.341}_{-0.293}$	$1.999^{+0.032}_{-0.032}$	0.724	0.478	0.599	4
110904163	PL	$-0.060^{+0.185}_{-0.212}$	-	$1.761^{+0.343}_{-0.308}$	$1.987^{+0.033}_{-0.033}$	0.048	0.029	0.050	3
110919634	PL	$-0.052^{+0.167}_{-0.190}$	-	$1.864^{+0.237}_{-0.216}$	$1.992^{+0.032}_{-0.032}$	0.200	0.993	0.998	3
110921912	BPL	$3.607^{+0.386}_{-0.298}$	$-1.039^{+0.173}_{-0.213}$	$2.347^{+0.178}_{-0.166}$	$1.991^{+0.033}_{-0.032}$	0.273	0.866	0.840	5
110926107	PL	$-1.024^{+0.403}_{-0.505}$	-	$2.318^{+0.484}_{-0.400}$	$1.987^{+0.031}_{-0.032}$	0.453	0.112	0.320	3
110928180	PL	$-1.521^{+0.425}_{-0.497}$	-	$2.228^{+0.383}_{-0.329}$	$1.979^{+0.031}_{-0.031}$	0.668	0.271	0.323	1
111003465	PL	$-0.224^{+0.333}_{-0.388}$	-	$3.206^{+0.658}_{-0.554}$	$1.988^{+0.033}_{-0.033}$	0.958	0.225	0.306	2
111009282	PL	$-1.239^{+0.538}_{-0.671}$	-	$3.242^{+0.737}_{-0.603}$	$1.989^{+0.033}_{-0.032}$	0.725	0.569	0.365	1
111010709	PL	$-1.451^{+0.691}_{-0.885}$	-	$2.714^{+0.864}_{-0.675}$	$1.990^{+0.032}_{-0.032}$	0.523	0.645	0.461	3
111012456	PL	$-0.008^{+0.282}_{-0.331}$	-	$2.422^{+0.540}_{-0.446}$	$1.996^{+0.033}_{-0.032}$	0.292	0.554	0.500	3
111012811	PL	$1.770^{+0.182}_{-0.167}$	-	$2.283^{+0.442}_{-0.392}$	$1.993^{+0.033}_{-0.032}$	0.992	0.369	0.425	1
111015427	BPL	$2.204^{+0.286}_{-0.230}$	$-1.014^{+0.186}_{-0.230}$	$2.410^{+0.477}_{-0.397}$	$1.987^{+0.032}_{-0.032}$	0.961	0.964	0.979	13
111017657	PL	$-0.989^{+0.507}_{-0.578}$	-	$3.809^{+0.796}_{-0.687}$	$1.988^{+0.032}_{-0.032}$	0.778	0.198	0.260	1
111024722	PL	$0.465^{+0.075}_{-0.076}$	-	$1.558^{+0.172}_{-0.159}$	$1.982^{+0.032}_{-0.032}$	0.791	0.108	0.287	5
111107076	PL	$-0.964^{+0.388}_{-0.445}$	-	$2.058^{+0.449}_{-0.390}$	$1.994^{+0.032}_{-0.031}$	0.470	0.671	0.313	2

Table 2.5 (cont'd)

GRB	Model	$\log N$	$\log f_{\rm b}$ (Hz)	α	B	$p(T_R)$[a]	$p_{\rm AD}$[b]	$p_{\rm KS}$[c]	$N_{\rm peak}$
111127810	PL	$-0.182^{+0.325}_{-0.387}$	-	$2.795^{+0.646}_{-0.534}$	$1.987^{+0.032}_{-0.033}$	0.202	0.009	0.014	2
111216389	BPL	$2.489^{+0.283}_{-0.230}$	$-0.796^{+0.198}_{-0.242}$	$2.018^{+0.252}_{-0.230}$	$1.982^{+0.032}_{-0.032}$	0.068	0.235	0.318	25
111221739	BPL	$2.121^{+0.436}_{-0.300}$	$-0.348^{+0.279}_{-0.406}$	$1.909^{+0.461}_{-0.392}$	$1.994^{+0.033}_{-0.032}$	0.446	0.101	0.093	2
111228657	BPL	$2.582^{+0.284}_{-0.234}$	$-0.724^{+0.148}_{-0.182}$	$2.989^{+0.546}_{-0.467}$	$1.990^{+0.033}_{-0.033}$	0.384	0.659	0.739	5
120119170	PL	$0.291^{+0.103}_{-0.108}$	-	$1.802^{+0.176}_{-0.161}$	$1.988^{+0.032}_{-0.033}$	0.146	0.204	0.138	7
120119229	PL	$0.150^{+0.142}_{-0.161}$	-	$1.402^{+0.272}_{-0.239}$	$1.991^{+0.033}_{-0.032}$	0.611	0.919	0.992	1
120129580	BPL	$4.237^{+0.289}_{-0.240}$	$-0.475^{+0.100}_{-0.113}$	$3.874^{+0.413}_{-0.368}$	$2.005^{+0.033}_{-0.033}$	0.075	0.017	0.001	2
120130699	PL	$0.311^{+0.167}_{-0.202}$	-	$1.533^{+0.292}_{-0.249}$	$1.991^{+0.033}_{-0.033}$	0.486	0.870	0.896	2
120204054	PL	$-0.356^{+0.147}_{-0.159}$	-	$2.693^{+0.226}_{-0.207}$	$1.982^{+0.032}_{-0.032}$	0.308	0.160	0.283	4
120206949	PL	$1.282^{+0.142}_{-0.137}$	-	$2.423^{+0.414}_{-0.365}$	$1.993^{+0.033}_{-0.033}$	0.810	0.711	0.438	2
120213606	PL	$0.693^{+0.146}_{-0.153}$	-	$1.708^{+0.375}_{-0.322}$	$1.991^{+0.033}_{-0.033}$	0.443	0.236	0.435	4
120217904	PL	$2.293^{+0.230}_{-0.208}$	-	$2.170^{+0.436}_{-0.401}$	$1.993^{+0.032}_{-0.033}$	0.931	0.244	0.294	1
120223933	PL	$-1.018^{+0.478}_{-0.577}$	-	$2.677^{+0.684}_{-0.580}$	$1.994^{+0.033}_{-0.033}$	0.873	0.750	0.759	1
120226447	PL	$0.689^{+0.154}_{-0.157}$	-	$1.359^{+0.309}_{-0.275}$	$1.992^{+0.034}_{-0.033}$	0.963	0.524	0.672	2
120226871	PL	$0.304^{+0.075}_{-0.078}$	-	$1.744^{+0.136}_{-0.126}$	$1.983^{+0.033}_{-0.032}$	0.432	0.197	0.334	10
120227725	PL	$0.701^{+0.109}_{-0.117}$	-	$1.800^{+0.265}_{-0.230}$	$1.992^{+0.033}_{-0.033}$	0.894	0.979	0.940	5
120304248	PL	$1.532^{+0.215}_{-0.200}$	-	$1.458^{+0.432}_{-0.402}$	$1.994^{+0.033}_{-0.033}$	0.649	0.995	0.915	3
120308588	PL	$0.481^{+0.172}_{-0.192}$	-	$2.268^{+0.414}_{-0.365}$	$1.993^{+0.033}_{-0.033}$	0.281	0.308	0.307	1
120316008	BPL	$2.007^{+0.389}_{-0.285}$	$-0.386^{+0.262}_{-0.349}$	$2.310^{+0.681}_{-0.552}$	$1.992^{+0.032}_{-0.033}$	0.081	0.393	0.303	12
120402669	PL	$-0.327^{+0.420}_{-0.499}$	-	$2.905^{+0.848}_{-0.710}$	$1.991^{+0.034}_{-0.033}$	0.931	0.608	0.527	1
120412920	PL	$-0.500^{+0.238}_{-0.264}$	-	$2.076^{+0.346}_{-0.307}$	$1.993^{+0.033}_{-0.033}$	0.454	0.283	0.147	2
120420858	PL	$-2.068^{+0.836}_{-1.035}$	-	$2.296^{+0.768}_{-0.636}$	$1.999^{+0.031}_{-0.032}$	0.256	0.656	0.664	1
120426090	PL	$1.872^{+0.152}_{-0.147}$	-	$2.743^{+0.401}_{-0.357}$	$1.995^{+0.032}_{-0.034}$	0.199	0.825	0.977	2
120427054	PL	$-0.307^{+0.406}_{-0.465}$	-	$3.370^{+0.708}_{-0.606}$	$1.996^{+0.033}_{-0.033}$	0.438	0.705	0.513	1
120429484	PL	$-0.990^{+0.527}_{-0.665}$	-	$2.036^{+0.703}_{-0.579}$	$1.995^{+0.032}_{-0.032}$	0.193	0.533	0.749	1
120522361	PL	$0.363^{+0.173}_{-0.192}$	-	$2.158^{+0.427}_{-0.368}$	$1.989^{+0.033}_{-0.033}$	0.961	0.664	0.871	4
120526303	PL	$0.204^{+0.128}_{-0.141}$	-	$1.323^{+0.172}_{-0.152}$	$1.996^{+0.033}_{-0.031}$	0.389	0.900	0.914	7
120624933	PL	$0.807^{+0.103}_{-0.108}$	-	$1.987^{+0.236}_{-0.216}$	$1.992^{+0.032}_{-0.033}$	0.643	0.737	0.638	2
120625119	PL	$1.098^{+0.187}_{-0.195}$	-	$2.479^{+0.604}_{-0.501}$	$1.993^{+0.033}_{-0.033}$	0.159	0.764	0.595	2
120703417	PL	$-1.255^{+0.446}_{-0.511}$	-	$2.758^{+0.560}_{-0.486}$	$1.994^{+0.032}_{-0.032}$	0.187	0.871	0.843	5
120703726	PL	$0.981^{+0.108}_{-0.112}$	-	$2.167^{+0.282}_{-0.253}$	$1.996^{+0.033}_{-0.032}$	0.982	0.358	0.293	2
120707800	PL	$0.207^{+0.143}_{-0.155}$	-	$2.176^{+0.257}_{-0.236}$	$1.991^{+0.033}_{-0.032}$	0.893	0.944	0.989	4
120711115	PL	$0.892^{+0.045}_{-0.046}$	-	$1.322^{+0.074}_{-0.071}$	$1.992^{+0.033}_{-0.033}$	0.730	0.484	0.570	14
120716712	PL	$0.133^{+0.068}_{-0.073}$	-	$1.327^{+0.108}_{-0.098}$	$1.983^{+0.032}_{-0.032}$	0.792	0.079	0.070	2
120719146	PL	$-0.393^{+0.216}_{-0.246}$	-	$1.933^{+0.311}_{-0.271}$	$1.989^{+0.032}_{-0.032}$	0.240	0.831	0.936	4
120728434	BPL	$4.015^{+0.406}_{-0.302}$	$-1.427^{+0.159}_{-0.201}$	$2.699^{+0.213}_{-0.197}$	$1.993^{+0.032}_{-0.031}$	0.842	0.424	0.143	19
120806007	PL	$0.011^{+0.234}_{-0.264}$	-	$2.188^{+0.494}_{-0.414}$	$1.991^{+0.033}_{-0.032}$	0.304	0.838	0.662	3
120830212	PL	$0.704^{+0.144}_{-0.152}$	-	$1.572^{+0.289}_{-0.252}$	$1.992^{+0.033}_{-0.033}$	0.407	0.654	0.796	1
120830702	PL	$0.165^{+0.159}_{-0.186}$	-	$1.340^{+0.322}_{-0.288}$	$1.993^{+0.033}_{-0.032}$	0.619	0.958	0.625	3
120909070	PL	$-0.968^{+0.341}_{-0.405}$	-	$1.810^{+0.362}_{-0.314}$	$1.994^{+0.031}_{-0.031}$	0.460	0.446	0.500	4
120913997	PL	$-1.307^{+0.433}_{-0.529}$	-	$2.359^{+0.478}_{-0.406}$	$1.992^{+0.032}_{-0.032}$	0.395	0.705	0.792	2
120919052	PL	$0.578^{+0.056}_{-0.059}$	-	$1.546^{+0.119}_{-0.110}$	$1.980^{+0.032}_{-0.032}$	0.195	0.130	0.182	10
120919309	PL	$0.674^{+0.135}_{-0.148}$	-	$2.338^{+0.268}_{-0.235}$	$1.990^{+0.032}_{-0.032}$	0.880	0.348	0.321	2
120921877	PL	$1.068^{+0.175}_{-0.175}$	-	$2.236^{+0.502}_{-0.439}$	$1.993^{+0.033}_{-0.033}$	0.767	0.837	0.706	1
120926335	PL	$1.549^{+0.275}_{-0.244}$	-	$2.202^{+0.677}_{-0.584}$	$1.993^{+0.034}_{-0.032}$	0.715	0.735	0.429	2
120926426	PL	$0.025^{+0.162}_{-0.184}$	-	$1.490^{+0.279}_{-0.247}$	$1.996^{+0.033}_{-0.032}$	0.275	0.498	0.267	5
121005340	PL	$-0.627^{+0.244}_{-0.285}$	-	$1.412^{+0.279}_{-0.244}$	$1.997^{+0.032}_{-0.032}$	0.114	0.658	0.674	4
121029350	PL	$1.386^{+0.116}_{-0.107}$	-	$1.915^{+0.268}_{-0.246}$	$1.991^{+0.033}_{-0.033}$	0.220	0.624	0.636	4
121031949	PL	$-1.192^{+0.360}_{-0.424}$	-	$1.915^{+0.345}_{-0.294}$	$1.986^{+0.031}_{-0.031}$	0.247	0.631	0.862	3
121113544	PL	$0.001^{+0.120}_{-0.133}$	-	$1.846^{+0.197}_{-0.180}$	$1.986^{+0.032}_{-0.032}$	0.191	0.112	0.296	9
121117018	PL	$-1.260^{+0.482}_{-0.607}$	-	$1.983^{+0.541}_{-0.444}$	$1.994^{+0.032}_{-0.033}$	0.213	0.167	0.176	2
121119579	PL	$0.608^{+0.204}_{-0.221}$	-	$1.735^{+0.575}_{-0.477}$	$1.993^{+0.033}_{-0.034}$	0.719	0.290	0.414	1
121122870	PL	$-0.628^{+0.243}_{-0.292}$	-	$1.850^{+0.301}_{-0.261}$	$1.990^{+0.032}_{-0.032}$	0.219	0.866	0.554	3
121122885	PL	$0.230^{+0.306}_{-0.342}$	-	$2.931^{+0.667}_{-0.542}$	$1.993^{+0.033}_{-0.034}$	0.440	0.236	0.262	2
121123442	PL	$-0.552^{+0.369}_{-0.453}$	-	$2.148^{+0.533}_{-0.431}$	$1.996^{+0.032}_{-0.032}$	0.831	0.617	0.806	2
121125356	PL	$-0.095^{+0.205}_{-0.245}$	-	$1.679^{+0.356}_{-0.297}$	$1.993^{+0.032}_{-0.032}$	0.909	0.486	0.623	4
130104721	PL	$0.364^{+0.110}_{-0.121}$	-	$1.494^{+0.212}_{-0.189}$	$1.992^{+0.033}_{-0.033}$	0.736	0.958	0.857	5
130106829	PL	$-0.160^{+0.171}_{-0.198}$	-	$1.527^{+0.305}_{-0.260}$	$1.988^{+0.032}_{-0.032}$	0.678	0.437	0.653	3
130106995	PL	$-1.079^{+0.457}_{-0.586}$	-	$2.357^{+0.586}_{-0.450}$	$1.988^{+0.032}_{-0.032}$	0.803	0.453	0.439	3
130112286	PL	$0.221^{+0.155}_{-0.170}$	-	$1.627^{+0.315}_{-0.267}$	$1.989^{+0.032}_{-0.033}$	0.623	0.478	0.511	3
130121835	PL	$-0.125^{+0.117}_{-0.126}$	-	$1.843^{+0.157}_{-0.147}$	$1.990^{+0.032}_{-0.031}$	0.241	0.850	0.726	7

Table 2.5 (cont'd)

GRB	Model	$\log N$	$\log f_{\rm b}$ (Hz)	α	B	$p(T_R)$[a]	$p_{\rm AD}$[b]	$p_{\rm KS}$[c]	$N_{\rm peak}$
130131511	PL	$0.069^{+0.089}_{-0.095}$	-	$1.721^{+0.145}_{-0.138}$	$1.986^{+0.032}_{-0.032}$	0.958	0.206	0.122	17
130206482	PL	$0.318^{+0.092}_{-0.098}$	-	$1.744^{+0.156}_{-0.145}$	$1.984^{+0.033}_{-0.033}$	0.921	0.315	0.290	2
130215649	PL	$-1.332^{+0.550}_{-0.696}$	-	$2.424^{+0.594}_{-0.479}$	$1.997^{+0.032}_{-0.032}$	0.887	0.433	0.420	3
130216790	PL	$0.737^{+0.160}_{-0.175}$	-	$2.223^{+0.520}_{-0.435}$	$1.993^{+0.033}_{-0.032}$	0.151	0.206	0.404	2
130216927	PL	$1.190^{+0.153}_{-0.146}$	-	$1.237^{+0.267}_{-0.241}$	$1.994^{+0.033}_{-0.033}$	0.323	0.964	0.975	2
130218261	PL	$-0.225^{+0.245}_{-0.295}$	-	$1.823^{+0.426}_{-0.361}$	$1.991^{+0.032}_{-0.032}$	0.190	0.509	0.288	4
130219775	PL	$0.153^{+0.119}_{-0.126}$	-	$2.070^{+0.209}_{-0.191}$	$1.995^{+0.032}_{-0.032}$	0.671	0.893	0.960	2
130220964	PL	$1.071^{+0.195}_{-0.204}$	-	$2.988^{+0.679}_{-0.573}$	$1.993^{+0.033}_{-0.033}$	0.386	0.820	0.898	2
130224370	PL	$-0.889^{+0.448}_{-0.593}$	-	$1.916^{+0.544}_{-0.439}$	$1.994^{+0.032}_{-0.032}$	0.241	0.428	0.226	1
130228111	PL	$-0.812^{+0.343}_{-0.428}$	-	$1.826^{+0.423}_{-0.354}$	$1.990^{+0.033}_{-0.033}$	0.841	0.229	0.242	4
130304410	PL	$0.316^{+0.107}_{-0.120}$	-	$1.264^{+0.162}_{-0.144}$	$1.999^{+0.033}_{-0.033}$	0.218	0.535	0.687	1
130305486	PL	$0.114^{+0.182}_{-0.201}$	-	$2.573^{+0.316}_{-0.279}$	$1.990^{+0.033}_{-0.032}$	0.359	0.254	0.290	2
130306991	PL	$-1.353^{+0.500}_{-0.601}$	-	$2.256^{+0.495}_{-0.420}$	$1.999^{+0.031}_{-0.031}$	0.471	0.774	0.880	3
130318456	PL	$-1.162^{+0.454}_{-0.600}$	-	$1.656^{+0.482}_{-0.393}$	$1.991^{+0.031}_{-0.032}$	0.617	0.849	0.834	2
130325203	PL	$0.680^{+0.205}_{-0.222}$	-	$2.564^{+0.514}_{-0.443}$	$1.992^{+0.032}_{-0.033}$	0.217	0.579	0.526	1
130327350	PL	$0.946^{+0.075}_{-0.075}$	-	$1.860^{+0.169}_{-0.158}$	$1.990^{+0.033}_{-0.033}$	0.334	0.404	0.345	8
130331566	PL	$-0.030^{+0.323}_{-0.393}$	-	$2.956^{+0.804}_{-0.673}$	$1.991^{+0.033}_{-0.033}$	0.658	0.416	0.621	1
130406288	PL	$1.037^{+0.189}_{-0.199}$	-	$2.027^{+0.438}_{-0.374}$	$1.993^{+0.032}_{-0.033}$	0.129	0.579	0.517	2
130409960	PL	$-0.421^{+0.398}_{-0.481}$	-	$2.615^{+0.661}_{-0.551}$	$1.993^{+0.033}_{-0.032}$	0.992	0.482	0.615	2
130418844	PL	$-1.764^{+0.656}_{-0.914}$	-	$2.020^{+0.641}_{-0.484}$	$1.990^{+0.031}_{-0.031}$	0.963	0.864	0.803	2
130420422	PL	$-0.330^{+0.394}_{-0.542}$	-	$1.972^{+0.693}_{-0.519}$	$1.994^{+0.033}_{-0.032}$	0.504	0.985	0.987	1
130425327	PL	$0.380^{+0.091}_{-0.099}$	-	$1.562^{+0.185}_{-0.174}$	$1.986^{+0.033}_{-0.033}$	0.499	0.171	0.226	8
130427324	PL	$2.314^{+0.024}_{-0.023}$	-	$2.164^{+0.032}_{-0.031}$	$1.552^{+0.023}_{-0.024}$	0.992	0.000	0.000	19
130502327	BPL	$3.425^{+0.160}_{-0.144}$	$-0.332^{+0.100}_{-0.111}$	$2.676^{+0.207}_{-0.193}$	$1.989^{+0.034}_{-0.033}$	0.000	0.036	0.032	25
130504978	BPL	$3.532^{+0.238}_{-0.202}$	$-0.860^{+0.115}_{-0.130}$	$2.678^{+0.193}_{-0.176}$	$1.993^{+0.032}_{-0.032}$	0.953	0.894	0.837	11
130517781	PL	$-0.342^{+0.263}_{-0.298}$	-	$2.232^{+0.456}_{-0.388}$	$1.991^{+0.033}_{-0.033}$	0.512	0.597	0.734	4
130518551	PL	$1.786^{+0.282}_{-0.248}$	-	$1.780^{+0.546}_{-0.482}$	$1.993^{+0.034}_{-0.033}$	0.716	0.947	0.597	1
130518580	PL	$0.226^{+0.104}_{-0.111}$	-	$2.439^{+0.174}_{-0.161}$	$1.981^{+0.032}_{-0.032}$	1.000	0.198	0.389	4
130523095	BPL	$2.317^{+0.456}_{-0.326}$	$-1.362^{+0.275}_{-0.364}$	$2.026^{+0.381}_{-0.311}$	$1.977^{+0.032}_{-0.031}$	0.855	0.028	0.012	3
130528695	PL	$-0.188^{+0.199}_{-0.223}$	-	$1.966^{+0.303}_{-0.267}$	$1.990^{+0.033}_{-0.033}$	0.634	0.715	0.736	4
130604033	PL	$0.927^{+0.082}_{-0.083}$	-	$1.739^{+0.205}_{-0.191}$	$1.991^{+0.032}_{-0.032}$	0.570	0.943	0.852	7
130606316	PL	$-0.736^{+0.569}_{-0.720}$	-	$2.613^{+0.846}_{-0.667}$	$1.993^{+0.033}_{-0.032}$	0.883	0.447	0.604	2
130606497	PL	$0.974^{+0.037}_{-0.038}$	-	$1.939^{+0.072}_{-0.070}$	$1.977^{+0.032}_{-0.033}$	0.442	0.111	0.098	11
130609902	PL	$-0.326^{+0.149}_{-0.159}$	-	$2.125^{+0.196}_{-0.178}$	$2.006^{+0.030}_{-0.030}$	0.331	0.201	0.220	4
130612456	PL	$0.761^{+0.270}_{-0.345}$	-	$2.734^{+0.703}_{-0.534}$	$1.996^{+0.033}_{-0.033}$	0.832	0.035	0.009	1
130614997	PL	$0.348^{+0.107}_{-0.115}$	-	$1.969^{+0.200}_{-0.180}$	$1.993^{+0.032}_{-0.032}$	0.135	0.766	0.873	2
130623790	PL	$-0.340^{+0.107}_{-0.118}$	-	$1.400^{+0.139}_{-0.124}$	$1.986^{+0.031}_{-0.031}$	0.119	0.602	0.551	3
130626596	PL	$0.217^{+0.108}_{-0.117}$	-	$1.342^{+0.194}_{-0.179}$	$1.990^{+0.033}_{-0.032}$	0.607	0.491	0.596	3
130628531	PL	$0.675^{+0.110}_{-0.115}$	-	$1.817^{+0.229}_{-0.203}$	$1.990^{+0.033}_{-0.033}$	0.743	0.305	0.168	4
130630272	PL	$0.679^{+0.136}_{-0.140}$	-	$1.499^{+0.309}_{-0.270}$	$1.991^{+0.033}_{-0.033}$	0.842	0.773	0.888	2
130702004	PL	$-1.652^{+0.512}_{-0.596}$	-	$2.257^{+0.481}_{-0.417}$	$1.993^{+0.031}_{-0.031}$	0.291	0.785	0.553	1
130704560	PL	$2.061^{+0.138}_{-0.133}$	-	$2.295^{+0.302}_{-0.278}$	$1.992^{+0.033}_{-0.033}$	0.842	0.910	0.879	6
130707505	PL	$-0.256^{+0.132}_{-0.150}$	-	$1.343^{+0.179}_{-0.157}$	$1.984^{+0.032}_{-0.031}$	0.473	0.470	0.483	6
130715906	PL	$-0.496^{+0.287}_{-0.335}$	-	$2.078^{+0.399}_{-0.338}$	$1.987^{+0.033}_{-0.033}$	0.950	0.403	0.749	4
130725527	PL	$1.366^{+0.200}_{-0.193}$	-	$2.726^{+0.751}_{-0.613}$	$1.993^{+0.033}_{-0.032}$	0.517	0.885	0.723	2
130727698	PL	$0.437^{+0.204}_{-0.223}$	-	$2.130^{+0.597}_{-0.486}$	$1.992^{+0.033}_{-0.033}$	0.914	0.611	0.651	4
130815420	PL	$-0.290^{+0.134}_{-0.153}$	-	$1.642^{+0.157}_{-0.141}$	$2.002^{+0.032}_{-0.032}$	0.455	0.515	0.788	11
130818941	PL	$0.341^{+0.088}_{-0.091}$	-	$1.450^{+0.170}_{-0.155}$	$1.985^{+0.033}_{-0.032}$	0.101	0.081	0.279	4
130821674	PL	$0.611^{+0.037}_{-0.038}$	-	$1.614^{+0.069}_{-0.068}$	$1.967^{+0.032}_{-0.032}$	0.984	0.052	0.048	9
130928537	PL	$-1.070^{+0.414}_{-0.495}$	-	$1.895^{+0.436}_{-0.366}$	$1.997^{+0.032}_{-0.031}$	0.914	0.216	0.209	1
131014215	BPL	$5.004^{+0.391}_{-0.296}$	$-0.760^{+0.163}_{-0.202}$	$2.543^{+0.166}_{-0.153}$	$1.992^{+0.033}_{-0.032}$	0.998	0.305	0.196	5
131021352	PL	$0.694^{+0.186}_{-0.182}$	-	$1.219^{+0.394}_{-0.348}$	$1.993^{+0.033}_{-0.033}$	0.427	0.554	0.470	2
131028076	PL	$0.763^{+0.117}_{-0.119}$	-	$2.550^{+0.268}_{-0.249}$	$1.991^{+0.033}_{-0.033}$	0.756	0.771	0.642	2
131029973	PL	$-0.582^{+0.256}_{-0.307}$	-	$1.781^{+0.299}_{-0.253}$	$1.989^{+0.032}_{-0.031}$	0.353	0.590	0.539	3
131030791	PL	$-0.906^{+0.383}_{-0.447}$	-	$2.125^{+0.463}_{-0.404}$	$2.001^{+0.032}_{-0.032}$	0.102	0.275	0.338	1
131031482	PL	$1.264^{+0.171}_{-0.157}$	-	$2.017^{+0.435}_{-0.370}$	$1.992^{+0.033}_{-0.034}$	0.790	0.932	0.937	3
131108024	PL	$-0.398^{+0.133}_{-0.148}$	-	$1.356^{+0.161}_{-0.146}$	$1.985^{+0.031}_{-0.030}$	0.876	0.560	0.675	3
131108862	PL	$1.760^{+0.080}_{-0.078}$	-	$1.486^{+0.152}_{-0.148}$	$1.992^{+0.033}_{-0.033}$	0.215	0.479	0.451	15
131113483	PL	$-1.496^{+0.529}_{-0.656}$	-	$2.692^{+0.592}_{-0.489}$	$1.992^{+0.032}_{-0.031}$	0.148	0.065	0.031	2
131122490	PL	$0.669^{+0.101}_{-0.105}$	-	$2.079^{+0.267}_{-0.243}$	$1.989^{+0.032}_{-0.033}$	0.964	0.650	0.633	5
131127592	BPL	$3.481^{+0.324}_{-0.261}$	$-0.632^{+0.148}_{-0.177}$	$2.831^{+0.294}_{-0.265}$	$1.991^{+0.033}_{-0.034}$	0.984	0.594	0.439	7

Table 2.5 (cont'd)

GRB	Model	$\log N$	$\log f_{\rm b}$ (Hz)	α	B	$p(T_R)$[a]	$p_{\rm AD}$[b]	$p_{\rm KS}$[c]	$N_{\rm peak}$
131209547	PL	$0.069^{+0.144}_{-0.162}$	-	$1.992^{+0.258}_{-0.234}$	$1.991^{+0.033}_{-0.032}$	0.025	0.788	0.696	2
131214705	PL	$-0.836^{+0.258}_{-0.282}$	-	$2.874^{+0.306}_{-0.277}$	$2.001^{+0.032}_{-0.032}$	0.057	0.635	0.412	3
131215298	PL	$0.596^{+0.117}_{-0.124}$	-	$1.577^{+0.273}_{-0.241}$	$1.992^{+0.032}_{-0.033}$	0.933	0.446	0.450	6
131216081	PL	$0.172^{+0.245}_{-0.294}$	-	$2.352^{+0.507}_{-0.425}$	$1.996^{+0.032}_{-0.032}$	0.467	0.707	0.853	1
131217183	PL	$0.787^{+0.125}_{-0.123}$	-	$1.356^{+0.259}_{-0.230}$	$1.993^{+0.033}_{-0.033}$	0.063	0.381	0.272	4
131229277	PL	$1.859^{+0.100}_{-0.094}$	-	$1.577^{+0.187}_{-0.173}$	$1.993^{+0.033}_{-0.032}$	0.831	0.762	0.837	11

[a] $p(T_R)$ is the significance associated to statistic T_R.

[b] $p_{\rm AD}$ is the significance of the Anderson–Darling test.

[c] $p_{\rm KS}$ is the significance of the Kolmogorov–Smirnov test.

Table 2.6. Best–fitting model and parameters for each GRB of the *Fermi* sample in the 200–1000 keV energy band.

GRB	Model	$\log N$	$\log f_{\rm b}$ (Hz)	α	B	$p(T_R)$[a]	$p_{\rm AD}$[b]	$p_{\rm KS}$[c]	$N_{\rm peak}$
080723557	BPL	$2.476^{+0.376}_{-0.283}$	$-1.005^{+0.248}_{-0.313}$	$1.771^{+0.203}_{-0.183}$	$1.982^{+0.033}_{-0.032}$	0.987	0.395	0.285	10
080723985	PL	$-0.218^{+0.222}_{-0.275}$	-	$1.620^{+0.348}_{-0.298}$	$1.991^{+0.033}_{-0.032}$	0.951	0.872	0.890	4
080807993	PL	$0.348^{+0.097}_{-0.101}$	-	$0.721^{+0.171}_{-0.163}$	$1.993^{+0.034}_{-0.033}$	0.575	0.987	0.973	2
080817161	PL	$-0.527^{+0.233}_{-0.273}$	-	$1.940^{+0.314}_{-0.270}$	$1.983^{+0.031}_{-0.031}$	0.624	0.110	0.134	3
080825593	PL	$0.377^{+0.142}_{-0.154}$	-	$1.509^{+0.287}_{-0.252}$	$1.993^{+0.033}_{-0.032}$	0.042	0.798	0.676	4
080916009	PL	$-0.458^{+0.289}_{-0.354}$	-	$1.808^{+0.384}_{-0.311}$	$1.999^{+0.033}_{-0.032}$	0.092	0.857	0.810	3
081129161	PL	$-0.323^{+0.374}_{-0.509}$	-	$1.850^{+0.722}_{-0.550}$	$1.993^{+0.033}_{-0.033}$	0.600	0.589	0.613	2
081215784	BPL	$2.982^{+0.199}_{-0.175}$	$-0.054^{+0.102}_{-0.110}$	$3.681^{+0.518}_{-0.446}$	$1.992^{+0.033}_{-0.033}$	0.969	0.036	0.025	3
081224887	PL	$-0.193^{+0.290}_{-0.336}$	-	$2.662^{+0.523}_{-0.448}$	$1.990^{+0.032}_{-0.033}$	0.832	0.439	0.854	1
090102122	PL	$0.677^{+0.077}_{-0.077}$	-	$1.153^{+0.138}_{-0.127}$	$1.991^{+0.032}_{-0.032}$	0.408	0.674	0.600	5
090217206	PL	$0.054^{+0.212}_{-0.256}$	-	$1.568^{+0.323}_{-0.263}$	$1.993^{+0.033}_{-0.033}$	0.900	0.716	0.534	1
090323002	PL	$-0.660^{+0.279}_{-0.346}$	-	$1.601^{+0.307}_{-0.257}$	$2.003^{+0.032}_{-0.032}$	0.676	0.314	0.175	5
090328401	PL	$0.255^{+0.094}_{-0.102}$	-	$1.402^{+0.173}_{-0.160}$	$1.987^{+0.033}_{-0.033}$	0.937	0.583	0.443	4
090424592	BPL	$2.583^{+0.403}_{-0.298}$	$-0.755^{+0.274}_{-0.351}$	$1.708^{+0.223}_{-0.199}$	$1.990^{+0.033}_{-0.033}$	1.000	0.527	0.528	3
090528516	PL	$-0.766^{+0.327}_{-0.426}$	-	$1.445^{+0.366}_{-0.301}$	$1.995^{+0.032}_{-0.032}$	0.919	0.745	0.683	3
090529564	PL	$0.797^{+0.161}_{-0.164}$	-	$1.422^{+0.399}_{-0.342}$	$1.993^{+0.033}_{-0.033}$	0.948	0.556	0.629	2
090618353	BPL	$3.061^{+0.493}_{-0.349}$	$-1.468^{+0.205}_{-0.270}$	$2.950^{+0.561}_{-0.457}$	$1.981^{+0.031}_{-0.031}$	0.953	0.469	0.569	2
090620400	PL	$-0.333^{+0.373}_{-0.462}$	-	$2.419^{+0.799}_{-0.633}$	$1.990^{+0.032}_{-0.033}$	0.580	0.154	0.133	1
090623107	PL	$-0.282^{+0.192}_{-0.225}$	-	$1.275^{+0.284}_{-0.245}$	$1.988^{+0.033}_{-0.033}$	0.355	0.199	0.175	3
090718762	PL	$-0.634^{+0.492}_{-0.633}$	-	$2.388^{+0.834}_{-0.665}$	$1.992^{+0.033}_{-0.033}$	0.603	0.689	0.677	2
090719063	PL	$-0.219^{+0.386}_{-0.466}$	-	$2.615^{+0.752}_{-0.608}$	$1.996^{+0.032}_{-0.033}$	0.482	0.084	0.038	1
090820027	PL	$-0.100^{+0.192}_{-0.206}$	-	$2.703^{+0.294}_{-0.264}$	$1.985^{+0.032}_{-0.032}$	0.217	0.131	0.144	1
090828099	PL	$-1.306^{+0.506}_{-0.641}$	-	$1.803^{+0.536}_{-0.443}$	$1.988^{+0.031}_{-0.031}$	0.928	0.388	0.270	1
090829672	PL	$0.050^{+0.110}_{-0.120}$	-	$1.287^{+0.148}_{-0.133}$	$1.991^{+0.032}_{-0.032}$	0.085	0.985	0.987	4
090902462	PL	$1.533^{+0.051}_{-0.050}$	-	$1.136^{+0.078}_{-0.077}$	$1.994^{+0.033}_{-0.033}$	0.553	0.270	0.290	16
090926181	PL	$1.099^{+0.068}_{-0.069}$	-	$1.705^{+0.139}_{-0.130}$	$1.991^{+0.033}_{-0.033}$	0.924	0.824	0.696	7
090929190	BPL	$1.413^{+0.190}_{-0.166}$	$-0.301^{+0.157}_{-0.184}$	$2.408^{+0.595}_{-0.497}$	$1.991^{+0.032}_{-0.032}$	0.311	0.727	0.765	2
091020977	PL	$0.058^{+0.169}_{-0.192}$	-	$1.514^{+0.327}_{-0.287}$	$1.988^{+0.033}_{-0.033}$	0.876	0.263	0.210	2
091127976	PL	$0.596^{+0.160}_{-0.165}$	-	$1.455^{+0.392}_{-0.337}$	$1.992^{+0.032}_{-0.032}$	0.340	0.968	0.878	1
100116897	PL	$-1.139^{+0.434}_{-0.522}$	-	$2.437^{+0.490}_{-0.415}$	$1.993^{+0.031}_{-0.031}$	0.360	0.873	0.727	3
100131730	PL	$0.820^{+0.177}_{-0.180}$	-	$1.468^{+0.430}_{-0.368}$	$1.994^{+0.033}_{-0.034}$	0.699	0.743	0.666	1
100322045	PL	$-0.014^{+0.186}_{-0.223}$	-	$1.642^{+0.256}_{-0.215}$	$1.999^{+0.032}_{-0.033}$	0.091	0.553	0.635	5
100324172	PL	$0.490^{+0.096}_{-0.103}$	-	$1.663^{+0.181}_{-0.164}$	$1.992^{+0.033}_{-0.033}$	0.868	0.803	0.736	3
100414097	PL	$0.428^{+0.100}_{-0.105}$	-	$1.400^{+0.152}_{-0.141}$	$1.995^{+0.033}_{-0.032}$	0.199	0.965	0.968	5
100511035	PL	$0.085^{+0.113}_{-0.127}$	-	$1.328^{+0.182}_{-0.167}$	$1.985^{+0.033}_{-0.032}$	0.780	0.463	0.430	3
100528075	PL	$-1.537^{+0.763}_{-0.940}$	-	$2.628^{+0.846}_{-0.691}$	$1.991^{+0.032}_{-0.032}$	0.411	0.641	0.745	1
100701490	PL	$1.479^{+0.080}_{-0.077}$	-	$1.325^{+0.149}_{-0.144}$	$1.993^{+0.033}_{-0.033}$	0.779	0.791	0.780	7
100707032	BPL	$3.324^{+0.375}_{-0.289}$	$-1.052^{+0.151}_{-0.183}$	$2.894^{+0.344}_{-0.297}$	$1.988^{+0.032}_{-0.033}$	0.667	0.789	0.637	1
100719989	BPL	$2.931^{+0.411}_{-0.317}$	$-0.724^{+0.205}_{-0.257}$	$2.757^{+0.503}_{-0.419}$	$1.990^{+0.033}_{-0.032}$	0.383	0.601	0.813	3
100724029	PL	$-0.296^{+0.125}_{-0.136}$	-	$1.753^{+0.151}_{-0.143}$	$1.983^{+0.031}_{-0.031}$	0.922	0.339	0.435	7
100728095	PL	$-0.511^{+0.176}_{-0.210}$	-	$1.433^{+0.185}_{-0.159}$	$1.983^{+0.031}_{-0.032}$	0.746	0.498	0.384	7
100826957	PL	$-0.233^{+0.163}_{-0.181}$	-	$1.798^{+0.190}_{-0.170}$	$1.990^{+0.031}_{-0.032}$	0.468	0.416	0.462	6
100906576	PL	$-0.941^{+0.426}_{-0.574}$	-	$1.474^{+0.457}_{-0.365}$	$1.997^{+0.032}_{-0.033}$	0.912	0.631	0.868	1
100910818	PL	$0.610^{+0.133}_{-0.137}$	-	$1.298^{+0.322}_{-0.287}$	$1.993^{+0.033}_{-0.034}$	0.246	0.959	0.949	3
100918863	PL	$-1.755^{+0.650}_{-0.864}$	-	$2.545^{+0.661}_{-0.511}$	$1.996^{+0.032}_{-0.032}$	0.729	0.756	0.758	3
101023951	PL	$-0.572^{+0.212}_{-0.239}$	-	$1.938^{+0.278}_{-0.253}$	$1.984^{+0.033}_{-0.032}$	0.867	0.194	0.074	2
101123952	PL	$0.583^{+0.053}_{-0.055}$	-	$1.444^{+0.097}_{-0.092}$	$1.984^{+0.032}_{-0.033}$	0.868	0.610	0.470	10
101126198	PL	$-1.673^{+0.796}_{-1.061}$	-	$2.419^{+0.893}_{-0.686}$	$1.992^{+0.032}_{-0.032}$	0.595	0.930	0.970	1
101227536	PL	$0.326^{+0.150}_{-0.171}$	-	$1.273^{+0.300}_{-0.262}$	$1.993^{+0.033}_{-0.032}$	0.312	0.740	0.629	1
101231067	PL	$-0.020^{+0.197}_{-0.247}$	-	$1.256^{+0.309}_{-0.262}$	$1.992^{+0.033}_{-0.033}$	0.763	0.184	0.333	1
110102788	PL	$-0.825^{+0.292}_{-0.369}$	-	$1.634^{+0.329}_{-0.277}$	$1.983^{+0.032}_{-0.032}$	0.577	0.667	0.837	3
110120666	PL	$0.270^{+0.144}_{-0.159}$	-	$1.622^{+0.290}_{-0.257}$	$1.993^{+0.033}_{-0.033}$	0.499	0.857	0.834	1
110402009	PL	$0.325^{+0.114}_{-0.120}$	-	$0.629^{+0.207}_{-0.198}$	$1.993^{+0.033}_{-0.034}$	0.867	0.476	0.342	2
110625881	BPL	$2.265^{+0.172}_{-0.148}$	$-0.561^{+0.101}_{-0.115}$	$3.300^{+0.528}_{-0.463}$	$1.982^{+0.032}_{-0.032}$	0.129	0.269	0.351	6
110709642	BPL	$2.004^{+0.369}_{-0.287}$	$-0.715^{+0.241}_{-0.318}$	$2.471^{+0.823}_{-0.612}$	$1.993^{+0.032}_{-0.032}$	0.143	0.626	0.466	5
110717319	PL	$-0.254^{+0.154}_{-0.174}$	-	$1.565^{+0.206}_{-0.182}$	$1.981^{+0.033}_{-0.032}$	0.052	0.013	0.033	4
110721200	BPL	$2.913^{+0.568}_{-0.399}$	$-0.913^{+0.234}_{-0.324}$	$3.154^{+0.863}_{-0.661}$	$1.992^{+0.032}_{-0.033}$	0.572	0.776	0.681	1
110729142	PL	$-1.412^{+0.460}_{-0.563}$	-	$1.730^{+0.421}_{-0.347}$	$1.984^{+0.031}_{-0.030}$	0.200	0.513	0.467	1
110731465	PL	$0.774^{+0.139}_{-0.147}$	-	$1.167^{+0.273}_{-0.231}$	$1.994^{+0.033}_{-0.033}$	0.765	0.830	0.817	2
110825102	PL	$0.916^{+0.050}_{-0.051}$	-	$1.183^{+0.090}_{-0.088}$	$1.990^{+0.033}_{-0.033}$	0.988	0.917	0.762	5
110919634	PL	$-0.761^{+0.388}_{-0.546}$	-	$1.561^{+0.469}_{-0.354}$	$1.990^{+0.033}_{-0.032}$	0.430	0.632	0.855	2

Table 2.6 (cont'd)

GRB	Model	$\log N$	$\log f_{\rm b}$ (Hz)	α	B	$p(T_R)$[a]	$p_{\rm AD}$[b]	$p_{\rm KS}$[c]	$N_{\rm peak}$
110921912	BPL	$2.459^{+0.378}_{-0.281}$	$-0.926^{+0.214}_{-0.278}$	$2.346^{+0.439}_{-0.371}$	$1.991^{+0.033}_{-0.033}$	0.749	0.481	0.691	3
111003465	PL	$-0.272^{+0.338}_{-0.420}$	-	$2.298^{+0.629}_{-0.512}$	$1.991^{+0.033}_{-0.033}$	0.967	0.461	0.412	1
111216389	PL	$-0.039^{+0.111}_{-0.123}$	-	$1.057^{+0.177}_{-0.159}$	$1.988^{+0.032}_{-0.032}$	0.474	0.280	0.233	7
120102095	PL	$0.069^{+0.263}_{-0.325}$	-	$1.918^{+0.606}_{-0.488}$	$1.993^{+0.032}_{-0.032}$	0.356	0.978	0.938	1
120119170	PL	$-0.857^{+0.421}_{-0.554}$	-	$1.750^{+0.506}_{-0.398}$	$1.994^{+0.032}_{-0.032}$	0.634	0.802	0.866	3
120129580	BPL	$3.052^{+0.247}_{-0.212}$	$-0.351^{+0.109}_{-0.123}$	$3.713^{+0.649}_{-0.529}$	$1.996^{+0.033}_{-0.033}$	0.972	0.153	0.205	2
120204054	PL	$-1.194^{+0.340}_{-0.396}$	-	$2.181^{+0.350}_{-0.298}$	$1.977^{+0.032}_{-0.032}$	0.593	0.080	0.155	1
120206949	PL	$0.694^{+0.173}_{-0.191}$	-	$1.593^{+0.476}_{-0.382}$	$1.994^{+0.033}_{-0.033}$	0.952	0.260	0.175	1
120217904	PL	$1.299^{+0.262}_{-0.237}$	-	$1.736^{+0.646}_{-0.544}$	$1.993^{+0.033}_{-0.033}$	0.495	0.621	0.535	1
120226871	PL	$-0.972^{+0.335}_{-0.430}$	-	$1.695^{+0.335}_{-0.273}$	$1.983^{+0.031}_{-0.031}$	0.628	0.239	0.193	4
120304248	PL	$1.543^{+0.228}_{-0.209}$	-	$1.466^{+0.450}_{-0.428}$	$1.994^{+0.034}_{-0.033}$	0.302	0.998	0.992	3
120316008	PL	$0.348^{+0.136}_{-0.143}$	-	$1.343^{+0.257}_{-0.238}$	$1.988^{+0.032}_{-0.032}$	0.574	0.122	0.081	3
120328268	BPL	$2.855^{+0.658}_{-0.417}$	$-1.332^{+0.250}_{-0.375}$	$2.930^{+0.724}_{-0.587}$	$1.989^{+0.031}_{-0.031}$	0.749	0.684	0.579	2
120426090	PL	$0.955^{+0.207}_{-0.232}$	-	$1.927^{+0.513}_{-0.404}$	$1.994^{+0.033}_{-0.033}$	0.491	0.340	0.241	1
120526303	PL	$-0.119^{+0.194}_{-0.242}$	-	$1.442^{+0.249}_{-0.211}$	$1.996^{+0.032}_{-0.032}$	0.755	0.842	0.808	3
120624933	PL	$0.087^{+0.200}_{-0.238}$	-	$1.973^{+0.425}_{-0.351}$	$1.990^{+0.033}_{-0.033}$	0.943	0.810	0.620	2
120703726	PL	$-0.045^{+0.258}_{-0.314}$	-	$2.038^{+0.531}_{-0.435}$	$1.991^{+0.033}_{-0.032}$	0.974	0.876	0.938	1
120707800	PL	$-0.334^{+0.260}_{-0.333}$	-	$1.617^{+0.353}_{-0.293}$	$1.996^{+0.032}_{-0.033}$	0.830	0.777	0.839	3
120709883	PL	$0.643^{+0.094}_{-0.096}$	-	$1.277^{+0.197}_{-0.181}$	$1.992^{+0.033}_{-0.033}$	0.640	0.505	0.497	3
120711115	PL	$0.496^{+0.068}_{-0.071}$	-	$1.282^{+0.095}_{-0.090}$	$1.998^{+0.033}_{-0.032}$	0.483	0.488	0.179	8
120728434	PL	$-0.848^{+0.231}_{-0.270}$	-	$1.715^{+0.266}_{-0.234}$	$1.978^{+0.030}_{-0.031}$	0.607	0.093	0.036	4
120919052	PL	$-0.430^{+0.189}_{-0.218}$	-	$1.349^{+0.228}_{-0.198}$	$1.983^{+0.032}_{-0.032}$	0.950	0.355	0.431	3
120919309	PL	$-0.404^{+0.342}_{-0.409}$	-	$2.529^{+0.621}_{-0.523}$	$1.988^{+0.033}_{-0.033}$	0.787	0.188	0.335	1
121113544	PL	$-1.282^{+0.560}_{-0.758}$	-	$1.763^{+0.595}_{-0.466}$	$1.997^{+0.032}_{-0.032}$	0.999	0.532	0.691	1
121122885	PL	$0.475^{+0.211}_{-0.239}$	-	$2.172^{+0.535}_{-0.450}$	$1.993^{+0.032}_{-0.032}$	0.497	0.507	0.450	1
121225417	PL	$0.064^{+0.117}_{-0.130}$	-	$1.563^{+0.177}_{-0.158}$	$1.994^{+0.032}_{-0.032}$	0.243	0.971	0.997	5
130121835	PL	$-0.808^{+0.264}_{-0.334}$	-	$1.550^{+0.287}_{-0.242}$	$1.979^{+0.032}_{-0.032}$	0.946	0.273	0.149	2
130131511	PL	$-0.848^{+0.267}_{-0.337}$	-	$1.355^{+0.278}_{-0.230}$	$1.977^{+0.032}_{-0.031}$	0.857	0.063	0.096	4
130219775	PL	$-0.943^{+0.373}_{-0.460}$	-	$1.844^{+0.432}_{-0.356}$	$1.988^{+0.032}_{-0.032}$	0.795	0.252	0.124	1
130304410	PL	$-0.248^{+0.212}_{-0.247}$	-	$1.636^{+0.300}_{-0.256}$	$1.994^{+0.032}_{-0.032}$	0.710	0.881	0.892	2
130305486	PL	$-0.436^{+0.279}_{-0.316}$	-	$2.495^{+0.418}_{-0.369}$	$1.991^{+0.033}_{-0.034}$	0.669	0.881	0.535	1
130306991	PL	$-1.763^{+0.669}_{-0.862}$	-	$2.089^{+0.625}_{-0.503}$	$1.991^{+0.032}_{-0.032}$	0.970	0.215	0.121	1
130327350	PL	$0.127^{+0.154}_{-0.177}$	-	$1.521^{+0.281}_{-0.247}$	$1.992^{+0.032}_{-0.032}$	0.940	0.949	0.915	4
130427324	BPL	$4.552^{+0.193}_{-0.172}$	$-1.156^{+0.095}_{-0.103}$	$2.214^{+0.045}_{-0.043}$	$1.189^{+0.020}_{-0.020}$	0.963	0.000	0.000	13
130502327	BPL	$2.679^{+0.324}_{-0.244}$	$-0.704^{+0.239}_{-0.304}$	$1.730^{+0.203}_{-0.185}$	$1.989^{+0.033}_{-0.033}$	0.314	0.287	0.565	15
130504978	BPL	$2.663^{+0.295}_{-0.239}$	$-0.934^{+0.176}_{-0.213}$	$2.309^{+0.306}_{-0.276}$	$1.992^{+0.032}_{-0.033}$	0.868	0.401	0.534	9
130518551	PL	$1.378^{+0.278}_{-0.249}$	-	$1.342^{+0.541}_{-0.488}$	$1.993^{+0.032}_{-0.032}$	0.516	0.960	0.782	1
130518580	PL	$-0.469^{+0.224}_{-0.258}$	-	$2.365^{+0.294}_{-0.259}$	$1.987^{+0.032}_{-0.032}$	0.813	0.724	0.842	3
130606497	PL	$0.581^{+0.051}_{-0.054}$	-	$1.678^{+0.089}_{-0.085}$	$1.996^{+0.032}_{-0.032}$	0.446	0.392	0.508	8
130609902	PL	$-0.822^{+0.239}_{-0.265}$	-	$1.956^{+0.267}_{-0.240}$	$1.996^{+0.031}_{-0.030}$	0.463	0.704	0.675	2
130704560	PL	$0.317^{+0.262}_{-0.331}$	-	$1.845^{+0.545}_{-0.441}$	$1.992^{+0.033}_{-0.033}$	0.912	0.813	0.805	1
130821674	PL	$-0.439^{+0.151}_{-0.178}$	-	$1.408^{+0.163}_{-0.144}$	$1.995^{+0.032}_{-0.031}$	0.517	0.343	0.419	7
130828306	PL	$-0.857^{+0.280}_{-0.341}$	-	$1.436^{+0.295}_{-0.247}$	$1.980^{+0.033}_{-0.032}$	0.364	0.142	0.243	4
131014215	BPL	$4.002^{+0.280}_{-0.228}$	$-0.535^{+0.135}_{-0.161}$	$2.487^{+0.172}_{-0.168}$	$1.993^{+0.033}_{-0.033}$	0.830	0.432	0.166	5
131028076	PL	$0.619^{+0.135}_{-0.140}$	-	$2.461^{+0.280}_{-0.248}$	$1.991^{+0.032}_{-0.032}$	0.349	0.405	0.572	2
131105087	PL	$-0.852^{+0.326}_{-0.407}$	-	$1.512^{+0.389}_{-0.323}$	$1.987^{+0.032}_{-0.032}$	0.821	0.815	0.897	2
131108862	PL	$1.012^{+0.084}_{-0.082}$	-	$1.161^{+0.158}_{-0.149}$	$1.991^{+0.032}_{-0.033}$	0.512	0.357	0.397	5
131118958	PL	$-0.108^{+0.117}_{-0.134}$	-	$1.217^{+0.175}_{-0.158}$	$1.985^{+0.032}_{-0.033}$	0.392	0.464	0.504	6
131122490	PL	$0.183^{+0.146}_{-0.167}$	-	$1.496^{+0.312}_{-0.273}$	$1.992^{+0.033}_{-0.034}$	0.150	0.608	0.787	4
131209547	PL	$-0.438^{+0.236}_{-0.276}$	-	$1.604^{+0.340}_{-0.298}$	$1.988^{+0.033}_{-0.033}$	0.597	0.305	0.130	2
131214705	PL	$-1.400^{+0.601}_{-0.762}$	-	$2.202^{+0.635}_{-0.517}$	$1.997^{+0.032}_{-0.032}$	0.100	0.668	0.704	1
131216081	PL	$-0.268^{+0.369}_{-0.494}$	-	$1.786^{+0.696}_{-0.532}$	$1.995^{+0.032}_{-0.033}$	0.119	0.617	0.778	1
131229277	PL	$1.293^{+0.104}_{-0.099}$	-	$1.252^{+0.196}_{-0.181}$	$1.994^{+0.033}_{-0.033}$	0.600	0.867	0.627	7
131231198	PL	$-0.030^{+0.133}_{-0.138}$	-	$2.322^{+0.242}_{-0.219}$	$1.981^{+0.032}_{-0.033}$	0.617	0.040	0.014	3

[a] $p(T_R)$ is the significance associated to statistic T_R.

[b] $p_{\rm AD}$ is the significance of the Anderson–Darling test.

[c] $p_{\rm KS}$ is the significance of the Kolmogorov–Smirnov test.

Table 2.7. Best-fitting model and parameters for each GRB of the *BeppoSAX* sample in the total 40–700 keV energy band.

GRB	Model	$\log N$	$\log f_{\rm b}$ (Hz)	α	B	$p(T_R)$[a]	$p_{\rm AD}$[b]	$p_{\rm KS}$[c]	$N_{\rm peak}$
970228	BPL	$2.725^{+0.219}_{-0.186}$	$-0.515^{+0.122}_{-0.140}$	$3.427^{+0.598}_{-0.501}$	$2.031^{+0.031}_{-0.031}$	0.189	0.177	0.261	2
970315A	BPL	$2.881^{+0.184}_{-0.160}$	$0.149^{+0.108}_{-0.121}$	$2.768^{+0.292}_{-0.261}$	$2.074^{+0.037}_{-0.037}$	0.063	0.820	0.800	21
970517B	BPL	$3.186^{+0.489}_{-0.357}$	$0.171^{+0.197}_{-0.255}$	$3.202^{+0.652}_{-0.544}$	$2.080^{+0.039}_{-0.038}$	0.140	0.468	0.215	9
970601	BPL	$3.526^{+0.437}_{-0.325}$	$-0.689^{+0.183}_{-0.231}$	$2.514^{+0.242}_{-0.219}$	$2.081^{+0.035}_{-0.035}$	0.144	0.268	0.338	8
970612B	PL	$0.100^{+0.202}_{-0.226}$	-	$1.994^{+0.419}_{-0.352}$	$2.081^{+0.035}_{-0.035}$	0.743	0.298	0.394	7
970625B	PL	$2.323^{+0.065}_{-0.062}$	-	$1.882^{+0.080}_{-0.077}$	$2.074^{+0.036}_{-0.036}$	0.438	0.047	0.085	30
970627B	BPL	$2.611^{+0.175}_{-0.151}$	$0.278^{+0.089}_{-0.101}$	$3.896^{+0.677}_{-0.572}$	$2.068^{+0.038}_{-0.037}$	0.504	0.982	0.991	20
970706	PL	$-0.587^{+0.272}_{-0.325}$	-	$2.579^{+0.376}_{-0.325}$	$2.074^{+0.030}_{-0.030}$	0.578	0.914	0.928	2
970816	PL	$1.826^{+0.197}_{-0.177}$	-	$2.493^{+0.426}_{-0.362}$	$2.068^{+0.039}_{-0.039}$	0.794	0.020	0.018	3
971027A	PL	$1.218^{+0.137}_{-0.132}$	-	$2.186^{+0.350}_{-0.305}$	$2.068^{+0.038}_{-0.037}$	0.021	0.802	0.827	2
971214B	PL	$0.530^{+0.120}_{-0.126}$	-	$1.572^{+0.208}_{-0.187}$	$2.052^{+0.036}_{-0.035}$	0.501	0.027	0.020	6
971223C	PL	$0.941^{+0.069}_{-0.068}$	-	$1.548^{+0.135}_{-0.127}$	$2.074^{+0.034}_{-0.034}$	0.354	0.926	0.891	8
980203B	BPL	$3.880^{+0.181}_{-0.161}$	$-0.255^{+0.086}_{-0.092}$	$2.871^{+0.150}_{-0.143}$	$2.045^{+0.035}_{-0.034}$	0.001	0.037	0.096	30
980306C	PL	$0.789^{+0.155}_{-0.162}$	-	$3.350^{+0.385}_{-0.346}$	$2.068^{+0.036}_{-0.036}$	0.010	0.261	0.228	2
980329A	PL	$1.226^{+0.078}_{-0.078}$	-	$2.100^{+0.160}_{-0.146}$	$2.045^{+0.034}_{-0.034}$	0.839	0.175	0.287	10
980428	PL	$0.292^{+0.103}_{-0.110}$	-	$1.958^{+0.183}_{-0.166}$	$2.068^{+0.030}_{-0.029}$	0.666	0.109	0.101	5
980615B	PL	$0.722^{+0.064}_{-0.065}$	-	$2.002^{+0.145}_{-0.132}$	$2.045^{+0.029}_{-0.029}$	0.586	0.399	0.320	8
980827C	PL	$1.765^{+0.049}_{-0.047}$	-	$2.031^{+0.081}_{-0.079}$	$2.045^{+0.031}_{-0.031}$	0.167	0.158	0.130	15
981111	PL	$0.747^{+0.082}_{-0.085}$	-	$1.576^{+0.122}_{-0.111}$	$2.045^{+0.034}_{-0.034}$	0.570	0.706	0.512	9
990128	PL	$1.480^{+0.161}_{-0.159}$	-	$3.279^{+0.496}_{-0.455}$	$2.045^{+0.038}_{-0.037}$	0.614	0.399	0.230	3
990620	PL	$1.529^{+0.125}_{-0.119}$	-	$2.247^{+0.308}_{-0.280}$	$2.068^{+0.037}_{-0.036}$	0.986	0.424	0.265	8
990705	BPL	$3.192^{+0.249}_{-0.203}$	$-0.360^{+0.138}_{-0.157}$	$2.495^{+0.228}_{-0.207}$	$2.067^{+0.035}_{-0.036}$	0.162	0.896	0.926	46
990913A	BPL	$3.838^{+0.283}_{-0.228}$	$-0.505^{+0.138}_{-0.160}$	$2.251^{+0.110}_{-0.105}$	$2.023^{+0.036}_{-0.037}$	0.998	0.042	0.044	11
991124B	PL	$-0.237^{+0.335}_{-0.392}$	-	$2.351^{+0.651}_{-0.547}$	$2.068^{+0.035}_{-0.036}$	0.896	0.358	0.333	1
991216B	BPL	$4.034^{+0.211}_{-0.186}$	$-0.102^{+0.097}_{-0.107}$	$3.052^{+0.192}_{-0.177}$	$2.045^{+0.037}_{-0.036}$	0.192	0.028	0.039	14
000115	BPL	$3.396^{+0.156}_{-0.141}$	$0.143^{+0.075}_{-0.082}$	$3.347^{+0.255}_{-0.230}$	$2.066^{+0.037}_{-0.036}$	0.617	0.520	0.422	15
000214A	PL	$2.291^{+0.164}_{-0.154}$	-	$2.125^{+0.257}_{-0.236}$	$2.045^{+0.037}_{-0.038}$	0.202	0.679	0.755	9
000218B	BPL	$3.761^{+0.320}_{-0.265}$	$-0.340^{+0.149}_{-0.179}$	$2.287^{+0.126}_{-0.121}$	$2.087^{+0.036}_{-0.037}$	0.864	0.083	0.164	11
000419	PL	$-0.042^{+0.392}_{-0.464}$	-	$2.815^{+0.745}_{-0.593}$	$2.087^{+0.036}_{-0.036}$	0.569	0.870	0.870	1
000718B	PL	$0.777^{+0.067}_{-0.069}$	-	$2.309^{+0.157}_{-0.146}$	$2.066^{+0.029}_{-0.029}$	0.630	0.728	0.842	7
001004	BPL	$3.826^{+0.483}_{-0.358}$	$-0.220^{+0.187}_{-0.236}$	$2.940^{+0.347}_{-0.310}$	$2.069^{+0.039}_{-0.038}$	0.774	0.710	0.596	8
001011C	PL	$1.104^{+0.090}_{-0.089}$	-	$1.831^{+0.176}_{-0.160}$	$2.069^{+0.035}_{-0.036}$	0.988	0.489	0.362	11
010109	BPL	$4.274^{+0.335}_{-0.272}$	$-0.349^{+0.132}_{-0.160}$	$2.681^{+0.147}_{-0.134}$	$2.057^{+0.037}_{-0.037}$	0.797	0.160	0.090	10
010317	BPL	$3.730^{+0.241}_{-0.208}$	$-0.277^{+0.102}_{-0.117}$	$3.436^{+0.314}_{-0.291}$	$2.097^{+0.034}_{-0.035}$	0.126	0.013	0.006	3
010408B	BPL	$3.964^{+0.685}_{-0.458}$	$-0.122^{+0.261}_{-0.352}$	$3.526^{+0.809}_{-0.629}$	$2.059^{+0.039}_{-0.039}$	0.962	0.131	0.105	3
010412	BPL	$2.979^{+0.254}_{-0.213}$	$-0.573^{+0.149}_{-0.173}$	$2.435^{+0.249}_{-0.220}$	$2.040^{+0.033}_{-0.032}$	0.745	0.134	0.109	28
010504	PL	$1.872^{+0.102}_{-0.100}$	-	$1.694^{+0.131}_{-0.123}$	$2.040^{+0.038}_{-0.037}$	0.604	0.204	0.410	16
010710B	PL	$1.963^{+0.088}_{-0.083}$	-	$1.866^{+0.125}_{-0.118}$	$2.040^{+0.037}_{-0.036}$	0.156	0.178	0.199	17
010922	BPL	$2.969^{+0.412}_{-0.310}$	$-0.678^{+0.174}_{-0.223}$	$3.495^{+0.786}_{-0.659}$	$2.059^{+0.034}_{-0.034}$	0.827	0.695	0.646	7
011003	PL	$0.668^{+0.096}_{-0.102}$	-	$1.959^{+0.208}_{-0.186}$	$2.040^{+0.033}_{-0.034}$	0.761	0.326	0.107	4

[a] $p(T_R)$ is the significance associated to statistic T_R.

[b] $p_{\rm AD}$ is the significance of the Anderson–Darling test.

[c] $p_{\rm KS}$ is the significance of the Kolmogorov–Smirnov test.

Table 2.8. Best-fitting model and parameters for each GRB of the *BeppoSAX* sample in the total 40–700 keV energy band. PDS are derived from a 100–s time interval.

GRB	Model	$\log N$	$\log f_{\rm b}$ (Hz)	α	B	$p(T_R)$[a]	$p_{\rm AD}$[b]	$p_{\rm KS}$[c]	$N_{\rm peak}$
970111	BPL	$4.337^{+0.504}_{-0.383}$	$-1.287^{+0.164}_{-0.203}$	$3.880^{+0.547}_{-0.474}$	$2.058^{+0.029}_{-0.029}$	0.353	0.605	0.352	2
970117B	BPL	$3.863^{+0.319}_{-0.262}$	$-0.989^{+0.113}_{-0.130}$	$4.635^{+0.731}_{-0.645}$	$2.119^{+0.029}_{-0.029}$	0.638	0.156	0.174	2
970228	BPL	$2.691^{+0.212}_{-0.182}$	$-0.602^{+0.123}_{-0.138}$	$2.989^{+0.433}_{-0.368}$	$2.021^{+0.026}_{-0.026}$	0.676	0.174	0.131	2
970315A	BPL	$2.874^{+0.141}_{-0.128}$	$-0.266^{+0.106}_{-0.114}$	$2.088^{+0.129}_{-0.118}$	$2.049^{+0.034}_{-0.034}$	0.052	0.416	0.261	21
970517B	BPL	$3.063^{+0.132}_{-0.120}$	$-0.265^{+0.080}_{-0.086}$	$2.479^{+0.134}_{-0.129}$	$2.079^{+0.032}_{-0.032}$	0.630	0.656	0.487	9
970601	BPL	$3.218^{+0.235}_{-0.199}$	$-0.725^{+0.122}_{-0.139}$	$2.482^{+0.186}_{-0.174}$	$2.103^{+0.030}_{-0.030}$	0.178	0.372	0.434	8
970612B	PL	$-0.101^{+0.157}_{-0.165}$	-	$1.749^{+0.236}_{-0.217}$	$2.103^{+0.030}_{-0.030}$	0.977	0.482	0.293	7
970625B	PL	$2.140^{+0.045}_{-0.044}$	-	$1.797^{+0.059}_{-0.057}$	$2.049^{+0.034}_{-0.034}$	0.613	0.010	0.030	30
970627B	BPL	$2.467^{+0.114}_{-0.102}$	$-0.029^{+0.083}_{-0.092}$	$2.762^{+0.257}_{-0.241}$	$2.055^{+0.031}_{-0.031}$	0.000	0.397	0.522	20
970706	PL	$-0.597^{+0.267}_{-0.315}$	-	$2.518^{+0.363}_{-0.305}$	$2.049^{+0.029}_{-0.029}$	0.911	0.816	0.929	2
970816	BPL	$3.528^{+0.483}_{-0.339}$	$-1.167^{+0.212}_{-0.283}$	$2.175^{+0.175}_{-0.160}$	$2.052^{+0.030}_{-0.030}$	0.899	0.491	0.566	3
971027A	PL	$0.636^{+0.071}_{-0.073}$	-	$1.945^{+0.151}_{-0.138}$	$2.052^{+0.029}_{-0.029}$	0.722	0.799	0.876	2
971214B	PL	$0.237^{+0.096}_{-0.106}$	-	$1.405^{+0.135}_{-0.128}$	$2.014^{+0.027}_{-0.027}$	0.578	0.531	0.676	6
971223C	PL	$0.751^{+0.057}_{-0.056}$	-	$1.453^{+0.108}_{-0.098}$	$2.049^{+0.031}_{-0.031}$	0.254	0.357	0.259	8
980203B	BPL	$3.974^{+0.147}_{-0.134}$	$-0.396^{+0.075}_{-0.080}$	$2.696^{+0.105}_{-0.100}$	$2.033^{+0.032}_{-0.032}$	0.001	0.023	0.015	30
980306C	BPL	$3.914^{+0.323}_{-0.263}$	$-1.007^{+0.115}_{-0.133}$	$3.484^{+0.313}_{-0.287}$	$2.078^{+0.029}_{-0.029}$	0.162	0.803	0.703	2
980329A	PL	$1.003^{+0.055}_{-0.054}$	-	$1.987^{+0.101}_{-0.096}$	$2.033^{+0.030}_{-0.029}$	0.096	0.641	0.306	10
980428	PL	$0.274^{+0.100}_{-0.106}$	-	$1.949^{+0.171}_{-0.161}$	$2.078^{+0.029}_{-0.029}$	0.526	0.740	0.800	5
980615B	PL	$0.715^{+0.063}_{-0.064}$	-	$1.997^{+0.138}_{-0.130}$	$2.033^{+0.029}_{-0.029}$	0.466	0.282	0.282	8
980827C	PL	$1.730^{+0.044}_{-0.043}$	-	$2.012^{+0.077}_{-0.073}$	$2.033^{+0.030}_{-0.030}$	0.462	0.277	0.306	15
981111	PL	$0.538^{+0.081}_{-0.083}$	-	$1.594^{+0.104}_{-0.093}$	$2.033^{+0.031}_{-0.030}$	0.947	0.421	0.525	9
990128	BPL	$4.144^{+0.331}_{-0.271}$	$-1.015^{+0.132}_{-0.152}$	$3.117^{+0.252}_{-0.237}$	$2.097^{+0.029}_{-0.030}$	0.346	0.013	0.003	3
990620	BPL	$2.744^{+0.249}_{-0.206}$	$-0.738^{+0.135}_{-0.161}$	$2.628^{+0.346}_{-0.309}$	$2.100^{+0.029}_{-0.029}$	0.477	0.250	0.360	8
990705	BPL	$3.857^{+0.318}_{-0.254}$	$-0.919^{+0.167}_{-0.200}$	$2.110^{+0.114}_{-0.109}$	$2.060^{+0.031}_{-0.031}$	0.637	0.932	0.768	46
990913A	BPL	$3.702^{+0.207}_{-0.182}$	$-0.660^{+0.115}_{-0.131}$	$2.076^{+0.080}_{-0.078}$	$2.019^{+0.033}_{-0.033}$	0.776	0.246	0.508	11
991124B	PL	$-0.351^{+0.205}_{-0.229}$	-	$1.846^{+0.269}_{-0.244}$	$2.100^{+0.029}_{-0.028}$	0.734	0.948	0.850	1
991216B	BPL	$4.158^{+0.133}_{-0.122}$	$-0.306^{+0.067}_{-0.071}$	$2.759^{+0.092}_{-0.088}$	$1.998^{+0.032}_{-0.032}$	0.107	0.011	0.051	14
000115	BPL	$3.106^{+0.087}_{-0.080}$	$0.057^{+0.048}_{-0.051}$	$3.069^{+0.140}_{-0.134}$	$2.050^{+0.031}_{-0.031}$	0.442	0.367	0.317	15
000214A	BPL	$3.600^{+0.373}_{-0.283}$	$-1.034^{+0.200}_{-0.251}$	$1.903^{+0.110}_{-0.103}$	$2.070^{+0.032}_{-0.032}$	0.665	0.815	0.743	9
000218B	BPL	$3.209^{+0.126}_{-0.114}$	$-0.263^{+0.066}_{-0.072}$	$2.441^{+0.100}_{-0.097}$	$2.122^{+0.032}_{-0.032}$	0.047	0.000	0.000	11
000630	PL	$1.017^{+0.050}_{-0.050}$	-	$1.687^{+0.109}_{-0.104}$	$2.118^{+0.030}_{-0.031}$	0.497	0.433	0.387	19
000718B	PL	$0.773^{+0.066}_{-0.068}$	-	$2.295^{+0.154}_{-0.145}$	$2.050^{+0.029}_{-0.030}$	0.637	0.637	0.807	7
001011C	PL	$0.793^{+0.059}_{-0.061}$	-	$1.719^{+0.100}_{-0.095}$	$2.050^{+0.030}_{-0.030}$	0.075	0.304	0.437	11
010109	BPL	$3.932^{+0.130}_{-0.119}$	$-0.334^{+0.062}_{-0.066}$	$2.749^{+0.096}_{-0.092}$	$2.094^{+0.032}_{-0.033}$	0.939	0.272	0.535	10
010317	BPL	$3.290^{+0.125}_{-0.115}$	$-0.280^{+0.063}_{-0.068}$	$3.418^{+0.216}_{-0.207}$	$2.087^{+0.030}_{-0.029}$	0.419	0.237	0.069	3
010408B	BPL	$3.738^{+0.201}_{-0.178}$	$-0.631^{+0.100}_{-0.109}$	$2.383^{+0.095}_{-0.091}$	$2.034^{+0.031}_{-0.031}$	0.307	0.096	0.047	3
010412	BPL	$3.203^{+0.269}_{-0.223}$	$-0.805^{+0.157}_{-0.179}$	$2.214^{+0.179}_{-0.158}$	$2.031^{+0.030}_{-0.030}$	0.485	0.120	0.124	28
010504	PL	$1.381^{+0.044}_{-0.044}$	-	$1.490^{+0.066}_{-0.064}$	$2.031^{+0.033}_{-0.033}$	0.555	0.300	0.366	16
010922	BPL	$2.904^{+0.317}_{-0.247}$	$-0.857^{+0.166}_{-0.208}$	$2.929^{+0.507}_{-0.436}$	$2.041^{+0.030}_{-0.029}$	0.155	0.436	0.514	7
011003	PL	$0.453^{+0.084}_{-0.090}$	-	$1.862^{+0.149}_{-0.139}$	$2.041^{+0.029}_{-0.029}$	0.974	0.180	0.176	4

[a] $p(T_R)$ is the significance associated to statistic T_R.

[b] $p_{\rm AD}$ is the significance of the Anderson–Darling test.

[c] $p_{\rm KS}$ is the significance of the Kolmogorov–Smirnov test.

Chapter 3

A search for pulsations in short GRBs to constrain their progenitors

3.1 Introduction

Several lines of evidence suggest that short duration gamma–ray bursts (hereafter, SGRBs; durations $T_{90} \leq 2$–3 s), or at least a sizeable fraction of them, have a cosmological origin and are the electromagnetic counterpart to the coalescence of compact binary systems, such as double neutron stars (NS) or neutron star and black hole (BH; e.g., see Nakar 2007; Berger 2011 for reviews; see also Fong & Berger 2013; Tanvir et al. 2013). During the merging, an accretion disc is thought to be produced by the tidal disruption of a NS around a more compact NS or before a NS is swallowed by a BH. Either way, eventually the system evolves towards the formation of a BH with a debris torus around it. The resulting neutrino–cooled accretion flow leads the hyper-accreting BH to develop a collimated outflow into a pair of anti–parallel jets (e.g., see Lee & Ramirez–Ruiz 2007).

A potential means to distinguish between NS–NS and NS–BH mergers concerns the signature of the disc and jet precession in the electromagnetic signal, i.e. the SGRB itself. In the case of a NS–BH merger, precession is expected for a tilted disc and jet due to Lense–Thirring torques from the BH spin (Stone et al. 2013 and references therein). These authors (hereafter, SLB13) assumed thick discs precessing as solid body rotators and built upon numerical relativity simulations of this kind of mixed mergers. According to their results, for a reasonable set of values in the parameter space, i.e. BH spin and mass, disc viscosity, misalignment angle between the accretion disc and the BH equatorial plane, a quasiperiodic modulation in the γ–ray signal is

to be expected for a sizeable fraction of NS–BH mergers. The predicted precession period $T_{\rm p}$ of the jet increases with time proportionally to $t^{4/3}$ due to viscous spreading of the disc and, for a given mixed compact system, starts from a few tens ms at the beginning of the SGRB, and ends with about one order of magnitude longer values. The average expected number of precession cycles is just a few, typically $N_{\rm cycles} \leq 10$. In all scenarios they considered, these two observables lie in the range $4.5 \leq \langle N_{\rm cycles} \rangle \leq 7.5$ and 30 ms$\leq \langle T_{\rm p}(t_{1/2}) \rangle \leq 100$ ms, where $T_{\rm p}(t_{1/2})$ is the half–way precession period for a given merger.

The aim of this work is to search for this kind of quasiperiodic signal in the data of the brightest SGRBs detected with the *Fermi* Gamma–ray Burst Monitor (GBM), the *Swift* Burst Alert Telescope (BAT), and the *Compton Gamma Ray Observatory* Burst And Transient Source Experiment (BATSE; Paciesas et al. 1999), exploiting the exquisite time resolution available with these instruments. This search offers the only direct way to observationally distinguish between the two classes of progenitors based on their electromagnetic emission and naturally complements the forthcoming gravitational wave studies.

3.2 Theoretical Model

The model proposed in SLB13 considers a thick disc precessing as a solid body rotator due to general relativistic Lense-Thirring torques (also known as frame–dragging effect). This effect essentially arises from an initial misalignment between the accretion disc and the BH equatorial plane. A thick disc is involved with a short sound-crossing time scale which will propagate warps in a wavelike manner, redistributing torques throughout. The rigid body precession regime (which is actually the most relevant scenario for compact object mergers) is imposed assuming $H/r > \alpha$, where H is the disc height and α the dimensionless viscosity parameter at a radius r. In the Newtonian limit, a solid body rotator will precess with a period

$$T_{\rm prec} = 2\pi \sin\psi_{\rm d} (J/\mathcal{N}) \tag{3.1}$$

where $\psi_{\rm d}$ is the misalignment angle between the accretion disc and the BH equatorial plane, J is the total angular momentum of the disc, and $\mathcal{N}$ is the Lense-Thirring torque integrated over the entire disc. Specifically, if the disc possesses a surface density profile $\Sigma(r)$ that is nonzero between an inner radius $R_{\rm i}$ and an outer radius $R_{\rm o}$, and the disc elements possess orbital frequency $\Omega(r)$ ($\Omega_{\rm r} = \sqrt{GM_{\rm BH}/r^3}$ for the classical Keplerian

case), then

$$J = 2\pi \int_{R_{\rm i}}^{R_{\rm o}} \Sigma(r)\Omega(r) r^3 {\rm d}r, \tag{3.2}$$

and

$$\mathcal{N} = 4\pi \frac{G^2 M_{\rm BH}^2 a_{\rm BH}}{c^3} \sin\psi_{\rm d} \int_{R_{\rm i}}^{R_{\rm o}} \frac{1}{r^3} \Sigma(r)\Omega(r) r^3 {\rm d}r, \tag{3.3}$$

where the BH's mass and dimensionless spin are $M_{\rm BH}$ and $a_{\rm BH}$, respectively. Considering the radiatively inefficient accretion flow stage, we can write the surface density as

$$\Sigma(r,t) = \frac{M_{\rm dis}(1-n/2)}{\pi R_{\rm dis}^2 x^{n+1/4}\tau} \exp\left(\frac{-(1+x^{2-n})}{\tau}\right) \times I_{1/|4-2n|}\left(\frac{2x^{1-n/2}}{\tau}\right). \tag{3.4}$$

Here $M_{\rm dis}$ is the initial disc mass, $R_{\rm dis}$ is the initial radius of the spreading mass ring (i.e. the radius where the NS is disrupted), I_m is a modified Bessel function of order m, $x = r/R_{\rm dis}$, $\tau = t(12\nu_0(1-n/2)^2/R_{\rm dis}^2)$, and they have assumed viscosity of the form $\nu = \nu_0 x^n$. They calibrate ν_0 with the initial relation $t_{\rm visc,0} = R_{\rm dis}^2/\nu$ and the equation

$$t_{\rm visc,0} \approx 0.11 \alpha_{-1}^{-1} M_8^{-1/2} R_{\rm dis,5}^{3/2} \times \left(\frac{H_0}{0.3 R_{\rm dis}}\right)^{-2} \ {\rm s}, \tag{3.5}$$

where α is the dimensionless Shakura-Sunyaev viscosity coefficient and H_0 is the characteristic disc height. The other normalized parameters are $\alpha_{-1} = \alpha/0.1$, $M_8 = M_{\rm BH}/8M_\odot$, and $R_{\rm dis,5} = R_{\rm dis}/10^5$ m. The resulting precession period evolves as $T_{\rm prec} \propto t^{4/3}$ where the time dependency is mainly due to $R_{\rm dis}(t)$ and $M_{\rm dis}(t)$. The Figure 1 in SLB13 (reported below as Figure 3.1) shows this kind of behaviour.

In their simulations SLB13 assumed $H_0 = 0.3R_{\rm dis}$ and n=1/2. Therefore α remains the only free parameter. To observe this kind of disc precession in GRB, they had to take into account how the jet is linked to the accretion disc. Indeed, this is the only way to identify the semi-periodicity introduced in the signal by the precession motion. For the two leading jets launching mechanism candidates in SGRBs - $\nu\bar{\nu}$ pair annihilation (Mészáros & Rees 1992; Ruffert & Janka 1999), and the Blandford-Znajek (BZ) mechanism (Blandford & Znajek 1977; Lee et al. 2000) - there are theoretical reasons to believe that the jet will align with angular momentum vector of the disc.

If jets align with the disc angular momentum axis, then they will precess around the total angular momentum vector by an angle $\approx \psi_{\rm d}$, because $J_{\rm BH}$ is significantly larger than $J_{\rm disc}$. In this case, observations of SGRBs associated with BH-NSs will often be marked by a clear "lighthouse effect," as long as $\psi_{\rm d} \geq \theta_{\rm jet}$. This seems plausible, as observations of jet breaks in SGRBs suggest typical opening angles of $\sim 10^\circ$ (Fong et

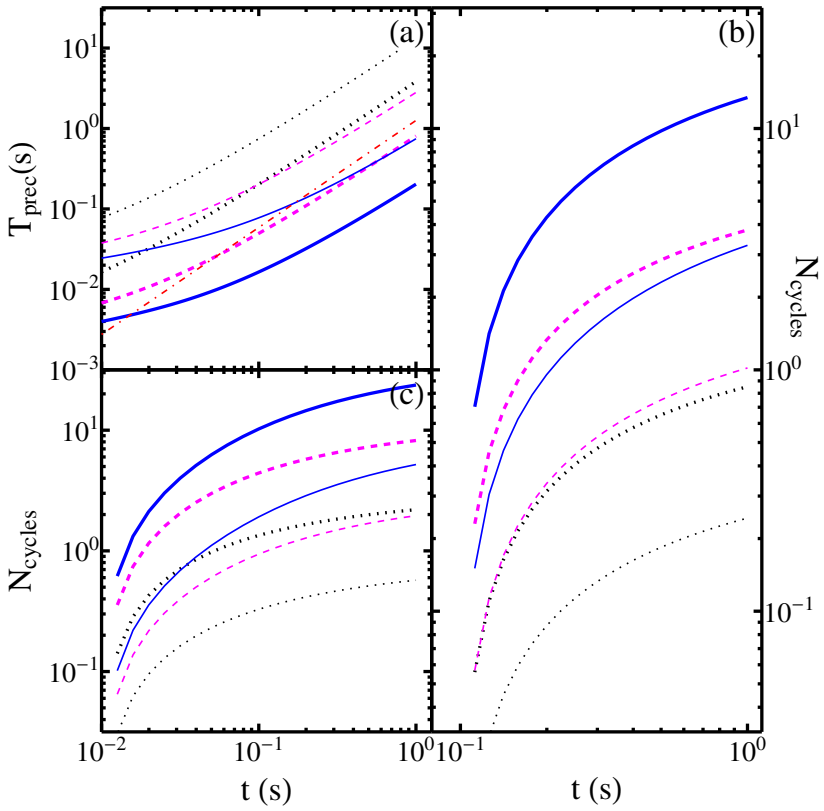

Figure 3.1 This picture was taken from Stone et al. 2013.(a) Time evolution of $T_{\rm prec}$ assuming a viscously spreading disc structure given by Eq 3.4. Black dotted curves represent $\alpha = 0.1$, dashed magenta curves $\alpha = 0.03$, and solid blue curves $\alpha = 0.01$. Thick curves are for nearly equatorial disruptions with $a_{\rm BH} = 0.9$, while thin curves are for $a_{\rm BH} = 0.9$ and initial spin-orbit misalignment of 70°, or equivalently a nearly aligned disruption with $a \approx 0.5$. The dash-dotted red line is $\propto t^{4/3}$, the rough time evolution of $T_{\rm prec}$. (b) and (c) show $N_{\rm cycles}$, the accumulated number of cycles for 0.1 s $< t <$ 1 s and 0.01 s $< t <$ 1 s, respectively.

al. 2014; Soderberg et al. 2006). If $\psi_{\rm d} \leq \theta_{\rm jet}$, then jet precession would, typically, be encoded more subtly as a variation in the portion of the jet.

Generally NS-NS mergers are unlikely to produce significantly misaligned discs ($\psi_{\rm d} \leq 1°$), also when the pre–merger spin–orbit would be highly misaligned. This makes the modulated signal almost impossible to be detected. On the other hand, in BH-NS mergers the BH may possess a larger natal reservoir of spin angular momentum, allowing for greater misalignment between the post–merger BH and the disc formed from NS debris ($\psi_{\rm d} \leq 30°$). Because of this simple reason they considered this configuration in the simulations. For different distributions of BH mass, NS mass, BH spin and initial spin-orbit misalignment in BH-NS binaries, they estimate the following set of values:

- The fraction of all BH-NS mergers which produces an accretion disc and jet ($f_{\rm GRB}$)
- The post–merger misalignment angles between the accretion discs and the BH equatorial planes ($\psi_{\rm d}$)
- The number of precession cycles, assuming 1 sec as the total duration of the event. ($N_{\rm cycles}$)
- The precession period values computed when half of the precession cycles occurred ($T_{\rm prec}(t_{1/2})$).

As a result of these simulations they found that the fraction of mergers which generate SGRB swings from 0.01 to 0.35. The mean value of $\psi_{\rm d}$ ranges from 9° to 32°. But the most important results for the following analysis are the predictions for the average number of precession cycles and the average precession periods. They found $4.5 \leq \langle N_{\rm cycles} \rangle \leq 7.5$ and 30 ms $\leq \langle T_{\rm prec}(t_{1/2}) \rangle \leq 100$ ms assuming a viscosity $\alpha = 0.03$ ("the fiducial case").

3.3 Data selection

3.3.1 Sample selection

We took all the events observed by the *Fermi*/GBM from July 2008 to December 2012. For each GRB I extracted and summed the 1–ms light curves of the two most illuminated NaI detectors in the 8–1000 keV energy band with the HEASOFT package (v6.12) following the *Fermi* team threads.[1] Light curves affected by spikes due to the

[1] http://fermi.gsfc.nasa.gov/ssc/data/analysis/scitools/gbm_grb_analysis.html

interactions of high–energy particles with the spacecraft were rejected (Meegan et al. 2009). We derived the T_{90} and $T_{5\sigma}$ time intervals, where the boundaries of the latter correspond to the first and the last bin whose counts exceed the 5σ signal threshold above background.

We selected the SGRBs by requiring $T_{90} < 3$ s [2] , and ended up with 160 GRBs, 18 out of which having a minimum signal–to–noise (S/N) ratio of 20, as computed over the $T_{5\sigma}$ interval. As far as the T_{90} distribution is concerned, our selected sample of S/N$>$ 20 SGRBs is representative of the full sample of SGRBs, as suggested by a Kolmogorov–Smirnov test.

The same selection criteria were applied to the *Swift*/BAT sample using all the events detected up to early June 2013. I found 30 GRBs with $T_{90} < 3$ s, 12 out of which passed the final S/N$>$ 20 threshold. The mask–weighted light curves had previously been extracted from the event files following the BAT team threads and concern the 15–150 keV detector passband. In addition to the 1–ms light curves, for the two brightest events of the sample, namely 051221A and 120323A, I used 0.1 ms resolution, to explore the very high–frequency behaviour.

From an initial sample of 61 BATSE SGRBs with high S/N I excluded all the cases for which the time–tagged event (TTE) data did not cover the entire profile. Unfortunately, several bright bursts were excluded, because the on board memory could record only up to $32,768$ events around the trigger time. Consequently, I were left with 14 SGRBs whose profiles were extracted in the 20–2000 keV energy range.

Summing up, our final sample includes 44 (18 *Fermi*, 12 *Swift*, and 14 *CGRO*) SGRBs with high S/N ($>$ 20). A finer subdivision of the final sample is provided in the following section, aimed at establishing how genuinely short each selected burst is.

3.3.2 Short vs. intermediate GRBs

Evidence for the existence of a third group of GRBs with intermediate durations and hardness ratios between short and long ones was found by several authors for different data sets (e.g., Horváth 1998; Mukherjee et al. 1998; Horváth et al. 2008; Huja et al. 2009; Řípa et al. 2009; Horváth 2009; but see also Koen & Bere 2012). In this context, I adopted the classification procedures obtained by Horváth et al. (2006) for *CGRO*/BATSE and by Horváth et al. (2010) for *Swift*/BAT to assess the nature of

[2]The usual boundary value of $T_{90} = 2$ s, which was inherited from the BATSE catalog, must not be taken too strictly, the two populations of short and long being partially overlapped. Moreover, this value strongly depends on the detector passband and triggering criteria, as proven by *Swift*/BAT, which detected several SGRBs with $T_{90} > 2$ s (e.g. Barthelmy et al. 2005).

our selected sample of bursts, based on the combination of hardness ratio (HR) and T_{90}. I assigned each GRB a probability p of belonging to the short group through the "indicator function", out of the three classes: short, intermediate, and long. As expected, all GRBs had negligible probability of belonging to the long group. We defined as "truly SGRB" (T–SGRB) the GRBs with $p > 0.9$. The GRBs with $0.8 < p < 0.9$ are defined as "likely SGRB" (L–SGRB), whereas the remaining cases ($p < 0.8$) were conservatively classified as "possibly intermediate" (P–IGRB). Actually, several members of the P–IGRB group are more likely to be genuine short than intermediate bursts. However, our choice was aimed at assuring the least possible contamination with ambiguous cases.

Figure 3.2 shows the HR–T_{90} diagram for the three different data sets: each panel compares the properties of our selected GRBs with those of the corresponding catalog: Sakamoto et al. (2011) for *Swift*/BAT, Paciesas et al. (2012) and Goldstein et al. (2012) for *Fermi*/GBM, and Paciesas et al. (1999) for *CGRO*/BATSE. The HR values for the *Swift*/BAT sample were calculated as the fluence ratio in the bands (50–100 keV)/(25–50 keV) as in Sakamoto et al. (2011), while (300–100 keV)/(50–100 keV) was adopted for the *Fermi*/GBM, and *CGRO*/BATSE sets. To compute the membership probability for the GRBs detected with the *Fermi*/GBM, I used the same parameters used for *CGRO*/BATSE owing to the similar energy passbands. Although in principle this may lead to some misclassified *Fermi*/GBM GRBs, in practice the two *Fermi* T–SGRBs appear to be robustly so (big filled circles in the mid panel of Fig. 3.2).

3.4 Data analysis procedure

We studied the power density spectrum (PDS) of each light curve in two different ways. PDS were calculated adopting the Leahy normalization (Leahy et al. 1983). To fit the PDS I used the technique set up by V10 based on a Bayesian treatment with Markov Chain Monte–Carlo techniques. Two analytical models were assumed to describe the PDS continuum: a simple power–law plus constant (hereafter, PL),

$$S_{\rm PL}(f) = N\, f^{-\alpha} + B\ , \tag{3.6}$$

or a broken power–law plus constant (hereafter, BPL),

$$S_{\rm BPL}(f) = N\left[1 + \left(\frac{f}{f_{\rm b}}\right)^{\alpha}\right]^{-1} + B \qquad , \tag{3.7}$$

whose low–frequency index is fixed to zero. In either model the constant term accounts for the uncorrelated statistical (white) noise. A likelihood ratio test is used to establish

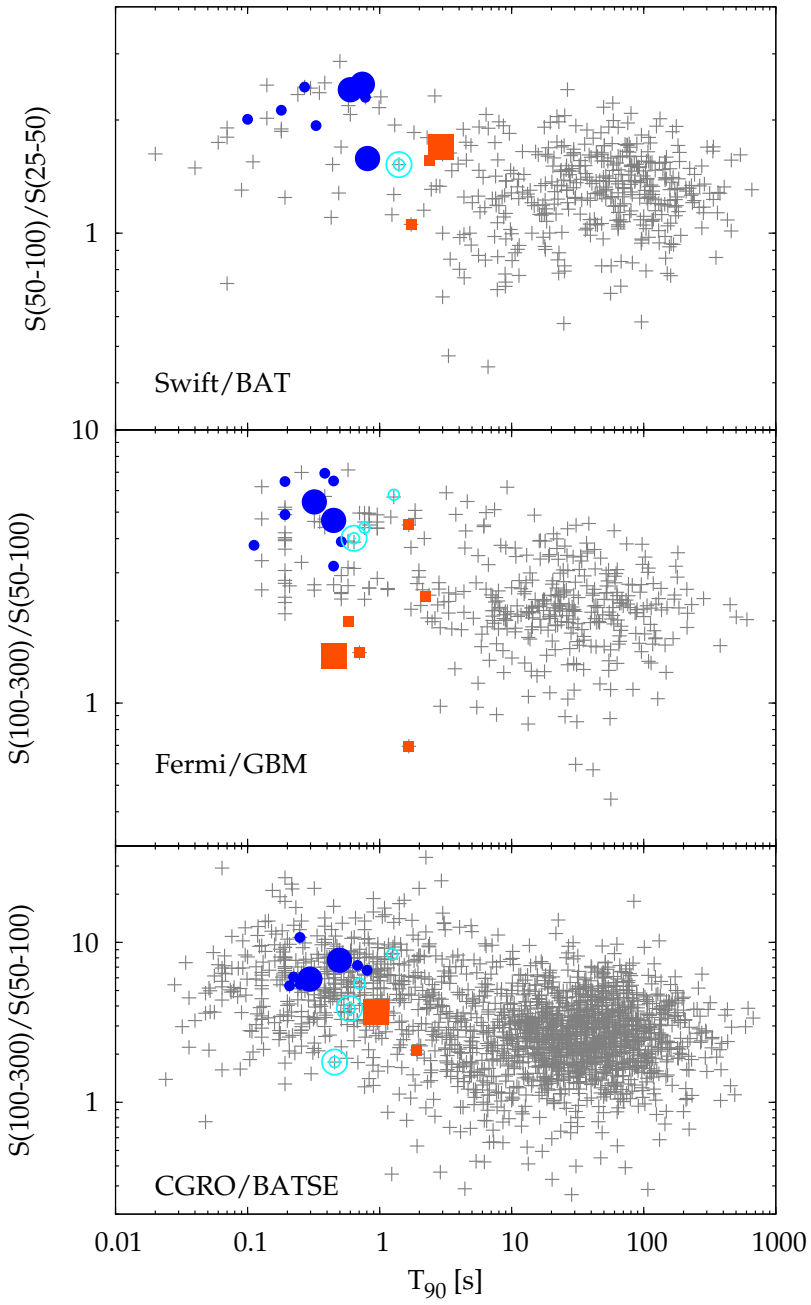

Figure 3.2 HR–T_{90} diagram for the three data sets: *Swift*/BAT (*top*), *Fermi*/GBM (*mid*), *CGRO*/BATSE (*bottom*). Each panel shows other catalog GRBs (crosses) for comparison. Filled circles, empty circles, and squares correspond to T–SGRBs, L–SGRBs, and P–IGRBs, respectively. Big (small) symbol sizes refer to whether each GRB can (cannot) provide useful constraints on the possible presence of pulsations using the stretched PDS technique (Section 3.4).

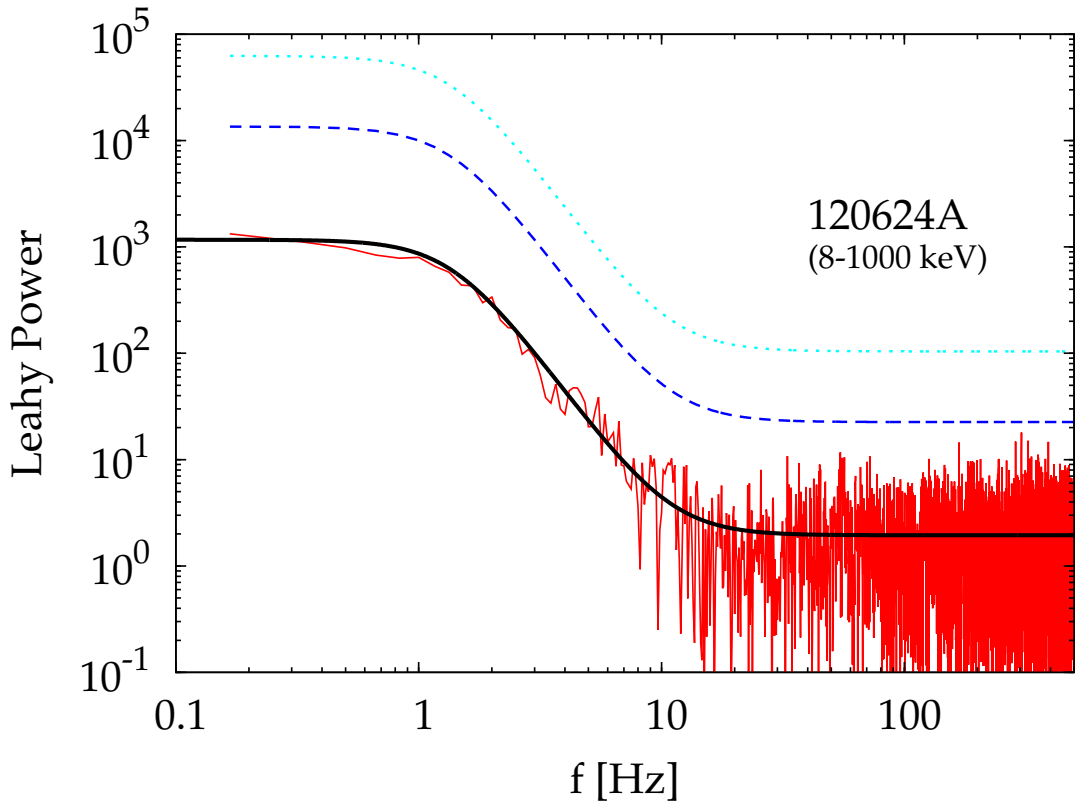

Figure 3.3 The PDS of GRB 120624A fitted using a Bayesian approach. The black solid line represents the best fit model (BPL in this case) while dashed and dotted lines give the probability thresholds at 4.5% and 0.27% to find a statistical fluctuation higher than these levels over the whole PDS, respectively. Confidence levels account for the multi–trial frequencies searched within a given PDS.

the best model for each PDS. This technique is particularly suitable to the temporal signal of SGRBs, because it searches for (quasi)periodic features superposed to a red–noise process and, as such, can confidently estimate both the best fit parameters of the PDS continuum and the significance of possible features superposed to it, taking into account the uncertainties of the model in a self–coherent way. Moreover, the thresholds for possible periodic features correspond to 2 and 3σ (Gaussian) probabilities of a statistical fluctuation and already account for the multi–trial search over the whole range of explored frequencies in each individual PDS. It is worth noting that power approximately fluctuates around the model according to a χ^2 distribution with 2 degrees of freedom, i.e. more wildly than a Gaussian variate. Actually, the true distribution deviates from a pure χ^2 in that the model itself is affected by uncertainties. This is properly taken into account by the procedure in determining the threshold for a given significance (see V10 and references therein for further details).

The first search was performed on the observed light curves with uniform binning of 1 ms as they were observed. Hereafter, times are referred to the detector trigger time. We carried out the same analysis in two different time intervals: i) from -3 to $+3$ s; ii) over the $T_{5\sigma}$ interval. For the BATSE sample the analysis was carried out just over the $T_{5\sigma}$ intervals due to the limited memory of TTE data. The two choices correspond to a fixed temporal range (and, therefore, equal frequency resolution) and to a S/N–driven scheme, respectively. For three GRBs, namely 110705A, 120323A, and 130603B, I chose a time interval of 2 s, spanning from -1 to $+1$ s instead of the $T_{5\sigma}$, to properly model the continuum shape. For 051221A and 120323A I manually selected the time intervals where the analysis was carried out to exploit at the full the 0.1–ms time resolution available in these cases: from -0.80 to $+1.20$ s, and from -0.01 to $+0.87$ s, respectively. These intervals were chosen to optimize the search for possible signals. Hereafter, I refer to this search as the canonical one, since it does not modify the light curves so as to account for the increasing precession period expected by SLB13. Figure 3.3 shows an example of PDS with the best fit model. Analogous searches which were already performed in the kHz frequency range in previous data sets of SGRBs, provided only upper limits to the amplitude of possible pulsations (Kruger et al. 2002). In the absence of any positive detection of periodic signal, I derived the 2σ upper limits to the amplitude of detectable periodic pulsations for the frequency range of 10–30 Hz. I expressed this value in terms of fractional amplitude by normalizing the amplitude limit to the peak count rate of each GRB.

We also performed a second, more sensitive search on the PDS of the same light curves after a proper stretching of the time axis. To this aim, I devised a technique which was tailored for the expected signal. For each GRB, I took the $T_{5\sigma}$ interval boundaries and associated two corresponding precession periods: let t_0 and t_1 the start and end times of the $T_{5\sigma}$ interval and let $T_{p,0}$ and $T_{p,1}$ the corresponding precession periods, respectively. We stretched the time axis according to the continuously increasing T_p as described by Eq. (3.8)

$$T_p(t) \;=\; T_{p,0}\,\Big(1+\frac{t-t_0}{t_{\rm s}}\Big)^{4/3}\,, \tag{3.8}$$

where the constant $t_{\rm s}$ is defined as

$$t_{\rm s} \;=\; \frac{t_1-t_0}{(T_{p,1}/T_{p,0})^{3/4}-1}\,. \tag{3.9}$$

The values of $T_{p,0}$ and $T_{p,1}$ were chosen so as to match the typical values obtained by SLB13 (typically values were $T_{p,0}=0.01$ and $T_{p,1}=0.6$ s).

We calculated the new count rates in each of the new temporal bins starting from the original photon arrival times at the detector. Earlier bins at $t<t_0$ were left unaffected.

I attributed a fictitious duration of 1 ms to the new bins. We made sure the new bins corresponded to a number of 5 bins per precession period. This automatically implies that a possible quasiperiodic pulsation such as that described by Eq. (3.8) should correspond to a frequency $5/2 = 2.5$ times as small as the Nyquist one (i.e., 200 Hz in our case) in the stretched PDS.

For each SGRB of our data set, I preliminarily carried out the same analysis on a set of synthetic curves which were derived from a smoothed version of the original light curve of the SGRB. The smoothed version was then modulated with different values of fractional amplitude with a periodic signal with a period varying according to Eq. (3.8). For each SGRB I determined the minimum amplitude for which the PDS of the synthetic stretched light curve gave a 2-σ detection. We also searched the synthetic PDS adopting slightly different trial $T_{p,0}$ and $T_{p,1}$ from the exact values used to build the corresponding stretched curves. As a result, the detection did not crucially depend on the choice of trial $T_{p,0}$ and $T_{p,1}$ within a given range. This check is important since this is the case for real curves for which the possible true periods are unknown a priori. Further details on how synthetic light curves were generated and on the calibration of this technique are given in AppendixB 3.7. Hereafter, I refer to this search as the stretched PDS one.

3.5 Results

The canonical search identified just a couple of SGRBs (GRB 081209 and GRB 110705A) with power exceeding the 2σ threshold (Gaussian units) in one frequency bin each (Figure 3.4).

The chance probability of a 2σ fluctuation occurring within a given PDS is 4.5%. Out of 44 different PDS, the expected number of $> 2\sigma$ fluctuations is 1.98, i.e. in agreement with the observed number of two cases. Hence, no evidence for the presence of periodic or quasiperiodic signal was found. In the absence of detection, for each GRB I derived a 2σ upper limit to the fractional amplitude averaged out over the frequency range of interest, i.e. from 10 to 30 Hz. The amplitude is normalized to the peak count rate of each SGRB. The average minimum detectable amplitude depends on the time interval the PDS is calculated: it clusters around a 3% (17%) of the peak for the fixed (5σ) time interval (Fig. 3.5).

Likewise, I did not find any evidence for the quasiperiodic signals in the stretched PDS search. However, as the calibration on synthetic curves has shown, I could obtain

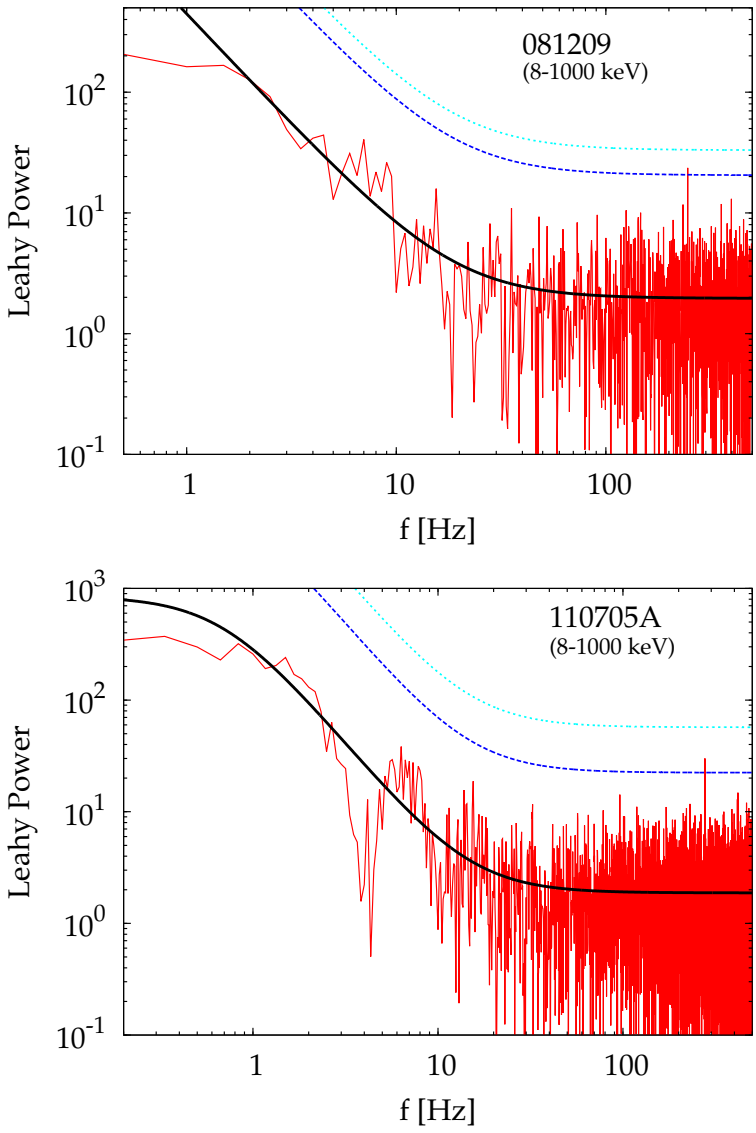

Figure 3.4 The two PDS are related to GRB 081209 and GRB 110705A. They show an excess above the 2σ threshold at frequency 246 Hz and 277 Hz, respectively

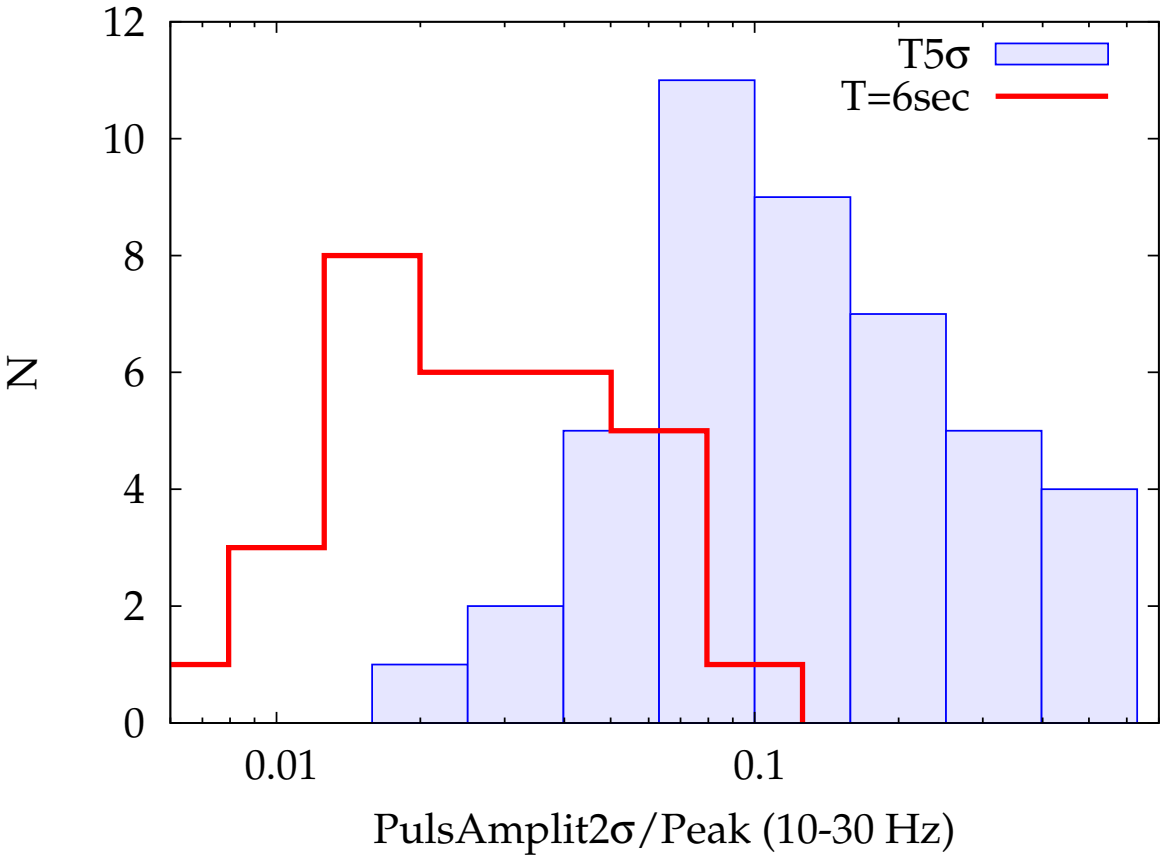

Figure 3.5 Distribution of the minimum detectable pulsation amplitude normalized to peak in the canonical PDS search. Two cases are shown: fixed time (solid) and 5σ (shaded) intervals. They refer to the 10–30 Hz frequency range.

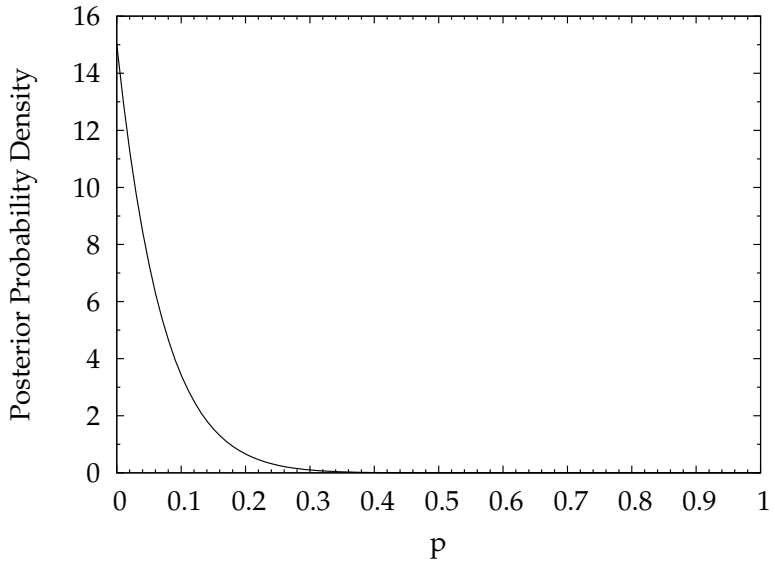

Figure 3.6 Probability density function of p.

useful upper limits to the pulsational amplitude for 14 GRBs.

Adopting the Bayesian approach I compute the posterior probability function of p, which represent the probability to find the predicted precession signal. Let n and m be the total number of stretched light curves examined and the number of QPOs detected, respectively.

$$P(n, m|p) \;=\; \binom{n}{m}\, p^m \;(1-p)^{n-m} \tag{3.10}$$

From the Bayes theorem we can derive the posterior probability distribution of the p values:

$$P(p|n, m) \;=\; \frac{P(n, m|p)\; P(p)}{P(n, m)} \tag{3.11}$$

Assuming an uniform distribution for the prior P(p) I obtain $P(p|n, m) = (n + 1)(1 - p)^n$. Since I don't find any detection (m=0) over a sample of 14 events (n=14) I can derive the 3σ limit of the p distribution from the probability density function $P(p|14, 0) = 15(1 - p)^{14}$ shown in Figure 3.6. This limit is $p < 0.33$.

I obtained useful upper limits to the pulsational amplitude for the four, five, and five SGRBs with highest S/N detected by *Fermi*, *Swift*, and *CGRO*, respectively. This reduced sensitivity with respect to the canonical search is a consequence of the low number of expected cycles coupled with the statistical quality of the data.

Figure 3.7 displays the 2σ upper limits to the fractional amplitude for a modulation with an increasing precession period superposed to the overall profile of each SGRB as

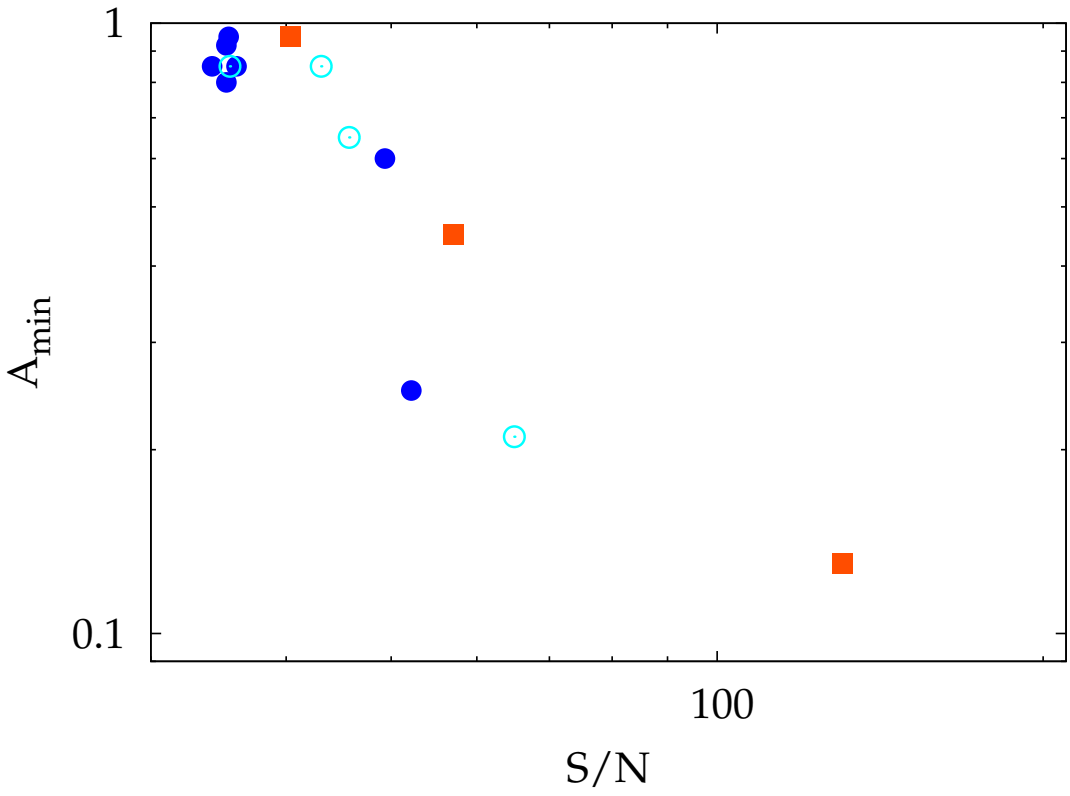

Figure 3.7 Minimum detectable fractional amplitude for an increasing precession period for 14 SGRBs, as determined from simulations in the stretched PDS search. Same symbols as in Figure 3.2 are used.

in Eq. (3.8) as a function of S/N for these 14 events. With reference to the short/intermediate classification provided in Section 3.3.2, 7 out of these 14 GRBs are T–SGRBs, while the remaining 4 and 3 are L–SGRBs and P–IGRBs, respectively. As shown in Figure 3.7, even neglecting the P–IGRB group our results do not change in essence, although the reduced number of events demands caution in generalizing them to larger samples of GRBs. The burst with the highest S/N and most stringent upper limit to the fractional amplitude corresponds to GRB 120323A (Figure 3.8) detected with *Fermi*/GBM and it is a P–IGRB, so the probability of being a misclassified intermediate GRB is not negligible. Still, it is worth noting that its probability of being a genuine SGRB is 78% against a mere 22% of being intermediate.

Although the S/N is one of the most important parameter connected with upper limits estimation, there are others parameters which is strictly related with that measure. As we can see in Table 3.2 the minimum detectable amplitude for the predicted pulsations depends also on the number pulses and on the peak count rates related to the different cases.

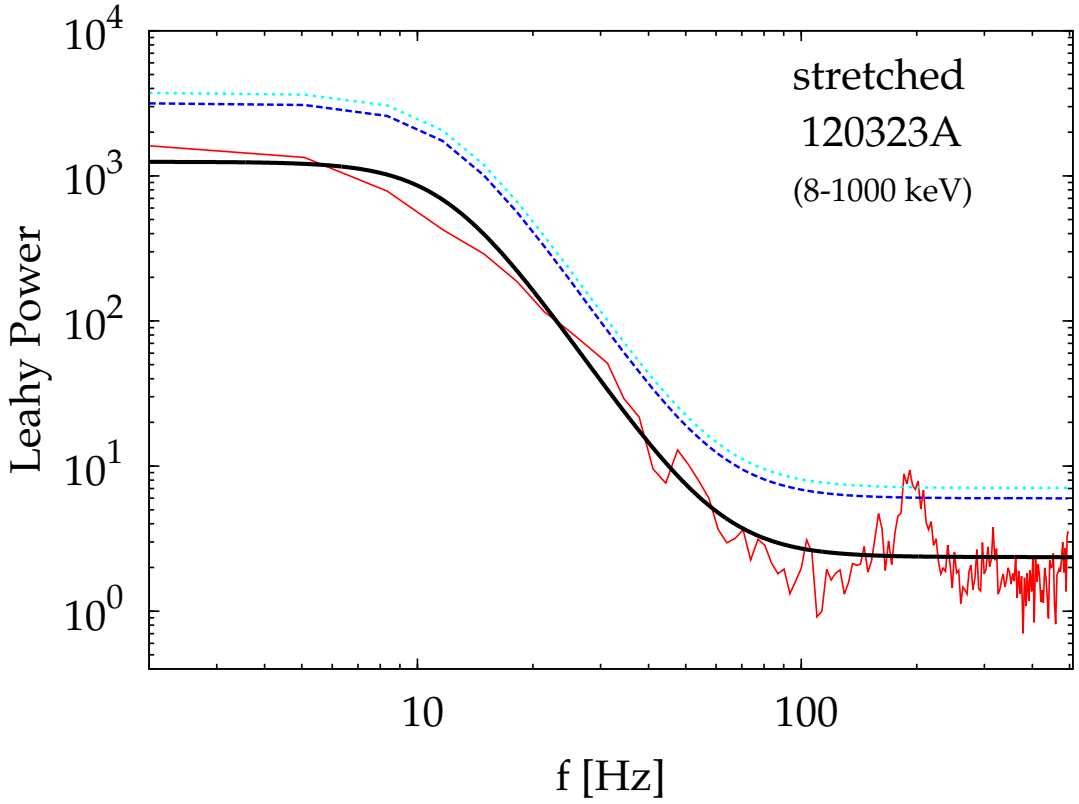

Figure 3.8 This image shows the PDS related to the simulated evolving-periodicity signal in the case of GRB 120323A. If the predicted modulation ($T_{\rm p} \propto t^{4/3}$) was hidden in the signal, I should detect it. I would be sensible to this kind of pulsations for amplitude ≥ 0.13

Table 3.1. 2σ upper limits the amplitude obtained with the stretched synthetic light curves analysis detected by the *Fermi* and *BeppoSAX*.

GRB	$A_{\rm min}$	S/N	$N_{\rm cycles}$	Peak rate (counts s^{-1})
051221A	0.21	64.97	19.82	9.56 ± 0.80
060313	0.60	49.34	11.13	5.41 ± 0.76
090228	0.25	52.20	4.19	66.59 ± 4.78
100816A	0.45	57.11	33.56	1.46 ± 0.06
101219A	0.85	34.17	9.07	1.71 ± 0.16
111222A	0.80	35.23	2.99	19.48 ± 2.33
120323A	0.13	130.48	8.25	108.90 ± 3.18
120624A	0.65	45.73	8.38	21.03 ± 1.47
120804A	0.92	35.23	11.78	2.91 ± 0.24

Note. — The upper limits are reported in comparison to the S/N, the number of precession cycles and the peak count rate

Although the QPO search has given negative results, an interesting product of the canonical search is the continuum properties for an ensemble of bright SGRBs, which is studied here for the first time. Figure 3.9 shows the distribution of the power–law indices for both PL and the BPL models, upon selection of the most accurately measured values ($|\sigma(\alpha)| < 0.5$). A comparison with analogous results obtained on a sample of long *Fermi*/GBM GRBs (a subsample of the long GRBs studied in Chapter 2) shows no outstanding difference in the power–law index distribution between short and long GRBs. Yet the small number of SGRBs lacks in sensitivity to reveal fine differences.

For the SGRBs whose PDS is best fit with a broken power–law, the break frequency is mostly connected to the overall duration of the main spike, whose timescale is predominant in the total PDS of SGRBs.

3.6 Discussion and Conclusions

The canonical search for periodic or quasiperiodic signal did not yield any detection, in agreement with previous analogous searches (Kruger et al. 2002), down to a limiting peak–normalized amplitude which is typically around 10–20% when the PDS is calculated over the 5σ time interval.

In addition, I devised and calibrated a technique to detect the signature of a periodic signal potentially hidden within the time profiles of some SGRBs, characterized by a

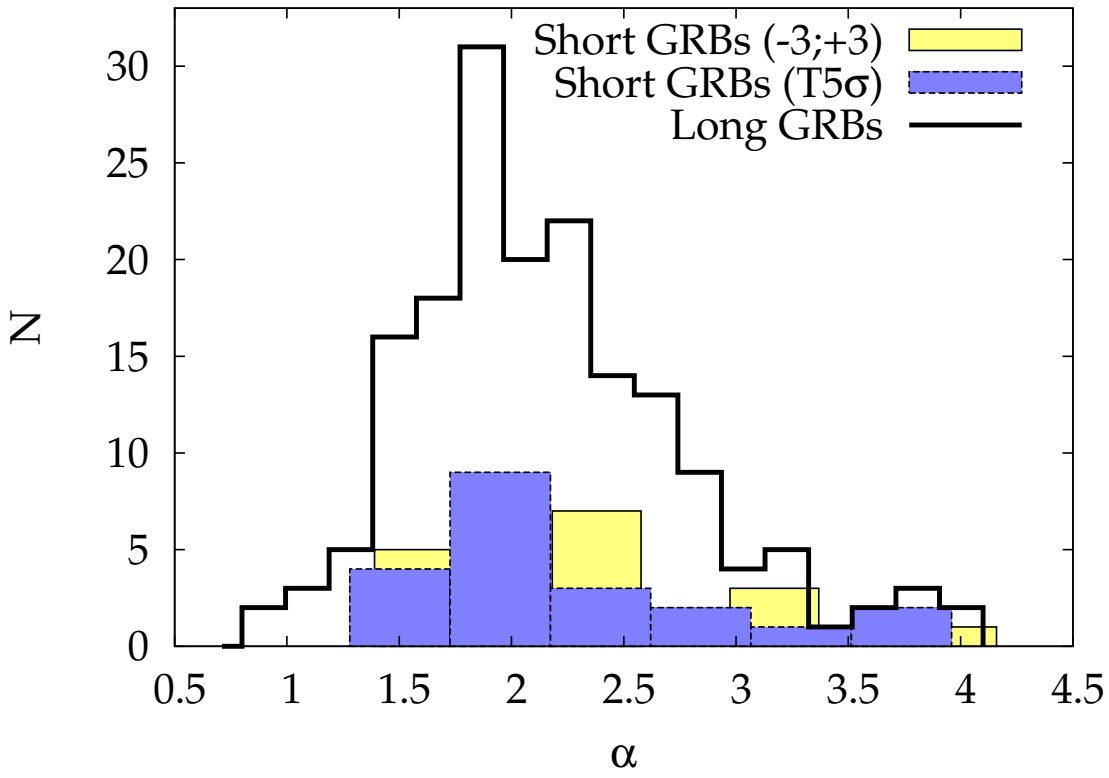

Figure 3.9 Distribution of the PDS slope as derived from the $[-3;3]$ s interval (light shaded), and the 5σ interval (dark shaded). Also shown is the same distribution for a sample of 170 long GRBs.

continuously increasing period, from a few tens ms up to a fraction of a second or so throughout the duration of SGRB. This kind of signal has theoretically been predicted in the case of a mixed merger (NS–BH), where the tilted jet and accretion disc with respect to the BH spin is expected to cause the jet precession and a periodic gamma–ray signal in the prompt emission such as that described above (SLB13). Likewise, no significant detection at 2σ out of a sample of 44 SGRBs was obtained by our tailored technique, named the stretched PDS search, either. However, we could extract useful upper limits to the fractional amplitude of such a modulated signal for 14 GRBs, with values distributed from 10 to 90%. When I exclude the 3 GRBs which appear to have a non–negligible ($p > 0.2$) probability of belonging to the intermediate duration group, the results do not change in essence. The reduced sensitivity of the stretched PDS search compared with that of the canonical one is due to smaller numbers of expected cycles, which couple with a more critical dependence on S/N, as revealed by the synthetic curves used for calibration.

An interesting outcome of our canonical PDS search concerns the continuum properties of the PDS for an ensemble of bright SGRBs (see Table 3.2). Unlike the case for long GRBs (e.g., see Dichiara et al. 2013 and references therein), this is the first time we could usefully study these properties for SGRBs, whose study has been hampered so far by lower S/N with respect to long GRBs. This was also made possible by the Bayesian procedure that was recently proposed by V10 to properly model the PDS of time series affected by a strong red noise component, such as the case of SGRBs' time histories (e.g., see Huppenkothen et al. 2013). Two alternative models were adopted: a simple or a broken power–law in addition to the white noise constant. A preliminary comparison with the analogous properties of a subsample of bright long GRBs reveals no striking difference between the two power–law index distributions (Fig. 3.9). Together with other observational evidences (e.g. similar spectral evolution (Ghirlanda et al. 2011), similar spectral shape of the early prompt emission of long GRBs (Calderone et al. 2015), similar distribution on the lag-luminosity plane (Bernardini et al. 2015)), this may suggest a common general mechanism which rules the shock formation and the gamma–ray emission production.

The implications of our results do not allow us to rule out the physical scenario envisaged by SLB13 as the possible interpretation of the prompt emission of SGRBs for two main reasons. First of all, the sample of SGRBs for which our non–detection is meaningful is still statistically too small to draw firm conclusions. This is even more so when one neglects the few GRBs which could belong to the intermediate duration

group. Secondly, the possibility that the few cases of interest could correspond to either other kind of mergers, such as NS–NS, or mixed mergers with unfavorable space parameters, such as the accretion disc viscosity or the misalignment angle between jet axis and BH spin, is not negligible for just a few cases. Furthermore, according to the recent physical classification proposed by Bromberg et al. (2013), there could be collapsar events disguised as SGRBs, whose presence could partially explain the observed lack of evidence for the pulsations expected for NS–BH mergers. Nonetheless, in addition to being the first attempt of a dedicated search on a valuable data set, our analysis indicates that such mixed systems might not be a dominant fraction among the population of currently detected SGRBs, at least as envisaged in the model by SLB13. A definitive answer will come from a larger sample with comparable statistical quality in combination with the wealth of information that will be independently gathered through the study of gravitation wave radiation.

Table 3.2. Best-fitting model and parameters for each SGRB of the total sample.

GRB	Model	$\log N$	$\log f_{\rm b}$ (Hz)	α	B	$p(T_R)$[a]	$p_{\rm AD}$[b]	$p_{\rm KS}$[c]	$PulseA_{2\sigma}/Peak$	T_{90}	$t^{\rm start}$	$t^{\rm stop}$	HR[g]	$p(Short)$
051221A[d]	sc bpl	$4.487^{7.780}_{-1.278}$	$-0.730^{+0.838}_{-4.961}$	$1.717^{+0.119}_{-0.110}$	$1.812^{+0.072}_{-0.076}$	0.138	0.654	0.884	0.014	1.370	−3.000	+3.000	1.522 ± 0.074	0.841
060313[d]	sc bpl	$3.066^{+0.519}_{-0.350}$	$0.089^{+0.276}_{-0.375}$	$1.968^{+0.247}_{-0.221}$	$1.925^{+0.073}_{-0.074}$	0.428	0.385	0.366	0.019	0.818	−3.000	+3.000	2.491 ± 0.151	0.999
061201[d]	sc pl	$1.569^{+0.193}_{-0.179}$	–	$1.398^{+0.239}_{-0.222}$	$2.025^{+0.071}_{-0.070}$	0.942	0.997	0.999	0.042	0.827	−3.000	+3.000	2.299 ± 0.299	0.999
080426[d]	sc pl	$1.555^{+0.213}_{-0.196}$	–	$2.507^{+0.592}_{-0.512}$	$1.954^{+0.060}_{-0.060}$	0.535	0.845	0.775	0.043	2.019	−3.000	+3.000	1.055 ± 0.125	0.123
081107[e]	sc pl	$1.209^{+0.226}_{-0.216}$	–	$2.274^{+0.585}_{-0.455}$	$1.958^{+0.060}_{-0.059}$	0.233	0.877	0.795	0.065	1.792	−3.000	+3.000	0.695 ± 0.200	0.006
081209[e]	sc bpl	$1.902^{+0.361}_{-0.271}$	$0.371^{+0.246}_{-0.323}$	$2.478^{+0.829}_{-0.632}$	$1.985^{+0.064}_{-0.063}$	0.625	0.488	0.664	0.019	0.960	−3.000	+3.000	4.897 ± 0.657	0.989
081216[e]	sc bpl	$2.342^{+0.271}_{-0.225}$	$0.385^{+0.131}_{-0.160}$	$6.775^{+5.190}_{-2.928}$	$1.981^{+0.059}_{-0.057}$	0.819	0.888	0.807	0.019	1.152	−3.000	+3.000	4.390 ± 0.271	0.854
081223[e]	sc pl	$1.622^{+0.216}_{-0.198}$	–	$2.368^{+0.535}_{-0.454}$	$1.980^{+0.060}_{-0.059}$	0.148	0.927	0.627	0.042	1.536	−3.000	+3.000	1.988 ± 0.953	0.747
090108[e]	sc bpl	$2.510^{+0.393}_{-0.300}$	$0.130^{+0.158}_{-0.205}$	$4.692^{+2.080}_{-1.432}$	$1.982^{+0.062}_{-0.061}$	0.797	0.499	0.559	0.024	0.768	−3.000	+3.000	1.531 ± 0.595	0.500
090228[e]	sc bpl	$2.977^{+0.199}_{-0.174}$	$0.648^{+0.124}_{-0.139}$	$2.339^{+0.190}_{-0.171}$	$1.911^{+0.076}_{-0.074}$	0.954	0.170	0.246	0.012	0.768	−3.000	+3.000	4.665 ± 0.208	0.941
090308B[e]	sc pl	$1.218^{+0.199}_{-0.181}$	–	$1.430^{+0.311}_{-0.262}$	$1.912^{+0.065}_{-0.064}$	0.876	0.949	0.746	0.055	2.176	−3.000	+3.000	4.486 ± 0.413	0.654
090514B[e]	sc pl	$0.933^{+0.272}_{-0.299}$	–	$2.931^{+1.088}_{-0.814}$	$1.919^{+0.058}_{-0.058}$	0.843	0.382	0.411	0.054	2.304	−3.000	+3.000	2.447 ± 1.010	0.187
091109B[d]	sc bpl	$2.726^{+2.528}_{-0.691}$	$-0.214^{+0.450}_{-1.588}$	$2.296^{+0.634}_{-0.497}$	$2.069^{+0.066}_{-0.064}$	0.750	0.959	0.987	0.023	0.272	−3.000	+3.000	2.446 ± 0.301	1.000
100213A[d]	sc pl	$1.402^{+0.204}_{-0.190}$	–	$1.730^{+0.441}_{-0.358}$	$1.957^{+0.062}_{-0.061}$	0.625	0.545	0.309	0.112	2.303	−3.000	+3.000	1.562 ± 0.220	0.496
100625A[d]	sc pl	$1.997^{+0.192}_{-0.174}$	–	$1.939^{+0.308}_{-0.275}$	$2.062^{+0.064}_{-0.063}$	0.994	0.545	0.562	0.025	0.376	−3.000	+3.000	1.933 ± 0.115	1.000
100811A[e]	sc pl	$1.644^{+0.201}_{-0.185}$	–	$1.796^{+0.364}_{-0.306}$	$2.067^{+0.066}_{-0.065}$	0.509	0.446	0.248	0.047	1.408	−3.000	+3.000	6.942 ± 0.841	0.962
100816A[d]	sc pl	$1.105^{+0.311}_{-0.373}$	–	$3.167^{+1.006}_{-0.735}$	$1.986^{+0.062}_{-0.059}$	0.081	0.970	0.995	0.043	2.622	−3.000	+3.000	1.692 ± 0.090	0.487
101219A[d]	sc bpl	$2.754^{+0.677}_{-0.425}$	$-0.018^{+0.300}_{-0.437}$	$3.005^{+1.207}_{-0.816}$	$2.054^{+0.065}_{-0.062}$	0.551	0.999	0.953	0.023	1.099	−3.000	+3.000	2.407 ± 0.214	1.000
110526A[e]	sc pl	$1.383^{+0.213}_{-0.197}$	–	$2.441^{+0.854}_{-0.652}$	$2.021^{+0.064}_{-0.061}$	0.947	0.464	0.360	0.055	1.280	−3.000	+3.000	3.173 ± 0.825	0.916
110529A[e]	sc bpl	$2.368^{+0.276}_{-0.230}$	$0.423^{+0.162}_{-0.197}$	$3.247^{+0.842}_{-0.682}$	$2.037^{+0.064}_{-0.061}$	0.175	0.984	0.925	0.013	0.512	−3.000	+3.000	3.902 ± 0.311	0.913
110705A[e]	sc bpl	$2.929^{+1.256}_{-0.592}$	$-0.151^{+0.409}_{-0.834}$	$2.021^{+0.338}_{-0.288}$	$1.877^{+0.062}_{-0.064}$	0.011	0.997	0.998	0.023	0.320	−3.000	+3.000	6.473 ± 0.635	0.988
111222A[e]	sc pl	$2.391^{+0.165}_{-0.153}$	–	$1.531^{+0.139}_{-0.131}$	$1.909^{+0.071}_{-0.071}$	0.497	0.898	0.890	0.014	0.320	−3.000	+3.000	5.449 ± 0.317	0.970
120305A[d]	sc bpl	$2.334^{+0.145}_{-0.128}$	$0.922^{+0.083}_{-0.094}$	$4.160^{+0.883}_{-0.714}$	$2.103^{+0.068}_{-0.067}$	0.417	0.105	0.142	0.011	0.121	−3.000	+3.000	2.008 ± 0.171	1.000
120323A[e]	sc bpl	$4.116^{+0.245}_{-0.211}$	$0.393^{+0.095}_{-0.106}$	$3.482^{+0.245}_{-0.229}$	$1.687^{+0.055}_{-0.053}$	0.661	0.572	0.582	0.006	0.576	−3.000	+3.000	1.491 ± 0.286	0.778
120624A[e]	sc bpl	$3.067^{+0.399}_{-0.310}$	$0.145^{+0.173}_{-0.211}$	$3.118^{+0.512}_{-0.452}$	$1.945^{+0.060}_{-0.059}$	0.279	0.834	0.970	0.010	0.768	−3.000	+3.000	4.013 ± 0.114	0.876
120804A[d]	sc pl	$1.958^{+0.209}_{-0.191}$	–	$2.188^{+0.366}_{-0.326}$	$1.972^{+0.062}_{-0.060}$	0.245	0.871	0.727	0.026	1.763	−3.000	+3.000	1.580 ± 0.125	0.983
120811B[e]	sc bpl	$1.998^{+0.666}_{-0.400}$	$0.261^{+0.396}_{-0.616}$	$3.906^{+6.794}_{-2.192}$	$1.974^{+0.067}_{-0.067}$	0.382	0.775	0.812	0.042	0.384	−3.000	+3.000	6.504 ± 0.803	0.952
120817B[e]	sc bpl	$1.958^{+0.147}_{-0.128}$	$0.935^{+0.086}_{-0.098}$	$4.002^{+0.879}_{-0.726}$	$2.035^{+0.066}_{-0.064}$	0.687	0.235	0.110	0.014	0.576	−3.000	+3.000	3.783 ± 0.385	0.997
120830A[e]	sc pl	$1.326^{+0.190}_{-0.183}$	–	$1.689^{+0.414}_{-0.330}$	$1.967^{+0.062}_{-0.062}$	0.899	0.729	0.538	0.078	1.152	−3.000	+3.000	5.788 ± 0.491	0.814
130603B[d]	sc bpl	$2.855^{+0.146}_{-0.129}$	$0.918^{+0.095}_{-0.103}$	$3.142^{+0.359}_{-0.319}$	$2.002^{+0.070}_{-0.068}$	0.267	0.979	0.908	0.015	0.192	−3.000	+3.000	2.123 ± 0.128	1.000
910718D[f]	sc pl	$4.607^{+1.029}_{-0.895}$	–	$2.070^{+0.603}_{-0.536}$	$1.885^{+0.620}_{-0.604}$	0.823	0.757	0.678	0.567	0.250	−0.032	+0.155	5.452 ± 0.658	0.981
921123B[f]	sc pl	$4.799^{+0.782}_{-0.638}$	–	$3.140^{+0.768}_{-0.601}$	$1.704^{+0.217}_{-0.194}$	0.774	0.827	0.947	0.065	0.591	−0.023	+0.437	3.855 ± 0.193	0.886
930110A[f]	sc pl	$5.059^{+0.661}_{-0.594}$	–	$2.328^{+0.398}_{-0.355}$	$1.642^{+0.335}_{-0.313}$	0.538	0.999	0.958	0.178	0.223	−0.017	+0.330	6.059 ± 0.235	0.984
930506C[f]	sc pl	$4.146^{+0.612}_{-0.527}$	–	$2.919^{+0.638}_{-0.548}$	$1.956^{+0.172}_{-0.163}$	0.759	0.998	0.999	0.048	0.804	−0.077	+0.765	6.682 ± 0.504	0.903
931101A[f]	sc pl	$3.837^{+0.479}_{-0.425}$	–	$1.930^{+0.335}_{-0.296}$	$1.877^{+0.338}_{-0.321}$	0.637	0.970	0.878	0.104	0.296	−0.047	+0.373	5.885 ± 0.396	0.974
940219[f]	sc pl	$3.703^{+0.423}_{-0.378}$	–	$2.162^{+0.337}_{-0.305}$	$2.057^{+0.202}_{-0.188}$	0.811	0.631	0.472	0.075	0.680	−0.113	+0.728	7.173 ± 0.385	0.924
940329B[f]	sc pl	$4.589^{+0.948}_{-0.753}$	–	$3.792^{+1.064}_{-0.879}$	$1.826^{+0.184}_{-0.170}$	0.715	0.948	0.831	0.036	0.456	−0.076	+0.547	1.785 ± 0.077	0.821

Table 3.2 (cont'd)

GRB	Model	$\log N$	$\log f_{\rm b}$ (Hz)	α	B	$p(T_R)$[a]	$p_{\rm AD}$[b]	$p_{\rm KS}$[c]	$PulseA_{2\sigma}/Peak$	T_{90}	$t^{\rm start}$	$t^{\rm stop}$	HR[g]	$p(Short)$
940918[f]	sc bpl	$2.897^{+0.364}_{-0.287}$	$1.456^{+0.150}_{-0.177}$	$4.625^{+1.580}_{-1.139}$	$1.752^{+0.305}_{-0.274}$	0.429	0.999	0.996	0.260	0.208	−0.113	+0.204	5.350 ± 0.269	0.986
960319[f]	sc pl	$3.719^{+0.555}_{-0.493}$	–	$1.913^{+0.391}_{-0.339}$	$1.685^{+0.264}_{-0.254}$	0.052	0.730	0.856	0.143	0.496	−0.027	+0.506	7.734 ± 0.463	0.949
980218B[f]	sc pl	$3.978^{+0.879}_{-0.706}$	–	$3.671^{+1.215}_{-0.947}$	$1.807^{+0.144}_{-0.131}$	0.208	0.923	0.976	0.078	0.704	−0.113	+0.845	$5.520 \pm 0.428(h)$	0.899
990126B[f]	sc bpl	$3.441^{+5.921}_{-1.128}$	$0.821^{+0.583}_{-2.679}$	$2.942^{+0.961}_{-0.754}$	$1.542^{+0.313}_{-0.280}$	0.807	0.631	0.634	0.276	0.249	−0.031	+0.305	10.742 ± 0.958	0.977
990208B[f]	sc pl	$3.016^{+0.354}_{-0.317}$	–	$1.658^{+0.265}_{-0.239}$	$1.781^{+0.166}_{-0.169}$	0.095	0.390	0.314	0.085	1.247	−0.077	+1.230	8.453 ± 0.622	0.889
990720[f]	sc pl	$3.232^{+0.639}_{-0.553}$	–	$2.173^{+0.598}_{-0.502}$	$1.910^{+0.196}_{-0.185}$	0.717	0.653	0.322	0.090	0.945	−0.041	+0.670	3.679 ± 0.158	0.754
991002[f]	sc pl	$4.483^{+1.017}_{-0.770}$	–	$3.792^{+1.315}_{-0.966}$	$1.876^{+0.183}_{-0.173}$	0.926	0.977	0.755	0.043	1.918	−0.062	+0.601	2.119 ± 0.112	0.170
051221A[d]	sc pl	$3.587^{+0.250}_{-0.233}$	–	$1.782^{+0.165}_{-0.153}$	$1.770^{+0.131}_{-0.131}$	0.011	0.658	0.507	0.038	1.369	−0.030	+2.090	1.522 ± 0.074	0.841
060313[d]	sc pl	$3.508^{+0.446}_{-0.384}$	–	$1.989^{+0.343}_{-0.303}$	$2.003^{+0.176}_{-0.167}$	0.817	0.972	0.996	0.084	0.818	−0.140	+1.050	2.491 ± 0.151	0.999
061201[d]	sc pl	$2.084^{+0.694}_{-0.601}$	–	$1.441^{+0.747}_{-0.596}$	$2.035^{+0.258}_{-0.302}$	0.543	0.925	0.956	0.184	0.827	0.000	+0.840	2.299 ± 0.299	0.999
080426[d]	sc pl	$2.159^{+0.505}_{-0.435}$	–	$3.436^{+1.516}_{-1.112}$	$1.837^{+0.104}_{-0.098}$	0.550	0.419	0.389	0.090	2.019	−0.030	+1.800	1.055 ± 0.125	0.123
081107[e]	sc pl	$1.415^{+0.583}_{-0.514}$	–	$2.126^{+1.232}_{-0.918}$	$1.963^{+0.113}_{-0.111}$	0.509	0.972	0.910	0.142	1.792	−0.105	+1.687	0.695 ± 0.200	0.006
081209[e]	sc pl	$3.861^{+1.537}_{-1.231}$	–	$2.164^{+1.156}_{-0.916}$	$2.192^{+0.548}_{-0.544}$	0.525	0.875	0.701	0.448	0.960	−0.014	+0.178	4.897 ± 0.657	0.989
081216[e]	sc pl	$3.237^{+0.602}_{-0.488}$	–	$2.825^{+1.038}_{-0.714}$	$1.883^{+0.142}_{-0.132}$	0.788	0.915	0.815	0.056	1.152	−0.057	+1.095	4.390 ± 0.271	0.854
081223[e]	sc pl	$2.694^{+0.803}_{-0.631}$	–	$2.997^{+1.415}_{-1.011}$	$1.897^{+0.158}_{-0.149}$	0.866	0.755	0.536	0.126	1.536	−0.046	+0.850	1.988 ± 0.953	0.747
090108[e]	sc pl	$4.015^{+1.408}_{-1.058}$	–	$4.754^{+2.340}_{-1.772}$	$2.003^{+0.196}_{-0.180}$	0.455	0.489	0.219	0.110	0.768	−0.069	+0.571	1.531 ± 0.595	0.500
090228[e]	sc pl	$4.073^{+0.477}_{-0.421}$	–	$1.753^{+0.281}_{-0.252}$	$1.822^{+0.445}_{-0.444}$	0.815	0.914	0.770	0.093	0.768	0.030	+0.478	4.665 ± 0.208	0.941
090308B[e]	sc pl	$1.554^{+0.446}_{-0.399}$	–	$1.288^{+0.501}_{-0.414}$	$1.857^{+0.146}_{-0.157}$	0.348	0.787	0.688	0.134	2.176	−0.072	+1.464	4.486 ± 0.413	0.654
090514B[e]	sc pl	$1.276^{+0.551}_{-0.632}$	–	$4.248^{+3.411}_{-2.042}$	$1.964^{+0.104}_{-0.099}$	0.953	0.646	0.574	0.113	2.304	−0.348	+1.764	2.447 ± 1.010	0.187
091109B[d]	sc pl	$3.545^{+1.846}_{-1.206}$	–	$2.627^{+1.970}_{-1.202}$	$1.915^{+0.310}_{-0.296}$	0.646	0.238	0.286	0.214	0.272	0.000	+0.300	2.446 ± 0.301	1.000
100213A[d]	sc pl	$1.734^{+0.340}_{-0.305}$	–	$1.935^{+0.655}_{-0.527}$	$1.890^{+0.094}_{-0.093}$	0.597	0.875	0.875	0.178	2.303	−0.390	+2.160	1.562 ± 0.220	0.496
100625A[d]	sc pl	$3.135^{+1.660}_{-1.185}$	–	$2.387^{+1.832}_{-1.190}$	$2.109^{+0.303}_{-0.307}$	0.388	0.985	0.947	0.192	0.376	−0.060	+0.320	1.933 ± 0.115	1.000
100811A[e]	sc pl	$3.235^{+1.518}_{-1.107}$	–	$2.583^{+1.743}_{-1.097}$	$2.339^{+0.311}_{-0.285}$	0.776	0.959	0.885	0.319	1.408	−0.001	+0.383	6.942 ± 0.841	0.962
100816A[d]	sc pl	$1.250^{+0.382}_{-0.464}$	–	$3.288^{+1.338}_{-0.895}$	$1.976^{+0.079}_{-0.077}$	0.778	0.318	0.240	0.063	2.622	−0.680	+2.910	1.692 ± 0.090	0.487
101219A[d]	sc pl	$2.864^{+0.632}_{-0.501}$	–	$2.381^{+0.865}_{-0.632}$	$2.067^{+0.170}_{-0.162}$	0.406	0.912	0.954	0.086	1.099	−0.040	+0.930	2.407 ± 0.214	1.000
110526A[e]	sc pl	$1.873^{+0.381}_{-0.320}$	–	$2.356^{+1.620}_{-0.786}$	$2.040^{+0.110}_{-0.108}$	0.417	0.843	0.680	0.105	1.280	−0.061	+0.451	3.173 ± 0.825	0.916
110529A[e]	sc pl	$4.376^{+1.094}_{-0.892}$	–	$2.980^{+1.034}_{-0.820}$	$2.006^{+0.248}_{-0.226}$	0.282	0.907	0.779	0.116	0.512	0.013	+0.461	3.902 ± 0.311	0.913
110705A[e]	sc pl	$4.002^{+1.078}_{-0.873}$	–	$2.480^{+0.887}_{-0.706}$	$1.846^{+0.288}_{-0.262}$	0.112	0.815	0.827	0.253	0.320	−1.000	+1.000	6.473 ± 0.635	0.988
111222A[e]	sc pl	$2.596^{+0.817}_{-0.751}$	–	$1.299^{+0.570}_{-0.511}$	$1.848^{+0.520}_{-0.653}$	0.236	0.665	0.444	0.137	0.320	0.006	+0.326	5.449 ± 0.317	0.970
120305A[d]	sc pl	$5.272^{+2.375}_{-1.453}$	–	$2.749^{+1.882}_{-1.041}$	$2.385^{+0.882}_{-0.808}$	0.801	0.642	0.574	0.444	0.121	0.000	+0.120	2.008 ± 0.171	1.000
120323A[e]	sc bpl	$4.287^{+0.529}_{-0.393}$	$0.400^{+0.169}_{-0.215}$	$3.566^{+0.429}_{-0.379}$	$1.577^{+0.088}_{-0.086}$	0.271	0.960	0.887	0.017	0.576	−1.000	+1.000	1.491 ± 0.286	0.778
120624A[e]	sc pl	$3.886^{+0.741}_{-0.570}$	–	$2.719^{+0.824}_{-0.633}$	$1.881^{+0.167}_{-0.164}$	0.399	0.646	0.783	0.053	0.768	0.012	+0.908	4.013 ± 0.114	0.876
120804A[d]	sc pl	$2.698^{+0.739}_{-0.560}$	–	$3.006^{+1.342}_{-0.961}$	$1.978^{+0.136}_{-0.129}$	0.803	0.641	0.873	0.077	1.763	−0.150	+1.110	1.580 ± 0.125	0.983
120811B[e]	sc pl	$3.410^{+1.641}_{-1.089}$	–	$2.674^{+1.957}_{-1.161}$	$1.859^{+0.264}_{-0.253}$	0.624	0.542	0.533	0.224	0.384	0.001	+0.356	6.504 ± 0.803	0.952
120817B[e]	sc pl	$4.838^{+1.727}_{-1.429}$	–	$2.259^{+1.079}_{-0.915}$	$2.463^{+0.980}_{-1.214}$	0.643	0.769	0.724	0.540	0.576	0.005	+0.133	3.783 ± 0.385	0.997
120830A[e]	sc pl	$1.150^{+0.537}_{-0.413}$	–	$0.865^{+0.766}_{-0.497}$	$1.655^{+0.387}_{-0.662}$	0.992	0.424	0.328	0.253	1.152	−0.007	+1.081	5.788 ± 0.491	0.814
130603B[d]	sc bpl	$2.991^{+0.217}_{-0.185}$	$1.062^{+0.125}_{-0.141}$	$3.957^{+0.895}_{-0.699}$	$2.146^{+0.130}_{-0.122}$	0.980	0.503	0.467	0.050	0.192	−1.000	+1.000	2.123 ± 0.128	1.000

Table 3.2 (cont'd)

GRB	Model	$\log N$	$\log f_{\rm b}$ (Hz)	α	B	$p(T_R)$[a]	$p_{\rm AD}$[b]	$p_{\rm KS}$[c]	$PulseA_{2\sigma}/Peak$	T_{90}	$t^{\rm start}$	$t^{\rm stop}$	HR[g]	$p(Short)$

Note. — Uncertainties on best-fit parameters are given at 90% confidence. This table is available in its entirety in a machine-readable form in the online journal.

[a] $p(T_R)$ is the significance associated to statistic T_R.

[b] $p_{\rm AD}$ is the significance of the Anderson–Darling test.

[c] $p_{\rm KS}$ is the significance of the Kolmogorov–Smirnov test.

[d] Detected by *Swift*/BAT

[e] Detected by *Fermi*/GBM

[f] Detected by *CGRO*/BATSE

[g] Uncertainty on hardness ratio are given at 1 sigma confidence

[h] In this case the time interval of PDS extraction is larger then the $T_{5\sigma}$ interval to fit properly the continuum shape

3.7 AppendixB

3.7.1 Calibration of the stretched PDS search

For each SGRBs we carried out a series of simulations aimed at calibrating the sensitivity of our stretched PDS search. We first binned the original curve to a rough resolution so as to reduce the high–frequency variability (both real and statistical fluctuations). The smoothed version of the light curve was then obtained by interpolation of the coarse binned curve by means of C–splines. To simulate the predicted periodicity we modulated a smoothed version of the original light curve with a sinusoidal signal:

$$(S - B)(1 + Asin(\phi(t))) + B \tag{3.12}$$

Where S is the smoothed signal, B is the background level and ϕ is the phase computed assuming the temporal evolution of T_p of Eq. (3.8). An example of this procedure is illustrated in Figure 3.10

Specifically, to obtain the synthetic light curves we preliminarily had to calculate the pulsational phase as a function of time, $\phi(t)$. Since T_p continuously varies with time, we had to integrate the infinitesimal relation $d\phi = 2\pi dN = 2\pi dt/T_p$, where dN is the infinitesimal increment to the total number of cycles starting from t_0. Using Equation (3.8) one obtains

$$\begin{aligned}\phi(t) &= 2\pi \int_{t_0}^{t} \frac{dt'}{T_p(t')} = 2\pi \int_{t_0}^{t} \frac{dt'}{T_{p,0}\left(1+\frac{t'-t_0}{t_s}\right)^{4/3}} = 2\pi \int_0^{\frac{t-t_0}{t_s}} \frac{t_s d\xi}{T_{p,0}\,(1+\xi)^{4/3}} \\ &= 2\pi \frac{t_s}{T_{p,0}} \int_0^{\frac{t-t_0}{t_s}} (1+\xi)^{-4/3} d\xi = \frac{6\pi t_s}{T_{p,0}} \left[1 - \left(1+\frac{t-t_0}{t_s}\right)^{-1/3}\right]\end{aligned} \tag{3.13}$$

Where we applied the substitution $\xi = \frac{t'-t_0}{t_s}$. Equivalently, the number of cycles at time t, $N(t)$ is given by

$$N(t) = \frac{\phi(t)}{2\pi} = \frac{3\,t_s}{T_{p,0}} \left[1 - \left(1+\frac{t-t_0}{t_s}\right)^{-1/3}\right]. \tag{3.14}$$

The final number of cycles is given by Eq. (3.14) at $t = t_1$. Then, using the Equation (3.8, we can write:

$$\begin{aligned}N = \frac{3\,t_s}{T_{p,0}} \left[1 - \left(1+\frac{t_1-t_0}{t_s}\right)^{-1/3}\right] &= \frac{3\,(t_1-t_0)}{T_{p,0}\left[\left(\frac{T_{p,1}}{T_{p,0}}\right)^{3/4} - 1\right]} \left[1 - \left(\frac{T_{p,1}}{T_{p,0}}\right)^{-1/4}\right] \\ &= \frac{3\,(t_1-t_0)}{T_{p,0}} \frac{(1-\zeta^{-1/4})}{(\zeta^{3/4}-1)} = \frac{3\,(t_1-t_0)}{T_{p,0}} \frac{(\zeta^{-1/4}-\zeta^{-1/2})}{(\zeta^{1/2}-\zeta^{-1/4})},\end{aligned} \tag{3.15}$$

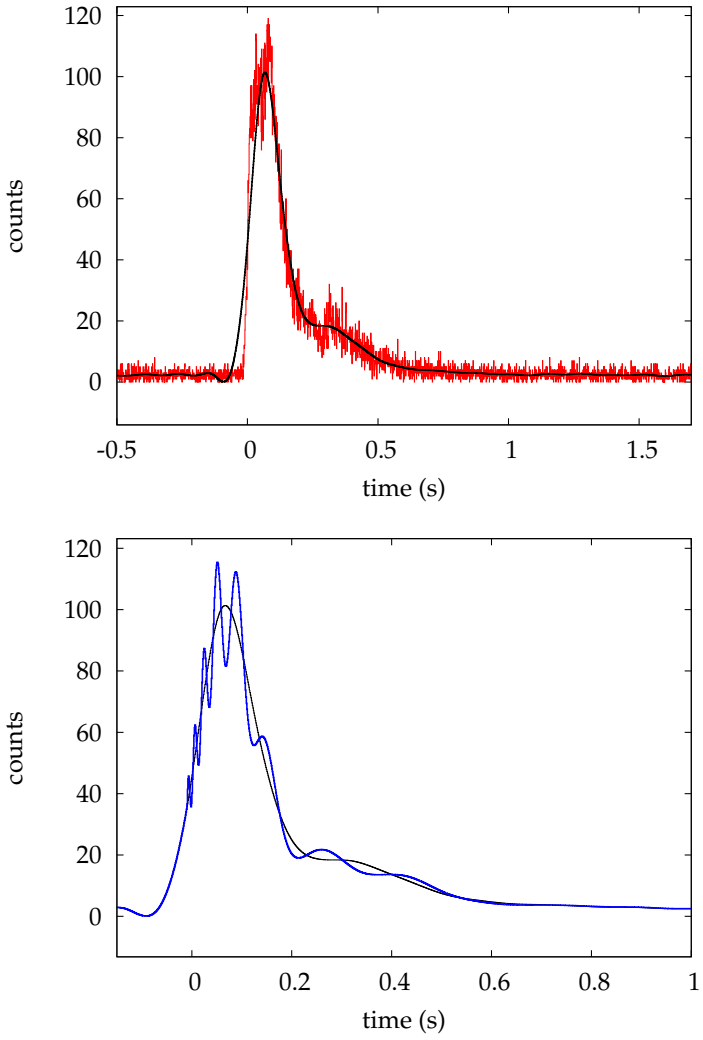

Figure 3.10 The smoothed version of the original GRB 120323A light curve is illustrate at the top. The bottom panel exhibits how the predicted signal arises above the original one

Where $\zeta = \frac{T_{p,1}}{T_{p,0}}$. So that we can end up with the more convenient form:

$$N = \frac{3\,(t_1 - t_0)}{T_{p,0}} \frac{x - x^2}{x^{-2} - x} = \frac{3\,(t_1 - t_0)}{T_{p,0}} \frac{x^2(x - x^2)}{1 - x^3} = \frac{3\,(t_1 - t_0)}{T_{p,0}} \frac{x^3(1 - x)}{(1 - x)(1 + x + x^2)} = \frac{(t_1 - t_0)}{T_{p,0}} \frac{3\,x^3}{1 + x + x^2} \quad (3.16)$$

where we defined $x = \zeta^{-1/4} = (T_{p,0}/T_{p,1})^{1/4}$. The trivial case of constant periodicity ($T_{p,1} = T_{p,0}$) is easily recovered, being $N = (t_1 - t_0)/T_{p,0}$. Finally, statistical noise was added to the synthetic light curves, which were then processed exactly in the same as real curves according to the stretched PDS search described in Section 3.4.

Chapter 4

2D Singular Spectrum Analysis and its application on the RINGO3 frames

4.1 Introduction

The study of the optical transient sky is one of the most interesting research areas that I can explore using the several robotic telescopes spread all over the word. They represent the essential tools to investigate the nature of the fast transient events detected at different energies (GRBs, Fast Radio Bursts, etc.) as well as the search for GW counterparts. The suppression of noise effects from the collected images can greatly improve the photometric analysis.

In this work I worked on the images collected by RINGO3, the new imaging polarimeter currently deployed at the focus of 2–m robotic Liverpool Telescope (LT) in La Palma (Canary Islands). The scientific outcomes yielded by this family of optical-polarimeters (RINGO, RINGO2) made it possible to study the GRB polarization and to provide strong evidence for the presence of a large ordered magnetic field (Mundell et al. 2007; Steele et al. 2009; Mundell et al. 2013). These measures enable us to study the reverse–shock generated when the GRB ejecta collide with the circumburst medium and begin to decelerate at the onset of the afterglow (Kobayashi et al. 1999). An example of forward and reverse shock is illustrated in Figure 4.1 in case Tychos supernova remnant (Warren et al. 2005).

Light from the reverse shock should be highly polarized if the jet magnetic field is globally ordered and advected from the central engine with a position angle that is

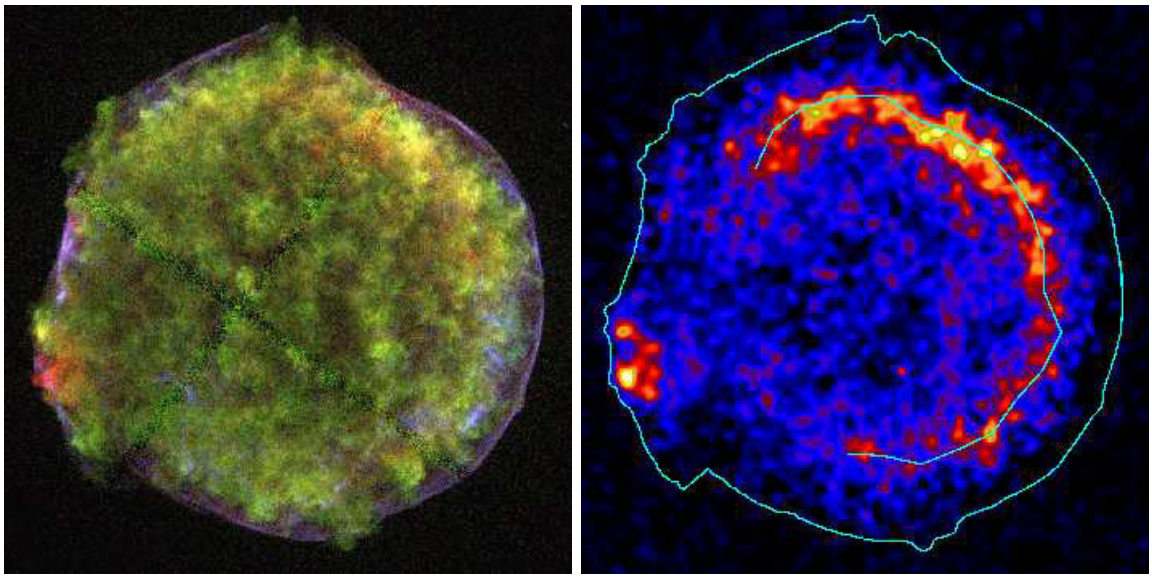

Figure 4.1 This figure is taken from Warren et al. (2005). *Left*: the three-color composite Chandra image of Tychos SNR. The red, green, and blue images correspond to photon energies in the 0.95–1.26 keV, 1.63–2.26 keV, and 4.1–6.1 keV bands, respectively. *Right*: the Fe K line image with continuum (4–6 keV band) subtracted. The inner (outer) contour shows the location of the reverse shock (blast wave).

predicted to remain stable in magnetized baryonic jet models. The RINGO2 measures provide us with strong indications in support of this kind of scenario. RINGO3 has recently become operative and a thorough calibration work is requested during this initial stage. My work is completely involved inside this phase. Using a particular method of time series analysis called Singular Spectrum Analysis (hereafter SSA) I process the frames with the aim of suppressing the noise. The SSA is a very powerful technique dealing with a wide range of tasks: time series decomposition, trend extraction, periodicity detection and extraction, signal extraction, denoising, filtering, forecasting, missing data imputation, change point detection, spectral analysis (see examples and references in Vautard & Ghil (1989); Golyandina et al. (2001); Ghil et al. (2002); Golyandina & Zhigljavsky (2013)). Here I mainly focused on the 2–D extension of this technique to the pixel array.

4.2 Ringo3

RINGO3 is a fast–readout optical imaging polarimeter. It uses a polaroid that rotates once per second to measure the polarisation of light. A pair of dichroic mirrors split the light into three beams for simultaneous polarised imaging in three wavebands

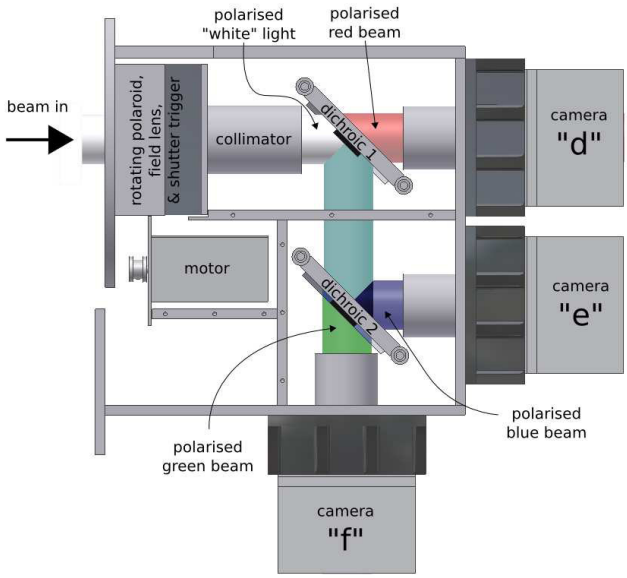

Figure 4.2 Sketch of the RINGO3 general configuration. The dichroic mirrors split the polarised "white light" and direct it towards the three different cameras: Red ("f"), Green ("d") and Blue ("e")

using three separate Andor cameras (Figure 4.2).

The three cameras, called "Red", "Green" and "Blue", collect images in the $770 - 1100$ nm, $650 - 760$ nm and $350 - 640$ nm wavebands, respectively, roughly matching the usual I, R and B optical filters. Each camera supplies eight exposures per second, synchronised with the phase of the polaroid's rotation. All images for each octal phase are stacked to obtain the final signal at each phase in the polaroid's rotation. Observing for longer and thus stacking more images in each octal phase increases the signal-to-noise ratio. Each camera uses a 512×512 pixel EMCCD with a gain of $\sim 0.32 e^{-}/ADU$ in a sigle 125 msec collected frame (under the standard configuration). Currently, there are two main issues. Slightly different vignetting effects, due to different lens configuration. The second issue is the presence of some wavy interference in the frames. This is likely due to stray light components coming from lateral sides of the telescopes which generate this sort of wave in the images background at different frequency scales (see the Figure 4.8 in Section 4.5). My analysis aims at reducing both effects.

4.3 Metod 2D-SSA

The SSA is a non–parametric technique which splits the signal into a number of basic components. It is very useful to recognise different patterns in a given time series

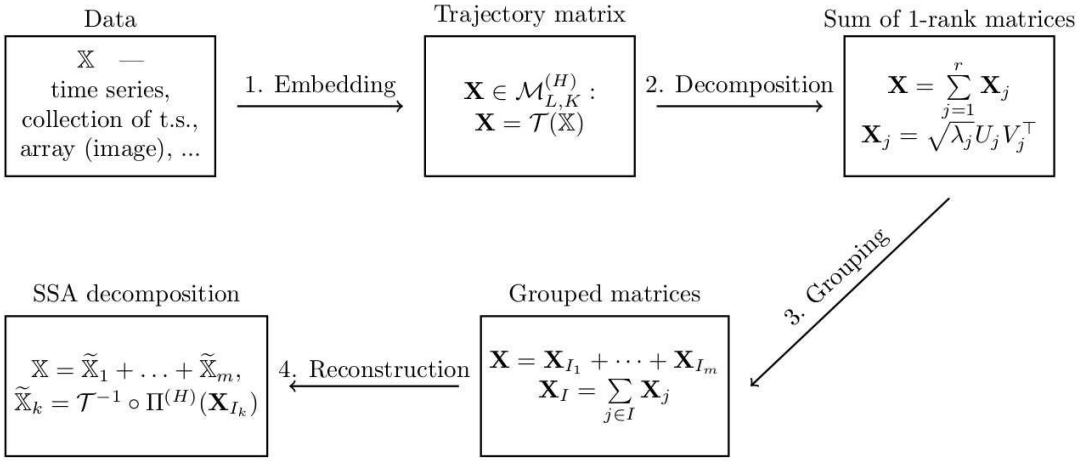

Figure 4.3 This image was taken from Golyandina et al. (2013). It simply describes the four main steps carried out by the SSA procedure

to extract the trend or to remove the noise. This method combines the basic idea of the embedding theorem with the power of the singular values decomposition. The technique is fully described in Golyandina et al. (2013). The basic idea behind this method is outlined in Figure 4.3

It consists of splitting a time series $X = (x_1, x_2, \ldots, x_N)$ using a fixed embedding length L. Then one can write the so–called 'trajectory matrix' $\mathbf{X}$ with L rows and K columns (where K=N-L+1).

$$\mathbf{X} = \begin{pmatrix} x_1 & x_2 & x_3 & \ldots & x_K \\ x_2 & x_3 & x_4 & \ldots & x_{K+1} \\ x_3 & x_4 & x_5 & \ldots & x_{K+2} \\ \vdots & \vdots & \vdots & \ddots & \vdots \\ x_L & x_{L+1} & x_{L+2} & \ldots & x_N \end{pmatrix}, \tag{4.1}$$

This matrix has a Hankelian structure, i.e. it has equal values on anti-diagonal positions ($x_{i,j}$=$x_{i-1,j+1}$). A spectrum of eigenvalues is found by applying the singular value decomposition to the covariance matrix $\mathbf{S}$=$\mathbf{X}^T\mathbf{X}$. $\mathbf{S}$ is called lagged-covariance matrix and its elements are proportional to the linear correlations between the different parts of the time series itself. $\mathbf{S}$ is a real and symmetric matrix, so one can diagonalise it and find an orthonormal base to decompose $\mathbf{X}$, finding $\mathbf{E}$=$\hat{e}_1$,$\hat{e}_2$,...., $\hat{e}_K$ and Λ=λ_1 ,λ_2,...., λ_K where $\hat{e}_i$ are orthonormal eigenvectors and λ_i the corresponding eigenvalues. At the same time, $\hat{e}_i$ and $\sqrt{\lambda_i}$ can be seen as the singular vectors and singular values

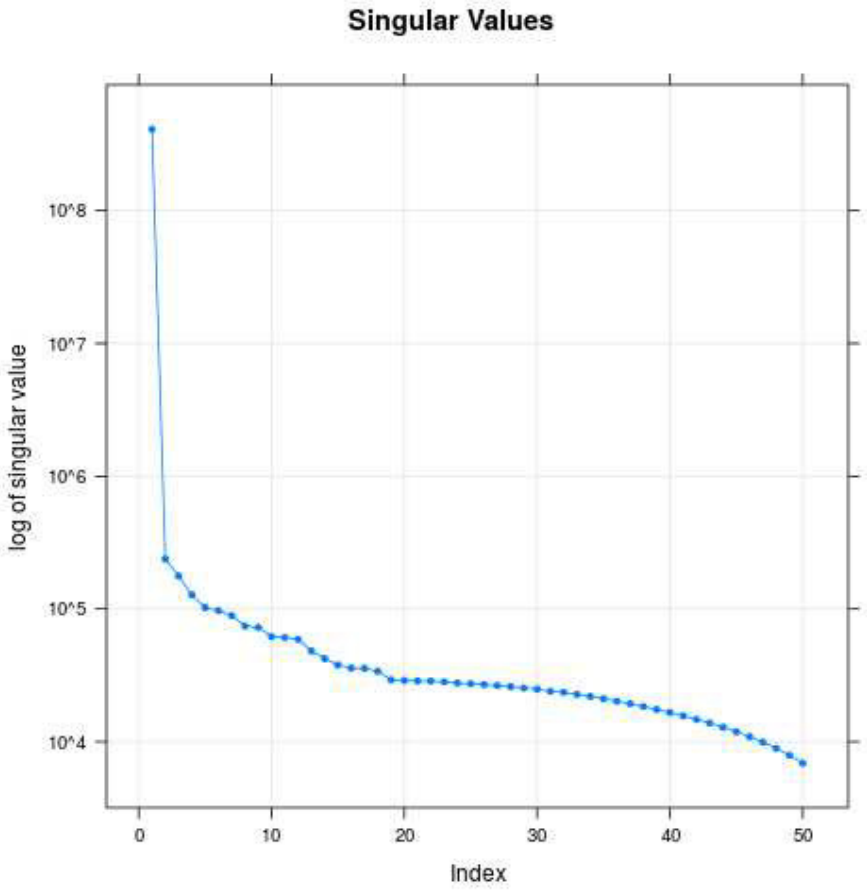

Figure 4.4 Singular values ordered from the higher to the lower ($\sqrt{\lambda_1} \geq \ldots \geq \sqrt{\lambda_K} \geq 0$)

of $\mathbf{X}$, respectively (the ordered singular values are plotted in Figure 4.4) .

One can apply the singular value decomposition on $\mathbf{X}$:

$$\mathbf{X} = \mathbf{DLE}^T \tag{4.2}$$

Where $\mathbf{D}$ is a unitary matrix ($\mathbf{D}$=$\bar{d}_1$, $\bar{d}_2$,...., $\bar{d}_k$) and $\mathbf{L}$ a non-negative diagonal matrix. From here one derives straightforwardly,

$$\mathbf{S} = \mathbf{X}^T\mathbf{X} = (\mathbf{DLE}^T)^T(\mathbf{DLE}^T) = \mathbf{ELD}^T\mathbf{DLE}^T \tag{4.3}$$

Since $\mathbf{D}^T\mathbf{D}$=$\mathbf{I}$,

$$\mathbf{S} = \mathbf{EL}^2\mathbf{E}^T \tag{4.4}$$

so that one can immediately see $\mathbf{L}^2$=Λ. Therefore

$$\mathbf{X} = \mathbf{X}_1 + \mathbf{X}_2 + ... + \mathbf{X}_l \tag{4.5}$$

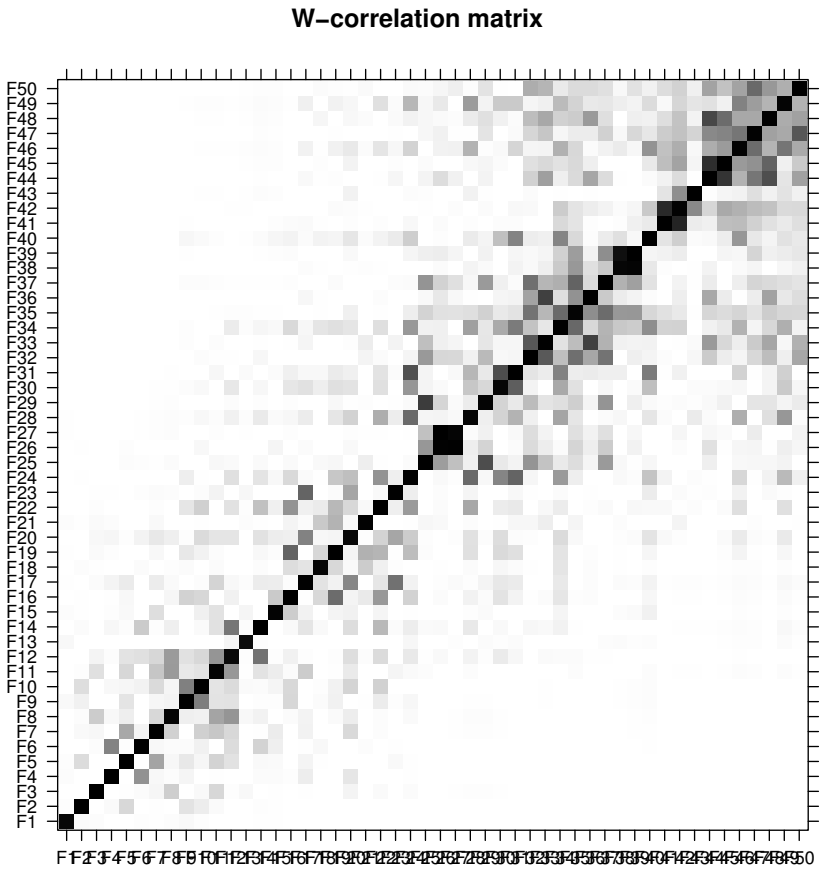

Figure 4.5 Example of w–correlation matrix. Different shades of grey are related to different levels of correlation between the respective components.

where $l = \max\{j : \lambda_j > 0\}$ and $\mathbf{X}_i = \sqrt{\lambda_i}\bar{d}_i\hat{e}_i$.

At this point one gathers the common components grouping the set of indices $\{1, \ldots, l\}$ into m disjoint subsets $I_1, \ldots, I_m$. For a subset $I = \{i_1, \ldots, i_p\}$, the matrix $\mathbf{X_I}$ corresponding to the group I is defined as $\mathbf{X}_I = \mathbf{X}_{i_1} + \ldots + \mathbf{X}_{i_p}$. Thus, the grouped matrix decomposition,

$$\mathbf{X} = \mathbf{X}_{I_1} + \ldots + \mathbf{X}_{I_m}. \tag{4.6}$$

The w–correlation matrix $\mathbf{W}$ provides a scale to measure the degree of correlation between this different eigenvectors. The elements of $\mathbf{W}$ can be written as

$$W_{i,j} = \frac{(X_1, X_2)}{\|X_1\|\|X_2\|} \tag{4.7}$$

where $(X, Y) = \sum_{i,j=1}^{L,K} x_{i,j}y_{i,j}$. An example of the the w–correlation matrix is illustrated in Figure 4.5

The last step of this procedure is the series reconstruction. To this aim, one has

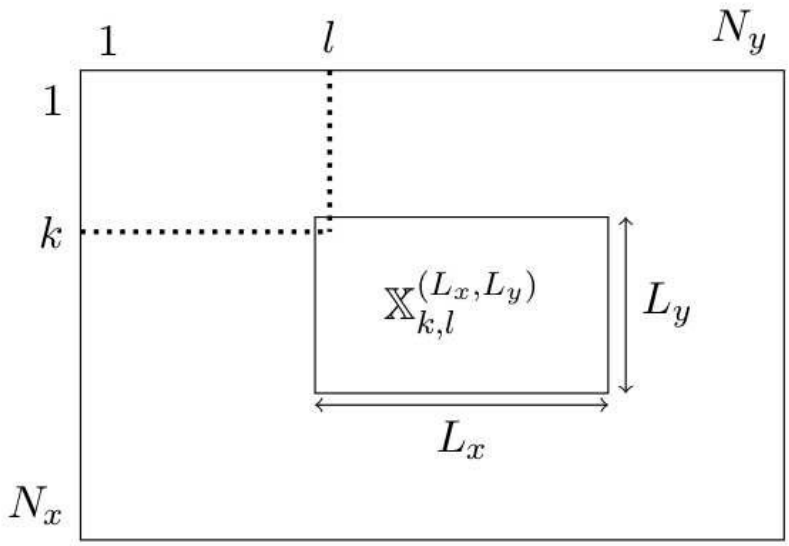

Figure 4.6 This image was taken from Golyandina et al. (2013). The figure exhibits how the sliding window moves in the 2–dimensions

to go through the 'hankelianisation' process. Each matrix $\mathbf{X}_I$ must be taken back to the hankelian form $\tilde{\mathbf{X}}_I$. This transition consists of averaging the anti diagonal elements of each matrix. From Eq. 4.6 one can write the corresponding series component and finally can write the the original series as the sum of different components.

$$X = X_1 + X_2 + \ldots + X_m \tag{4.8}$$

This technique can be readily extended to the 2–D case. This specific development is called 2D–SSA and is important to identify the noise components affecting the various images. The basic idea essentially remains unchanged. The main difference is in the structure of the trajectory matrix, in that it follows a Hankel-block-Hankel configuration rather than a simple Henkel. X is a 2–D data array of size $N_x \times N_y$ represented as $X = X_{N_x,N_y} = (x_{ij})_{i,j=1}^{N_x,N_y}$. A typical example could be a 2D–array of pixel values collected by a CCD of a standard digital camera. In this case I have to choose two different embedding lengths, L_x and L_y. Then I move to 2–D space with a $L_x \times L_y$ sliding window (Figure 4.6)

So, I can define a set of submatrices $X_{k,l}^{(L_x,L_y)} = (x_{i,j})_{i=k,j=l}^{L_x+k-1,L_y+l-1}$. In this context, the trajectory matrix is defined as:

$$\mathbf{X} = [\bar{X}_1 : \ldots : \bar{X}_{K_x K_y}], \tag{4.9}$$

where the columns are vectorizations of $L_x \times L_y$ submatrices:

$$\bar{X}_{k+(l-1)K_x} = vec(X_{k,l}^{(L_x,L_y)})$$

As defined above, the trajectory matrix has the following structure

$$\mathbf{X} = \begin{pmatrix} \mathbf{H}_1 & \mathbf{H}_2 & \mathbf{H}_3 & \dots & \mathbf{H}_{K_y} \\ \mathbf{H}_2 & \mathbf{H}_3 & \mathbf{H}_4 & \dots & \mathbf{H}_{K_y+1} \\ \mathbf{H}_3 & \mathbf{H}_4 & \ddots & \ddots & \vdots \\ \vdots & \vdots & \ddots & \ddots & \vdots \\ \mathbf{H}_{L_y} & \mathbf{H}_{L_{y+1}} & \dots & \dots & \mathbf{H}_{N_y} \end{pmatrix}, \tag{4.10}$$

where each $\mathbf{H}_j$ is an $L_x \times K_x$ Hankel matrix. This kind of configuration is called Hankel-block-Hankel. So, I have to bring back to this kind of structure during the reconstruction process.

Further details about the 2–D decomposition could be found in Golyandina et al. (2013) (Section 4).

4.4 Noise suppression procedure

To write a procedure that suppresses the noise effectively, I focus on the background part of the image. I implemented an iterative loop into my original R script to remove all the field sources. To this aim, I iteratively requested that the signal (counts) in each pixel must be lower than the average 2σ level. All the pixels above this limit were replaced with the average counts of the pixel array $\hat{C}$. This operation is repeated until the 2σ condition is fulfilled for all the pixels. After this source removal process, I decomposed the source–free image using the 2–D SSA resorting the R package proposed in Golyandina et al. (2013) (*Rssa*). An example of the different components is shown in Figure 4.7

I suppress the noise by removing the first 30 components. This is somehow arbitrary and depends on a trade–off based on the outcome of several preliminary trials. I remove this fixed number of components assuming that the dominant effects in the background are essentially noise (light gradient, wavy,..etc). This allows us to make the procedure unmanned and usable in an automatic way. To decompose the image, I have to choose an embedding length for both the 2–D: L_x, L_y (deriving K_x=N_x-L_x+1, K_y=N_y-L_y+1 respectively). Generally, both are assumed to be half of the total pixel size in the corresponding axis: L_x=N_x/2 and L_y=N_y/2. I take this as the best compromise, even

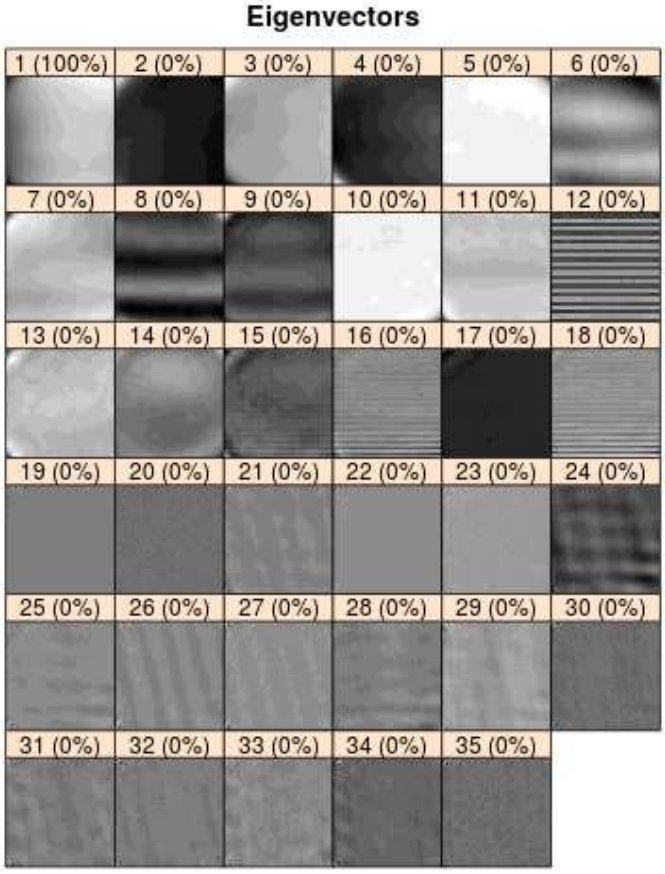

Figure 4.7 Classical example of 2D–SSA decomposition for a frame collected by RINGO3. The characteristic wavy components ere well identified (e.g. see 8 for low frequency and 16 for high frequency).

if in some cases I made a different choice. The prominent light gradient effects and the main noise components were removed effectively. By definition our method conceives the decomposition of the original series in an additive way.

$$C = C_1 + C_2 + ... + C_n n = K_x K_y \tag{4.11}$$

Therefore, each component is detected and removed by subtraction. In our procedure I also replace the removed components with their average value to keep the general counts level stable. This could be a problem when the noise is introduced by flat field distortions. As it is known, these corrections are being applied by division. In order to do this properly, I run our procedure on the logarithmic counts pixel matrix $\bar{C}$=$log(C)$. In this way I end up with a list of multiplicative components:

$$\bar{C} = \bar{C_1} + \bar{C_2} + ... + \bar{C_n} = log(\tilde{C_1}) + log(\tilde{C_2}) + ... + log(\tilde{C_n}) = log(\tilde{C_1} \cdot \tilde{C_2} ... \cdot \tilde{C_n}) \tag{4.12}$$

This simple trick allows us to suppress the selected components by division, applying a sort of flat field correction. In addition to *Rssa*, I used *FITSio* package to handle the frames reconstruction. The full code of these procedures (which remove the noise by subtraction and by division) are reported in AppendixC (Section 4.7).

In a further development of my procedure, I also tried to remove the vignetting effect through a dedicated procedure which isolates the image sides affected by such noise. Then I removed the vignetting components by division. Unfortunately, this process in its current implementation seems to impact on the photometric measures.

4.5 Results from the RINGO3 frames analysis

I applied this technique to several frames collected by different instruments. I test its wide versatility by applying it to RINGO3 frames as well as to other camera images, which are affected to a different extent from each other. The only limitation is given by the maximum size of the input frame which must be lower than 2000 pixels. Above this limit computational issues can arise and the procedure may become too slow or even crash.

In my analysis I used the RINGO3 frames collected from the observations of the GRB 140430A and GRB 140709A, consisting of a set of 10 exposures of 60 s each. Since the polaroid rotates through the 8 phase angles every second, each frame has an exposure time of $\sim$ 7.5 s. Co-adding these 10 frames collected for each angle, I end up with 8 images with $\sim$ 75 s of total exposure.

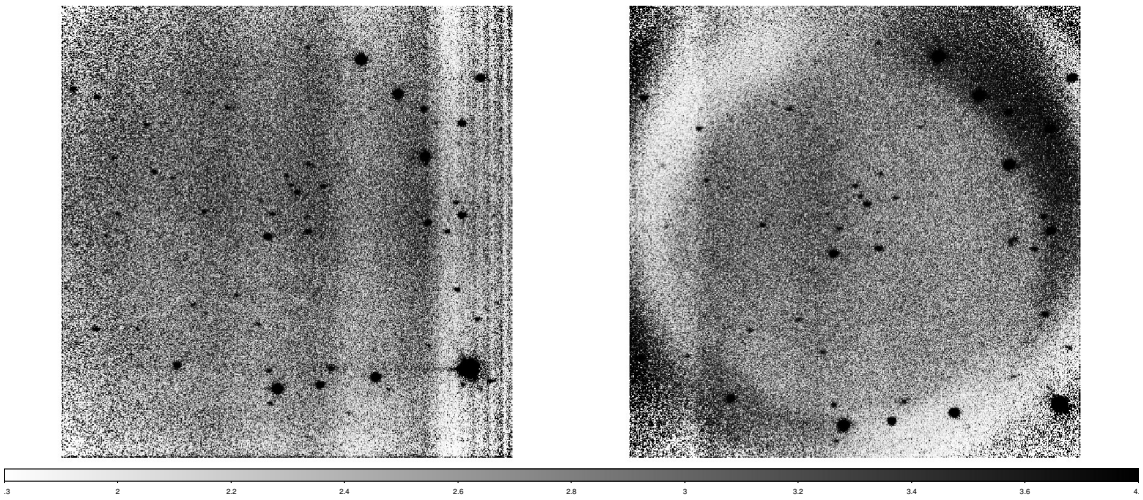

Figure 4.8 Two kinds of noises affecting the RINGO3 frames. *Left*: the linear wavy effect in the "Red" camera. *Right*: circular waves in the "Green" camera.

The main contribution to the noise is given by the wavy component which alters the background introducing either linear or circular pleating (Figure 4.8).

As a first step I investigate the nature of these components. In case of flat field components I should observe the same effect for all the frames collected in the same filter. To check this, I identified the noise components in each frame as described in Section 4.4. Then I compute the noise averaged matrix for each filter. I finally remove the respective averaged noise by division from each single frame of a given filter. As a final result the wavy effect does not disappear properly (see Figure 4.9).

Indeed the noise is still present and behaves differently in each frame. Therefore I excluded the possibility of a flat field distortion. I then decided to suppress the noise component by subtraction proceeding each frame at a time. The wavy effect now disappears almost completely (Figure 4.10).

4.5.1 Source extractor analysis

One of the basic goals of the cleaning process is to favour the source identification. To assess its capability, I took different frames collected with the three cameras. I analysed 6 frames linked to the two different sets of observations (GRB 140430A and GRB 140709A). Using a customised version of SExtractor 2.3.2 (Bertin & Arnouts 1996) I found a list of sources detected for each specific frame. Some fake sources were detected due to the vignetting effect. This effect is a bit more noticeable for the cleaned images. Obviously, only the real detected sources were considered for the assessment. I took into account only the real sources identified in both raw and original images. Concerning the

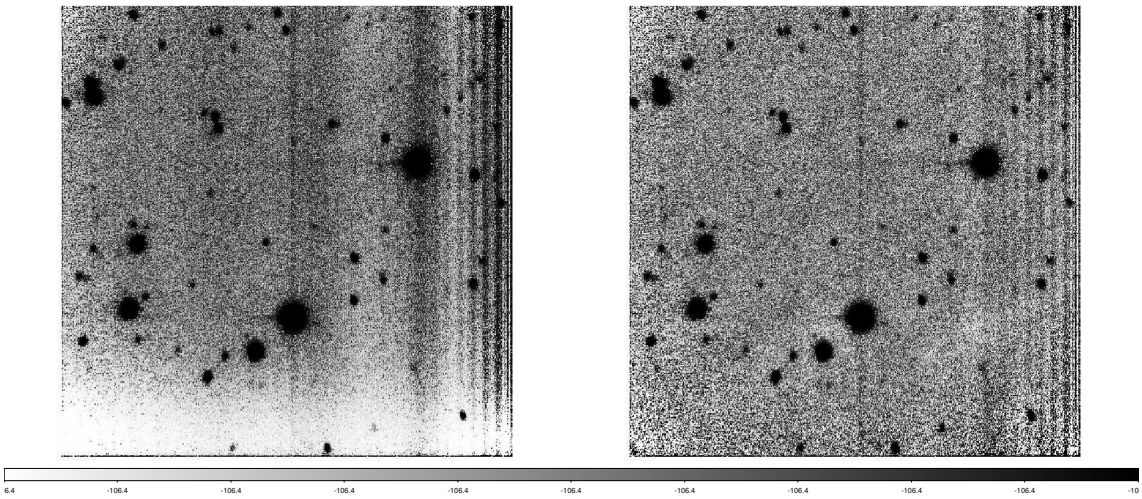

Figure 4.9 *Left*: original frame collected by the "Blue" camera. *Right*: cleaned frame in which I removed the average noise component computed for that filter. The wavy effect is not properly removed.

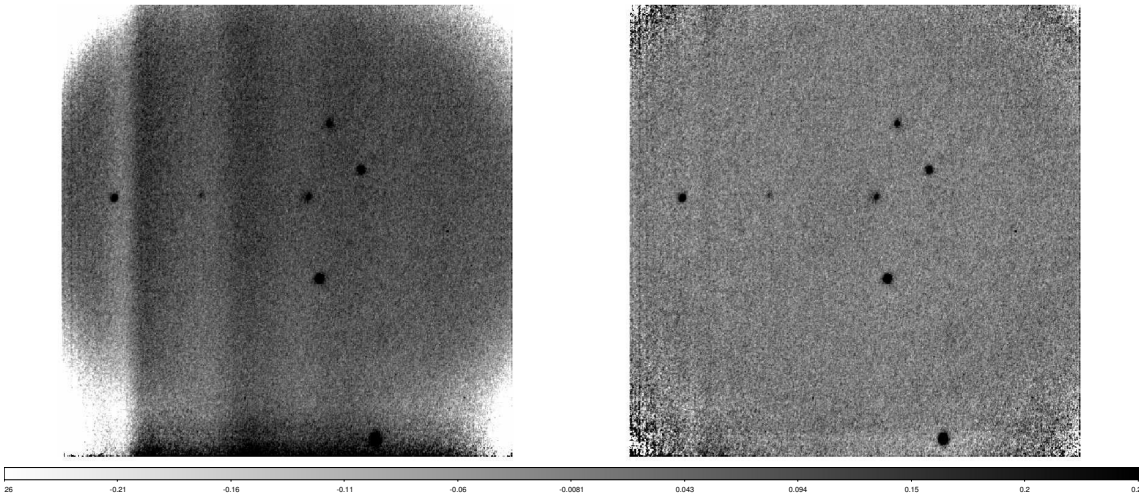

Figure 4.10 The potential of SSA method is illustrated in this figure. The wavy component is almost completely suppressed in this case. Also the vignetting effect is marginally reduced.

GRB 140430A frames I spotted a slight improvement in the "Red" and "Blue" filters. The average S/N value increases by 6.45% and 5.43% for the "Red" and "Blue" frames, respectively. The improvement is negligible in the images collected by the "Green" camera (0.46%).

A similar improvement can be seen for the frames collected for GRB 140709A, where the average gain is 5.71%, 8.28% and 5.69% observing with the "Red", "Blue" and "Green" filter respectively.

A brief report of this analysis is summarised in Table 4.1

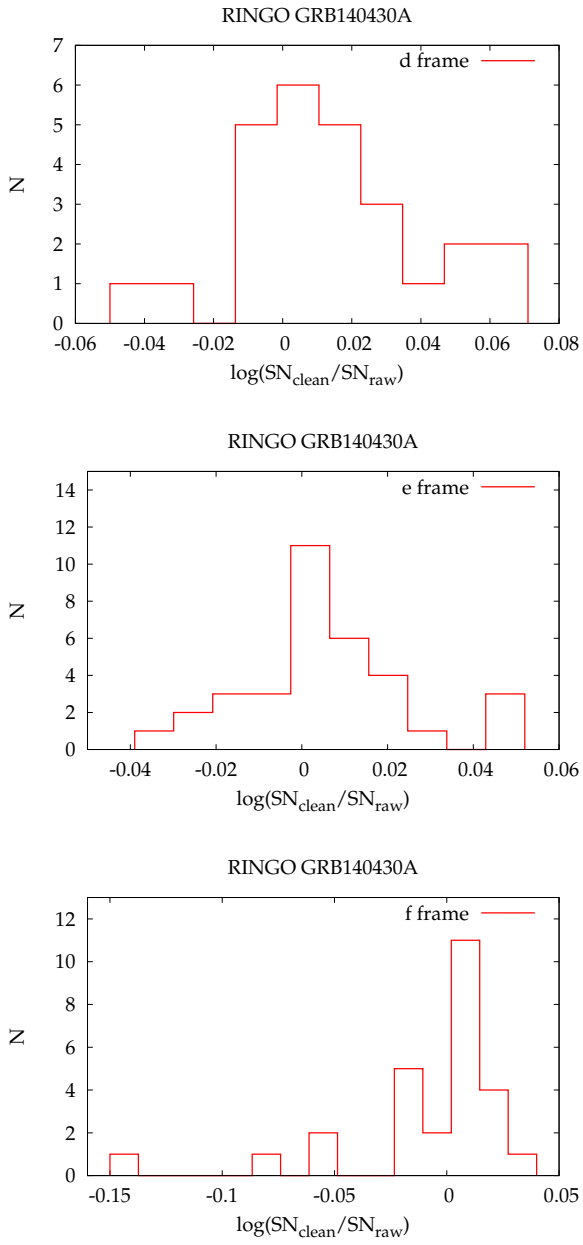

Figure 4.11 The logarithmic distributions of the S/N gain in the three cameras. The frames are collected during the optical observations of GRB 140430A. The S/N gain is expressed as the ratio between the S/N of a source in the cleaned image and the S/N of the same source in the raw frame

Table 4.1. Source Extractor analysis results.

Frame Name	Camera	Exposure (s)	Detected Sources Raw Frames	Real Sources Raw Frames	Average S/N [a] Raw Frames	Detected Sources Cleaned Frames	Real Sources Cleaned Frames	Average S/N [a] Cleaned Frames
RINGO3 140430A d	Red	74.68	27	27	168.56	26	26	179.44
RINGO3 140430A e	Blue	74.67	52	34	111.33	51	35	117.383
RINGO3 140430A f	Green	74.68	51	28	105.45	56	27	105.93
RINGO3 140709A d	Red	74.62	43	43	181.75	39	39	187.44
RINGO3 140709A e	Blue	69.31	42	41	195.06	46	36	211.22
RINGO3 140709A f	Green	71.48	42	32	189.22	42	31	199.98

Note. — Summary of the source extractor analysis conducted on the RINGO3 frames. The observations are referred to GRB 140430A and GRB 140709A optical counterparts. The extraction is performed for a frame in each filter.

[a]The average S/N value is computed considering only the real sources detected in both raw and cleaned frames.

Moreover, I inspected the possible gain or loss in terms of the S/N of each source with respect to the source brightness. In Figure 4.12 it is possible to see how the gain varies compared with the original S/N values. The gain expressed as the ratio between the S/N of the source in the cleaned image and the S/N measured in the raw one.

Overall the S/N tends to improve at S/N higher than ~ 20.

It is worth noting that the S/N improvement becomes more important for longer exposure times. The average S/N gain increases from $\sim$2% to $\sim 6\%$ passing from 7.5 s to 75 s exposure times. Hence the SSA cleaning technique can become more effective (in terms of S/N enhancement) for longer exposure times.

4.6 Conclusions

I exploited the potential of the SSA by applying 2–D extension of this technique to decompose an image into a set of fundamental components. I wrote an automatic R–procedure which resorts the 2D–SSA method to identify and suppress the noise components observed in the frames collected by RINGO3 (the optical polarimeter mounted at the focus of Liverpool Telescope). Then I studied the nature of this noise testing the case of a possible flat field distortion. The results show that this is not the case given that the noise contribution changes for different frames. Most likely this effect is due to stray light of the telescope. Moreover, I checked the effects of the cleaning procedure in terms of S/N. A slight improvement is observed $\sim 5\%$ for the sources with $S/N > 20$. Nevertheless I note that this improvement becomes more substantial for longer exposure times. Such a result is important especially during the *real–time* astrometric fit process. Indeed, the higher S/N ratio helps us to better recognise the known sources in the field of view and hence to provide a more robust sky mapping, with the possible identification of dim optical counterparts to GRBs or any other transients to be followed up. Unlike other more sophisticated techniques, this simple procedure is highly adaptable and it works individually on each single frame suppressing a wide range of noisy effects. Most of the noise removal methods are strongly specific (tailored to peculiar kind of noise) and they require a large amount of frames to characterise the noise components properly. Our approach is completely data driven. This allows us to better decompose the image compared with the other parametric techniques and, therefore, to better suppress the noise. The potential of this technique should be better explored by further analysis on new frames and cameras. A wide range of different kinds of effects can be suppressed in this way improving the data analysis process and

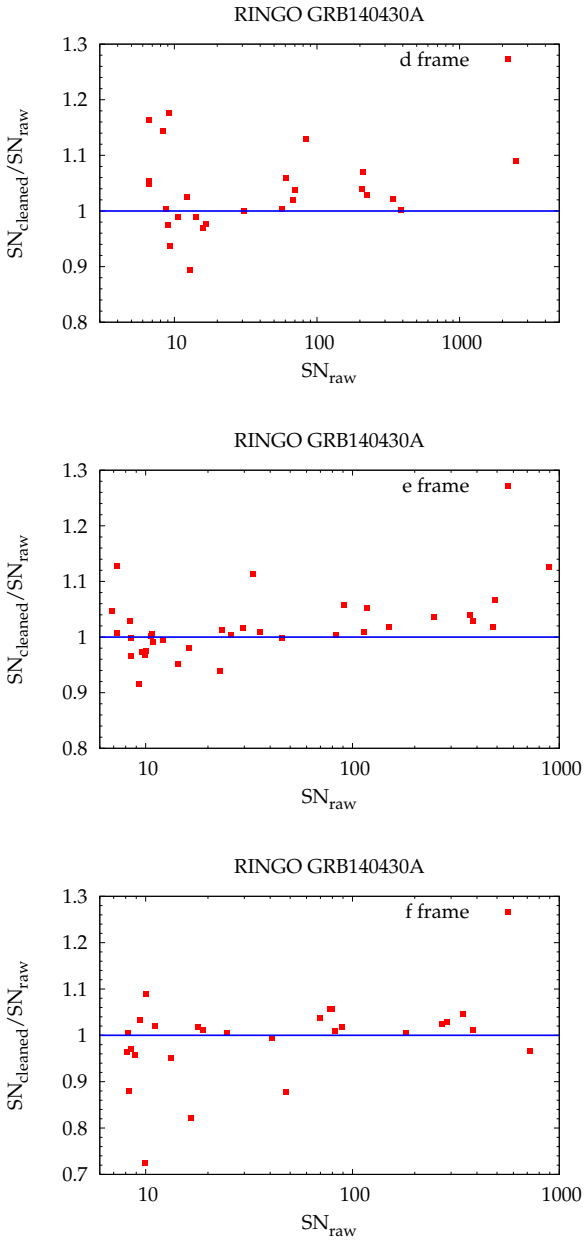

Figure 4.12 The S/N gain for each source is shown in comparison with the original S/N in the raw frame.

maximising the scientific outcome from the optical observations.

4.7 AppendixC

4.7.1 R procedure - Removal by subtraction

```
library(lattice)
library(Rssa)
require(FITSio)

#The aim of this software is to suppress the noise components from an arbitrary
#frame. It works on the pixel array by the sources removing iteratively and
#decomposing the background in order to identify and remove the noise.
#We apply the Singular Spectrum Analysis (SSA) technique using Rssa package
#proposed by Golyandina et al. (2013).

# Author: S. Dichiara
# Date: July 2014
# Version: 1.0


args=(commandArgs(TRUE))

root <- args[1]


fitsnamegz <- paste(root,".fits.gz",sep="")


if (file.exists(fitsnamegz)){
cpfitsnamegz <- paste("tmp_",root,".fits.gz",sep="")
commstring <- paste("cp",fitsnamegz,cpfitsnamegz,sep=" ")
system(commstring)
fitsname <- paste("tmp_",root,".fits",sep="")
commstring <- paste("gunzip ",cpfitsnamegz,sep="")
system(commstring)
} else {
fitsname <- paste(root,".fits",sep="")
}
fname3 <- paste(root,"_det0_sub.fits",sep="")


fits <- readFITS(fitsname)
data_pre <- (fits$imDat)

dimx <- dim(data_pre)[1]
dimy <- dim(data_pre)[2]


bs <- as.numeric(fits$hdr[which(fits$hdr=="BSCALE")+1])
bz <- as.numeric(fits$hdr[which(fits$hdr=="BZERO")+1])
bitpix <- as.numeric(fits$hdr[which(fits$hdr=="BITPIX")+1])
offset <- 32768
```

```
if (length(bs)==0) {
bs <- 1
}

if (length(bz)==0) {
bz <- 0
}

if (bitpix>0) {
data <- (((data_pre-bz)/bs)+offset)
} else {
data <- data_pre
}



# Sources iterative removal
ndata <- data
nsig <- 2.0

repeat {
   m <- mean(ndata)
   sigma <- sd(ndata)
   lim <- m + nsig*sigma

   nsources <- 0

   for(i in 1:dimx) {
      for(j in 1:dimy) {
         if(ndata[i,j] > lim) {
            nsources <- nsources+1
            ndata[i,j] <- m
         }
      }
   }

   if(nsources < 1) {
      break
   }
}


######## SSA
Lx <- dimx/2
Ly <- dimy/2

# SSA Decomposition
s.data <- ssa(ndata,kind="2d-ssa",L=c(Lx,Ly))

# to group the noise components (we assume the first 30).
r.data <- reconstruct(s.data,groups=list(1:30))

#To compute the average value of noise components
meanr <- mean(r.data$F1)
```

```
#Image reconstruct (to replace the noise with its average value)
if (bitpix>0) {
writeFITSim16i((((data-r.data$F1+meanr-offset)*bs)+bz),
 file = fname3, axDat=fits$axDat , header=fits$header)
} else {
writeFITSim((data-r.data$F1+meanr),
  file = fname3, axDat=fits$axDat , header=fits$header)
}

if (file.exists(fitsnamegz)){
commstring <- paste("rm ",fitsname,sep="")
system(commstring)
}
```

4.7.2 R procedure - Removal by division

```
library(lattice)
library(Rssa)
require(FITSio)

#The aim of this software is to suppress the noise components from an arbitrary
#frame. It works on the pixel array by the sources removing iteratively and
#decomposing the background in order to identify and remove the noise.
#We apply the Singular Spectrum Analysis (SSA) technique using Rssa package
#proposed by Golyandina et al. (2013).


# Author: S. Dichiara
# Date: July 2014
# Version: 1.0



args=(commandArgs(TRUE))

root <- args[1]


fitsnamegz <- paste(root,".fits.gz",sep="")

if (file.exists(fitsnamegz)){
cpfitsnamegz <- paste("tmp_",root,".fits.gz",sep="")
commstring <- paste("cp",fitsnamegz,cpfitsnamegz,sep=" ")
system(commstring)
fitsname <- paste("tmp_",root,".fits",sep="")
commstring <- paste("gunzip ",cpfitsnamegz,sep="")
system(commstring)
} else {
fitsname <- paste(root,".fits",sep="")
}
fname3 <- paste(root,"_det0_div.fits",sep="")
```

```
fits <- readFITS(fitsname)
data_pre <- (fits$imDat)

dimx <- dim(data_pre)[1]
dimy <- dim(data_pre)[2]



bs <- as.numeric(fits$hdr[which(fits$hdr=="BSCALE")+1])
bz <- as.numeric(fits$hdr[which(fits$hdr=="BZERO")+1])
bitpix <- as.numeric(fits$hdr[which(fits$hdr=="BITPIX")+1])
offset <- 32768

if (length(bs)==0) {
bs <- 1
}

if (length(bz)==0) {
bz <- 0
}

if (bitpix>0) {
data <- (((data_pre-bz)/bs)+offset)
} else {
data <- data_pre
}

for(i_ck in 1:dimx) {
    for(j_ck in 1:dimy) {
         if(data[i_ck,j_ck] <= 0){
         print("NEGATIVE_ELEMENTS")
         quit("yes")
         }
    }
}

# I work on the logarithmic counts array

logdata <- log10(data)


# Sources iterative removal
ndata <- data
nsig <- 2.0

repeat {
   m <- mean(ndata)
   sigma <- sd(ndata)
   lim <- m + nsig*sigma

   nsources <- 0

   for(i in 1:dimx) {
```

```
        for(j in 1:dimy) {
            if(ndata[i,j] > lim) {
                nsources <- nsources+1
                ndata[i,j] <- m
            }
        }
    }

    if(nsources < 1) {
        break
    }
}

logndata <- log10(ndata)

######## SSA
Lx <- dimx/2
Ly <- dimy/2

# SSA Decomposition
s.data <- ssa(logndata,kind="2d-ssa",L=c(Lx,Ly))

# Grouping noise components.
r.data <- reconstruct(s.data,groups=list(1:30))



# Average noise computation
meanr <- mean(r.data$F1)


# Reconstrucion. In this case raise the result as a power
# of 10 to return a counts array
if (bitpix>0) {
writeFITSim16i((((10^(logdata-r.data$F1+meanr)-offset)*bs)+bz),
 file = fname3, axDat=fits$axDat , header=fits$header)
} else {
writeFITSim((10^(logdata-r.data$F1+meanr)),
 file = fname3, axDat=fits$axDat , header=fits$header)
}


if (file.exists(fitsnamegz)){
commstring <- paste("rm ",fitsname,sep="")
system(commstring)
}
```

Chapter 5

Optical followup of fast transient events

5.1 Introduction

The real–time optical followup of the transient sky provides a basic tool to explore temporal properties of these kind of fast fading events. It is one of the main activities from the wide field of Time Domain Astronomy (TDA) which has been growing considerably in the latest years thanks to the development of synoptic sky surveys which have been providing and will provide us with large data sets. A wealth of new transient sources is to be expected in the near future, as is already the case for new classes of SNe. Some of the currently operational experiments in this field are CRTS, iPTF, Pan–STARRS for the optical and LOFAR, ALMA for the radio. TDA does not exclusively concern the electromagnetic emission, but also non–e.m. messengers, such as astrophysical neutrinos, cosmic rays, and gravitational waves. Main goals of these synoptic surveys are the identification, characterisation and monitoring of transient sources. GRB optical afterglows are one of the most common examples, but other new phenomena can also be investigated in the near future, *e.g.* the optical counterparts of a new class of transient radio sources known as Fast Radio Bursts (FRBs). These sources were discovered in the latest years by radio surveys with the Australian Parks telescope (Lorimer et al. 2007; Thornton et al. 2013), and recently confirmed in the Arecibo pulsar alfa survey (Spitler et al. 2014).

Several small telescopes are currently involved in the observation of GRB optical followup and other kind of transient phenomena, *e.g.* the ETC, LOTIS, ROTSE, and RAPTOR systems (Vanderspek et al. 1992; Park et al. 1998; Akerlof et al. 2000; Ves-

trand et al. 2002). But such projects are hampered by the lack of flexibility in their observation scheduling, since they cannot provide time-sampled data over a range of temporal cadences, dataset durations, and observing modes, in a routine and systematic way. Las Cumbres Observatory Global Telescope (LCOGT) is more suitable to meet all these requirements. It is the first general–purpose, flexibly–scheduled, multi–instrument optical observatory designed expressly to pursue astronomical research in time domain (Brown et al. 2013). Its success does not depend much on advancing the state of the art in telescope technology as on deploying a global network of telescopes that exploits all the communication, coordination, automation, and data-processing strategies made possible by modern computing networks. The combination of robotic telescopes with internet communication is a winning strategy, and one that should bring major advances in some branches of astronomical observing.

My goal here is to build up a set of automatic procedures which allow us to submit the observation requests, retrieve the data and process them in the most efficient way. Another goal is the testing of the network status (e.g. some bugs in the scheduler procedure or some problems with the cameras) and the response times in this very early stage of its operational life. All these activities were fulfilled under the proposal: "Fast Transients in the Era of Rapid Followup" (PI: Carole Mundell, Co-PI:Cristiano Guidorzi, other members: Drejc Kopac, Jure Japelj, Robert Smith, Andreja Gomboc).

5.2 Las Cumbres Observatory Global Telescope Network

The LCOGT network currently consists of two 2-m telescopes and nine 1-m telescopes scattered in different places of the world. The 1-m network consists of one telescope in the northern hemisphere at McDonald Observatory in Texas, and eight in the southern hemisphere (see Figure 5.1).

There are 3 units at Cerro Tololo InterAmerican Observatory (CTIO), 3 at South African Astronomical Observatory (SAAO) and 2 at Siding Spring Observatory in Australia. The 2–m telescopes (called Faulkes telescopes) are installed at Haleakala Observatory on Maui in Hawaii and at Siding Spring Observatory in Australia. The cameras of each telescope are different. The SciCam–Sinistro camera is currently (January 2015) working only in two of the three domes at Cerro Tololo. In all the others 1–m telescopes the SciCam-SBIG camera is operating, although a sequential replacement is planned. Indeed, all the SBIG cameras are going to be replaced with Sinistro given the better

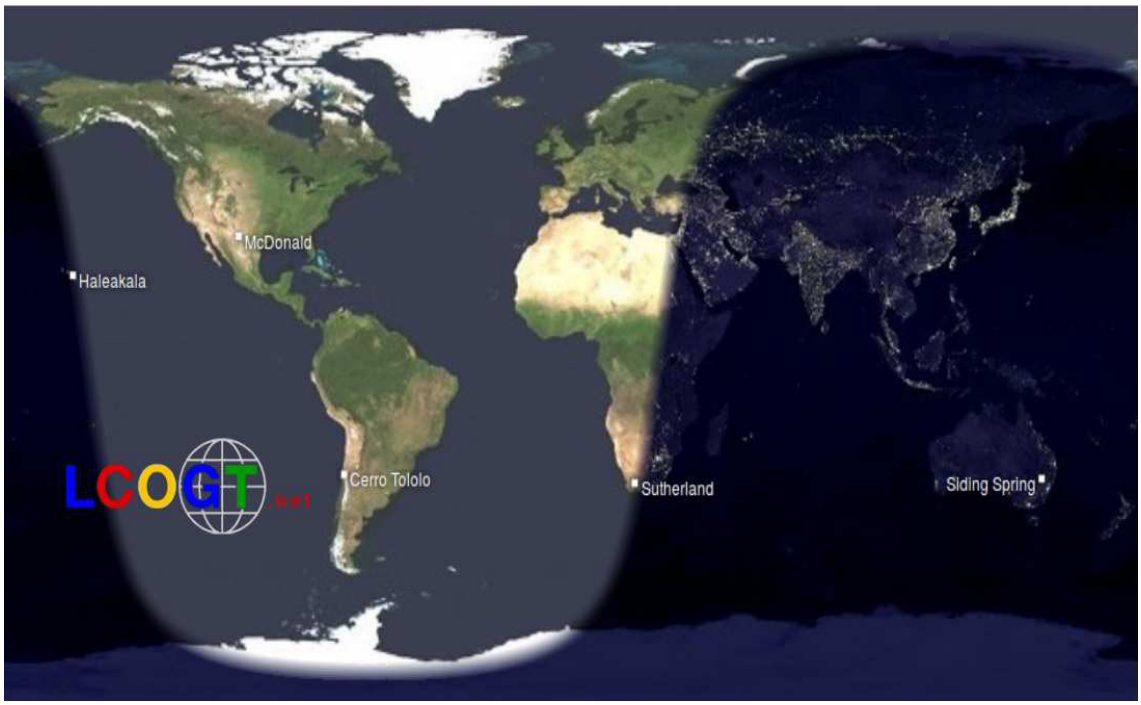

Figure 5.1 A world wide depiction of the Las Cumbres Observatory Global Telescope Network.

performance of latter. SciCam-Spectral is mounted on the two 2–m telescopes. All the camera features are summarized in Table 5.1

5.3 Software development

Using the potential of API (Application Programming Interface) we developed a set of simple scripts which allow the GRB team to submit observation requests, to monitor the status and to retrieve the collected frames as soon as they are made available, which typically happens within minutes of their acquisition. We implemented a set of routines which was able to pass all the main information to the scheduler procedure. Basically the following input information is requested:

- The observation name
- The equatorial coordinate (RA and DEC with reference to J2000 standard epoch.) Both the formats are allowed (degrees.hundredth as well as hour:minute:second.hundredth)
- Type of telescope (either 1 m or 2 m)
- Modality of observation: Normal mode or Target of Opportunity

Table 5.1. LCOGT Network Imager Characteristics.

Instrument name Camera type Detector type	Detector format Plate scale	QE_{max}	Readout (s)	$m(1e)$ (r')	Filters
Spectral (2.0) Spectral 600 FI CCD486 BI	4096 × 4097 × 15.0 10′.5 @ 0″.309 (2 × 2)	90%	11	24.6	u' g' r' i' z_s Y UV B V R_C I_C Hα Hβ [O III] DDO51 V+R ND2 V_s
SBIG (1.0) SBIG STX-16803 Kodak KAF-16803 FI	4096 × 4096 × 9.0 15′.8 @ 0″.464 (2 × 2)	50%	12	23.0	u' g' r' i' z_s Y w UV Bu V R_C I_C
Sinistro (1.0) Sinistro (LCOGT) FI CCD486 BI	4096 × 4097 × 15.0 26′.4 @ 0″.387 (1 × 1)	90%	4	23.5 est.	u' g' r' i' z_s Y w UV Bu V R_C I_C

Note. — (1) Instrument name, (telescope aperture in m), generic type of dewar/readout electronics, manufacturer's designation of detector chip. (2) Detector format shown as (X-dimension) × (Y-dimension) × (pixel size in μm); Plate scale shows field of view in arcmin, projected pixel size in arcsec at the indicated binning (e.g., 2 × 2). (3) Maximum detector quantum efficiency (percent). (4) Full image readout time, at the binning shown in column (2). (5) Stellar magnitude in r' producing 1 photoelectron per s. (6) List of filters normally mounted on the imager.

- The camera that we want to use in the case of 1 m telescope (SBIG, Sinistro)
- The window time within the requested observations must be collected
- The maximum value of the allowed airmass
- Sequence of exposures specifying the time and the filter for each one
- Pixels binning scale for each exposure.

The last parameter yields the number of pixels combined on the read-out to manage the S/N ratio. 1 × 1 provides no pixel combining with high resolution and low or poor S/N and is usually suitable for the Sinistro camera. 2 × 2 provides better S/N and a better match to the typical seeing conditions. The normal binning for Sinistro will be 1 (plate scale is 0.387 $''/pixel$) and 2 for SBIG and Spectra (0.467 $''/pixel$ and 0.309 $''/pixel$, respectively). All this information is implemented into the main body of the script, so-called "molecule". This script was developed in Python importing the following libraries:*os*, *string*, *re*, *sys*, *glob*, *datetime*, import *astLib*, *httplib*, *urllib* and *json*. The most important ones for our purpose are *httplib* and *urllib*. These modules define the classes to implement the client side of the HTTP and HTTPS

protocols and provide a high-level interface for fetching the data across the World Wide Web. *astLib* is the astronomy library and is mainly used to convert the coordinate from hour:minute:second to degrees (only degrees must be passed inside the "molecule" part). The airmass maximum value is usually fixed at 3. This configuration sets a minimum altitude of the source in the sky ($\geq 30°$). After the submission phase one checks the observation request status using another Python script. In this case the only input are the ID and the file name which is eventually created once the request has been completed. The output information summarised in this file is:

- Frame name
- Filter used to collect that frame
- Exposure time
- Start time of the observation
- Camera ID

Through another simple script we can also compute the time since the corresponding satellite trigger time. Once we have this list of frames we can download them directly from the main server using a devoted Shell script which combines the *wget* program capability with PHP server-side scripting language potential. When all the collected frames are downloaded and are ready to be processed, we fit the astrometry using the Astrometry.net routine ([1]). This basic step allows us to inspect the transient position looking for possible optical counterparts. Moreover the astrometry is a mandatory step for stacking. Then we selected the observations collected in different filters neglecting all the very noisy or poor images. Using a co–adding procedure, we stacked all these frames ending up with a single frame in each filter. This procedure resorts to the WCS tools and the HEASARC ftool in order to remap (*remap*) and to add different frames (*fcarith*), respectively.

Lastly, we can decide to crop the image around the target of interest shrinking the large FOV of LCO frames. This is particularly useful during a real–time followup to speed up the process. Therefore we also implement this program which takes the input as the coordinates of the OT (or the pixel position on the CCD). As an output, it crops the image around this position using a given size.

[1] http://astrometry.net/

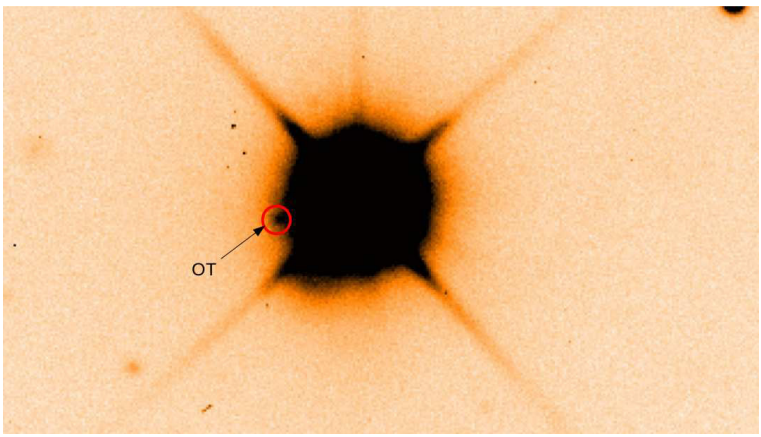

Figure 5.2 r'–band optical counterpart of GRB 140903A. The source lies right behind a 13.8 magnitude star and the photometry measure is heavily affected.

5.4 GRBs Followup activity

Since early June 2014 I repointed the network telescopes to 11 GRB optical counterparts. The results are summarised in Table 5.2

I extracted the photometry using starlink GAIA [2]. When feasible, the magnitude values are derived using the PSF technique (which takes into account the proper shape of the Point Spread Function), with the exception of GRB 140903A for which I used the aperture photometry. Indeed, in this case the OT stands right on the side of a very bright field star (see Figure 5.2).

Further observations along with precise source subtraction showed that the real flux was actually lower compared to the values reported in the early GCNs. The magnitude measure was strongly influenced by the brightness of the star and the host galaxy. This GRB was particularly interesting considering its short nature and surrounding field. Indeed it lies at the centre of a galaxy cluster. The two nearest galaxies with known redshifts are SDSS J155208.34+273631.8 at $z = 0.073$ (1.05' angular distance) and 2MASX J15520787+2735016 at $z = 0.075$ (1.47' angular distance). I kept on monitoring two GRBs discovered by *Fermi*/LAT during our activity, GRB 140928A (Desiante et al. 2014, GCN 16847), GRB 141028A (Bissaldi et al. 2014, GCN 16969). In case of GRB 140928A I also identified the possible host galaxy (Figure 5.3). Indeed, in the late observations of this GRB ($\sim$ 2.84 day after the trigger) I spotted a faint structure at $\sim$ 2.3 arcsec from the OT. Just as a simple exercise I tried to estimate the distance assuming an arbitrary redshift $z = 1.5$. I found a distance of $\sim 20kpc$ (ΛCDM model) from the possible "host" which does not sounds like a totally unrealistic case.

[2] http://star-www.dur.ac.uk/ pdraper/gaia/gaia.html

Table 5.2. Short list of optical transients re–pointed using the LCO telescopes.

Targhet name	GCN number	Mid. time from trigger (hours)	Exposure (s)	Filters	Magnitude	Telescope
GRB 140705A[c]	16529	0.87	120x4	i'	> 21	2.0m @ Haleakala
GRB 140719A[c]	16612	3.64	120x4	r'	> 21	2.0m @ Siding Spring
		3.80	120x4	i'	> 20.2	
GRB 140730A[a]	16647	5.64	120x5	r'	> 20	1.0m @ Sutherland
		5.83	120x5	i'	> 19.8	
Fermi 430148973 MASTER candidate [a]	16723	4.51	120x9	r'	> 20.4	1.0m @ Sutherland
		4.57	120x8	i'	> 19.6	
GRB 140903A[c]	16781	15.71	120x8	r'	20.04 ± 0.50	2.0m @ Haleakala
		16.03	120x8	i'	19.54 ± 0.50	
GRB 140916A[c]	16821	1.26	60x7	r'	> 20.4	2.0m @ Siding Spring
		1.44	60x5	i'	> 18.7	
GRB 140928A[b]	16851	18.9	120x5	r'	20.10 ± 0.20	2.0m @ Cerro Tololo
	16853	45.04	120x14	r'	21.20 ± 0.10	
GRB 141015A[a]	16915	0.91	120x5	r'	> 19.6	1.0m @ McDonald
		0.99	120x5	i'	> 18.7	
GRB 141028A[a,b]	16985	10.2	120x5	r'	19.40 ± 0.10	1.0m @ Sutherland
		10.6	120x8	i'	19.30 ± 0.20	1.0m @ Sutherland
		14.9	120x5	i'	19.90 ± 0.20	1.0m @ Cerro Tololo
GRB 141121A[c]	17082	7.0	120x5	r'	19.62 ± 0.06	2.0m @ Haleakala
		7.2	120x5	i'	19.42 ± 0.06	
	17092	55.44	120x10	r'	20.61 ± 0.04	
		54.96	120x10	i'	20.34 ± 0.05	

Note. — All observations were reported in Gamma-ray Coordinates Network circular archive.

[a]Collected with SBIG camera

[b]Collected with Sinistro camera

[c]Collected with Spectral camera

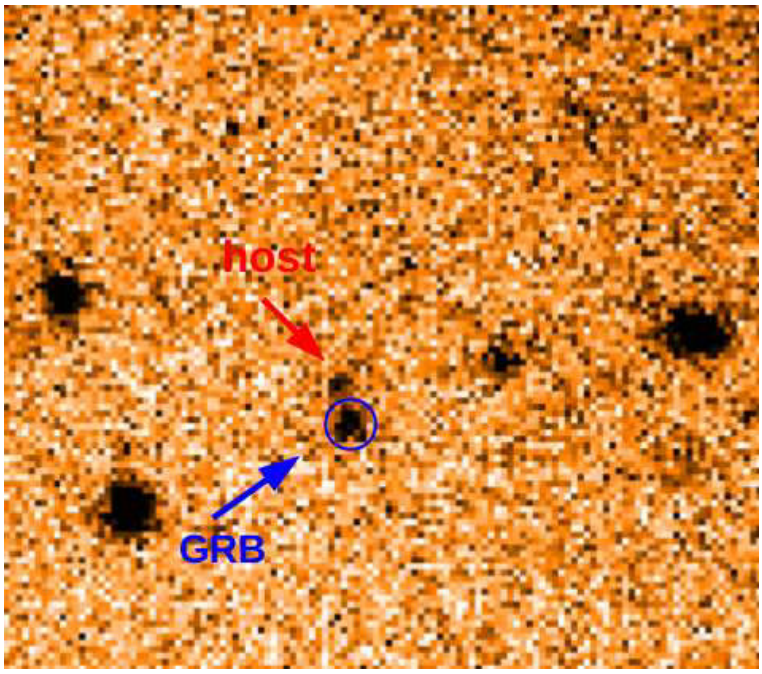

Figure 5.3 Optical counterpart of GRB 140928A. After $\sim$ 2.8 days since the GRB I could identify the possible host galaxy $\sim 2.3''$ away from the OT.

I estimated an afterglow decay index of -1.2 ± 0.2 and -1.6 ± 0.1 for GRB 140928A and GRB 141028A, respectively. These indices are referred to the r' and i' filter for GRB 140928A and GRB 141028A, respectively.

5.4.1 GRB 141121 Optical rebrightening

For this GRB I re–pointed at the position $\sim$ 6.9 hrs after the trigger. I immediately noticed that the magnitude values (r' and i') were slightly higher with respect to the first measures provided by GROND at $\sim$ 2.02 hrs from the trigger (Tanga et al. GCN 17078). I found $r' = 19.62 \pm 0.04$ with respect to the value $r'_{GROND} = 19.80 \pm 0.10$ about 4.6 hours before. The same behaviour was also observed using the i' filter. This evidence can be interpreted both as either the peak of the optical afterglow (which would have occurred later than usual), or as a late rebrightening. After a shallow decay the light–curve breaks into a steep decay passing from $\alpha = -0.76 \pm 0.04$ to $\alpha \sim -1.4$ at $\sim$ 0.8 days. After this break a new rebrightening set in at $\sim$ 1.16 days peaking after $\sim$ 3.5 days from the initial trigger. A new steep decay phase finally took over after this second peak ($\alpha = -1.73 \pm 0.05$).

This very peculiar behaviour makes this GRB afterglow one of a kind. Similarities can be identified comparing the X-ray and optical light curves (Figure 5.5), even if the optical curve seems delayed with respect to the X.

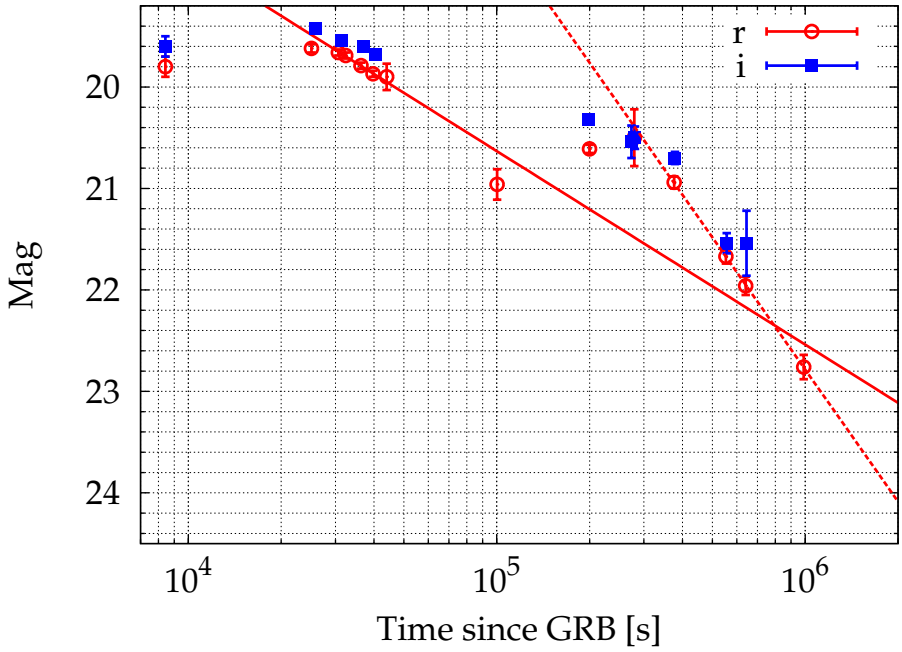

Figure 5.4 The lightcurve of GRB 141121A in the r' and i' filters. The first peak is followed by a second rebrightening. Solid and dashed lines show the shallow decay after the first peak ($\alpha \sim -0.8$) and the final steep decay after the rebrightening ($\alpha \sim -1.7$), respectively.

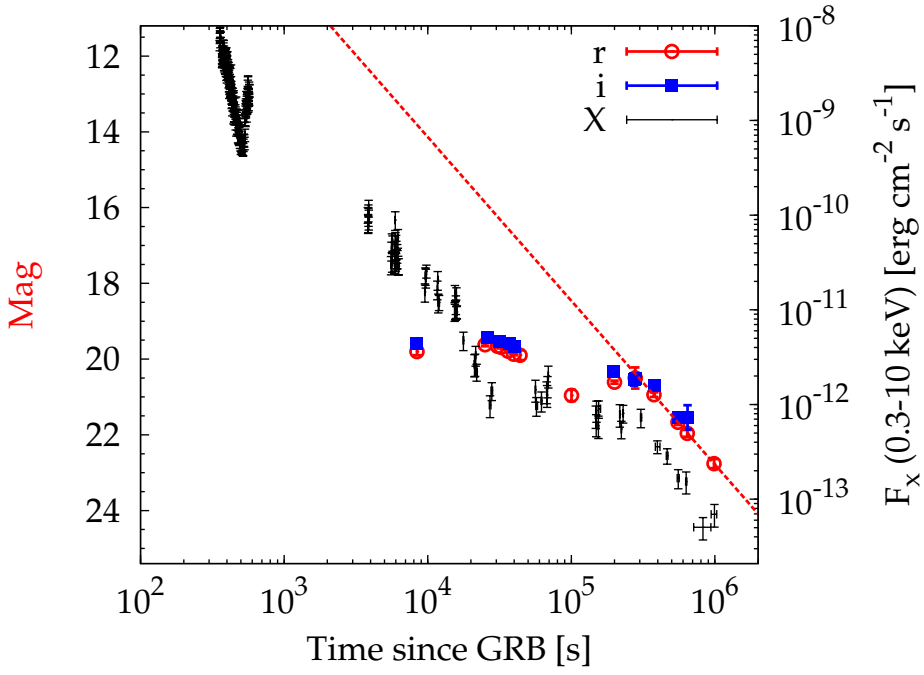

Figure 5.5 GRB 141121A X-ray lightcurve (XRT data) is shown with the optical ones (r' and i') to emphasise the possible common behaviour.

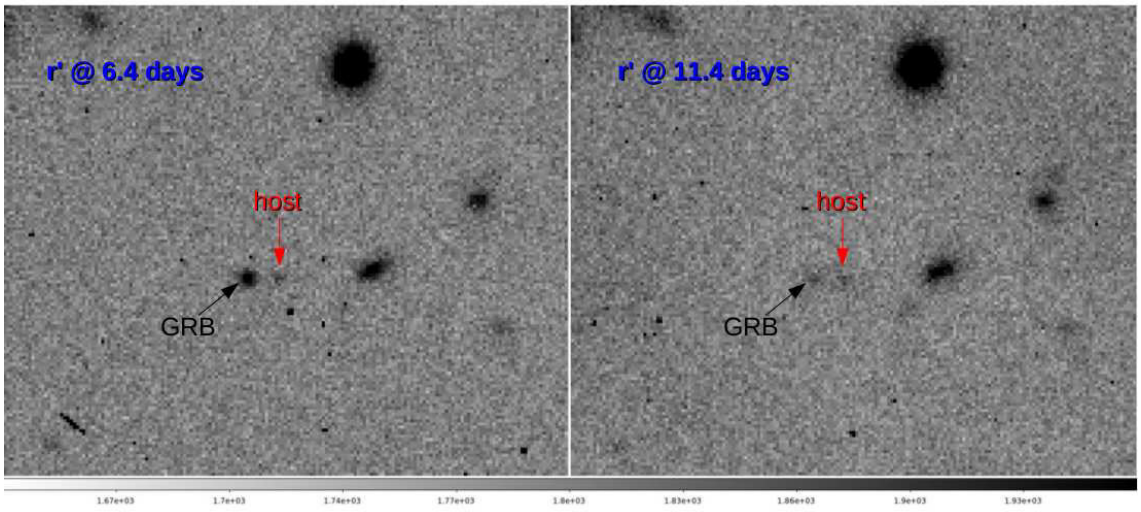

Figure 5.6 Fading GRB 141121A optical counterpart at 6.4 days (left) and at 11.4 days (right). The possible host lies in the nearby. This source lies at $\sim 2.8''$ which corresponds to a distance of ~ 23 kpc, assuming $z = 1.47$ and a standard cosmology (ΛCDM).

These similarities indicate that the same source region is likely to be responsible for the emission in both bands. However, the two curves do not appear to track each other exactly, which indicates that multi-band modeling is crucial to explore the rich physics probed by this event.

The Keck I 10–m telescope observations provided a redshift value ($z = 1.47$, Perley et al. 2014, GCN 17081) allowing to study the intrinsic properties of this GRB. After ~ 2.3 days a faint source appeared in the 1200-s exposure frames at $\sim 2.8''$ from the OT. At ~ 11.4 days from the trigger the two magnitudes became comparable (Figure 5.6). Assuming it as the host galaxy and considering the provided redshift ($z = 1.47$), I estimated the GRB-host corresponding distance, ~ 23 kpc. The obseved magnitude for this source ($r' = 23.06 \pm 0.27$) is consistent with the values found for the GRB host galaxies at that redshift (see Figure 5.7).

We still (January 2015) monitor this source planning a set of radio observations involving the e-MERLIN/VLBI facility and the Very Large Array (VLA) radio telescope.

5.5 Interactive Debugging and Response times

Another important contribution is given in terms of network testing and debugging. In its prime, a thorough calibration work of the network was required. Different sorts of problems were diagnosed during our activity, e.g. camera malfunctioning, slow reaction

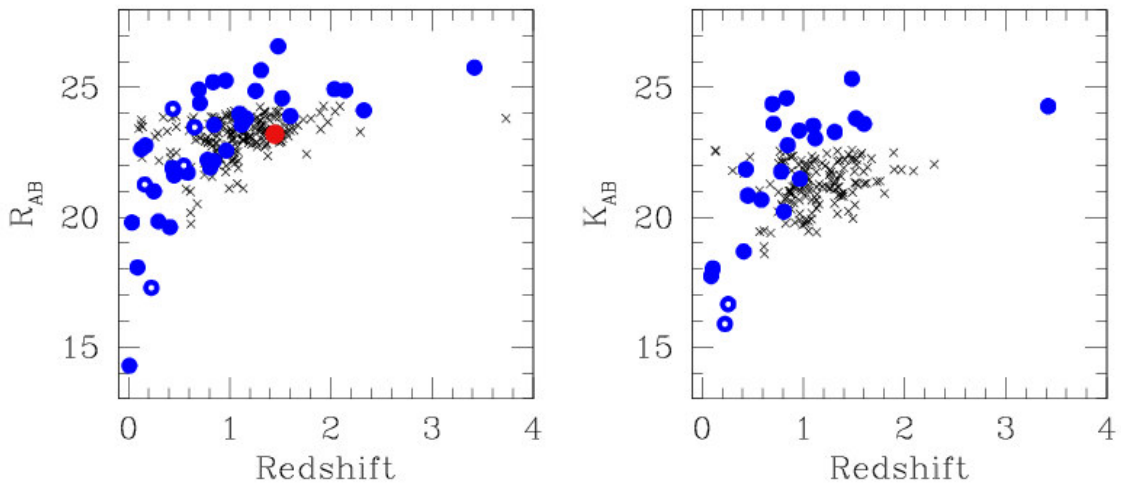

Figure 5.7 This picture was taken from Savaglio et al. (2009). R_{AB} (left plot) and K_{AB} (right plot) observed magnitudes as a function of redshift, for GRB hosts (filled circles) and Gemini Deep Deep Suvey field galaxies (crosses). The filled circles with white dots are short-GRB hosts. The red filled circle shows the GRB 141121A host candidate.

times, data retrieval problems, etc. The SBIG cameras are affected by "ghost" sources problem. Indeed, in some cases fake sources are clearly recognizable in the collected frames, as was the case of GRB 140723A. In a first quick look at the collected images I found an OT exactly in the middle of the error box provided by Fermi/LAT (Bissaldi et al. GCN Circ 16623). This object turned out to be spurious in the processed images (see Figure 5.8). Maybe this effect is derived from the remains of the very bright source at that position, inherited from the previous scheduled observation.

Another important issue is the time needed for submitting the request, initiating the followup observation. As soon the target becomes observable from a given site, speed is a key ingredient to avoid waste of time. Although the announced execution time for the Target of Opportunity (ToO) request was less than 15 minutes, earliest attempts revealed quite longer reaction times. When I tried to observe GRB 140706A, the telescope had a delay of > 2 hrs after it became observable. Thanks to my own feedback, the LCOGT scheduler has improved substantially. Currently, the observations start within a few minutes from the ToO submission. A key ingredient to optimise the response is the time window chosen for the observation. I found out that very long time intervals make a prompt reaction less likely to be performed, because the priority of the request lowers down. On the other side, too short time windows can make the request unschedulable. A fair trade–off for default requests seems to be a ~ 3 hours window time.

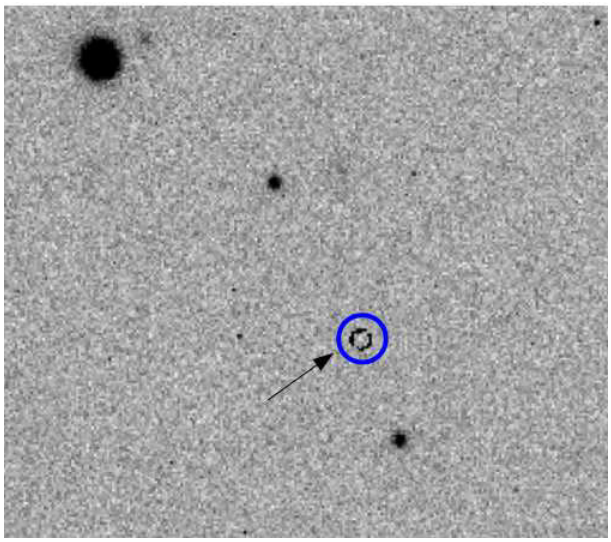

Figure 5.8 Processed frame collected by the SBIG camera on the south african 1–m telescope (dome C). After the reduction process the source (blue circle) disappeared leaving the ring–shaped structure on the CCD.

We also reported other problems in the scheduler procedure. In some cases the same request was rescheduled several times in a row and the observations were attempted repeatedly and unsuccessfully. In a test carried out on the McDonald 1-m telescope I tried to submit a request to collect a single frame with 30 sec exposure. In this case the observation was rescheduled 4 times and 3 different images were collected. For longer exposure, this multiple observations can generate substantial loss of allocated observational time. This problem seems to be resolved now (January 2015), but the complications in managing long sequences remains unsettled. I decided to face this limitation by splitting the single request into a list of simpler/shorter requests following a modular philosophy, e.g. I manage filters separately (5×60 sec $i' + 5 \times 60$ sec r') in two different requests (one for each filter). Also in this case it was a matter of trade–off. I could not split too much, otherwise the scheduler procedure could get overloaded.

Recently (January 2015), some data retrieval problem was noticed for the frames collected from the new SBIG camera mounted in the dome A at Cerro Tololo. The first images became available only after 2 days from the observation. I reported on this telemetry problem to the LCOGT staff who quickly fixed the bug.

Many other little issues have continuously been found, but a close interaction with the LCO team could improve the efficiency of this facility substantially.

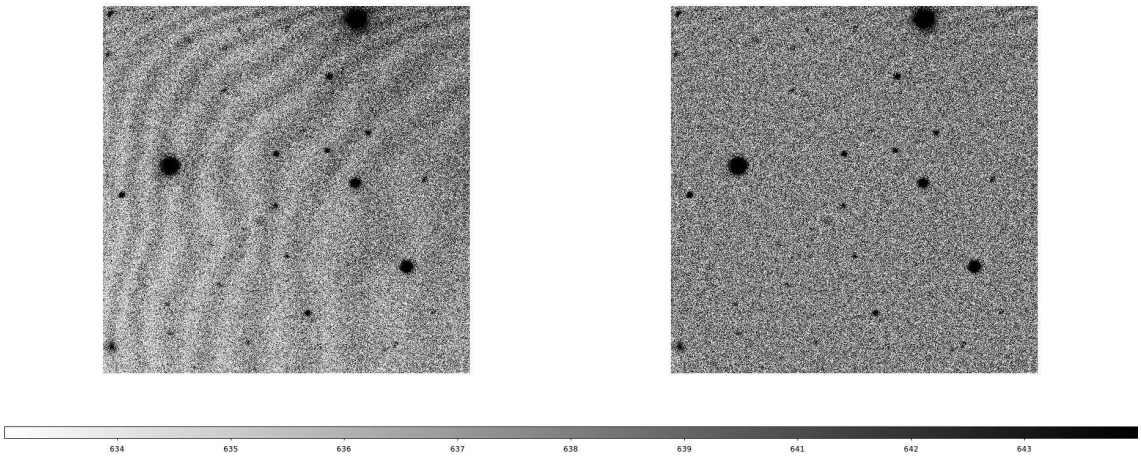

Figure 5.9 Example of 2D-SSA cleaning applied to i' frames obtained with the Spectral camera mounted on the Haleakala 2–m telescope. The fringing is completely removed using this method.

5.5.1 2D-SSA on LCO frames

The high versatility of the 2D–SSA technique is described in Chapter 4 allowing us to test its capability on the LCO as well. In this case, the main problem is the strong fringing effect of the Sinistro cameras and the Spectral camera. Fringing in CCD images occurs due to an interference effect. The occurrence of the constructive and destructive interference patterns can cause substantial quantum efficiency variations in the thinned CCDs. The reason behind this is the fact that the long wavelength light is multiply reflected between the front and back surfaces. It starts being an issue when the absorption depth within the silicon becomes comparable to the thickness of the CCD. This occurs for optical wavelengths of 700 nm or longer for which the light is internally reflected several times before finally being absorbed (Howell 2006). Indeed, this effect is markedly visible for the frames collected using the i, z and Y filters. This kind of noise is suppressed satisfactorily using this peculiar method (Figure 5.9).

In this case the noise component is to be removed by division considering the nature of this kind of distortion.

5.6 Conclusions

In this early stage of the new LCOGT network, our work delivered useful tools which substantially improve its performance. I refined the network capability to followup transients effectively and promptly. Through a set of newly developed software,

I optimised the observational procedures: request submission, reaction time in starting observations, reaction time in data retrieval, and effectiveness in real–time data analysis. I supplied some scripts to allow a very fast submission ending up with the best parameters to achieve it. Then I developed a set of programs to retrieve the frames, to custom them for the analysis as soon as the observation is completed. These scripts allow the GRB team to detect several optical counterparts (Table 5.2) and to describe the very peculiar behaviour of GRB 141221A. In some cases I was able to recognise the GRB host galaxy. Moreover, several issues concerning the reaction time, camera problems and data retrieval were sorted out thanks the close interaction with the LCO team. Ultimately, I also explored the potential of SSA technique described in the previous chapter to suppress the noise due to fringing-field effect. Future efforts will aim at tailoring the pipeline to the new targets and to the new network of 1–m and 2–m LCO telescopes. Our group has a major 5-year guaranteed time observing programme begun 2014. The combination of automatic followup, robotic imaging and source identification followed by fully automatic spectroscopy is a major new capability that will be further developed in the next years.

Chapter 6

BeppoSAX/GRBM Catalogue of Solar X–ray Flares

6.1 Introduction

Solar X–ray flares are some of the most powerful transient energy emissions released from the Sun ($\sim 10^{28} - 10^{32}$ ergs in $10^2 - 10^3$ s). The standard theoretical explanations proposed resort to fractal-diffusive avalanche model of a slowly driven self-organized criticality (FD-SOC) (Lu & Hamilton (1991),Aschwanden (2011), Aschwanden (2013); Pruessner (2012)). In this interpretation the process is dominated by a non–linear dynamics. Such non–linear systems are driven into a critical state, which is maintained by a self–organizing feedback mechanism. The magnetic reconnection model can be included in this scenario Shibata & Magara (2011). Other results support the collisional thick-target model in which the non–thermal electrons are accelerated in the corona and are streamed into the lower atmosphere (Su et al. 2011). Some authors also propose some possible connection between the physical mechanism at the origin of the solar flare emission and the X–ray flares observed during the GRB X–ray afterglow based on the similar waiting time distributions (Wang & Dai 2013; Guidorzi et al. 2015). This distributions exhibit a power–law tail behaviour with indices in the range $2.0 - 2.4$ across several decades (Boffetta et al. 1999; Wheatland 2000), depending on the class of the flares and flux thresholds. Related bursty emission from the Sun such as coronal mass ejections (CMEs) are found to show very similar distributions, whose index ranges from ~ 1.9 to ~ 3.0 in low to high activity periods of the solar cycle (Wheatland 2003). Likewise, the waiting time distributions of solar radio storms (Eastwood et al. 2010), of solar energetic particle and of solar electron events show very similar power–law indices

(Li et al. 2014).

The spectra of solar X–ray flares are definitely non–thermal and are fitted using either a single or a double power–law models with a break around 50 keV. In some models, this break can be due to a non–uniform ionization in the emission region. This can generate a flattening slope in the spectra depending on the power law index of the energy injection distribution (Su et al. 2009, 2011). A spectral evolution was also observed. Actually this break can also arise from different processes as additional components (X–ray photons reflected at the solar photosphere (Kontar et al. 2006; Kontar & Brown 2006; Zhang & Huang 2004) or instrumental effects.

The aim of the following work is the compilation of a comprehensive catalogue of the solar X–ray flares detected with *BeppoSAX*/GRBM. The aim of this project is to make publicly available the GRBM data on this kind of solar transients, exploiting the unique combination of temporal resolution, stable background and large effective area of the GRBM so as to further characterise spectral and timing properties of the high–energy activity of our own star.

6.2 Detection Algorithm

We analysed the entire GRBM archive from April 1996 to April 2002. Using a designed detection algorithm we passed through the continuous mode light curves (1.024 s time resolution) looking for possible transient events. I first extracted the light curves in two energy ranges: $40 - 700$ keV and > 100 keV. I then corrected each light curve for the specific dead time (4μs). The detection algorithm analysed the $40 - 700$ keV data within a moving window of 300 s. It fitted each 300 s interval using a two–degree polynomial selecting all the poor fit cases. The procedure used different methods to check the goodness of the fit. We set a threshold on the reduced χ^2 value (3.0) as well as on the maximum discrepancy between the fit model and the data in individual bins (expressed in terms of Gaussian sigma. I fixed this value at 5). Moreover, we introduced another criterion which set a limit on the run test probability. The run test (also called WaldWolfowitz test) is non–parametric and tests the hypothesis that the elements of a given sequence are mutually independent and oscillate around a given value independently. In our case we have a sequence of flags, 'up' or 'down', according to the observed value in each time bin being above or below the model. The number of runs, in this context, is the number of consecutive intervals in which the flag remains the same (e.g. a sequence 'up', 'up', 'up', 'down', 'down', 'up', 'up', 'down', 'down', 'down'

consists of 4 runs). The run test is based on the null hypothesis that each element in the sequence is independent from the others. In this way we actually test possible degree of correlation between residuals. If there are too few runs, data oscillate too few times around the model, which is evidence for the presence of trends in the residuals, that is, a poor description of the data. On the other side, too many runs tell that data points are oscillating around the model too frequently with respect to the case of statistical independence. In our survey we set a lower limit for the run test probability at 10^{-4}.

One might wonder why applying the run test in addition to the χ^2 one. The reason is that the latter tests the distribution of the discrepancy between data and model as a whole regardless of the sequence, which is instead what the former cares about. In other words, in the presence of trends between data and model, too few runs are expected because data points are no more independent from each other. For example, in the absence of trends but when the data are too scattered around the model only the run test is fulfilled. By contrast, when the failure of the χ^2 test is also due to the presence of trends in the residuals, the run test will fail too. Thus, applying the run test is key to the identification of trends, which is exactly what one ends up with when the parabolic fit is screwed up by the presence of huge transients, such as energetic solar X–ray flares: an example of this is displayed in Figure 6.1.

The algorithm also copes with telemetry gaps in the light curves, e.g. when the satellite crosses the South Atlantic Geomagnetic Anomaly (SAGA). It automatically requires that minimum 70% of the time window gets covered by the data, otherwise it is just overlooked. The procedure reports the following output information:

- Reduced χ^2 at the detection time
- Residual (Gaussian σ's) of the maximum excess from the fit model
- Number of runs
- Run–test probability
- Time of the maximum excess (detection time), time boundaries and central time
- Best fit parameters.

Another simple script is then used to convert all the detected times from Seconds of Day (SOD) to Universal Time (UT).

The same detecting procedure provides information about the position of the Sun both in terms of equatorial coordinates (J2000) and local coordinates to the spacecraft

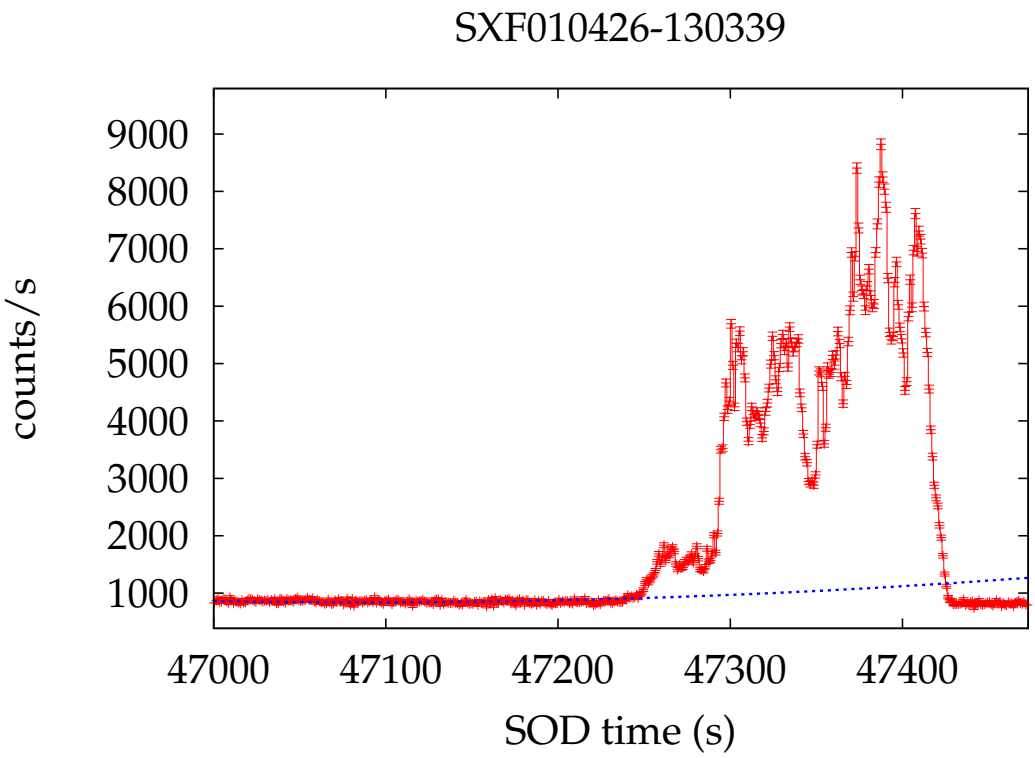

Figure 6.1 Example of solar X–ray flare automatic detection. The dotted line is the best fit model for the background. As soon as the transient event arises, the model exhibits trends which make the run test fail. This solar flare occurred on April 26, 2001 (UT 13:03:39). Time is expressed in terms of "Second of Day" (SOD).

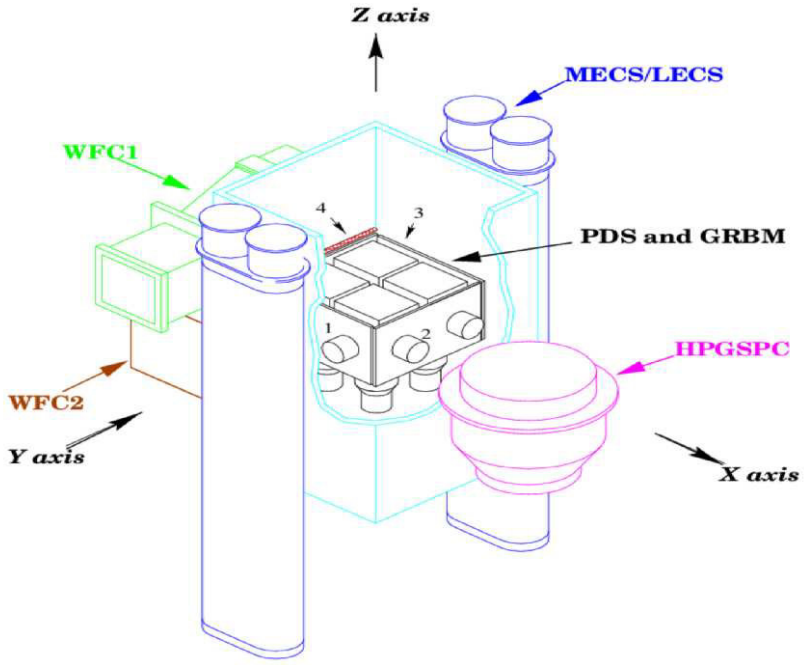

Figure 6.2 *BeppoSAX* payload. The Sun was mostly facing GRBM unit 2.

reference frame (ϕ and θ). The *BeppoSAX* payload is shown in Figure 6.2 with the Cartesian reference frame.

The information about the Sun position is crucial to assess the solar origin of a flare candidate. Since the GRBM unit 2 continuously faced the Sun (because of the solar panel orientation), the same unit was systematically expected to exhibit the highest rate due to solar events compared with the other GRBM units. So, only if ϕ and θ are around 0 (which corresponds to the normal direction to GRBM unit 2), the signal is possibly due to the Sun.

Another important piece of information is the position of the Earth with respect to the satellite. Knowing that the Earth diameter spans an angle of 130-140 degree from the spacecraft viewpoint, one must make sure the Sun is not hidden by the Earth during the occurrence of the flare candidate. We isolated each specific light curve cutting the time interval around the event and we saved all these data as solar X–ray flare candidates. Then we start our sample selection excluding the already catalogued GRBs (Frontera et al. 2009). During this removal process, we identified an undetected GRB. This event was observed at 18:26:42 UT of July, 13 2000 (Figure 6.3). The nature is clearly recognisable from the hardness ratio value. Indeed a large part of the emission occurred above 100 keV.

Furthermore, we removed all the false positives and the phosphorescence spikes due to high–energy particles, which usually increased near the SAGA (Figure 6.4).

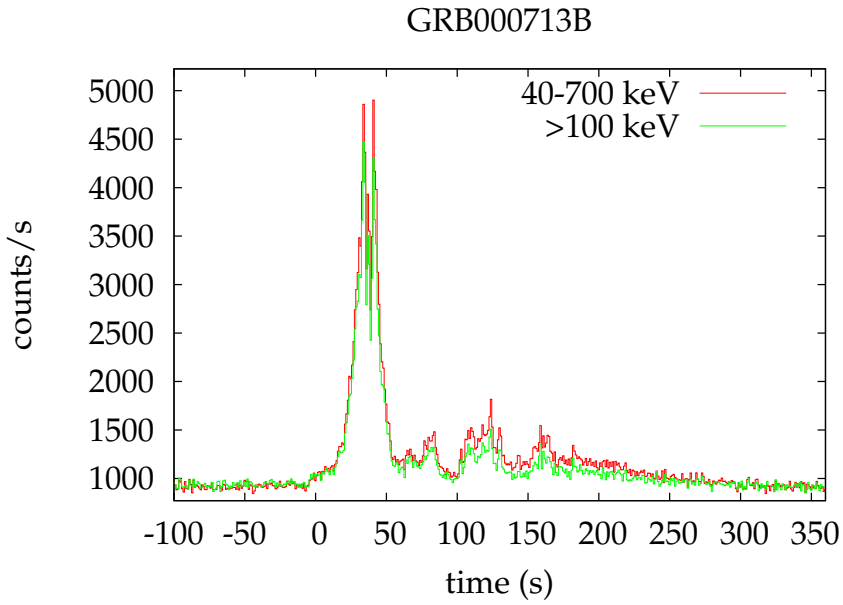

Figure 6.3 Light curve of GRB 000713B in the two energy ranges $40 - 700$ kev and > 100 keV.

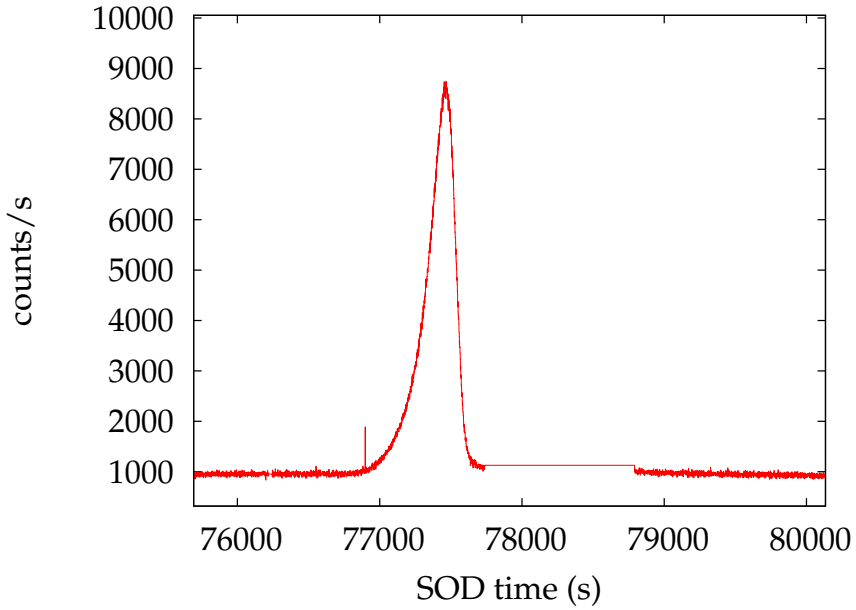

Figure 6.4 The typical emission originated from particles avalanche interaction observed just before the SAGA "gap" in the light curve.

Finally, all the anomalies produced due to data processing were removed. I ended up with 380 solar flare candidates. Moreover, I extracted the 128–s 256–channel energy spectra for all of them. In addition to the individual 128-s integrated spectra, for each event I also studied the total (time–integrated) spectrum. A systematic analysis of the energy spectra of all candidates is still under way.

6.3 Solar Flare Sample

Once the list of solar X–ray flare candidate was obtained, I extracted some basic information. I first wrote a script to check whether each event had also triggered the on board electronic logic. This was carried out by searching within a time window ± 300 s of the on board trigger time. To this aim I referred to so–called Mission Elapsed Time (MET). Following the same procedure I checked if the same solar flare had also been observed by BATSE or GOES spacecraft.

I used a polynomial up to the second order to interpolate the background for each candidate. I subsequently determined the $T_{5\sigma}$ interval by applying our script to the background subtracted curves. All the derived information for each solar flare candidate is reported in Table 6.1.

I chose and defined the spectral hardness ratio parameter as the ratio between the count–fluences collected in the highest energy range (> 100 keV) over that in the $40 - 700$ keV energy range over the $T_{5\sigma}$ interval. The average value is ~ 0.2 and its distribution is illustrated in Figure 6.5. Only $\sim 5\%$ of the total sample is harder than 0.4, clearly showing the soft nature of this kind of phenomena compared with other high–energy transients such as GRBs.

In some cases the huge peak count rates made the 1 s ratemeters recycle. In fact the memory allocated for each time bin counter is 16 bit, so it can go up to 65535 counts. Above this limit, the ratemeters recycle. We could reconstruct the light–curve accordingly for these few cases though, by comparing the counts of a given flare between different energy bands and GRBM units, trying to reproduce the behaviours of the time series which had not been affected by count recycling (due to lower rate in the harder band and/or the lower rate in other GRBM units significantly less illuminated by the Sun).

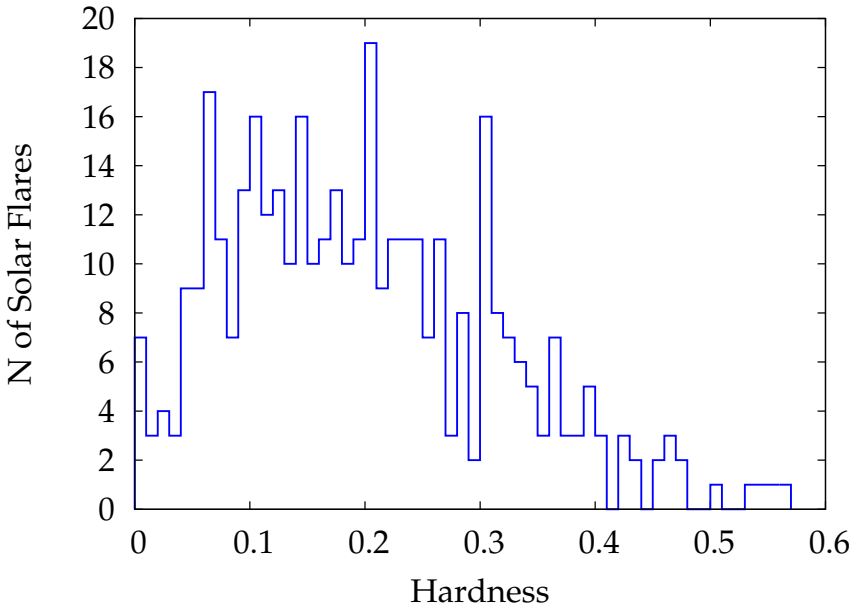

Figure 6.5 Distribution of the spectral hardness ratio for our sample of solar X–ray flare candidates.

6.3.1 May 04, 1998 – A spurious event

At 07:40:00 UT and 09:28:20 of May 4, 1998 the GRBM detected two different and very bright, soft (HR$\sim$ 0.2) events (the peak flux was $\sim 3 \times 10^4$ counts/s and $\sim 4.5 \times 10^4$ counts/s, respectively) with a long duration ($\sim$ 30 minutes and $\sim$ 25 minutes, respectively). All these features led us to think of a possible solar flare. Actually, during both those periods the Sun was hidden by the Earth. Moreover we noted that the emission is well observable in 3 different units (unit1, unit2 and unit3. The flux is lowest in unit 4 but still clearly visible). The four detectors' light curves are shown in Figure 6.7. Considering that in both cases the signal was observed just in proximity of the SAGA, we could conclude that the count rate enhancement was very likely due to that.

The two structures observed in the light curves seem to keep the memory of the original particle emission. One might possible argue that the SAGA was particularly and exceptionally filled up with solar energetic particles, possibly connected to a previous coronal mass ejection as well as to magnetic reconnection phenomena. In a recent work Adriani et al. (2015) studied the effects of solar energetic particles transport in the Earths magnetosheath. It's interesting to note how the particles rigidity grows just in proximity of the SAGA (Figure 6.8). At this stage this is still speculative though.

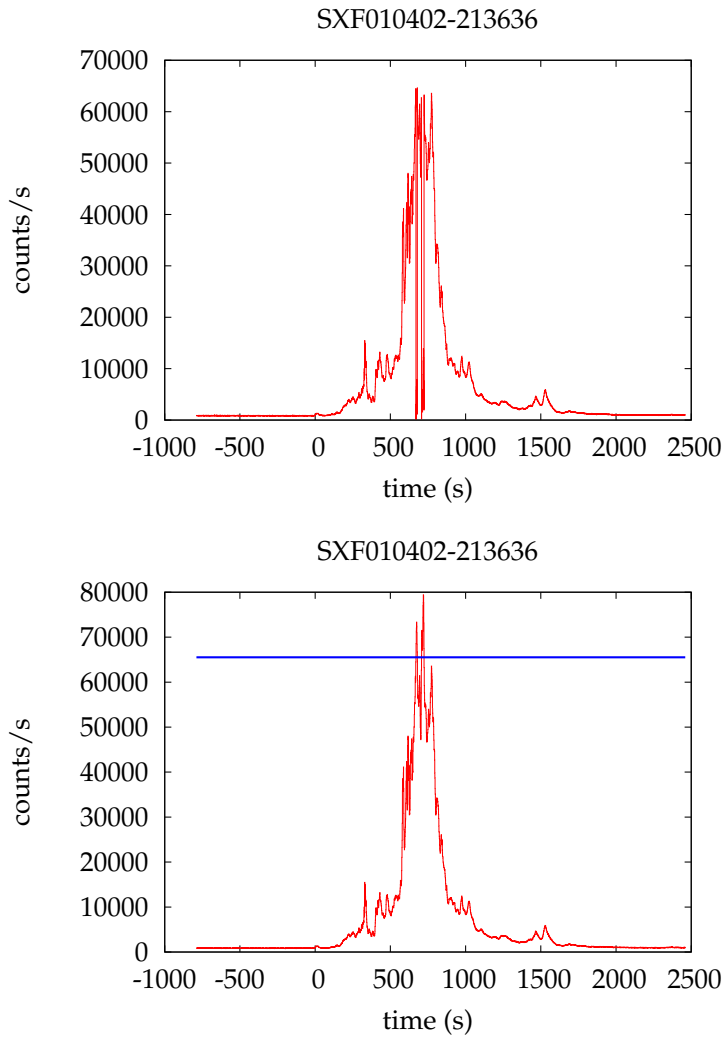

Figure 6.6 Solar X–ray flare of April 2, 2001. In this case the flux was so high that the ratemeter recycled. The blue line shows the recycle limit. The bottom panel shows the reconstructed light–curve. The time is referred to the start of the $T_{5\sigma}$ time.

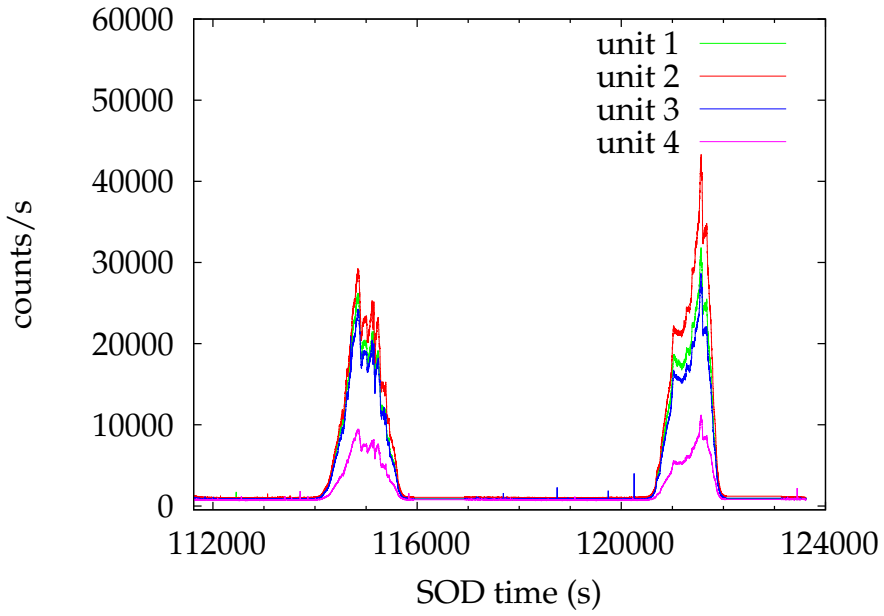

Figure 6.7 Two events observed on May 4, 1998. Different light–curves are related to different GRBM units.

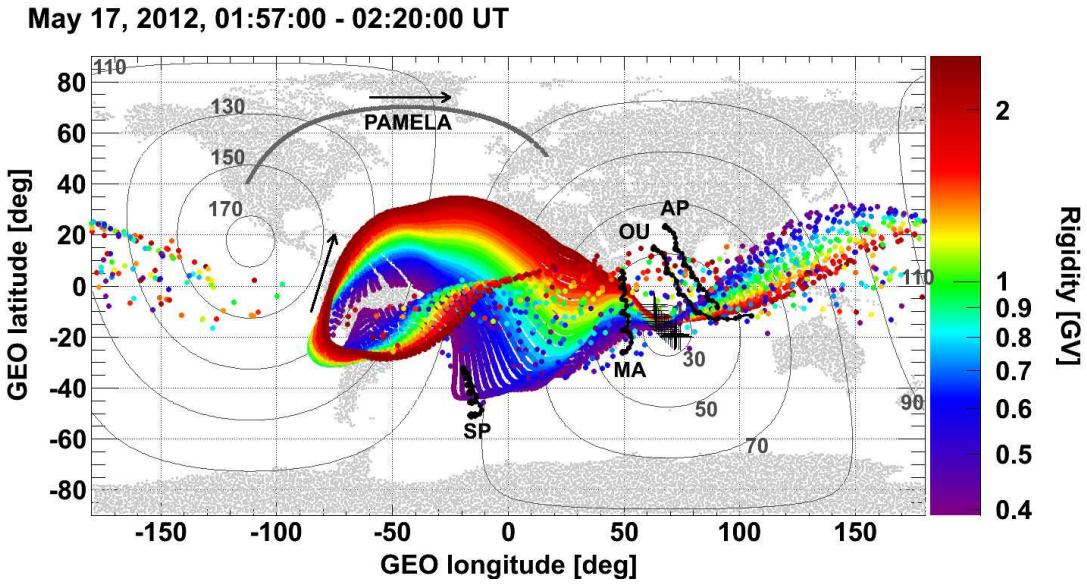

Figure 6.8 The rigidity of the solar energetic particles trapped in the Earths magnetosphere is shown in this figure taken from Adriani et al. (2015)

6.4 Conclusions

My purpose was to compile a comprehensive catalogue of solar X–ray flares detected with the *BeppoSAX*/GRBM. These events were extracted by systematically screening all the continuous mode light curves by means of an algorithm that had specifically been devised to this aim. I ended up with a final catalogue of 380 solar X–ray flare candidates. I found that all of them were also detected simultaneously by either BATSE, or GOES, or both. I provided a basic characterisation for all these candidates: I computed the $T_{5\sigma}$ time interval and the spectral hardness parameter ($\frac{(FLuence(>100\ keV)}{FLuence(40-700\ keV)}$). I noted that only for the 5% of the total sample the hardness ratio is higher than 0.4 and it is on average around 0.2. This analysis clearly reveals the soft nature of these kind of events compared with other harder transients, such as GRBs.

I happened to discover an uncatalogued GRB (GRB 000713B) which had gone missed by the official catalogue (Frontera et al. 2009). Moreover, I identified a peculiar event which revealed a very high concentration of high–energy charged particles over the South Atlantic Anomaly, which could be related to previous solar activity.

An in–depth study of the time properties of these solar flares will provide more insights in the physical mechanism of the origin of this class of high–energy bursty emission from our own star, exploiting the unique combination of high-time and spectral resolution and large effective area of *BeppoSAX* GRBM which operated during one of the latest intense maxima of the 11–year solar cycle.

Table 6.1. Comprehensive list 380 Solar X–ray flare candidates detected by *BeppoSAX*/GRBM and discovered using our algorithm.

Year	month	day	time[a] (UT)	RA (deg)	DEC (deg)	ϕ (deg)	θ (deg)	Trigger	BATSE	GOES	$T_{5\sigma}$ (s)	Hardness[b]
1997	04	01	07 : 56 : 25	10.7	4.6	14.6	−2.5	*YES*	*NO*	*YES*	38	0.074
1997	09	09	09 : 47 : 24	167.8	5.2	18.9	17.7	*NO*	*YES*	*YES*	195	0.139
1997	09	24	02 : 46 : 33	181.0	−0.4	27.2	2.2	*YES*	*NO*	*YES*	648	0.144
1997	11	04	05 : 56 : 06	219.4	−15.4	7.1	−26.9	*YES*	*YES*	*YES*	229	0.349
1997	11	15	22 : 38 : 54	231.2	−18.7	340.5	−14.4	*YES*	*NO*	*NO*	333	0.172
1997	11	27	16 : 13 : 13	243.5	−21.2	338.3	−16.7	*NO*	*YES*	*YES*	59	0.036
1997	11	28	04 : 56 : 00	244.1	−21.3	338.2	−17.2	*YES*	*YES*	*YES*	1028	0.081
1997	11	29	22 : 33 : 12	246.0	−21.6	3.5	−2.2	*YES*	*NO*	*YES*	699	0.061
1997	11	30	06 : 52 : 49	246.3	−21.7	3.2	−2.2	*YES*	*NO*	*YES*	85	0.071
1998	01	25	21 : 30 : 38	308.1	−18.8	339.0	−3.3	*YES*	*NO*	*YES*	341	0.229
1998	02	20	10 : 06 : 55	333.6	−10.9	21.0	11.2	*YES*	*NO*	*YES*	46	0.114
1998	03	15	21 : 42 : 19	355.5	−1.9	19.9	−17.5	*YES*	*NO*	*YES*	137	0.160
1998	03	20	04 : 44 : 39	359.4	−0.2	24.5	−13.9	*YES*	*YES*	*YES*	95	0.065
1998	03	20	11 : 59 : 54	359.7	−0.1	357.4	0.9	*NO*	*NO*	*YES*	538	0.312
1998	04	27	09 : 10 : 28	34.6	13.8	17.9	−17.7	*YES*	*NO*	*NO*	341[c]	0.259
1998	04	29	16 : 35 : 46	36.8	14.6	356.9	15.9	*NO*	*NO*	*NO*	706[c]	0.108
1998	04	30	21 : 20 : 57	37.9	14.9	344.5	3.6	*YES*	*YES*	*YES*	54	0.041
1998	05	02	13 : 34 : 45	39.5	15.4	16.1	16.2	*NO*	*NO*	*YES*	655[c]	0.175
1998	05	03	21 : 17 : 05	40.8	15.8	20.3	0.1	*YES*	*NO*	*YES*	889	0.125
1998	05	07	05 : 32 : 36	44.0	16.8	12.3	14.9	*YES*	*YES*	*NO*	6	0.301
1998	05	08	05 : 57 : 38	45.0	17.0	13.4	15.0	*YES*	*YES*	*YES*	1477	0.372
1998	05	28	19 : 00 : 44	65.4	21.5	23.1	−9.5	*YES*	*YES*	*YES*	349	0.352
1998	05	29	00 : 55 : 15	65.7	21.6	23.3	−9.6	*YES*	*YES*	*YES*	87[c]	0.163
1998	06	13	04 : 18 : 16	81.3	23.2	26.0	2.7	*YES*	*NO*	*YES*	64	0.265
1998	06	28	11 : 41 : 03	97.2	23.3	14.7	20.3	*YES*	*YES*	*YES*	18	0.125
1998	08	08	03 : 14 : 32	137.9	16.2	12.2	−22.6	*YES*	*NO*	*YES*	185	0.400
1998	08	13	17 : 54 : 03	143.2	14.6	23.8	−12.6	*YES*	*NO*	*YES*	27	0.308
1998	08	14	08 : 25 : 31	143.7	14.4	344.4	−18.4	*YES*	*NO*	*YES*	134	0.422
1998	08	18	08 : 20 : 20	147.5	13.1	356.5	−24.2	*NO*	*NO*	*NO*	553[c]	0.465
1998	08	19	21 : 40 : 01	148.9	12.6	353.1	−25.4	*YES*	*YES*	*YES*	673	0.550
1998	08	22	15 : 05 : 21	151.4	11.7	332.3	−2.0	*YES*	*NO*	*YES*	45	0.240
1998	08	24	22 : 01 : 09	153.5	10.9	359.7	−26.7	*YES*	*NO*	*NO*	1071[c]	0.335
1998	09	23	00 : 29 : 26	179.8	0.1	359.5	−0.7	*NO*	*NO*	*YES*	208	0.239
1998	09	23	06 : 45 : 36	180.0	−0.0	359.7	−0.8	*YES*	*YES*	*YES*	2093	0.136
1998	09	23	22 : 46 : 15	180.6	−0.3	3.7	−4.6	*YES*	*NO*	*YES*	67	0.072
1998	09	26	16 : 23 : 07	183.1	−1.3	4.2	6.1	*NO*	*NO*	*YES*	15	0.183
1998	09	27	23 : 37 : 09	184.3	−1.9	22.0	−8.1	*YES*	*YES*	*YES*	217	0.322
1998	09	30	13 : 21 : 55	186.6	−2.9	10.0	1.6	*NO*	*NO*	*NO*	1321[c]	0.132
1998	10	07	12 : 50 : 18	192.9	−5.5	338.0	−11.9	*NO*	*YES*	*NO*	21[c]	0.227
1998	10	07	15 : 37 : 28	193.0	−5.6	338.1	−11.9	*YES*	*NO*	*YES*	124	0.203
1998	11	06	09 : 09 : 53	221.3	−16.0	9.3	−23.3	*YES*	*YES*	*YES*	9	0.306
1998	11	06	12 : 04 : 08	221.4	−16.0	9.3	−23.4	*YES*	*YES*	*YES*	21	0.203
1998	11	08	12 : 08 : 25	223.4	−16.6	23.4	6.6	*NO*	*NO*	*NO*	97[c]	0.538
1998	11	08	22 : 53 : 00	223.9	−16.7	23.7	6.9	*YES*	*NO*	*NO*	157	0.068

Table 6.1 (cont'd)

Year	month	day	time[a] (UT)	RA (deg)	DEC (deg)	ϕ (deg)	θ (deg)	Trigger	BATSE	GOES	$T_{5\sigma}$ (s)	Hardness[b]
1998	11	22	06 : 32 : 10	237.6	−20.1	13.5	15.7	*YES*	*YES*	*YES*	1105	0.564
1998	11	22	16 : 16 : 48	238.0	−20.2	12.8	−20.6	*YES*	*YES*	*YES*	575[c]	0.165
1998	11	23	06 : 31 : 16	238.6	−20.3	334.8	−8.6	*YES*	*NO*	*YES*	1531	0.074
1998	11	24	02 : 09 : 33	239.5	−20.5	11.2	−18.1	*YES*	*YES*	*YES*	934	0.210
1998	11	27	07 : 27 : 09	242.9	−21.1	337.2	−0.9	*YES*	*YES*	*NO*	786	0.231
1998	11	28	05 : 36 : 15	243.9	−21.3	18.4	19.5	*YES*	*YES*	*NO*	1477	0.115
1998	12	14	22 : 24 : 17	262.1	−23.2	338.3	−14.3	*YES*	*YES*	*NO*	35	0.060
1998	12	19	06 : 49 : 30	266.9	−23.4	337.8	−11.5	*NO*	*YES*	*NO*	18[c]	0.315
1998	12	22	23 : 47 : 22	271.0	−23.4	2.4	26.4	*YES*	*NO*	*YES*	262[c]	0.437
1998	12	26	05 : 58 : 14	274.6	−23.4	337.2	13.2	*YES*	*YES*	*YES*	49	0.319
1998	12	28	05 : 46 : 42	276.8	−23.3	13.9	21.5	*NO*	*NO*	*YES*	58[c]	0.095
1999	01	01	00 : 24 : 02	281.0	−23.1	24.8	5.3	*NO*	*YES*	*YES*	295	0.099
1999	01	23	19 : 15 : 11	305.7	−19.4	335.8	−3.2	*YES*	*YES*	*YES*	499[c]	0.398
1999	01	23	23 : 48 : 02	305.9	−19.4	335.9	−3.3	*YES*	*NO*	*YES*	179	0.205
1999	01	24	22 : 29 : 00	306.8	−19.1	336.8	−3.7	*YES*	*YES*	*NO*	42	0.343
1999	01	25	13 : 59 : 29	307.5	−19.0	337.4	−4.1	*YES*	*YES*	*YES*	504	0.421
1999	02	01	08 : 35 : 38	314.5	−17.2	333.8	−8.1	*YES*	*YES*	*YES*	108	0.383
1999	02	16	00 : 00 : 15	329.1	−12.6	15.9	−1.0	*YES*	*YES*	*YES*	227	0.101
1999	02	16	02 : 52 : 15	329.2	−12.5	15.9	−0.9	*YES*	*YES*	*YES*	2304	0.159
1999	02	17	16 : 30 : 10	330.7	−12.0	355.3	18.3	*YES*	*NO*	*YES*	27	0.319
1999	02	21	09 : 39 : 53	334.3	−10.6	335.6	1.5	*NO*	*YES*	*YES*	923[c]	0.543
1999	02	28	16 : 35 : 01	341.2	−7.9	0.3	17.5	*YES*	*YES*	*YES*	304[c]	0.167
1999	03	02	12 : 08 : 35	342.9	−7.3	0.4	−6.8	*YES*	*NO*	*YES*	297	0.127
1999	03	12	17 : 23 : 08	352.4	−3.3	354.9	−0.3	*YES*	*NO*	*YES*	241	0.307
1999	03	12	20 : 36 : 35	352.5	−3.2	355.0	−0.3	*YES*	*NO*	*YES*	163	0.151
1999	03	18	08 : 28 : 39	357.5	−1.1	26.0	4.2	*YES*	*YES*	*YES*	150	0.062
1999	03	18	14 : 12 : 52	357.8	−1.0	26.0	4.0	*YES*	*NO*	*YES*	164	0.024
1999	05	03	23 : 09 : 58	40.6	15.8	349.9	−13.4	*YES*	*YES*	*YES*	46	0.307
1999	05	08	14 : 23 : 20	45.1	17.1	336.0	−12.0	*NO*	*NO*	*YES*	719	0.090
1999	05	09	17 : 55 : 59	46.2	17.4	336.2	−10.9	*YES*	*YES*	*YES*	74[c]	0.040
1999	05	16	17 : 23 : 12	53.1	19.1	338.2	−6.5	*YES*	*NO*	*YES*	85	0.306
1999	05	16	22 : 29 : 43	53.3	19.2	338.0	−6.4	*YES*	*NO*	*YES*	202	0.194
1999	05	17	00 : 21 : 32	53.4	19.2	337.9	−6.4	*YES*	*NO*	*YES*	183	0.218
1999	05	17	04 : 52 : 17	53.6	19.2	20.8	15.2	*YES*	*NO*	*YES*	224	0.298
1999	05	29	20 : 07 : 08	66.3	21.6	23.7	−0.6	*YES*	*YES*	*YES*	92	0.209
1999	06	17	17 : 18 : 23	85.7	23.4	355.8	26.1	*YES*	*NO*	*NO*	628	0.458
1999	06	19	22 : 54 : 46	88.1	23.4	21.1	11.4	*YES*	*NO*	*NO*	20	0.286
1999	06	20	04 : 53 : 49	88.3	23.4	21.2	11.2	*YES*	*NO*	*YES*	296	0.208
1999	06	20	08 : 36 : 16	88.5	23.4	21.3	11.1	*YES*	*YES*	*YES*	24	0.137
1999	06	27	08 : 37 : 02	95.8	23.3	337.6	−8.4	*YES*	*NO*	*YES*	481	0.270
1999	06	30	11 : 26 : 36	99.0	23.2	352.8	24.1	*YES*	*NO*	*YES*	555	0.338
1999	06	30	18 : 05 : 44	99.3	23.2	353.0	24.2	*YES*	*NO*	*YES*	203	0.151
1999	06	30	20 : 10 : 07	99.4	23.2	353.1	24.3	*YES*	*NO*	*YES*	27[c]	0.360
1999	07	25	13 : 12 : 07	124.4	19.7	23.3	−11.9	*YES*	*YES*	*YES*	1346[c]	0.473

Table 6.1 (cont'd)

Year	month	day	time[a] (UT)	RA (deg)	DEC (deg)	ϕ (deg)	θ (deg)	Trigger	BATSE	GOES	$T_{5\sigma}$ (s)	Hardness[b]
1999	07	30	15 : 13 : 04	129.4	18.5	340.7	−3.0	*YES*	*YES*	*YES*	400	0.289
1999	07	30	16 : 03 : 12	129.5	18.5	340.7	−3.0	*YES*	*YES*	*YES*	134	0.242
1999	07	30	22 : 58 : 08	129.7	18.4	340.8	−2.7	*YES*	*YES*	*NO*	7	0.171
1999	08	01	06 : 40 : 49	131.0	18.1	341.4	−1.6	*YES*	*NO*	*YES*	12	0.147
1999	08	02	00 : 25 : 55	131.7	17.9	17.3	−21.6	*YES*	*NO*	*YES*	75	0.161
1999	08	02	11 : 49 : 19	132.2	17.8	332.8	2.1	*YES*	*YES*	*YES*	222	0.193
1999	08	02	14 : 40 : 26	132.3	17.8	332.7	2.2	*YES*	*YES*	*YES*	569	0.320
1999	08	02	21 : 21 : 25	132.6	17.7	332.6	2.4	*YES*	*YES*	*YES*	694	0.180
1999	08	02	21 : 36 : 26	132.6	17.7	332.6	2.4	*YES*	*NO*	*NO*	201[c]	0.165
1999	08	02	22 : 52 : 17	132.7	17.7	332.6	2.5	*YES*	*YES*	*NO*	37	0.348
1999	08	05	23 : 28 : 26	135.6	16.9	10.0	15.8	*YES*	*YES*	*YES*	101[c]	0.237
1999	08	06	16 : 30 : 32	136.2	16.7	352.4	16.6	*YES*	*YES*	*YES*	251	0.129
1999	08	20	18 : 27 : 32	149.5	12.4	9.9	−22.2	*YES*	*YES*	*YES*	65	0.328
1999	08	21	22 : 12 : 50	150.6	12.0	9.4	−23.3	*YES*	*YES*	*YES*	43	0.260
1999	08	25	01 : 33 : 38	153.5	11.0	334.4	−1.8	*NO*	*YES*	*YES*	492	0.233
1999	08	28	17 : 55 : 01	156.8	9.7	8.0	−14.4	*YES*	*YES*	*YES*	355	0.208
1999	09	01	18 : 56 : 12	160.5	8.2	341.9	−1.1	*YES*	*NO*	*YES*	60	0.087
1999	09	18	18 : 20 : 04	175.8	1.8	358.3	0.5	*YES*	*NO*	*YES*	23[c]	0.239
1999	10	01	14 : 58 : 07	187.3	−3.2	10.8	1.7	*YES*	*NO*	*YES*	100	0.144
1999	10	25	06 : 29 : 09	209.3	−12.0	350.4	−18.5	*YES*	*NO*	*YES*	89	0.231
1999	10	26	06 : 07 : 52	210.2	−12.3	9.6	23.2	*YES*	*NO*	*NO*	8	0.042
1999	11	09	08 : 26 : 19	224.0	−16.8	345.2	−11.2	*YES*	*NO*	*NO*	62	0.178
1999	11	16	21 : 20 : 54	231.7	−18.8	19.0	−4.8	*YES*	*NO*	*YES*	176	0.061
1999	11	17	09 : 55 : 03	232.2	−18.9	22.5	−3.0	*NO*	*NO*	*NO*	467[c]	0.254
1999	11	18	21 : 35 : 21	233.8	−19.3	22.2	−1.5	*YES*	*YES*	*NO*	8	0.186
1999	11	21	00 : 09 : 21	236.0	−19.8	19.3	10.1	*YES*	*YES*	*YES*	285	0.040
1999	11	21	10 : 05 : 18	236.4	−19.9	19.0	10.4	*YES*	*NO*	*YES*	626	0.074
1999	11	21	18 : 13 : 28	236.8	−19.9	18.8	10.7	*NO*	*YES*	*YES*	140[c]	0.093
1999	11	26	13 : 41 : 00	241.9	−20.9	19.9	−16.3	*YES*	*YES*	*YES*	485	0.147
1999	11	27	12 : 08 : 20	242.8	−21.1	20.2	−15.3	*YES*	*NO*	*YES*	403	0.100
1999	11	28	11 : 52 : 13	243.9	−21.3	20.4	−14.4	*YES*	*NO*	*YES*	84	0.123
1999	12	02	20 : 00 : 56	248.6	−22.0	22.6	3.1	*YES*	*NO*	*NO*	25	0.228
1999	12	06	07 : 04 : 04	252.3	−22.4	345.5	−7.0	*NO*	*NO*	*YES*	261	0.042
1999	12	07	21 : 17 : 16	254.1	−22.6	337.1	−9.3	*YES*	*NO*	*YES*	101	0.281
1999	12	16	07 : 36 : 22	263.4	−23.3	27.2	6.0	*NO*	*YES*	*NO*	163[c]	0.356
1999	12	21	17 : 15 : 10	269.3	−23.4	338.3	−10.7	*YES*	*NO*	*YES*	175	0.239
1999	12	22	10 : 53 : 16	270.2	−23.4	338.5	−11.4	*YES*	*YES*	*YES*	85	0.098
1999	12	23	19 : 33 : 04	271.7	−23.4	10.8	24.5	*YES*	*NO*	*YES*	173	0.209
1999	12	27	12 : 00 : 39	275.8	−23.3	338.8	−11.3	*YES*	*YES*	*NO*	398[c]	0.203
1999	12	28	00 : 42 : 05	276.3	−23.3	339.0	−11.8	*YES*	*YES*	*YES*	697	0.359
2000	01	13	15 : 11 : 58	294.6	−21.5	340.2	−9.1	*YES*	*YES*	*YES*	32	0
2000	01	20	02 : 24 : 11	301.5	−20.3	352.0	−20.9	*YES*	*YES*	*YES*	23	0.455
2000	01	22	17 : 58 : 37	304.3	−19.7	339.4	−10.4	*YES*	*YES*	*YES*	154	0.115
2000	02	04	17 : 58 : 50	317.7	−16.3	334.6	−7.9	*NO*	*NO*	*YES*	68	0.145

Table 6.1 (cont'd)

Year	month	day	time[a] (UT)	RA (deg)	DEC (deg)	ϕ (deg)	θ (deg)	Trigger	BATSE	GOES	$T_{5\sigma}$ (s)	Hardness[b]
2000	02	05	19 : 29 : 20	318.8	−15.9	334.2	−8.9	*YES*	*YES*	*NO*	325	0.385
2000	02	08	08 : 43 : 41	321.3	−15.2	334.3	3.8	*NO*	*YES*	*NO*	1727	0.184
2000	02	10	01 : 50 : 54	323.0	−14.6	343.0	7.0	*YES*	*YES*	*NO*	1102	0.191
2000	02	20	00 : 53 : 51	332.8	−11.2	28.2	−1.8	*YES*	*YES*	*YES*	139	0.045
2000	02	23	19 : 36 : 39	336.4	−9.9	14.9	−2.9	*NO*	*NO*	*NO*	126	0.107
2000	02	23	20 : 57 : 44	336.4	−9.8	14.8	−2.9	*YES*	*NO*	*YES*	154	0.278
2000	02	24	01 : 03 : 51	336.6	−9.8	14.7	−2.8	*YES*	*YES*	*YES*	270	0.375
2000	02	24	14 : 37 : 00	337.1	−9.6	14.2	−2.6	*YES*	*NO*	*YES*	27	0.365
2000	02	29	15 : 16 : 38	341.9	−7.7	357.8	9.7	*NO*	*NO*	*YES*	287	0.070
2000	03	01	11 : 47 : 31	342.7	−7.4	358.8	−6.9	*YES*	*NO*	*YES*	33	0.161
2000	03	01	12 : 10 : 07	342.7	−7.4	358.9	−6.9	*YES*	*NO*	*NO*	9	0.236
2000	03	02	13 : 36 : 46	343.7	−6.9	359.8	−6.5	*YES*	*NO*	*YES*	470	0.368
2000	03	02	16 : 09 : 19	343.8	−6.9	359.9	−6.5	*YES*	*NO*	*YES*	104	0.171
2000	03	03	02 : 11 : 21	344.2	−6.7	359.1	−6.3	*YES*	*YES*	*YES*	275	0.204
2000	03	05	16 : 08 : 00	346.6	−5.8	342.9	15.7	*YES*	*YES*	*YES*	63	0.210
2000	03	06	16 : 17 : 41	347.5	−5.4	350.1	−0.0	*YES*	*NO*	*YES*	83	0.150
2000	03	07	15 : 11 : 07	348.4	−5.0	351.0	−0.1	*YES*	*YES*	*YES*	41	0.166
2000	03	07	16 : 02 : 19	348.4	−5.0	351.0	−0.1	*YES*	*NO*	*YES*	386	0.393
2000	03	07	19 : 46 : 27	348.6	−4.9	351.2	−0.2	*NO*	*YES*	*YES*	216[c]	0.141
2000	03	08	00 : 24 : 40	348.7	−4.8	351.4	−0.2	*YES*	*YES*	*YES*	37	0.242
2000	03	08	09 : 37 : 36	349.1	−4.7	342.2	13.1	*YES*	*YES*	*NO*	104[c]	0.101
2000	03	11	00 : 15 : 41	351.5	−3.7	354.5	−2.0	*YES*	*YES*	*YES*	69	0.062
2000	03	11	11 : 07 : 52	351.9	−3.5	354.4	−2.5	*NO*	*NO*	*YES*	347[c]	0.005
2000	03	12	23 : 05 : 28	353.3	−2.9	7.5	3.7	*NO*	*NO*	*YES*	37[c]	0.066
2000	03	13	05 : 02 : 27	353.5	−2.8	359.7	4.0	*YES*	*YES*	*YES*	131	0.108
2000	03	14	20 : 46 : 10	355.0	−2.1	8.2	5.4	*YES*	*NO*	*YES*	393[c]	0.025
2000	03	15	03 : 17 : 08	355.3	−2.0	358.5	−0.9	*YES*	*NO*	*YES*	71	0.019
2000	03	15	03 : 34 : 48	355.3	−2.0	358.5	−0.9	*YES*	*YES*	*YES*	504	0.051
2000	03	16	11 : 03 : 02	356.5	−1.5	359.8	−1.0	*NO*	*YES*	*YES*	192	0
2000	03	17	04 : 55 : 21	357.2	−1.2	359.3	0.1	*YES*	*YES*	*YES*	85	0.052
2000	03	17	17 : 46 : 59	357.7	−1.0	3.3	7.9	*YES*	*NO*	*YES*	27	0.174
2000	03	18	20 : 50 : 15	358.7	−0.6	3.2	6.8	*NO*	*YES*	*YES*	875	0.110
2000	03	18	23 : 43 : 29	358.8	−0.5	3.2	6.7	*YES*	*NO*	*YES*	800	0.138
2000	03	19	11 : 38 : 06	359.3	−0.3	3.2	6.2	*NO*	*NO*	*YES*	415[c]	0.201
2000	03	20	08 : 23 : 12	0.1	0.0	349.6	−9.6	*YES*	*NO*	*NO*	1006	0.243
2000	03	20	10 : 03 : 33	0.1	0.0	349.6	−9.6	*YES*	*YES*	*YES*	51	0.067
2000	03	20	10 : 53 : 59	0.1	0.1	349.6	−9.7	*YES*	*YES*	*YES*	204	0.100
2000	03	22	01 : 15 : 06	1.6	0.7	5.2	27.1	*YES*	*YES*	*NO*	227[c]	0.094
2000	03	24	07 : 47 : 16	3.7	1.6	7.6	−1.7	*YES*	*NO*	*NO*	508[c]	0.198
2000	03	24	11 : 26 : 23	3.8	1.6	7.7	−1.7	*YES*	*YES*	*YES*	198	0.159
2000	04	04	15 : 14 : 51	14.0	6.0	350.4	21.9	*YES*	*YES*	*YES*	1611[c]	0.406
2000	04	08	02 : 37 : 26	17.1	7.3	27.0	4.6	*NO*	*YES*	*YES*	314	0.116
2000	04	09	23 : 29 : 28	18.9	8.0	355.4	19.6	*YES*	*YES*	*NO*	904	0.398
2000	05	01	10 : 20 : 32	38.9	15.2	6.7	−17.3	*YES*	*YES*	*YES*	105	0.307

Table 6.1 (cont'd)

Year	month	day	time[a] (UT)	RA (deg)	DEC (deg)	ϕ (deg)	θ (deg)	Trigger	BATSE	GOES	$T_{5\sigma}$ (s)	Hardness[b]
2000	05	04	04 : 35 : 26	41.6	16.1	26.8	1.5	*NO*	*YES*	*YES*	298	0.116
2000	05	05	15 : 35 : 18	43.0	16.5	16.7	7.0	*YES*	*NO*	*NO*	482[c]	0.262
2000	05	14	09 : 16 : 35	51.5	18.7	347.9	16.4	*YES*	*YES*	*YES*	199	0.264
2000	05	15	10 : 47 : 59	52.6	19.0	348.3	17.3	*YES*	*NO*	*YES*	131	0.284
2000	05	15	15 : 53 : 55	52.8	19.0	348.4	17.5	*YES*	*YES*	*YES*	744[c]	0.314
2000	05	15	18 : 50 : 24	52.9	19.1	348.5	17.6	*YES*	*NO*	*YES*	235	0.162
2000	05	16	15 : 47 : 37	53.8	19.3	28.5	1.4	*NO*	*NO*	*YES*	390	0.164
2000	05	16	23 : 58 : 26	54.1	19.4	28.5	1.1	*NO*	*YES*	*NO*	87	0.216
2000	05	17	04 : 02 : 23	54.3	19.4	28.5	1.0	*YES*	*NO*	*YES*	35	0.084
2000	05	18	01 : 25 : 07	55.2	19.6	338.6	3.8	*YES*	*YES*	*YES*	92	0.125
2000	05	18	07 : 21 : 56	55.4	19.6	338.5	4.1	*YES*	*YES*	*NO*	38	0.170
2000	05	18	07 : 27 : 13	55.4	19.6	338.5	4.1	*YES*	*YES*	*NO*	45	0.159
2000	05	18	15 : 54 : 48	55.8	19.7	338.4	4.4	*YES*	*NO*	*YES*	140	0.223
2000	05	18	22 : 58 : 14	56.1	19.8	338.3	4.6	*YES*	*YES*	*NO*	166	0.081
2000	05	20	08 : 55 : 31	57.5	20.1	337.7	5.9	*YES*	*YES*	*NO*	21	0.094
2000	05	20	20 : 19 : 43	57.9	20.2	347.7	−19.5	*YES*	*NO*	*YES*	83	0.435
2000	05	24	02 : 22 : 50	61.2	20.8	353.0	22.1	*YES*	*YES*	*NO*	21	0.229
2000	05	27	08 : 38 : 14	64.5	21.4	349.3	19.6	*YES*	*NO*	*YES*	15	0.297
2000	06	02	19 : 18 : 29	71.1	22.3	27.5	2.7	*YES*	*NO*	*NO*	310	0.093
2000	06	03	19 : 16 : 43	72.1	22.4	8.9	1.6	*YES*	*NO*	*YES*	560	0.108
2000	06	04	22 : 02 : 13	73.3	22.5	7.9	1.6	*YES*	*NO*	*YES*	1023	0.078
2000	06	06	13 : 58 : 31	75.0	22.7	22.9	4.7	*NO*	*NO*	*YES*	292	0
2000	06	07	04 : 40 : 36	75.6	22.8	351.5	−22.2	*YES*	*NO*	*YES*	68	0.157
2000	06	07	15 : 43 : 07	76.1	22.8	351.0	−22.0	*YES*	*NO*	*NO*	287	0.187
2000	06	08	09 : 40 : 50	76.9	22.9	334.4	7.0	*NO*	*NO*	*YES*	32	0.112
2000	06	10	16 : 49 : 58	79.2	23.1	333.6	9.0	*YES*	*NO*	*NO*	839[c]	0.247
2000	06	11	12 : 50 : 42	80.1	23.1	25.9	4.4	*YES*	*NO*	*YES*	153[c]	0.269
2000	06	12	11 : 15 : 27	81.1	23.2	26.5	3.7	*YES*	*NO*	*YES*	141	0.207
2000	06	15	19 : 43 : 39	84.6	23.3	24.1	9.2	*YES*	*NO*	*YES*	330[c]	0.320
2000	06	15	21 : 22 : 06	84.6	23.3	24.2	9.2	*YES*	*NO*	*YES*	126	0.050
2000	06	15	23 : 38 : 14	84.7	23.4	24.3	9.2	*YES*	*NO*	*YES*	519	0.218
2000	06	17	02 : 29 : 48	85.9	23.4	25.4	9.4	*YES*	*NO*	*YES*	392	0.125
2000	06	23	04 : 02 : 29	92.2	23.4	17.1	−10.4	*YES*	*NO*	*YES*	337	0.205
2000	06	27	21 : 03 : 00	97.1	23.3	334.8	−10.7	*NO*	*NO*	*YES*	289	0.248
2000	07	06	20 : 40 : 52	106.4	22.6	22.9	−2.7	*YES*	*NO*	*YES*	39	0.098
2000	07	12	09 : 13 : 48	112.0	21.9	18.7	12.0	*YES*	*NO*	*YES*	206	0.264
2000	07	12	10 : 29 : 45	112.0	21.9	18.7	12.0	*YES*	*NO*	*NO*	878	0.079
2000	07	12	20 : 06 : 38	112.5	21.8	18.8	11.6	*YES*	*NO*	*NO*	572[c]	0.138
2000	07	12	21 : 38 : 39	112.5	21.8	18.9	11.6	*YES*	*NO*	*YES*	171	0.125
2000	07	13	05 : 21 : 20	112.8	21.8	335.3	−0.6	*YES*	*NO*	*YES*	442	0.289
2000	07	13	06 : 59 : 35	112.9	21.8	335.4	−0.6	*YES*	*NO*	*NO*	126	0.301
2000	07	13	12 : 04 : 56	113.1	21.7	335.5	−0.4	*YES*	*NO*	*NO*	244	0.064
2000	07	16	11 : 54 : 26	116.2	21.3	24.5	1.0	*YES*	*NO*	*YES*	84	0.063
2000	07	16	19 : 37 : 10	116.5	21.2	24.7	0.7	*YES*	*NO*	*YES*	50	0.060

Table 6.1 (cont'd)

Year	month	day	time[a] (UT)	RA (deg)	DEC (deg)	ϕ (deg)	θ (deg)	Trigger	BATSE	GOES	$T_{5\sigma}$ (s)	Hardness[b]
2000	07	17	08 : 25 : 19	117.0	21.1	24.9	0.3	*YES*	*NO*	*NO*	794	0.381
2000	07	17	13 : 36 : 35	117.2	21.1	24.9	0.1	*YES*	*NO*	*YES*	67[c]	0.033
2000	07	17	13 : 42 : 35	117.2	21.1	24.9	0.1	*YES*	*NO*	*NO*	84	0.055
2000	07	21	05 : 17 : 33	120.9	20.4	349.1	−24.4	*YES*	*NO*	*YES*	324	0.347
2000	07	23	09 : 49 : 03	123.1	20.0	337.2	−4.2	*YES*	*NO*	*YES*	544	0.212
2000	07	23	10 : 07 : 11	123.1	20.0	337.2	−4.2	*YES*	*NO*	*NO*	36	0.140
2000	08	06	02 : 10 : 05	136.4	16.6	342.0	−0.0	*YES*	*NO*	*NO*	39	0.170
2000	09	04	17 : 49 : 40	163.9	6.9	345.9	12.6	*NO*	*NO*	*YES*	20	0.112
2000	09	15	20 : 52 : 35	173.9	2.7	356.3	0.4	*YES*	*NO*	*YES*	280	0.065
2000	09	21	20 : 17 : 41	179.2	0.3	2.1	0.9	*YES*	*NO*	*NO*	145	0.058
2000	09	22	04 : 15 : 24	179.5	0.2	2.4	0.9	*YES*	*NO*	*YES*	114[c]	0.123
2000	09	22	15 : 34 : 24	179.9	0.0	2.9	1.0	*YES*	*NO*	*NO*	30	0.101
2000	09	22	23 : 44 : 14	180.2	−0.1	3.2	1.0	*NO*	*NO*	*YES*	353	0.267
2000	09	23	04 : 50 : 33	180.4	−0.2	3.4	1.0	*NO*	*NO*	*YES*	267	0.158
2000	09	24	14 : 04 : 45	181.7	−0.7	350.9	11.3	*NO*	*NO*	*YES*	47[c]	0
2000	09	25	00 : 44 : 46	182.1	−0.9	350.7	11.7	*NO*	*NO*	*YES*	522	0
2000	09	25	02 : 10 : 44	182.1	−0.9	350.7	11.8	*YES*	*NO*	*YES*	319	0.093
2000	09	25	14 : 57 : 03	182.6	−1.1	356.2	6.2	*YES*	*NO*	*YES*	7	0.103
2000	09	30	23 : 16 : 56	187.4	−3.2	351.3	−20.5	*YES*	*NO*	*YES*	197[c]	0.278
2000	10	28	18 : 48 : 43	213.4	−13.4	16.9	11.2	*NO*	*NO*	*NO*	36	0.020
2000	10	29	01 : 48 : 10	213.6	−13.5	17.1	11.4	*YES*	*NO*	*NO*	590[c]	0.282
2000	11	07	11 : 58 : 43	222.9	−16.5	0.1	26.2	*YES*	*NO*	*YES*	273[c]	0.106
2000	11	08	06 : 11 : 45	223.7	−16.7	16.7	5.4	*YES*	*NO*	*NO*	30	0.508
2000	11	08	23 : 03 : 41	224.4	−16.9	16.8	6.1	*YES*	*NO*	*NO*	3099[c]	0.209
2000	11	24	22 : 39 : 34	240.9	−20.8	16.9	22.1	*YES*	*NO*	*NO*	24	0.227
2000	11	25	00 : 59 : 02	241.0	−20.8	16.9	22.2	*YES*	*NO*	*YES*	528[c]	0.188
2000	11	25	01 : 43 : 23	241.1	−20.8	17.0	22.2	*YES*	*NO*	*NO*	2196	0.466
2000	11	25	18 : 36 : 27	241.8	−20.9	21.9	6.8	*NO*	*NO*	*YES*	105[c]	0.155
2000	11	25	19 : 38 : 43	241.9	−20.9	21.9	6.8	*NO*	*NO*	*NO*	337	0.252
2000	11	26	16 : 46 : 06	242.8	−21.1	22.1	7.7	*NO*	*NO*	*NO*	524[c]	0.225
2000	12	19	10 : 18 : 19	267.6	−23.4	20.5	−21.5	*YES*	*NO*	*NO*	376	0.319
2000	12	24	01 : 01 : 39	272.8	−23.4	353.2	24.4	*YES*	*NO*	*YES*	403	0.282
2000	12	24	11 : 05 : 41	273.2	−23.4	353.6	24.6	*YES*	*NO*	*YES*	590	0.364
2000	12	27	15 : 38 : 43	276.8	−23.3	26.6	−4.2	*NO*	*NO*	*NO*	207	0.110
2000	12	27	18 : 16 : 55	276.9	−23.3	26.6	−4.3	*YES*	*NO*	*YES*	90	0.186
2001	01	04	20 : 06 : 21	285.8	−22.6	339.9	−11.3	*YES*	*NO*	*YES*	187	0.262
2001	01	09	06 : 47 : 54	290.7	−22.1	1.2	25.1	*NO*	*NO*	*YES*	254	0.264
2001	01	10	10 : 11 : 14	291.9	−21.9	16.2	−15.4	*YES*	*NO*	*YES*	750	0.336
2001	01	20	21 : 10 : 21	303.1	−20.0	5.2	−21.6	*YES*	*NO*	*YES*	794	0.392
2001	01	26	06 : 02 : 09	308.7	−18.7	12.5	14.0	*YES*	*NO*	*NO*	388	0.333
2001	02	01	07 : 10 : 04	315.0	−17.1	15.0	−10.3	*YES*	*NO*	*YES*	61	0.112
2001	02	02	23 : 52 : 41	316.7	−16.6	15.3	−12.0	*YES*	*NO*	*NO*	864[c]	0.361
2001	02	21	14 : 20 : 00	335.0	−10.4	27.2	2.4	*YES*	*NO*	*YES*	379	0.087
2001	03	10	04 : 02 : 09	350.5	−4.1	19.6	−3.5	*YES*	*NO*	*YES*	455	0.309

Table 6.1 (cont'd)

Year	month	day	time[a] (UT)	RA (deg)	DEC (deg)	ϕ (deg)	θ (deg)	Trigger	BATSE	GOES	$T_{5\sigma}$ (s)	Hardness[b]
2001	03	20	03 : 26 : 13	359.6	−0.2	5.6	7.7	*YES*	*NO*	*NO*	407	0.192
2001	03	24	01 : 30 : 51	3.2	1.4	27.1	−5.7	*YES*	*NO*	*YES*	495[c]	0.396
2001	03	25	04 : 14 : 52	4.2	1.8	12.7	23.3	*YES*	*NO*	*YES*	225	0.134
2001	03	25	11 : 08 : 07	4.5	1.9	12.4	23.2	*YES*	*NO*	*NO*	667	0.302
2001	03	27	02 : 24 : 38	6.0	2.6	2.5	−2.3	*NO*	*NO*	*YES*	523	0.050
2001	03	27	02 : 32 : 57	6.0	2.6	2.5	−2.3	*NO*	*NO*	*NO*	697	0.213
2001	03	27	14 : 47 : 30	6.4	2.8	2.4	−2.8	*YES*	*NO*	*YES*	217	0.076
2001	03	27	16 : 22 : 35	6.5	2.8	2.4	−2.9	*YES*	*NO*	*YES*	540	0.306
2001	03	28	10 : 45 : 37	7.2	3.1	15.4	−24.1	*YES*	*NO*	*YES*	353	0.308
2001	03	29	10 : 03 : 28	8.1	3.5	16.1	−23.4	*YES*	*NO*	*NO*	635[c]	0.345
2001	03	29	15 : 15 : 51	8.3	3.6	5.9	3.0	*NO*	*NO*	*NO*	71	0.040
2001	03	30	05 : 05 : 25	8.8	3.8	6.1	2.4	*YES*	*NO*	*YES*	619	0.013
2001	03	30	17 : 51 : 38	9.3	4.0	6.3	1.9	*YES*	*NO*	*NO*	8	0.220
2001	04	02	00 : 16 : 27	11.4	4.9	357.0	16.2	*NO*	*NO*	*YES*	111[c]	0.193
2001	04	02	11 : 03 : 03	11.8	5.1	20.8	−18.7	*YES*	*NO*	*NO*	1541[c]	0.306
2001	04	02	18 : 38 : 15	12.1	5.2	21.0	−18.4	*YES*	*NO*	*NO*	86	0.086
2001	04	02	21 : 36 : 36	12.2	5.2	21.1	−18.3	*YES*	*NO*	*YES*	2413	0.233
2001	04	03	12 : 31 : 53	12.7	5.5	16.9	−2.4	*NO*	*NO*	*YES*	95	0.054
2001	04	04	03 : 46 : 48	13.3	5.7	17.6	−2.4	*NO*	*NO*	*YES*	54	0.025
2001	04	04	05 : 47 : 16	13.4	5.7	17.6	−2.4	*YES*	*NO*	*NO*	427	0.281
2001	04	04	12 : 13 : 36	13.6	5.8	16.9	6.5	*NO*	*NO*	*YES*	385[c]	0.100
2001	04	05	02 : 00 : 09	14.2	6.1	17.4	6.7	*NO*	*NO*	*YES*	926	0.079
2001	04	05	08 : 37 : 27	14.4	6.2	17.7	6.8	*YES*	*NO*	*NO*	2537[c]	0.147
2001	04	06	19 : 15 : 46	15.7	6.7	353.3	19.0	*YES*	*NO*	*YES*	1970	0.259
2001	04	06	22 : 27 : 31	15.9	6.8	353.4	18.9	*YES*	*NO*	*NO*	114	0.177
2001	04	10	05 : 09 : 55	18.9	8.0	16.8	−22.6	*YES*	*NO*	*YES*	144	0.248
2001	04	12	03 : 00 : 06	20.6	8.7	339.3	−6.0	*YES*	*NO*	*YES*	260	0.140
2001	04	12	10 : 44 : 56	20.9	8.8	339.6	−5.8	*YES*	*NO*	*NO*	201	0.328
2001	04	14	17 : 44 : 17	23.0	9.6	10.4	−5.2	*YES*	*NO*	*NO*	475	0.148
2001	04	15	04 : 05 : 50	23.4	9.8	10.6	−5.6	*YES*	*NO*	*YES*	33	0.240
2001	04	15	13 : 37 : 29	23.8	9.9	10.7	−5.9	*YES*	*NO*	*NO*	490	0.109
2001	04	18	07 : 52 : 31	26.4	10.9	16.3	11.6	*YES*	*NO*	*NO*	193	0.317
2001	04	20	21 : 29 : 47	28.7	11.8	27.0	−1.6	*NO*	*NO*	*YES*	167	0.122
2001	04	23	10 : 09 : 33	31.1	12.6	22.1	−7.0	*YES*	*NO*	*YES*	535	0.326
2001	04	24	22 : 17 : 40	32.5	13.1	347.4	24.1	*YES*	*NO*	*YES*	353	0.123
2001	04	25	09 : 36 : 47	33.0	13.3	347.3	24.6	*NO*	*NO*	*YES*	52	0.096
2001	04	26	13 : 03 : 39	34.1	13.6	14.3	10.3	*YES*	*NO*	*NO*	407	0.075
2001	05	01	19 : 06 : 47	39.0	15.3	20.4	−7.1	*NO*	*NO*	*NO*	380[c]	0.064
2001	05	02	00 : 33 : 39	39.3	15.3	20.5	−7.3	*YES*	*NO*	*YES*	246	0.114
2001	05	12	23 : 26 : 03	49.9	18.3	348.0	16.3	*YES*	*NO*	*NO*	1030	0.207
2001	05	13	03 : 00 : 57	50.0	18.4	348.0	16.4	*YES*	*NO*	*YES*	506	0.145
2001	05	17	09 : 59 : 04	54.3	19.4	339.5	1.0	*NO*	*NO*	*YES*	47	0.196
2001	05	17	20 : 43 : 58	54.7	19.5	341.9	9.9	*YES*	*NO*	*YES*	89	0.140
2001	05	17	23 : 54 : 05	54.7	19.5	341.9	9.9	*YES*	*NO*	*YES*	53	0.376

Table 6.1 (cont'd)

Year	month	day	time[a] (UT)	RA (deg)	DEC (deg)	ϕ (deg)	θ (deg)	Trigger	BATSE	GOES	$T_{5\sigma}$ (s)	Hardness[b]
2001	05	20	06 : 01 : 00	57.1	20.0	19.0	−19.2	*YES*	*NO*	*YES*	248	0.260
2001	05	20	09 : 19 : 39	57.2	20.0	19.1	−19.1	*YES*	*NO*	*YES*	65	0.426
2001	06	04	08 : 06 : 13	72.4	22.5	6.4	23.2	*YES*	*NO*	*YES*	267	0.203
2001	06	05	04 : 43 : 49	73.3	22.6	7.2	22.9	*YES*	*NO*	*YES*	551	0.253
2001	06	15	10 : 05 : 24	83.9	23.3	338.7	16.1	*YES*	*NO*	*YES*	1823	0.308
2001	06	24	03 : 13 : 17	92.9	23.4	25.6	−9.7	*YES*	*NO*	*YES*	37	0.206
2001	08	05	15 : 28 : 43	135.7	16.8	25.6	7.4	*YES*	*NO*	*YES*	187	0.066
2001	08	05	22 : 19 : 46	136.0	16.8	11.9	−25.3	*YES*	*NO*	*YES*	83	0.043
2001	08	07	07 : 28 : 37	137.3	16.4	347.4	10.5	*YES*	*NO*	*YES*	427	0.249
2001	08	25	16 : 26 : 51	153.9	10.8	345.9	−14.6	*YES*	*NO*	*NO*	151	0.092
2001	08	25	23 : 55 : 46	154.5	10.6	346.3	−14.0	*YES*	*NO*	*YES*	908	0.138
2001	09	05	14 : 27 : 16	164.4	6.6	346.3	−0.5	*YES*	*NO*	*YES*	474	0.265
2001	09	06	03 : 43 : 41	164.9	6.4	346.9	−0.5	*NO*	*NO*	*YES*	88	0.127
2001	09	08	23 : 48 : 30	167.5	5.4	25.9	9.6	*YES*	*NO*	*NO*	167	0.185
2001	09	09	02 : 36 : 02	167.6	5.3	25.8	9.7	*YES*	*NO*	*NO*	230[c]	0.134
2001	09	09	08 : 01 : 24	167.8	5.2	25.7	9.9	*YES*	*NO*	*YES*	219	0.245
2001	09	09	15 : 11 : 51	168.0	5.1	25.5	10.1	*YES*	*NO*	*YES*	955	0.333
2001	09	09	18 : 24 : 09	168.2	5.1	25.4	10.2	*YES*	*NO*	*YES*	1008	0.057
2001	09	10	05 : 41 : 47	168.6	4.9	25.1	10.6	*YES*	*NO*	*YES*	76	0.217
2001	09	11	00 : 52 : 49	169.3	4.6	24.6	11.2	*NO*	*NO*	*NO*	538	0.010
2001	09	13	00 : 36 : 47	171.1	3.8	353.2	0.0	*NO*	*NO*	*YES*	16	0.033
2001	09	13	03 : 52 : 58	171.2	3.8	353.4	0.0	*YES*	*NO*	*YES*	36	0.083
2001	09	13	15 : 57 : 06	171.7	3.6	353.8	0.1	*YES*	*NO*	*YES*	326	0.400
2001	09	14	21 : 44 : 33	172.8	3.1	2.5	−12.5	*YES*	*NO*	*YES*	410	0.238
2001	09	15	11 : 07 : 28	173.3	2.9	2.3	−13.0	*YES*	*NO*	*YES*	222	0.097
2001	09	16	07 : 42 : 21	174.0	2.6	27.5	−7.0	*YES*	*NO*	*YES*	115	0.174
2001	09	17	16 : 13 : 55	175.3	2.1	27.6	−5.6	*YES*	*NO*	*NO*	117	0.121
2001	09	17	21 : 04 : 16	175.4	2.0	27.6	−5.4	*YES*	*NO*	*YES*	327	0.301
2001	09	18	15 : 10 : 00	176.1	1.7	27.6	−4.7	*YES*	*NO*	*NO*	187	0.199
2001	09	18	20 : 48 : 02	176.3	1.6	27.6	−4.5	*YES*	*NO*	*YES*	25	0.205
2001	09	21	06 : 39 : 22	178.5	0.7	1.2	0.8	*NO*	*NO*	*YES*	48	0.042
2001	09	22	05 : 42 : 48	179.4	0.3	347.6	10.4	*YES*	*NO*	*YES*	55	0.185
2001	09	23	01 : 03 : 43	180.1	−0.0	347.2	11.1	*YES*	*NO*	*YES*	62	0.108
2001	09	27	22 : 15 : 07	184.5	−1.9	10.4	1.5	*YES*	*NO*	*NO*	11	0.170
2001	10	01	04 : 56 : 00	187.4	−3.2	5.1	−12.0	*YES*	*NO*	*NO*	1054	0.363
2001	10	03	06 : 41 : 27	189.3	−4.0	0.2	12.6	*NO*	*NO*	*YES*	80	0.146
2001	10	20	12 : 16 : 41	205.2	−10.5	357.2	21.1	*YES*	*NO*	*NO*	28	0.193
2001	10	20	21 : 45 : 42	205.6	−10.6	357.2	21.5	*YES*	*NO*	*YES*	39	0.114
2001	10	21	04 : 35 : 39	205.9	−10.7	357.1	21.7	*YES*	*NO*	*YES*	77	0.177
2001	10	21	14 : 24 : 36	206.3	−10.9	357.0	22.1	*YES*	*NO*	*NO*	14	0.144
2001	10	22	14 : 46 : 21	206.7	−11.0	356.9	22.5	*YES*	*NO*	*NO*	1450[c]	0.206
2001	10	22	24 : 34 : 32	207.2	−11.2	356.6	23.1	*YES*	*NO*	*NO*	178	0.316
2001	10	23	00 : 10 : 56	207.6	−11.4	356.6	23.5	*YES*	*NO*	*YES*	418	0.245
2001	10	23	02 : 15 : 02	207.7	−11.4	356.6	23.6	*YES*	*NO*	*YES*	453[c]	0.063

Table 6.1 (cont'd)

Year	month	day	time[a] (UT)	RA (deg)	DEC (deg)	ϕ (deg)	θ (deg)	Trigger	BATSE	GOES	$T_{5\sigma}$ (s)	Hardness[b]
2001	10	30	08 : 33 : 39	214.7	−13.8	13.1	5.1	*YES*	*NO*	*NO*	301	0.057
2001	11	01	07 : 42 : 54	216.6	−14.5	16.2	3.9	*NO*	*NO*	*YES*	83	0.004
2001	11	01	15 : 17 : 08	216.9	−14.6	16.1	4.2	*YES*	*NO*	*NO*	213	0.198
2001	11	01	19 : 51 : 28	217.1	−14.6	16.0	4.3	*YES*	*NO*	*YES*	187	0.069
2001	11	04	06 : 40 : 41	219.5	−15.4	15.0	6.6	*YES*	*NO*	*YES*	136	0.172
2001	11	11	10 : 57 : 13	226.7	−17.5	339.5	−8.4	*YES*	*NO*	*YES*	349	0.365
2001	11	22	22 : 45 : 42	238.6	−20.3	12.9	25.5	*YES*	*NO*	*NO*	3146[c]	0.222
2001	11	28	18 : 01 : 21	244.7	−21.4	342.6	−17.0	*YES*	*NO*	*YES*	24	0.203
2001	11	29	01 : 44 : 41	245.1	−21.5	342.9	−17.2	*YES*	*NO*	*YES*	278	0.198
2001	11	29	05 : 16 : 43	245.2	−21.5	343.1	−17.2	*YES*	*NO*	*YES*	334	0.189
2001	12	29	16 : 35 : 01	278.8	−23.2	342.8	−16.6	*NO*	*NO*	*YES*	324	0.100
2001	12	30	15 : 03 : 29	279.8	−23.1	343.7	−17.1	*YES*	*NO*	*YES*	158	0.230
2002	01	13	03 : 06 : 43	294.6	−21.5	337.8	−12.3	*YES*	*NO*	*YES*	35	0.229
2002	02	10	18 : 40 : 39	324.2	−14.2	337.4	10.1	*YES*	*NO*	*YES*	373	0.214
2002	03	04	07 : 31 : 26	344.9	−6.5	354.5	−3.5	*YES*	*NO*	*YES*	47	0.144
2002	03	08	09 : 04 : 51	348.6	−4.9	355.1	2.1	*NO*	*NO*	*YES*	25	0.228
2002	03	08	16 : 52 : 17	348.9	−4.8	355.2	1.8	*YES*	*NO*	*YES*	86[c]	0.309
2002	03	10	01 : 34 : 40	350.2	−4.2	350.8	25.3	*YES*	*NO*	*YES*	156	0.466
2002	03	18	19 : 11 : 26	358.2	−0.8	359.4	14.0	*NO*	*NO*	*YES*	289	0.165
2002	04	02	04 : 33 : 15	11.3	4.9	3.9	6.5	*NO*	*NO*	*YES*	23	0.108
2002	04	09	00 : 39 : 29	17.5	7.4	7.5	−5.4	*YES*	*NO*	*YES*	224	0.258
2002	04	09	12 : 59 : 32	18.0	7.6	7.7	−5.8	*YES*	*NO*	*NO*	277	0.335
2002	04	14	03 : 24 : 25	22.2	9.3	346.7	22.2	*YES*	*NO*	*YES*	41	0.132
2002	04	14	04 : 49 : 56	22.3	9.3	346.6	22.2	*NO*	*NO*	*YES*	90	0.146
2002	04	15	02 : 48 : 39	23.2	9.7	346.1	23.0	*YES*	*NO*	*YES*	98	0.322
2002	04	17	07 : 53 : 48	25.2	10.5	347.1	26.0	*YES*	*NO*	*NO*	774	0.151
2002	04	17	16 : 50 : 49	25.5	10.6	346.9	26.4	*NO*	*NO*	*YES*	431	0.476
2002	04	21	01 : 03 : 54	28.7	11.7	12.5	−14.2	*YES*	*NO*	*NO*	826	0.250

[a] It is meant to be the time at which the signal exceeds the $5sigma$ level above the background.

[b] The spectral hardness parameter is defined as the ratio between the count–fluences collected in the hardest energy range (> 100 keV) over that in the softer -and strongly overlapping- $40 - 700$ keV energy range over the $T_{5\sigma}$ time. Zero means no observed photons above 100 keV.

[c] The gap in the light curve occurred during the passage of the spacecraft over the SAGA.

Conclusions

I have dealt with different aspects of the modern time domain astronomy. In the first part I studied the time variability of the prompt γ–ray emission of a sample of long GRBs detected by *Fermi*/GBM and *BeppoSAX*/GRBM. This analysis was done through a Fourier approach. I inspected the properties of the average PDS as well as the behaviour of individual PDS of GRBs. From the average analysis we found a clear trend which connects the average PDS slope with the the energy range. Indeed, the power–law index increases from -1.97 to -1.47 (the average PDS gets flatter) passing from the low (8–40 keV) to the high (200–1000 keV) energy channel. This reflects the fact that GRB light–curve spikiness increases with energy. We extended this analysis using a completely independent sample over the broad energy range allowed by *Fermi*/GBM (from 8 keV to 1 MeV). For the first time I extended the study of PDS up to 1 kHz in frequency with the very high time resolution provided by *BeppoSAX*/GRBM. The data revealed a sharp break at 1–2 Hz which provides a strong clue of the minimum characteristic time variability. The break is also slightly visible in the GBM data, however the instrument is not sensitive enough to make a strong statement. Combining our results with what was obtained from the *Swift* data set (Guidorzi et al. 2012), we observed that the presence of this break emerges only in the harder energy channels ($\geq$ 100 keV). Although a detailed theoretical explanation for this break is missing, it could be connected with different processes: e.g. an intrinsic inner engine variability, the dispersion of the bulk Lorentz factor distribution for a wind of relativistic shells, the average distance at which internal collisions dissipate energy into gamma–rays.

Several interpretations are also proposed to explain the average PDS slope. It is in broad agreement with a classical Kolmogorov spectrum generated from velocity fluctuations occurring in a turbulent medium. Also the jet breakout scenario as well as the magnetically–dominated outflows model or the neutrino cooling model could reasonably describe such slope. On the other hand, the individual PDS analysis provides information about the typical timing behaviour of each single event spotting the cases in which a characteristic time scale (τ) dominates the variance of the light curve. This

was made possible by the Bayesian procedure that was recently proposed by (Vaughan 2010) to properly model the PDS of time series affected by a strong red noise component (e.g., see Huppenkothen et al. 2013), which notoriously makes it difficult to establish proper thresholds for the detection of periodic features.

I found a robust relation between the characteristic duration of the individual pulses in the light curve (τ) and the overall duration of GRB ($\frac{T_{5\sigma}}{\tau} \sim 60$). The same trend was observed for both the *Fermi* sample as well as the *BeppoSAX* sample. Moreover we observed different PDS slope indices α for different values of peak energy $E_{\rm p}$. Indeed flatter PDS ($\alpha < 2$) are associated with higher $E_{\rm p}$ values than steep PDS ($\alpha > 2$). PDS of GRBs with high $E_{\rm p}$ values tend to be preferentially best fitted with power–laws instead of bent power–laws, with an average index around 1.7, similar to that found for the average PDS. The same analysis on the light curves of the lowest energy range (8–40 keV), shows that a simple power–law is the preferred model. Considering that for most GRBs $E_{\rm p}$ lies above 40 keV, I infer that no dominant time scale can be unambiguously found at energies below $E_{\rm p}$.

In addition, I observed another intriguing spectro–temporal link connected with the Band high–energy spectral index $\beta_{\rm B}$ and the PDS slope α: shallower PDS preferentially couple with shallower high–energy ($E > E_{\rm p}$) spectra.

Concerning the short GRBs (SGRBs) analysis, the canonical search for periodic or quasi–periodic signal did not yield any detection. Using the same sample I calibrated a specific technique devoted to detect the signature of an incoherent periodic signal potentially hidden within the time profiles of some SGRBs. I devised this peculiar procedure to search for the features predicted theoretically in the model by Stone et al. (2013), in which a NS–BH merger has a tilted accretion disc and jet with respect to the BH spin, which then induces the jet precession and oscillations in the gamma–ray flux with increasing period. No significant detection at 2σ out of a sample of 44 SGRBs was obtained by my tailored technique. I extracted useful upper limits to the fractional amplitude of any possible modulated signal for 14 GRBs with particularly high S/N ratio.

Notably, this is the first time that a Fourier study of SGRB prompt emission was feasible, since their study has traditionally been hampered by lower S/N with respect to long GRBs. A preliminary comparison between the analogous properties of a subsample of bright long GRBs and of SGRBs has revealed no striking difference between the two PDS power–law index distributions. Hence I found no evidence against a possible common general mechanism involved in the shock formation and the gamma–ray emission.

Although the poor statistics of these analysis does not allow me to rule out the physical scenario envisaged by Stone et al. (2013), I can state that the mixed mergers (BH–NS; the only one which is expected to give rise the evolving periodic signal I searched for) might not be a dominant fraction among the population of currently detected SGRBs, at least as pictured by such theoretical model. A more complete answer will come from a larger sample with comparable statistical quality in combination with the wealth of information that will be independently gathered through the study of gravitation wave radiation.

In the context of the systematic analysis of the *BeppoSAX*/GRBM data analysis, another project I carried out in the present work concerned the catalogue of solar X–ray flares. I devised a specific algorithm devoted to scan the continuous mode light–curves of the whole GRBM operational life. I ended up with a list of 380 solar flares. The $T_{5\sigma}$ time interval and the spectral hardness parameter ($\frac{(FLuence(>100\ keV)}{FLuence(40-700\ keV)}$) were computed for each catalogued event. We also reported the cases for which a common detection occurred by other experiments which were working during the same period. Spectral and timing analysis of these solar flares in the near future will provide more insights in the physical mechanism hidden behind the origin of this phenomena, exploiting the unique quality of these data owing to the large effective area of the GRBM in the interested energy band.

At optical wavelengths my activity was mainly focused on the development of new techniques to conduct an accurate and efficient followup activity of fast transient events. I ended up with a procedure which resorts the 2D–SSA method to identify and suppress the noise components observed in the frames collected by RINGO3, the optical polarimeter mounted at the focus of 2–m robotic Liverpool Telescope. The SSA technique is completely data–driven and is particularly suitable to characterise the different image components. This cleaning passage produced a slight improvement in the S/N ratio which was discovered favouring the source identification and simplifying the astrometric fitting process. Unlike the other complex techniques, this simple procedure is highly adaptable and it works frame by frame removing a large variety of noisy effects. We also inspected the possible nature of the observed distortions. Indeed we noticed that these components change with time ruling out the possibility of a flat field distortion. The potential of this technique had better be explored by further analysis on new frames and cameras. A wide range of different kinds of effects can be suppressed improving the data analysis process and maximising the scientific outcomes from the optical observations.

Finally, I performed real time GRB followup activity using the LCOGT telescopes. Together with other team members I developed a set of new scripts aimed to speed up the observational procedures faster and make them more effective. These scripts allowed us to detect several GRB optical counterparts and to identify GRBs exhibiting unusual behaviours (as was the case of GRB 141221A). Thanks to a close interaction with the LCOGT team we contributed to fix several problems in this first stage of network calibration: e.g., reaction times, temporary problems with instrumentation and data retrieval. The 2D–SSA technique is also used to suppress the noise in the i' filter frames affected by strong flat field fringing. Further efforts are aimed at tailoring the pipeline to the new targets and to future upgrades of the network.

In summary, time domain astronomy was the broad context in which I carried out multi–wavelength analysis both on archival high–energy data and on real–time optical data.increase I dealt with several advanced timing analysis, advanced Bayesian statistical techniques and applied to the broad wavelength data range from optical to gamma–rays. I also developed software which is being used by an international GRB collaboration to submit ToO requests, retrieve and promptly analyse real–time data from transient followup campaign. The astrophysical sources I targeted in my work mainly include GRBs, although other high–energy transients such as solar X–ray flares were also considered.

Some of these works were published in peer–review journals (2 accepted + 1 submitted as a lead author; 2 accepted + 1 submitted as a second author).

Last but not least, I actively joined a collaboration between my GRB team and a broad radio collaboration for the rapid followup of yet elusive radio transients such as the recently discovered fast radio bursts.

Bibliography

Actis M., et al., 2011, ExA, 32, 193

Adriani O., et al., 2015, arXiv 1502.00935

Akerlof C., et al., 2000, AJ, 119, 1901

Amati L., et al., 2002, A&A, 390, 81

Anderson T. W., Darling D. A., 1952, Annals of Math. Statistics, 23, 193

Aschwanden M. J., 2011, Self-Organized Criticality in Astrophysics. The Statistics of Nonlinear Processes in the Universe (New York: Springer- Praxis)

Aschwanden M. J., Zhang Jie, Liu Kai, 2013, ApJ, 775, 23

Atwood W.B., et al, 2009, ApJ, 697, 1071

Band D., 1993, ApJ, 413, 281

Barthelmy S. D., et al., 2005, Space Sci. Rev., 120, 143

Barthelmy, S. D., et al. 2005b, Nature, 438, 994

Bernardini M. G., et al, 2015, MNRAS, 446, 1129

Bhat P. N., Fishman G. J., Meegan C. A., Wilson R. B., Brock M. N., Paciesas W. S., 1992, Nature, 359, 217

Belli B. M., 1992, ApJ, 393, 266

Beloborodov A. M., Stern B. E., Svensson R., 1998, ApJ, 508, L25 (BSS98)

Beloborodov A. M., Stern B. E., Svensson R., 2000, ApJ, 535, 158 (BSS00)

Beloborodov A. M., 2010, MNRAS, 407, 1033

Berger, E., 2011, NewAR, 55, 1

Bertin E., Arnouts S., 1996, A&AS, 117, 393

Blandford, R. D., & Znajek, R. L. 1977, MNRAS, 179, 433

Boffetta G., Carbone V., Giuliani P., Veltri P., Vulpiani A., 1999, Physical Review Letters, 83, 4662

Bromberg, O., Nakar, E., Piran, T., Sari, R., 2013, ApJ, 764, 179

Brown, T. M., et al., 2013, PASP, 125, 1031

Calderone G, et al., 2015, MNRAS, 448, 403

Carballido A., Lee W. H., 2011, ApJ, 727, L41

Carilli C. L., Rawlings S., 2004, New Astron. Rev., 48, 979

Craiu Radu V. & Rosenthal Jeffrey S., 2014, Annual Review of Statistics and Its Application, 1, 179

D'Agostini G., 2005, physics/0511182

Degallaix J., et al., 2013, ASP Conf. Ser. 467 (9th LISA Symposium: Advanced Virgo Status), 151

Dichiara, S., Guidorzi, C., Amati, L., Frontera, F., 2013, MNRAS, 431, 3608

Dichiara S., Guidorzi C., Frontera F., Amati L., 2013b, ApJ, 777, 132

Derishev E. V., Kocharovsky V. V., 1999, ApJ, 521, 640

Eastwood J. P., Wheatland M. S., Hudson H. S., Krucker S., Bale S. D., Maksimovic M., Goetz K., Bougeret J.-L., 2010, ApJ, 708, L95

Fenimore E. E., in't Zand J. J. M., Norris J. P., Bonnell J. T., Nemiroff R. J., 1995, ApJ, 448, L101

Fong, W., Berger, E., 2013, ApJ, 776, 18

Fong, W. et al., 2014, ApJ, 780, 118

Frontera F., Fuligni, F., 1979, ApJ, 232, 590

Frontera F., et al., 2009, ApJS, 180, 192

Galassi M., et al., 2009, GNU Scientific Library Reference Manual (3rd Ed.), ISBN 0954612078

Gao H., Zhang B.-B., Zhang B., 2012, ApJ, 748, 134

Ghirlanda G., Ghisellini G., Nava L., 2011, MNRAS, 418, L109

Ghisellini G., 2011, in IAU Conf. Proc. 275, Jets at all Scales, 335

Ghil M, et al., 2002, Rev. Geophys., 40, 1

Giannios D., 2008, A&A, 480, 305

Giannios D., 2012, MNRAS, 422, 3092

Goldstein A., et al., 2012, ApJS, 199, 19

Golyandina N, Nekrutkin V, Zhigljavsky A, 2001, Analysis of Time Series Structure: SSA and Related Techniques, Chapman&Hall/CRC.

Golyandina N, Zhigljavsky A, 2013, Singular Spectrum Analysis for Time Series, Springer Briefs in Statistics. Springer-Verlag.

Golyandina N., Korobeynikov A., Shlemov A., Usevich K., 2013, arXiv 1309.5050

Greco G., Rosa R., Beskin G., Karpov S., Romano L., Guarnieri A., Bartolini C., Bedogni R., 2011, Nat. Sci. Rep., 1, 91

Gruber D., et al., 2011, A&A, 531, 20

Gruber D., et al., 2014, ApJS, 211, 12

Guidorzi C., Lacapra M., Frontera F., Montanari E., Amati L., Calura F., Nicastro L., Orlandini M., 2011, A&A, 526, A49

Guidorzi C., 2011, MNRAS, 415, 3561

Guidorzi C., Margutti R., Amati L., Campana S., Orlandini M., Romano P., Stamatikos M., Tagliaferri G., 2012, MNRAS, 422, 1785 (G12)

C. Guidorzi, S. Dichiara, F. Frontera, R. Margutti, A. Baldeschi, L. Amati, 2015, ApJ (accepted), arXiv 1501.02706

Harry, G. M., CQGra, 2010, 27, 084006

Horváth, I., 1998, ApJ, 508, 757

Horváth I., Balázs L. G., Bagoly Z., Ryde F., Mészáros A., 2006, A&A, 447, 23

Horváth, I., Balázs, L. G., Bagoly, Z., Veres, P., 2008, A&A, 489, L1

Horváth, I., 2009, Ap&SS, 323, 83

Horváth, I., et al., 2010, ApJ, 713, 552

Howell S. B., 2006, Handbook of CCD Astronomy, 2nd Ed., Cambridge University Press, Chps. 3,4

Huja, D., Mészáros, A., Řípa, J., 2009, A&A, 504, 67

Huppenkothen, D., et al., 2013, Apj, 768, 87

Huppenkothen D., et al., 2014, Apj, 787, 128

Ivezic Z., et al., 2008, arXiv 0805.2366

Kaneko Y., Preece R. D., Briggs M. S., Paciesas W. S., Meegan C. A., Band D. L., 2006, ApJS, 166, 298

Karle A., et al., 2003, NuPhS, 118, 388

S. Kobayashi, T. Piran, R. Sari, 1999, ApJ, 513, 669

Koen C., Bere A., 2012, MNRAS, 420, 405

Kruger A. T., Loredo T. J., Wasserman I., 2002, ApJ, 576, 932

Kumar P., Narayan R., Johnson J. L., 2008, MNRAS, 388, 1729

Lazzati D., 2002, MNRAS, 337, 1426

Law N. M., et al., 2009 ,PASP , 121, 1395

Leahy D. A., Darbro W., Elsner R. F., Weisskopf M. C., Sutherland P. G., Kahn S., Grindlay J. E., 1983, ApJ, 266, 160 (L83)

Lee H. K., Wijers R. A. M. J., Brown G. E., 2000, Physics Reports, 325, 83

Lorimer D. R., Bailes M., McLaughlin M. A., Narkevic D. J., Crawford F., 2007, Sci, 318, 777

Lee W. H., Ramirez–Ruiz E., 2007, New Journal of Physics , 9, 17

Li C., Zhong S. J., Wang L., Su W., Fang C., 2014, ApJ, 792, L26

Lu E. T., Hamilton R. J. 1991, ApJL, 380, L89

Lyutikov M., 2006, NJPh, 8, 119

Margutti R., 2009, PhD thesis, Univ. Bicocca, Milan, http://boa.unimib.it/handle/10281/7465

Margutti R., Bernardini G., Barniol Duran R., Guidorzi C., Shen R. F., Chincarini G., 2011, MNRAS, 410, 1064

Meegan C., et al., 2009, ApJ, 702, 791

Mészáros P., Rees M. J., 1992, MNRAS, 257, 29P

Mészáros P. & Rees M. J., 2011, ApJ, 733, L40

Morsony B. J., Lazzati D., Begelman M. C., 2010, ApJ, 723, 267

Mundell C. G., et al., 2007, Science, 315, 1822

Mundell C. G., et al., 2013, Nature, 504, 119

Mukherjee S., et al., 1998, ApJ, 508, 314

Nakar E., 2007, Phys. Rep., 442, 166

Narayan R.,Paczynski B.,Piran T., 1992, ApJ, 395, L83

Norris J. P., Nemiroff R. J., Bonnell J. T., Scargle J. D., Kouveliotou C., Paciesas W. S., Meegan C. A., Fishman G. J., 1996, ApJ, 459, 393

Paciesas W.S., et al., 1999, ApJS, 122, 465

Paciesas, W. S., et al., 2012, ApJS, 199, 18

Park H.-S., Ables E., Barthelmy S. D., Bionta R. M., Ott L. L., Parker E. L., Williams G. G., 1998, in Society of Photo-Optical Instrumentation Engineers (SPIE) Conference Series, 3355, 658

Panaitescu A., Spada M., Mészáros P., 1999, ApJ, 522, L105

Pe'er A., Mészáros P., Rees M. J., 2006, ApJ, 642, 995

Perna R., Armitage P. J., Zhang B., 2006, ApJ, 636, L29

Piran T., 1999, Phys. Rev., 314, 575

Piran T., 2004, Rev. Mod. Phys., 76, 1143

Piro L., et al., 1998, A&A, 329, 906

Preece R. D., Briggs M. S., Mallozzi R. S., Pendleton G. N., Paciesas W. S., Band D. L., 2000, ApJS, 126, 19

Proga D., Zhang B., 2006, MNRAS, 370, L61

Pruessner G., 2012, Self-Organised Criticality. Theory, Models and Characterisation (Cambridge: Cambridge Univ. Press)

Rees M. J., Mészáros P., 1994, ApJ, 430, L93

Rees M. J., Mészáros P., 2005, ApJ, 628, 847

Řípa, J., et al., 2009, A&A, 498, 399

Rossi E. M., Beloborodov A. M., Rees M. J., 2006, MNRAS, 369, 1797

Ryde F., Borgonovo L., Larsson S., Lund N., von Klienin A., Lichti G., 2003, A&A, 411, L331

Ruffert, M., & Janka, H.-T. 1999, A&A, 344, 573

Sakamoto T., et al., 2011, ApJS, 195, 2

Savaglio S., Glazebrook K., Le Borgne D., ApJ, 691, 182

Scargle J. D., Norris J., Bonnell J., 1998, in AIP Conf. Proc. 428, Gamma- Ray Bursts, ed C. Meegan, R. Preece, & T. Koshut (New York: AIP), 181

Shibata K., Magara T., 2011, Living Rev. Solar Phys. 8, 6

Soderberg, A. M., Berger, E., Kasliwal, M., et al. 2006, ApJ, 650, 261

Spada M., Panaitescu A., Mészáros P., 2000, ApJ, 537, 824

Spergel D. N., et al., 2003, ApJS, 148, 175

Spitler L. G., et al., 2014, ApJ, 790, 101

Stone, N., Loeb, A, & Berger, E, 2013, Phys. Rev., D87, 084053 (SLB13)

Steele I. A., Mundell C. G., Smith R. J., Kobayashi S., Guidorzi C., 2009, Nature, 462, 767

Su Y., Holman G. D., Dennis B. R., Tolbert A. K., Schwartz R. A., 2009, ApJ, 705, 1584

Su Y., Holman G. D., Dennis B. R., 2011, ApJ, 731, 106

Tanvir N.R., et al., 2013, Nature, 500, 547

Temperton C., 1983, J. of Computational Physics, 52, 1

Titarchuk L., Shaposhnikov N., Arefiev V., 2007, ApJ, 660, 556

Titarchuk L., Farinelli R., Amati L., Frontera F., 2012, ApJ, 752, 116

Thompson C., Mészáros P., Rees M. J. 2007, ApJ, 666, 1012

Thornton D., et al., 2013, Sci, 341, 53

van der Klis M., 1989, in NATO/ASI Ser. C, Vol. 262, Timing Neutron Stars, ed. H. Ögelman E. P. J. van den Heuvel (Dordrecht: Kluwer), 27

Kontar E. P., Brown J. C., 2006, ApJ, 653, 149

Kontar E. P., MacKinnon A. L., Schwartz R. A., Brown J. C. 2006, A&A, 446, 1157

Ulrich F. K., 2014, arXiv 1403.4065

Vanderspek R. K., Ricker G. R., Doty J. P., 1992, Astronomical Society of the Pacific Conference Series, 34, 123

Vaughan S., 2010, MNRAS, 402, 307 (V10)

Vaughan S., 2013, Royal Society of London Philosophical Transactions Series A, 371, 2011.0549

Vautard M, Ghil M, 1989, Physica D, 35, 395

Vestrand W. T., et al., 2002, Society of Photo-Optical Instrumentation Engineers (SPIE) Conference Series, 4845, 126

Vetere L., Massaro E., Costa E., Soffitta P., Ventura G., 2006, A&A, 447, 499

Walker K. C., Schaefer B. E., Fenimore E. E., 2000, ApJ, 537, 264

Wang F. Y., Dai Z. G., 2013, Nature Physics, 9, 465

Warren J. S., Hughes J. P., Badenes C., 2005, Bulletin of the American Astronomical Society, 37, 1437

Wheatland M. S., 2000, ApJ, 536, L109

Wheatland M. S., 2003, Sol. Phys., 214, 361

Zhang J., Huang G. L., 2004, Sol. Phys., 219, 135

Zhang B., MacFadyen A., Wang P., 2009, ApJ, 692, L40

Zhang B., 2011, C. R. Phys., 12, 206

Zhang B., Yan H., 2011, ApJ, 726, 90

Ringraziamenti

Vorrei innanzitutto ringraziare il Dr. Cristiano Guidorzi per l'impagabile aiuto offerto e per il preziosissimo bagaglio di conoscenze che mi ha reso accessibile introducendomi ai concetti di base dell'analisi statistica ed alle varie branche della time domain astronomy. Lo ringrazio soprattutto per l'infinita pazienza con la quale mi ha sempre assistito e guidato durante tutte le varie fasi di questo percorso. Il suo contributo è stato di fondamentale importanza.

Desidero poi ringraziare il Dr. Lorenzo Amati ed il Prof. Filippo Frontera per il costante interesse e la disponibilità con la quale si sono sempre adoperati al fine di migliorare ed arricchire il lavoro svolto.

Inoltre vorrei ringraziare tutti gli altri membri del gruppo di ricerca con cui ho lavorato a partire dal il Prof. Lev Titarchkuc, il Prof. Piero Rosati, il Dr. Enrico Virgilli, il Dr. Gabriel Bartosch Caminha e tutti i miei colleghi dottorandi del progetto IRAP: Dr. Disha Sawant, Dr. Tais Maiolino e Dr. Camillo Delgado. Ringrazio soprattutto Disha per l'aiuto offertomi durante la stesura di questa tesi.

Vorrei poi ringraziare anche la Prof.ssa Carole Mundell per l'enorme aiuto fornitomi durante il mio periodo di lavoro a Liverpool e per la fiducia che ha riposto in me.

Ringrazio in fine tutte le persone che mi sono state vicine e che mi hanno mostrato affetto e amicizia durante tutto questo periodo; in particolar modo tutti i dottorandi del dipartimento di Fisica ed i miei coinquilini.

Il ringraziamento più sentito (nonchè doveroso) va alla mia famiglia per l'immancabile supporto e il costante affetto con il quale mi sono stati sempre vicino durante tutte le fasi della mia vita accademica e non.

List of Publications

Dichiara, S.; Guidorzi, C.; Amati, L.; Frontera, F., 2013, Monthly Notices of the Royal Astronomical Society, 431, 3608-3617, *"Average power density spectrum of long GRBs detected with BeppoSAX/GRBM and with Fermi/GBM"*

Dichiara, S.; Guidorzi, C.; Frontera, F.; Amati, L., 2013, The Astrophysical Journal, 777, article id. 132, *"A Search for Pulsations in Short Gamma-Ray Bursts to Constrain their Progenitors"*

Guidorzi, C.; **Dichiara, S**.; Frontera, F.; Margutti, R.; Baldeschi, A.; Amati, L., 2015, The Astrophysical Journal, accepted for publication, 2015 January 12, arXiv:1501.02706, "A common stochastic process rules gamma-ray burst prompt emission and X-ray flares"

Amati, Lorenzo; **Dichiara, Simone**, 2013, Acta Polytechnica (supplement), 53, 686, *"Investigating the Ep, i –Eiso Correlation"*

Frontera, F.; Amati, L.; Farinelli, R.; **Dichiara, S**.; Guidorzi, C.; Landi, R.; Titarchuk, L., 2013, The Astrophysical Journal, 779, article id. 175, *"Comptonization Signatures in the Prompt Emission of Gamma-Ray Bursts"*

Castignani, G.; Guetta, D.; Pian, E.; Amati, L.; Puccetti, S.; **Dichiara, S.**, 2014, Astronomy & Astrophysics, 565, id.A60, *"Time delays between Fermi-LAT and GBM light curves of gamma-ray bursts"*

in preparation...

Guidorzi, C.; **Dichiara, S.** et al. , Monthly Notices of the Royal Astronomical Society, *"Clues on the gamma--ray burst prompt emission from the study of power density spectra --I. The Swift sample"*

Dichiara, S.; Guidorzi, C. et al. , Monthly Notices of the Royal Astronomical Society, *"Clues on the gamma--ray burst prompt emission from the power density spectra --II. The BeppoSAX and Fermi samples"*

Dichiara, S.; Amati, L. et al. , Astronomy & Astrophysics, *"An Investigation of the Instrumental Selection Effects affecting the measures of GRB parameters"*

Dereli, H.; Böer, M.; Gendre B.; Amati, L; **Dichiara, S**, Monthly Notices of the Royal Astronomical Society, *"Properties of Low Luminosity Afterglow Gamma-ray Bursts"*